

THE INFLUENCE OF STRAIN RATE, TEMPERATURE EFFECTS, AND
INSTABILITIES IN FAILURE MODELING FOR METAL ALLOYS

by

Stefano Dolci
A Dissertation
Submitted to the
Graduate Faculty
of
George Mason University
in Partial Fulfillment of
The Requirements for the Degree
of
Doctor of Philosophy
Physics

Committee:

_____	Dr. Cing-Dao Kan, Committee Chair
_____	Dr. Dhafer Marzougui, Committee Member
_____	Dr. Chi Yang, Committee Member
_____	Dr. Girum Solomon Urgessa, Committee Member
_____	Dr. Kelly Carney, Committee Member
_____	Dr. Paul So, Department Chairperson
_____	Dr. Donna M. Fox, Associate Dean, Office of Student Affairs & Special Programs, College of Science
_____	Dr. Fernando Miralles-Wihelm, Dean, College of Science
Date: _____	Summer Semester 2021 George Mason University Fairfax, VA

The Influence of Strain Rate, Temperature Effects, and Instabilities in Failure Modeling
for Metal Alloys

A Dissertation submitted in partial fulfillment of the requirements for the degree of
Doctor of Philosophy at George Mason University

by

Stefano Dolci
Master of Science
Politecnico di Milano, 2012
Bachelor of Science
Politecnico di Milano, 2007

Director: Cing-Dao Kan, Professor
Department of Physics and Astronomy

Summer Semester 2021
George Mason University
Fairfax, VA

Copyright 2021 Stefano Dolci
All Rights Reserved

DEDICATION

This is dedicated to my loving wife Ghazaul, my wonderful daughter Shirin Maddalena, and my adopted feathered son Mishan “the Babaloo” Luigi.

ACKNOWLEDGEMENTS

I would like to thank my dissertation committee, Dr. Cing-Dao Kan, Dr. Chi Yang, Dr. Dhafer Marzougui, Dr. Kelly S. Carney, and Dr. Girum S. Urgessa, who provided helpful advice throughout my research. Thank you to all the faculty and staff of the Center for Collision Safety and Analysis (CCSA) at George Mason University. I am especially grateful to Professor Cing-Dao Kan for his continued support and advice, both academic and technical, throughout my professional and academic career. I would also like to acknowledge Dr. Chung-Kyu Park and Dr. Leyu Wang from the CCSA, whom I have worked side by side for many years. I would like to thank Dr. Amos Gilat, Dr. Jeremy Seidt from the Ohio State University, Dr. Daniel Cordasco and William Emmerling from the Federal Aviation Administration (FAA) , Dr. Michael Pereira from the National Aeronautics and Space Administration (NASA), for their technical and financial support under the Aircraft Catastrophic Failure Prevention Research Program (ACFPP) project for the Development and Implementation of a new material model in LS-DYNA® for metallic materials under FAA cooperative agreement 13-G-020. Acknowledgments to Gunther Blankenhorn from Ansys for his support while implementing the developed material model. Thanks to Dr. Tobias Achstetter from Tesla for his availability in helping an old friend even when he found a new job on the other side of the continent. A heartfelt thank you to Dr. Kelly S. Carney for his guidance on metals high strain behavior and for his fatherly advice. The in-depth knowledge he provided in this research was truly appreciated but even more appreciated was his friendship. I would like to especially thank Paul Du Bois for his invaluable advice and mentorship throughout my PhD research. His expertise was essential, and I cannot thank him enough for all he has taught me over the years I have been fortunate to work alongside him. Without his support this research would not have been possible. Finally, I would like to thank my friends and family, especially my in-laws Nahid and Homayoon for welcoming me in their lives, my sisters Federica and Cristina and my parents, Daniela and Camillo, who have always encouraged and supported me even from far away. Without them I would not be where I am today. Special thanks to my wife Ghazaul, who recently gave me the most precious gift of all, our daughter Shirin. Last but not least, a thank you to my green friend Mishan who is always there to cheer me up when I had a bad day.

TABLE OF CONTENTS

List of Tables	viii
List of Figures	x
List of Equations	xiv
List of Abbreviations	xvi
Abstract	xvii
1. Introduction.....	1
1.1. Motivation.....	1
1.2. Problem Definition.....	4
1.2.1. Material Model.....	6
1.2.2. Materials Selected for the Study	7
1.2.3. Incorporation of Material Properties at High Strain Rates	11
1.2.4. Adiabatic Shear Band Simulation Issues	12
1.3. Approach.....	14
2. Literature Review.....	16
2.1. Material Behavior at High Strain Rate.....	16
2.2. Differences Between FCC, BCC, and HPC Materials.....	26
2.3. Adiabatic Shear Bands	33
2.4. Taylor-Quinney Coefficient.....	40
2.5. Mesh Sensitivity Regularization for ASB.....	42
3. Material Model and Characterization	44
3.1. Introduction.....	44
3.2. Theoretical Approach.....	44
3.2.1. Constitutive Relationship.....	44
3.2.2. Accumulated Failure	46

3.3.	Incorporation of Inconel-718 Material Test Data into Material Model Input Parameters for Tabulated Johnson-Cook Material [25].....	48
3.3.1.	Common Elastic-Plastic Modeling Revisited	49
3.3.2.	Violations of Common Assumptions.....	55
3.3.3.	Stress Strain Relationship after Necking	56
3.3.4.	Isothermal Effect.....	62
3.3.5.	Temperature Dependent Tabulated Input	62
3.3.6.	Strain Rate Dependent Tabulated Input	63
3.3.7.	Conversion of Plastic Work into Heat (Taylor-Quinney Effect)	64
	Strain Rate Is Not a Constant.....	65
3.3.8.	High Strain Rate Sensitivity.....	66
3.3.9.	Stress Strain Tabulated Input of Multiple Strain Rates and Temperatures.	69
3.4.	Inconel-718 Updated Very High Strain Rate Model	73
3.4.1.	Stress flow sensitivity at very high strain rates.....	73
3.4.2.	Indentation Comparison using Hybrid Analysis.....	77
3.5.	Characterization of the Failure Surface Locus.....	80
3.5.1.	Failure Surface	84
3.5.2.	Temperature Scaling Function	89
3.5.3.	Strain Rate Scaling Function	90
3.5.4.	Element size regularization curve	91
4.	Adiabatic Shear Band 2D Simulation.....	92
4.1.	Boundary Conditions	93
4.2.	Results.....	94
4.3.	Discussion	110
5.	Implementation	111
5.1.	Taylor-Quinney Coefficient.....	111
5.2.	Algorithm.....	116
5.2.1.	Flow chart	117
5.3.	Single Element Verification.....	121
5.4.	2D Simulation Verification.....	127
6.	Validation/Ballistic Limit Simulations	131
6.1.	Ballistic Impact Tests.....	132
6.1.1.	Target Geometry	132

6.1.2. Cylindrical Projectile	132
6.1.3. Ballistic Impact Tests Apparatus	134
6.1.4. Test Results	135
6.2. Ballistic Impacts Simulations	138
6.2.1. Numerical models of the ballistic impact with cylindrical projectiles	138
6.2.2. Tabulated Beta Characterization	139
6.2.3. Results	141
6.3. Discussion	153
7. Regularization for Element Size	154
7.1. Numerical models of the ballistic impact with cylindrical projectiles	154
7.2. Procedure	156
7.3. Results	158
7.4. Discussion	179
8. Conclusions	181
Appendix	185
Appendix A.	185
Appendix B.	190
Appendix C.	197
Appendix D.	201
References	205

LIST OF TABLES

Table	Page
Table 1: Certificated chemical composition in %wt. of Inconel 718 nickel-base superalloy	10
Table 2: Temperature raise in 0.5” Inconel-718 plate. Impact velocity 203 [m/s], 80 elements trough the thickness, elastic projectile	76
Table 3: Data used to construct the failure surface	87
Table 4: 2D simulations	93
Table 5: Inco_100x100_BC1_05 simulation	96
Table 6: Inco_100x100_BC1_1 simulation	97
Table 7: Inco_100x100_BC1_4 simulation	98
Table 8: Inco_100x100_BC1_20 simulation	99
Table 9: Inco_100x100_BC1_200 simulation	100
Table 10: Inco_100x100_BC8_05 simulation	101
Table 11: Inco_100x100_BC8_1 simulation	102
Table 12: Inco_100x100_BC8_4 simulation	103
Table 13: Inco_100x100_BC8_20 simulation	104
Table 14: Inco_100_4_BC1 simulation	105
Table 15: Inco_100_4_BC8 simulation	106
Table 16: Inco_100_10_BC1 simulation	107
Table 17: Inco_100_10_BC8 simulation	108
Table 18: TQC β_{test}^* : parameters for the transition from normal to ASB condition and maximum value of TQC inside the ASB for each element size.	121
Table 19: Comparison of simulation Inco_100x100_BC1_200: original vs. modified material model	128
Table 20: Projectile dimensions.....	133
Table 21: Panel Impact Test Results [118]	135
Table 22: Ballistic impact simulations 0.2 mm elements mesh characteristics	139
Table 23: Taylor-Quinney Tabulated input parameter set	139
Table 24: Ballistic simulations exit velocity results	141
Table 25: DB266 Simulation Results. Temperature line contours $\beta_{TAB,0.2}^*$ (left) vs. $\beta=0.8$ (right)	149
Table 26: Meshes for various element sizes	155
Table 27: Maximum shear strain and plastic strain rate where the transition from normal to ASB condition initiate and maximum value of TQC inside the ASB for each mesh.	156
Table 28: Element size regularization procedure: exit velocity simulated for 3 tests for each mesh using a specifically characterized TQC for each element size.....	157

Table 29: Comparison of the exit velocities between the simulations of the modified J-C material model equipped with the TQC developed for the 0.2mm mesh ($\beta_{TAB,0.2}^*$), equipped with the TQC regularized per mesh element size (β_{TAB}^*) and tests.....	159
Table 30: Modified J-C material model simulations with the TQC regularized per mesh element size (β_{TAB}^*), estimated crack propagation velocity	160
Table 31: DB272 temperature comparison at 0.5ms for all meshes	162
Table 32: DB268 temperature comparison at 0.5ms for all meshes	163
Table 33: DB266 temperature comparison at 0.5ms for all meshes	164
Table 34: DB266 temperature comparison sequence for 0.2mm mesh. β_{TAB}^* (left) vs. $\beta_{TAB,0.2}^*$ (right).....	165
Table 35: DB266 temperature comparison sequence for 0.4mm mesh. β_{TAB}^* (left) vs. $\beta_{TAB,0.2}^*$ (right).....	168
Table 36: DB266 temperature comparison sequence for 0.8mm mesh. β_{TAB}^* (left) vs. $\beta_{TAB,0.2}^*$ (right).....	171
Table 37: DB266 temperature comparison sequence for 1.6mm mesh. β_{TAB}^* (left) vs. $\beta_{TAB,0.2}^*$ (right).....	174

LIST OF FIGURES

Figure	Page
Figure 1: NTSB investigators examine the damaged Southwest Airlines engine on April 17 2018 [8].....	3
Figure 2: Adiabatic shear bands and the micro-crack near crater wall in 2519-T87 aluminum alloy target [19].....	6
Figure 3: Schematic illustration of a) FCC-structure b) BCC-structure and c) HCP-structure [23]	8
Figure 4: Typical Material Distribution in Jet Engine [26]	9
Figure 5: Line sketch of an ordered FCC crystal structure of gamma' phase. Solid circles represent nickel atoms, shared with adjacent cube. Open circles represent aluminum or titanium atoms, shared with eight cubes at each corner. dotted lines show hidden atoms [35].....	10
Figure 6: Different extrapolation of high strain stress flow [15]	11
Figure 7: a) Titanium and b) Inconel 0.5-inch plates ballistic limits [15], [39]	13
Figure 8: Variation of the lower yield stress with strain rate in a 0.12% C steel. Three characteristic regions of the flow stress sensitivity may be distinguished: (I) small temperature and strain rate sensitivity; (II) greater temperature and strain rate sensitivity; (IV) rapid increase of strain rate sensitivity [43]	17
Figure 9: The relationship between dynamic increase factor (DIF), defined as the ratio of dynamic strength or yield stress to the quasi-static strength or yield stress of materials, and common logarithmic of strain-rate for 7075 aluminum [56]	20
Figure 10: Variation of stress with strain rate at temperature of 25°C [64].....	21
Figure 11: Hardness versus strain rate for 1018 steel [68]	22
Figure 12: Schematic behavior of yield stress versus temperature of metals [72]	23
Figure 13: Variation of flow stress with strain rate as function of temperature at true strains of 0.1 [80]	25
Figure 14: Yield stress versus strain rate for a nickel against two formulations of the Johnson-Cook model [83].....	27
Figure 15: Normalized flow stress versus strain rate of OFHC copper [72]	30
Figure 16: Strain rate sensitivity definition for BCC and FCC metals [36]	31
Figure 17: Evolution of the normalized equivalent stress with strain rate for different BCC and FCC metals [36]	31
Figure 18: Calibration of the viscous drag stress component for a FCC metal [36]	32
Figure 19: Inconel 718 EBSD map (superimposed on the band contrast) of the region adjacent to the shear [103]	39
Figure 20: *MAT_224 input deck	49

Figure 21: Standard Tensile Test [28]	50
Figure 22: Left: Necking Judgment Line and Stress Strain Curve. Right: Stress Strain Curve after Trimming	59
Figure 23: Extrapolated Curves after Necking	60
Figure 24: Force Displacement Result of Tensile Test Simulation with Matching Hardening Curve Inputs	61
Figure 25: First Principal Plastic Strain Contour at Failure Comparison	61
Figure 26: Temperature dependent input curves	63
Figure 27: Stress at 5% strain. All tests	67
Figure 28: Stress at 5% strain. Global data curve fit	68
Figure 29: Final strain rate sensitivity at 5% strain	70
Figure 30: Force vs. displacement	72
Figure 31: Strain rate vs. strain	72
Figure 32: Stress at 5% strain curve fit. Different very high strain rate extrapolations ...	75
Figure 33: 3D comparison of the scanned plates from the tests and the simulation results	78
Figure 34: Indentation comparison of unpenetrated test DB271 (see Figure 33) and hybrid simulation results in x and y direction for 3 material very high strain rate models (see Table 21)	79
Figure 35: Comparison of the resulting indentation in a section of the top surface of the Inco 0.5" plate for 3 different material high strain rate extrapolations (see Figure 32). Test DB272 (see Table 21)	79
Figure 36: Comparison of the resulting indentation in a section of the bottom surface of the Inco 0.5" plate for 3 different material high strain rate extrapolations (see Figure 32). Test DB272 (see Table 21)	79
Figure 37: Tests Triaxiality vs Lode Parameter	86
Figure 38: Failure Surface. The red points are the data from Table 3. The green point are used to generate the failure surface and are generated through 3D spline of the data over the plane stress curve, and Lode =1,0 and -1 lines (see Figure 39)	88
Figure 39: 3D spline interpolation of data points	88
Figure 40: Temperature failure strain scaling function	89
Figure 41: Strain rate failure strain scaling function	90
Figure 42: Element size failure strain scaling function	91
Figure 43: 2D meshes: 10000 elements, 225 elements and 100 elements	93
Figure 44: Boundary conditions a) 1 and b) 2	94
Figure 45: 5 elements across the shear band selection example	95
Figure 46: Boundary conditions of the one element simulations	122
Figure 47: Single element 0.2 mm, Tension. Transition to $\beta_{max}^* = 10$ expected at $\gamma_{max} > 0.25$ and $\dot{\epsilon}_p > 8000 \text{ s}^{-1}$	123
Figure 48: Single element 0.4 mm, Tension. Transition to $\beta_{max}^* = 12.5$ expected at $\gamma_{max} > 0.23$ and $\dot{\epsilon}_p > 8000 \text{ s}^{-1}$	123
Figure 49: Single element 0.8 mm, Tension. Transition to $\beta_{max}^* = 13$ expected at $\gamma_{max} > 0.18$ and $\dot{\epsilon}_p > 8000 \text{ s}^{-1}$	124

Figure 50: Single element 1.6 mm, Tension. Transition to $\beta_{max}^* = 23$ expected at $\gamma_{max} > 0.15$ and $\dot{\epsilon}_p > 8000 \text{ s}^{-1}$	124
Figure 51: Single element 0.2 mm, Shear. Transition to $\beta_{max}^* = 10$ expected at $\gamma_{max} > 0.25$ and $\dot{\epsilon}_p > 8000 \text{ s}^{-1}$	125
Figure 52: Single element 0.4 mm, Shear. Transition to $\beta_{max}^* = 12.5$ expected at $\gamma_{max} > 0.23$ and $\dot{\epsilon}_p > 8000 \text{ s}^{-1}$	125
Figure 53: Single element 0.8 mm, Shear. Transition to $\beta_{max}^* = 13$ expected at $\gamma_{max} > 0.18$ and $\dot{\epsilon}_p > 8000 \text{ s}^{-1}$	126
Figure 54: Single element 1.6 mm, Shear. Transition to $\beta_{max}^* = 23$ expected at $\gamma_{max} > 0.15$ and $\dot{\epsilon}_p > 8000 \text{ s}^{-1}$	126
Figure 55: 0.2mm mesh 2D simulation. Element in the shear band transition to $\beta_{max}^* = 15$ expected at $\gamma_{max} > 0.25$ and $\dot{\epsilon}_p > 8000 \text{ s}^{-1}$	130
Figure 56: Specimen and fixture geometry [36]	133
Figure 57: Projectile geometry (dimensions in mm) [36]	133
Figure 58: Large vacuum gas gun. Shown with 76.2mm (3 inch) diameter gun barrel [118]. (Image with 50.8 mm diameter barrel is not available.)	134
Figure 59: Ballistic limit Inconel-718 12.7mm (0.5inch) plate tests	136
Figure 60: Penetration results for 12.7mm (0.5inch) panels. Velocity at which probability of penetration is 50% was 195m/s [118]	136
Figure 61: Fully contained test (DB269 – 180.4 m/s) plate post-test. Clock wise: rear view, front view, front view close-up, rear view close up	137
Figure 62: Fully penetrated tests (DB266 – 203.8 m/s) plate post-test. Clock wise: front view, rear view, rear view close up, front view close-up	137
Figure 63: TQC discretization curves TQC as function of maximum shear strain and strain rate	140
Figure 64: Ballistic limit Inconel 718 12.7mm (0.5inch) plate tests vs. simulations	142
Figure 65: Projectile bottom node z-velocity SAE 6000Hz filter	142
Figure 66: DB266 – 203.8m/s ballistic impact simulation	143
Figure 67: “Bull's eye” part	144
Figure 68: “Bull's eye” part section (A-A) and elements selected in the section	144
Figure 69: DB266 – 203.8m/s $\beta_{TAB,0.2}^*$ temperature of the elements across the ASB (see Figure 68)	145
Figure 70: DB266 – 203.8m/s ballistic impact simulation. ASB development on the “bull's eye” part, section A-A (see Figure 68). Temperature contours.	147
Figure 71: Plates cut for results visualization purpose	148
Figure 72: Evolution of transition maximum shear strain and maximum TQC inside the ASB with element size	157
Figure 73: Crack propagation velocity	160
Figure 74: β_{max}^* data curve fitting of 2D simulations and ballistic limit simulations with various element size	161
Figure 75: Ballistic limit simulations, β_{TAB}^* vs. $\beta_{TAB,0.2}^*$	177
Figure 76: Energies for the simulations of test DB266	177

Figure 77: Energy by part for 0.2mm element size mesh of test DB266.....	178
Figure 78: Energy by part for 0.4mm element size mesh of test DB266.....	178
Figure 79: Energy by part for 0.8mm element size mesh of test DB266.....	178
Figure 80: Energy by part for 1.6mm element size mesh of test DB266.....	179

LIST OF EQUATIONS

Equation	Page
Equation 1: Constitutive relationship.....	44
Equation 2: Jaumann rate of the stress tensor	45
Equation 3: Young's modulus	45
Equation 4: Poisson's ratio	45
Equation 5: Von Mises-type yield surface.....	45
Equation 6: Dependency of the yield surface upon plastic strain and plastic strain rate..	46
Equation 7: Plastic strain rate	46
Equation 8: Triaxiality	47
Equation 9: Lode parameter.....	47
Equation 10: Plastic failure strain	47
Equation 11: Damage parameter.....	48
Equation 12: Engineering stress.....	50
Equation 13: Engineering strain.....	51
Equation 14: True stress.....	51
Equation 15: True strain.....	51
Equation 16: Plastic strain	52
Equation 17: Effective plastic strain	53
Equation 18: Plastic strain rate at constant volume	53
Equation 19: Yield surface.....	54
Equation 20: Effective von Mises stress	54
Equation 21: Stress under uniaxial tension	54
Equation 22: Stresses in tension post necking	55
Equation 23: Necking conditions.....	57
Equation 24: Hardening curves extrapolation formula.....	57
Equation 25: Hardening curves continuity conditions.....	58
Equation 26: Hardening curves smoothing conditions	58
Equation 27: Fitting parameters relationships	58
Equation 28: Strain rate is not a constant.....	65
Equation 29: Engineering strain rate before necking.....	65
Equation 30: Engineering strain rate after necking.....	66
Equation 31: Before and after necking engineering strain rate relationship	66
Equation 32: Constitutive relationship.....	111
Equation 33: Temperature increment.....	112
Equation 34: Nonlinear equation system for tabulated J-C material model	112
Equation 35: TQC integral formulation.....	113

Equation 36: TQC differential formulation used in tabulated J-C material model.....	113
Equation 37: Definition of TQC in J-C material model	114
Equation 38: Definition of modified TQC in modified J-C material model.....	114
Equation 39: Tabulated modified TQC as a function of tabulated parameters.....	115
Equation 40: Maximum shear strain	115
Equation 41: Nonlinear equation system for the modified tabulated J-C material model	116

LIST OF ABBREVIATIONS

Johnson Cook	J-C
Taylor-Quinney Coefficient.....	TQC
Uncontained engine event.....	UEE
Finite Element Model	FEM
Finite Element	FE

ABSTRACT

THE INFLUENCE OF STRAIN RATE, TEMPERATURE EFFECTS, AND INSTABILITIES IN FAILURE MODELING FOR METAL ALLOYS

Stefano Dolci, Ph.D.

George Mason University, 2021

Dissertation Director: Dr. Cing-Dao Kan

To improve the survivability of structures it is important to understand the dynamic failure behavior under impact loading. Impact tests have revealed that mode of failure on metal superalloys thick plate at high-speed impact is what is known as Adiabatic shear band (ASB). The tabulated J-C material model is the current state of the art for FEM of high velocity impacts. The development of the tabulated J-C material model started from the consideration that materials under impact are affected by large deformations, high strain rates, temperature softening, and varying stress-states and that the failure is also changing as a function of the state of stress.

Validated numerical 2D simulations revealed that the current J-C material model is successful in predicting this mode of failure only under the condition of using meshes composed of elements with a size that is of the same magnitude order of the ASB width.

Because the ASB width of some high performance metal alloys is in the order of $1\mu\text{m}$, the material model cannot be use in practical real application to predict ASB.

This thesis describes the upgrades implemented in the current Finite Element Model (FEM) of tabulated Johnson Cook (J-C) material model that allow the development of Adiabatic Shear Bands (ASBs) under the correct loading conditions in meshes with element size of practical use in current engineering applications. Ductile deformation and failure mechanism of Inconel 718 superalloy were investigated experimentally and numerically for quasi-static and dynamic conditions at various temperatures and stress states. Impact tests were used to derive high strain rate strain-stress characteristics, proven to be vital to correctly simulate ASBs, using hybrid explicit-implicit simulations. Tabulated inputs of characterized material tests results were directly used to describe both the constitutive and failure characteristics of the material model. Full scale impact tests were used to validate and show robustness, accuracy, and efficiency of the modified material model. It is shown that the modified J-C material model can predict ballistic limit and failure modes accurately for structures under impact, modeled with meshes composed of element of size compatible with modern commonly available computational resources even when the failure mode is ASB.

The presented material model can be implemented into most available Finite Element software. As part of this research, it was implemented into the commercial Finite Element Solver LS-DYNA[®] as a modification of *MAT_TABULATED_JOHNSON_COOK (*MAT 224) for solid elements.

1. INTRODUCTION

1.1. Motivation

An uncontained engine event (UEE) occurs when an engine failure results in fragments of rotating engine parts penetrating and exiting through the engine case. Uncontained turbine engine disk failures within an aircraft engine present a direct hazard to an airplane and its passengers because the high-energy disk fragments can penetrate the cabin or fuel tanks, damage flight control surfaces, or sever flammable fluid or hydraulic lines [1]. An UEE is a significant concern for the airworthiness of aircrafts and the safety of their operations. Over 340 uncontained failures have been identified by SAE Aerospace Information Reports (AIR 4003, AIR 4770, SP 1270) for the period from 1976 to 1989 [2]. 119 uncontained failures in jet engines were reported by the Federal Aviation Administration (FAA) and the Aerospace Industries Association (AIA) between the years 1992 and 2000 [3]. These reports identify fan, compressor disks, and blades as some of the most critical and potentially dangerous failures. Over half of the reported cases involve uncontained fan and compressor disks, and blades impacting the fuselage, making an accurate analysis of the fragments impact a high priority. In the last years, several cases of UEE came to the media's attention:

- On October 28, 2016. American Airlines Flight 383 was scheduled to fly from Chicago O'Hare International Airport to Miami International Airport. The Boeing

767-300ER was accelerating for takeoff when the aircraft's right engine suffered an uncontained failure that led to a severe fire [4].

- On September 30, 2017. Air France Flight 66, a scheduled international passenger flight from Paris Charles de Gaulle Airport to Los Angeles International Airport, suffered an uncontained engine failure. The Air France Airbus A380-861 made an emergency landing at Goose Bay Airport, Canada [5].
- On April 17, 2018, Southwest Airlines Flight 1380, a Boeing 737-700, experienced an engine failure after departing from New York–LaGuardia Airport en route to Dallas Love Field. Debris from the failed engine damaged the fuselage, causing rapid depressurization of the aircraft after damaging a cabin window. The crew conducted an emergency descent and diverted to Philadelphia International Airport (Figure 1) [6].
- On February 20, 2021, United Airlines Flight 328, a domestic passenger flight from Denver International Airport to Honolulu International Airport it experienced a right engine failure shortly after takeoff. The Boeing 777-200 suffered an uncontained engine failure resulting in a debris field at least 1 mile (1.6 km) wide over the Commons Park suburb of Broomfield, Colorado and surrounding area. The flight landed safely with no injuries or loss of life to those in the aircraft or on the ground [7].



Figure 1: NTSB investigators examine the damaged Southwest Airlines engine on April 17 2018 [8]

To ensure the safety of passengers and flight crew, governmental aviation authorities, such as the FAA (United States) and the European Aviation Safety Agency (EASA) require that commercial jet engines contain any single compressor or turbine blade after a failure during engine operation [9], [10, p. 33], [11, p. 25]. The FAA further requires that jet engine manufacturers demonstrate (through certification testing), that the most critical blade stays contained within the engine when a blade is released, and while the engine is running at full rated thrust [12]. Due to the complexity and cost of the machineries involved, these certification tests are extremely costly. Therefore, accurate

computer simulations help ensure that these tests are successful and may provide an efficient and economical alternative to certification tests in the future.

1.2. Problem Definition

The loss of blades in turbine engines, as depicted in Figure 1, can be caused by material failure due to fatigue, bird strike [13], or other foreign objects ingested by the engine. On a modern high-bypass turbofan the fan blades rotate at a very high rate, on the order of 5000 rpm. The turbine and high-pressure compressor stages rotate at an even higher rate, above 10000 rpm. When one of the blades is released, the impact produces a strain rate level much higher than in common automotive crashes but not as high as fully adiabatic ballistic impacts.

The maximum plastic strain rate occurring during a blade containment impact ranges between 5×10^3 to 10^5 s^{-1} . Measuring the properties of the materials experimentally at these strain rate levels is difficult and requires specialized equipment and techniques. Characterizing the material properties at strain rates above 10^4 s^{-1} is even more challenging. However, determining the behavior of the metals at strain rates greater than 10^4 s^{-1} is a crucial factor in defining the dynamic and failure response of the complete system. Accurately modeling the strain rate sensitivity of the metal alloys is crucial for precise ballistic limit predictions [14]. Moreover, modeling this behavior accurately allows for simulation failure mechanisms consistent with the failures observed in the ballistic tests [15].

Additionally, a common failure mechanism occurring when blunt projectiles impact thick plates of many metals is known as an adiabatic shear band. Adiabatic shear

bands (ASB) are thermodynamic phenomena occurring at high strain rates and are characterized by large deformations localized in a narrow band, typically 5-500 μm and consisting of very highly sheared material. "Adiabatic" is a thermodynamic term defined as an absence of heat transfer. The heat produced by the large plastic deformations is retained in the zone where it is created [16] (Figure 2). ASBs are observed in many applications such as chips formation in machining, forging, and ballistic impact loading. In most cases, the occurrence of adiabatic shearing is undesirable, as the formation of ASBs causes the material to lose its load carrying and energy dissipation capacity. Moreover, adiabatic shearing is known to be a precursor to failure [17]. The ASB unique dynamic failure mechanism typically results in a catastrophic failure due to the concentrated shear deformation mode. It is generally considered as a material or structural instability and as such, to some extent ASB is hard to control or predict [18].

Prediction of ASBs is difficult due to the extreme narrowness, or localization, of the shear band. Due to the extreme localization of the shear band, it is exceptionally difficult to model ASBs using the Finite Element Method (FEM) because the mesh size required is often too small to be practical for real applications. A numerical material model that has predictive capabilities under these circumstances and is suitable for large scale application must incorporate all these effects and be able to neutralize the effects of a large, practical mesh size.

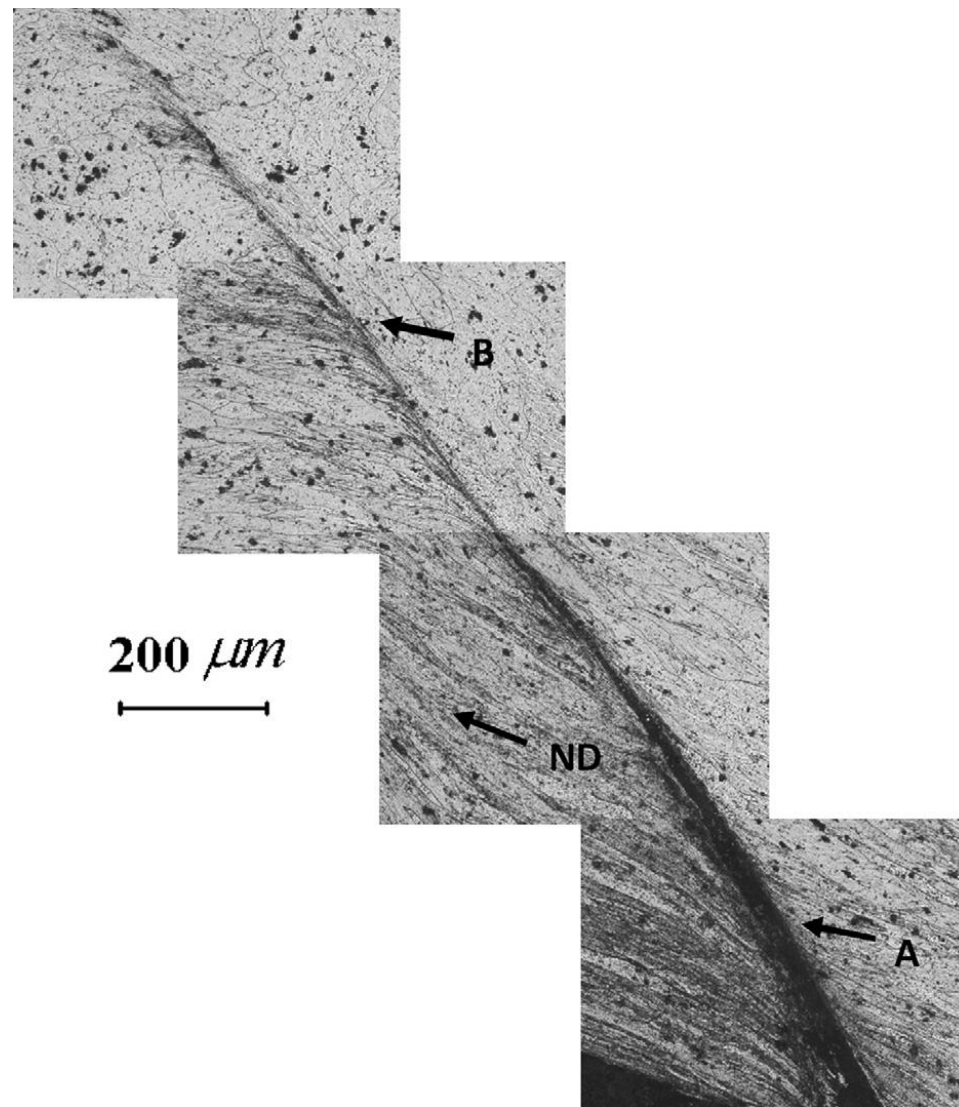


Figure 2: Adiabatic shear bands and the micro-crack near crater wall in 2519-T87 aluminum alloy target [19]

1.2.1. Material Model

Past research efforts have identified that one of the challenges in the creation of reliable, verifiable, and potentially predictive ballistic simulations is the modeling of material behavior at high rates of strain. For example, the high speed of the impacts

causes significant variations in material yield, thermal effects, and final rupture, all as a function of strain rate.

The Aircraft Catastrophic Failure Prevention Research Program (ACFPR)¹ has worked to develop a new material constitutive model to support certification by analysis. The research was directed toward improving the numerical modeling of turbine engine blade-out containment tests required for certification of aircraft engines. Specifically, a modified Johnson-Cook [20] material constitutive model with tabulated properties that is based on the generalized Von-Mises plasticity theory has been successfully implemented [21]. This material constitutive model is able to account for the effects stated above and was selected as preferred tool to perform this effort. It is an elasto-viscoplastic model with arbitrary stress versus strain curve(s) and arbitrary strain rate dependency. Moreover, the model accounts for plastic heating that causes adiabatic temperature increasing and material softening. Finally, tabulated plastic failure strain can be defined as a function of the state of stress (triaxiality and Lode parameter), strain rate, temperature and/or element size [22].

1.2.2. Materials Selected for the Study

The atoms in a perfect crystal are arranged in a regular and repeated three-dimensional array. Several different possible arrangements of the individual atoms exist and hence, different crystal structures exist. Hexagonal close packed (HCP), body-centered cubic (BCC) and face-centered cubic (FCC) are the most common crystal

¹ACFPR members: George Mason University (GMU), Ohio State University (OSU), National Aeronautics and Space Administration (NASA) Glenn Research Center, and Federal Aviation Administration (FAA)

structures in metals, (Figure 3). The regular crystal structure is usually, however, delimited in their extensions [23].

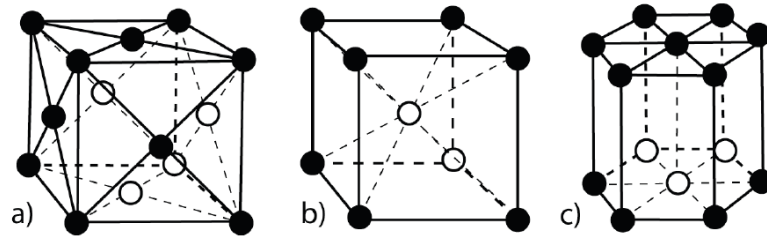


Figure 3: Schematic illustration of a) FCC-structure b) BCC-structure and c) HCP-structure [23]

The following materials were chosen for this study, because they are commonly found in modern jet engine components (Figure 4) and because of their different and representative crystalline structures.

- Titanium Ti6Al4V (Aluminum Vanadium)

Ti6Al4V is an α -rich α - β Ti-alloy at room temperature. Its properties provide a good balance between high strength, high toughness, and positive response to heat treatment. The α -phase of Ti6Al4V has a hexagonal (HCP) crystal structure whereas the β -phase has a body-centered cubic (BCC) structure. Thermally-induced transformation of α into β phase typically occurs between 600 °C and 995 °C [24]. In Ti6Al4V, small amounts of β -phase exist at room temperature due to the stabilizing effect of vanadium. The presence of other elements than V and Al such as O, N, and C (α -stabilizing) and H, Mo, Fe, and Cr (β -stabilizing) also plays an important role in the metallurgy of Ti6Al4V. Typically, all the Fe present in the alloy is confined to the β -phase [17], [25].

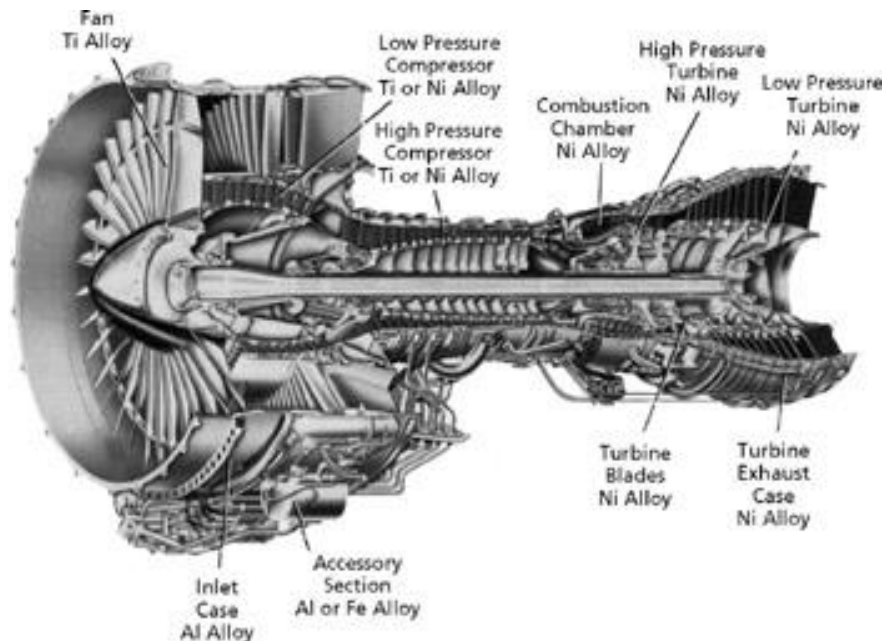


Figure 4: Typical Material Distribution in Jet Engine [26]

- Inconel 718

Alloy Inconel-718 is a precipitation hardenable nickel-based alloy designed to display exceptionally high yield, tensile and creep-rupture properties at temperatures up to 1300°F. The chemical composition in weight percentage is summarized in Table 1 [27]. The sluggish age-hardening response of alloy 718 permits annealing and welding without spontaneous hardening during heating and cooling. This alloy has been used for jet engine and high-speed airframe parts such as wheels, buckets, spacers, and high temperature bolts and fasteners [28]. The great properties of this alloy are due to the unique microstructure, consisted of matrix γ , precipitates γ'' , γ' , δ and carbides. The matrix γ is a solid solution of alloying elements like Cr, Fe, Mo in Ni, and it has an FCC crystal lattice. Gamma double prime (γ'') is the metastable phase (Ni_3Nb), with

tetragonal, space centered crystal structure ($D0_{22}$). It is the main strengthening phase in Inconel 718, and the volume fraction of γ'' in the structure is typically 15-20%. When exposed to high temperature for enough time, the gamma double prime transforms to the stable δ phase. Delta phase (δ) is the stable form of Ni_3Nb with orthorhombic crystal structure. It is known that the presence of δ phase in large quantity is undesirable, but precipitated at the grain boundaries, δ prevents to grain growth, thus, in this form it has a positive effect on the mechanical properties. In microstructure of Inconel 718 γ' phase is also present (see Figure 5), but due to low volume fraction of this phase, γ' has only minor effect on the properties of this alloy. At high temperatures (over 700°C) and at sufficient long exposure, the γ'' tends to transform to the δ phase, so this transformation sets the upper temperature limit for the operational condition of Inconel 718 [29] [30] [31] [32] [33] [34].

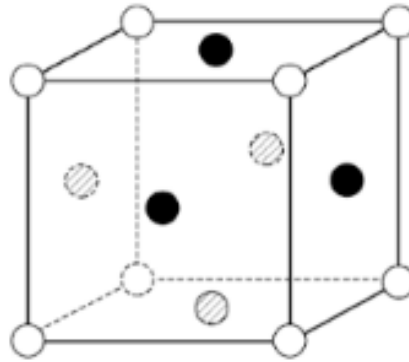


Figure 5: Line sketch of an ordered FCC crystal structure of gamma' phase. Solid circles represent nickel atoms, shared with adjacent cube. Open circles represent aluminum or titanium atoms, shared with eight cubes at each corner. dotted lines show hidden atoms [35]

Table 1: Certificated chemical composition in %wt. of Inconel 718 nickel-base superalloy

Cr	Ni	Mo	Nb	Ti	Al	F	C	Cu
19	52.5	3	5.1	0.9	0.5	18.5	0.08max	0.15max

1.2.3. Incorporation of Material Proprieties at High Strain Rates

As stated in previously, material proprieties above 10^4 s^{-1} are crucial but hard to test. A highly desirable feature is also a material model that can be extrapolated outside the calibration range. This is not trivial since materials exhibit different strain hardening and softening characteristics at different strains, strain rates, and temperatures. Up to now, the stress flow at very high strain rate has been characterized by matching the data available from the material test (SPHB), typically up to strain rate around $5 \times 10^3 \text{ s}^{-1}$ and then extrapolating stress flow with a heuristic procedure that in the past has given satisfactory results but does not guarantee the required accuracy (Figure 6).

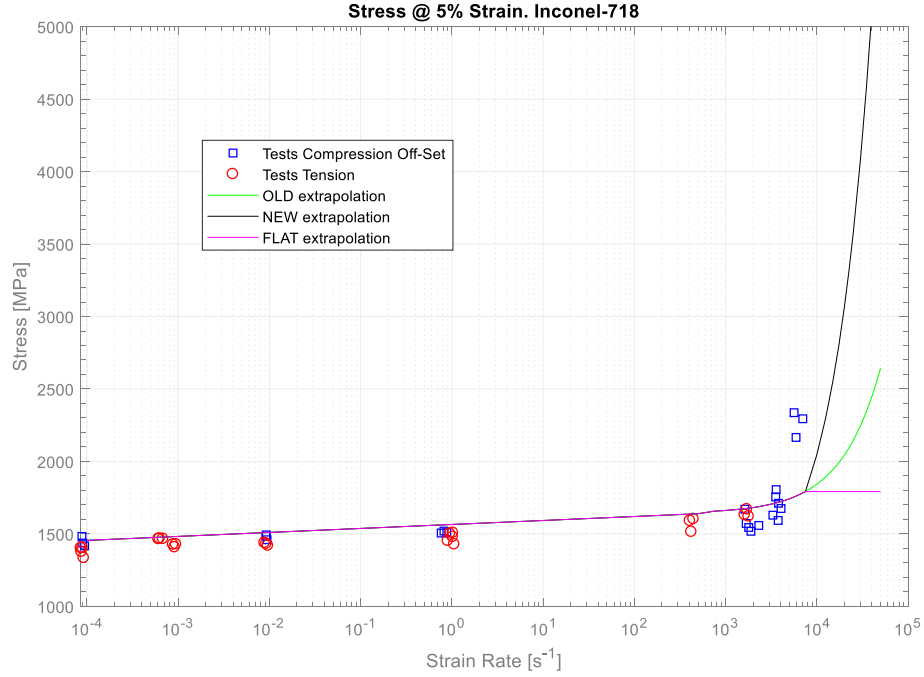


Figure 6: Different extrapolation of high strain stress flow [15]

This approach has two flaws. First it is not a robust procedure, meaning that from the data, different characterizations can lead to the same final result. Second, the method currently in place does not take into consideration the different nature of the lattice structure of the alloys modeled which can lead to different high rate flows [36]. Different crystalline structure of metals creates significant differences regarding both the evolution of the stress flow at high strain rates and the development of ASBs.

1.2.4. Adiabatic Shear Band Simulation Issues

Inconel 718 has a Young's Modulus of 210 GPa, a yield stress of 980 MPa, at a quasi-static rate and at room temperature, and an ultimate stress of 1375 MPa [37] in the same quasi-static condition. Titanium 6Al4V, under the same conditions, has a Young modulus of 113.8 GPa, a yield stress of 880 MPa, and an ultimate stress of 950 MPa [38]. Comparing these numbers, the ballistic limit for the same geometry plates of these materials, impacted by the same projectiles, should be very different. Inconel should have a significantly higher the ballistic limit than Titanium. Unexpectedly, tests show that the materials have a similar ballistic limit for the 0.5-inch plate (Figure 7), impacted by identical cylindrical projectiles manufactured using tool steel.

In the impacts above the ballistic limits, both materials have ASB failure modes. The similar results in the ballistic performances, despite the superiority of the Inconel in material yield and ultimate stress, is most likely caused by the different microstructure of Inconel 718 in comparison to Ti6Al4V HPC lattice. Inconel at temperature above 700°C undergoes a phase transformation that makes it brittle [33]. Moreover, Inconel has a melting point of 1260°C [37] while Ti6Al4V has a melting point of 1604°C [38]. The

proposed explanation for this peculiar result is that inside the ASB the temperature raises to the point where Inconel becomes brittle, causing a sudden failure. Unfortunately, the ASB of 0.5 inches Inconel plates has a width of approximately $5\text{ }\mu\text{m}$, compared to Ti6Al4V which have an approximately $50\text{ }\mu\text{m}$ ASB width. This narrowness is one of the reasons why the current material models are unable to predict ballistic impacts producing an ASB using a “industrial size mesh”. The elements of the mesh need to be smaller than the ASB width in order to capture the localization in shear and the consequent temperature raise in that region. This indicates the need for a mesh size smaller than $5\text{ }\mu\text{m}$ (for Inconel), which would lead to a model of many tens of millions of elements and a prohibitive computational time. The proposed solution to this problem, which will be executed in this project, is to implement a regularization method that would allow (under the proper loading conditions, strain, strain rate, and temperature) the material failure with an ASB mechanism, using a practical size.

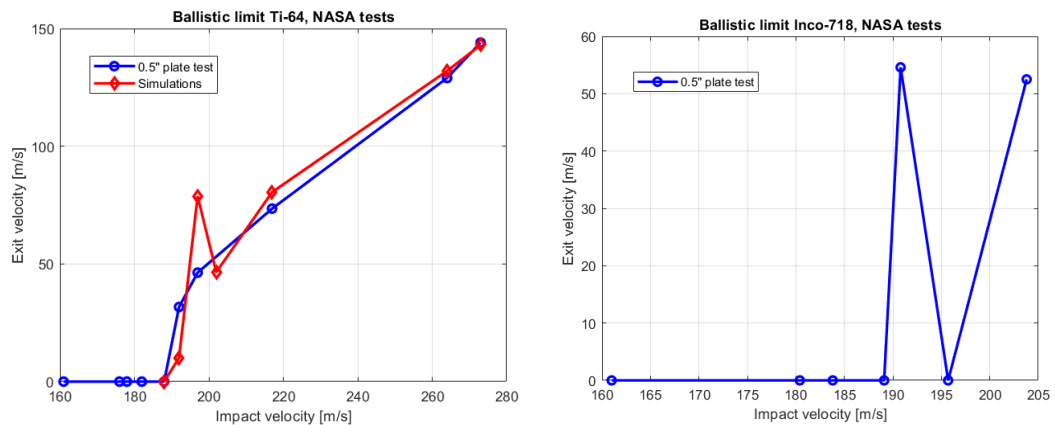


Figure 7: a) Titanium and b) Inconel 0.5-inch plates ballistic limits [15], [39]

1.3. Approach

To establish the importance of the high-strain-rate vs. stress relation, simulations on Inconel 718 with different strain rate dependence characteristics were executed to demonstrate how the rate effects, and the very local temperature increase, changes the material response at large deformations.

To validate the results of the high strain rate characterization, a novel method, which consists of comparing the simulations with the indentation on impacted (but unpenetrated) plates made of Inconel, was performed using a hybrid explicit/implicit simulation approach. The dynamic impact is modeled using explicit numerical integration, and an implicit springback analysis was used to determine the static deformed shape.

As adiabatic shear band modelling properties exhibit a strong dependency on mesh size, the effects of different mesh dimensions were neutralized by implementing a temperature regularization applied to the tabulated Johnson-Cook [20], [40] material model. 2D and 3D analyses were carried out. The 2D analysis was used to assess the ASB nucleation and its width, local temperature, strain and strain rate with the current FEM material model. The model was then updated with a newly defined tabulated Taylor-Quinney coefficient (TQC) as function of state of stress, strain rate, and mesh size. Using these parameters as metrics for when an ASB should occur, the amount of heating was raised sufficiently to obtain the development of ASBs in a range of element sizes, suitable for full scale simulations.

The updated material model was verified using one element simulations and 2D simulations to verify respectively the correct implementation of the material in terms of TQC input and output and the capability of enucleating ASB in 2D meshes with element sizes that were not predicting ASB previously.

The modified material model was then validated by simulating the ballistic impact tests performed by NASA Glenn Research Center Ballistic Impact Laboratory. The updated model was able to replicate the ASB characteristics obtained with the ultra-fine 2D mesh on an “industrial size” mesh in 3D simulations. Finally, the tabulated TQC was regularized for element size.

The extensive verification and validation tasks ensured the reliability and robustness of the newly developed modified material model. Additionally, the simulation results were compared against the original J-C material model available in LS-DYNA® (*MAT_224).

2. LITERATURE REVIEW

2.1. Material Behavior at High Strain Rate

As previously mentioned, it is crucial for the accurate simulation of ballistic impacts to include the material behavior at strain rates greater than 10^4 s^{-1} . In this range, it is difficult to measure the material properties experimentally, and there is some debate concerning the physical nature of the assumed material behavior.

The tensile behavior, including full stress–strain curves, of 21 different metals and alloys under low to high strain rates is given by Nicholas [41]. The tests were conducted using a split-Hopkinson pressure bar. The maximum strain rate achieved in these tests is approximately 10^3 s^{-1} . A survey of strain rate effects on mechanical properties of 13 metals of interest at elevated temperatures in the range from 10^{-4} to 10^3 s^{-1} from room temperatures to melting point is presented by Salam [42].

Campbell and Ferguson [43] found that for a mild steel, EN3B, the shear strength is dependent on strain rate as follows: at low strain rate, region I is characterized by a small, nearly constant increase in strength with the logarithm of shear strain rate; region II where the rate dependency is considerably higher but the increase is still constant with the logarithm of the strain rate; and region IV, corresponding to strain rates of $5 \times 10^3 \text{ s}^{-1}$ or greater, where the increase in shear strength is directly proportional to the strain rate (Figure 8).

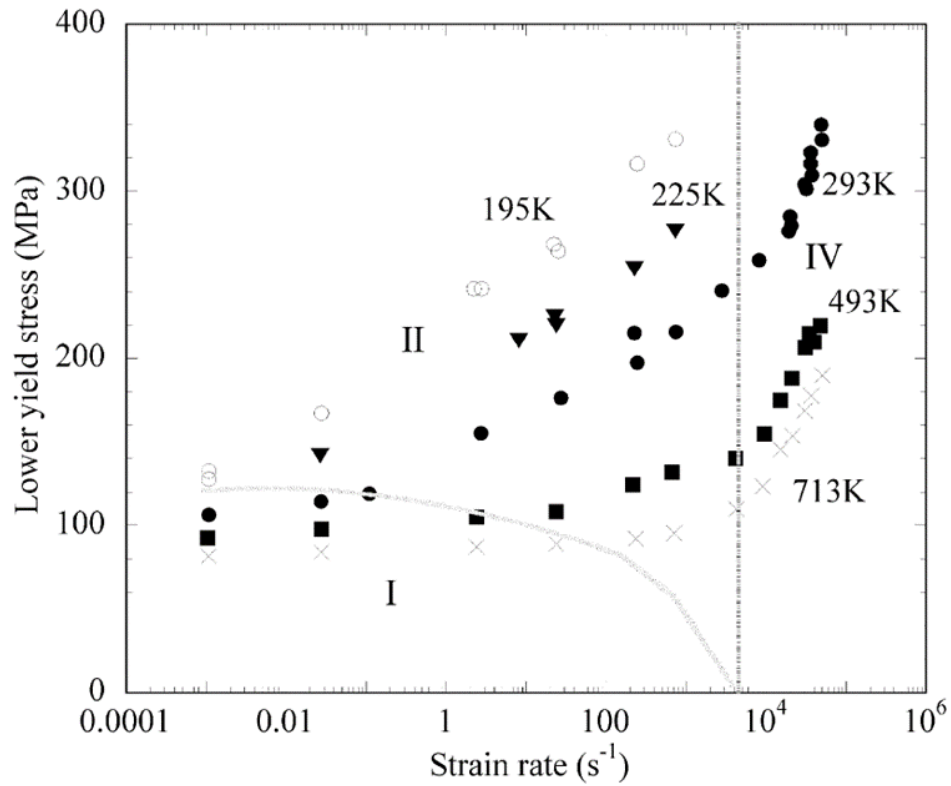


Figure 8: Variation of the lower yield stress with strain rate in a 0.12% C steel. Three characteristic regions of the flow stress sensitivity may be distinguished: (I) small temperature and strain rate sensitivity; (II) greater temperature and strain rate sensitivity; (IV) rapid increase of strain rate sensitivity [43]

Region I is identified by the authors as being dominated by long-range internal stresses due to dislocations, precipitate particles, and grain boundaries while region II is identified as being controlled by the thermal activation of dislocation motion, and finally Region IV is identified as being governed by short-range barriers in combination with an additional dissipative mechanism, however failure is not a function of temperature. It is also shown that strain rate sensitivity behavior for room temperature steel obtained from

dynamic punching, using data from Dowling and Harding [44], and tension, using data from Campbell and Cooper [45], it is almost identical as that from shear loading.

Dowling, Harding, and Campbell [43], [44], [46], extended the work on mild steel to aluminum, copper, and brass. The dynamic punch loading of all four of these materials showed the same general strain rate sensitivity as in the mild steel in shear. For all four of these materials, there was a small increase in strength at room temperature. At rates below 10^1 s^{-1} , the increase in flow stress was proportional to the logarithm of strain rate. At rates between 10^1 s^{-1} and 10^3 s^{-1} , greater increase in sensitivity still proportional with the logarithm of the strain rates. Finally, at rates above 10^3 s^{-1} greater sensitivity with the increase being proportional to the strain rate. While the general behavior of the four metals is similar, the strain rate sensitivity of the four metals is not identical. Lesuer [47], used the available stress–strain rate response of Ti6Al4V titanium alloy from literature, and included some additional test data. Wulf [48] and Meyer [49] included very high strain rate data ($> 10^3 \text{ s}^{-1}$). This data shows titanium exhibiting the same regime transition documented by Dowling et al., [46] for the other metals. When strain rates surpass approximately $5 \times 10^3 \text{ s}^{-1}$, the strain rate sensitivity becomes a function of the strain rate, while at lower strain rates it is a function of the logarithm of the strain rate. Wulf[48] also shows that the strain rate sensitivity is not constant.

In the recent past, there was debate about the veracity of the behavior proposed by Campbell et al. for the linear proportionality between strain rate and stress at high strain rates, particularly from Gorham [50], Dioh et al. [51], Field et al. [52], Jia et al. [53] and Oosterkamp et al. [54]. Gorham presented evidence that the noted increase is due to

inertial confinement, specimen dimensions, and a switch away from a one-dimensional state of stress. As a result, the argument was made that this transition is not a result of material properties of the specimen, but rather the test specimen's structure. Field et al. concurred with Gorham that the transition between Region I, II, and IV is an artifact of the test configuration. However, he points out that some non-compression tests, where inertia should not be a factor, also show this phenomenon. In Jia et al. article the use of miniaturization of the Split-Hopkinson Pressure Bar to obtain stress-strain behavior at strain rates of up to $5 \times 10^4 \text{ s}^{-1}$ is assessed in detail and applied to 6061-T651 aluminum. Due to the small size of the specimens they avoided geometries which would cause errors due to inertia confinement and demonstrated this by using Gorham's equations [55]. The comparison of the presented strain rate sensitivity at strain rates greater than 10^3 s^{-1} with published quasi-static values of this particular alloy appear to show an increase in strain rate sensitivity. The author also states that the explanations of the dramatic increases are occasionally controversial. Diah et al. presented analytical and numerical evidence which shows that the apparent increase in the strain rate sensitivity reported in the literature may result from stress wave propagation effects present in the test. Oosterkamp et al. tested Aluminum Alloys 6082 and 7108 and found that the sudden change in the strain rate sensitivity is the result of testing conditions. Shui-sheng et al. [56] found that the dynamic strength or yield stress of these materials was not sensitive to strain-rate in the low and high strain-rate range (corresponding to weak sensitivity area and saturated zone). The ultra-high strain rate tests were obtained with uniaxial strain flyer impact tests performed

by the use of $\Phi 57$ mm light gas gun combined with single point and double sensitivity VISAR testing system (see Figure 9).

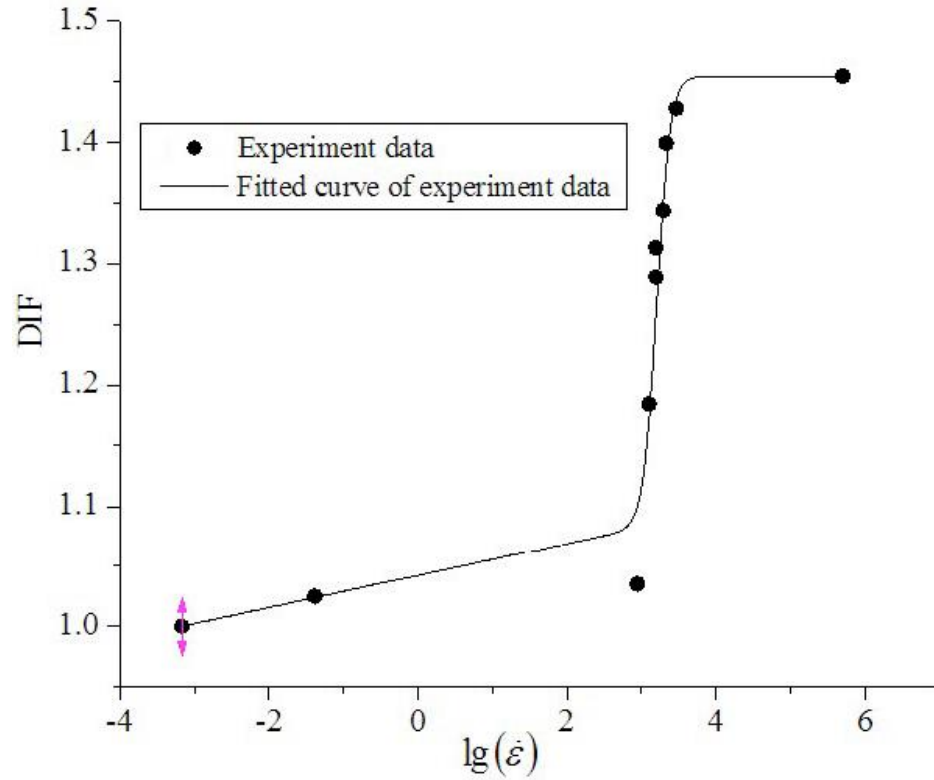


Figure 9: The relationship between dynamic increase factor (DIF), defined as the ratio of dynamic strength or yield stress to the quasi-static strength or yield stress of materials, and common logarithmic of strain-rate for 7075 aluminum [56]

There is disagreement in both the qualitative and quantitative nature of strain rate sensitivity in metals at strain rates greater than approximately 10^5 s^{-1} . However, the vast majority of publications in the last few years agree with the behavior for the stress flow proposed by Campbell and Cooper and most of the debate is concerning the causal mechanism, as well as differences between the different alloys.

Steinberg et al. [57], Rodriguez-Martinez et al. [58], Klepaczko et al. [59], Rittel et al. [60], Vural et al. [61], Remington et al. [62], Blazynski et al. [63], Wedberg et al. [23], Gilat et al. [64] (Figure 10), Gruzdkov et al. [65], Armstrong et al. [66] and Carney et al. [14] included the transition between logarithmic and linear dependence of the stress on strain rate in their material models.

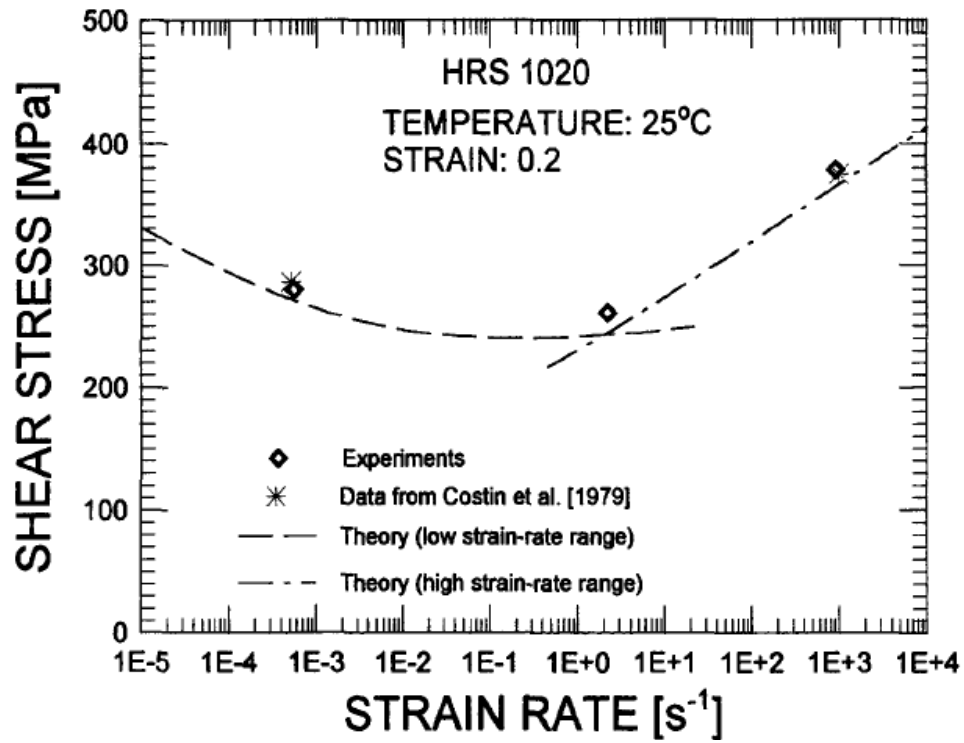


Figure 10: Variation of stress with strain rate at temperature of 25°C [64]

Nemat-Nasser et al. [67], show that in a NiTi alloy there is a dramatic increase in strain rate sensitivity at approximately $5 \times 10^3 s^{-1}$. They compare images of the failed material at low and high strain rates, demonstrating a different failure mechanism.

Almasri and Voyiadjis [68], and Mocko et al. [69], proposed region definitions similar to Campbell on 1018 Steel, where they highlighted a region dominated by thermally activated behavior and a region controlled by a viscous drag behavior (Figure 11). The role of the drag stress term, which allows the definition of the drastic rise in rate sensitivity shown by this material for $\dot{\epsilon}_p > 10^4 \text{ s}^{-1}$, becomes particularly relevant. This result is significant because, as demonstrated by Vadillo et al. [70] and Carney et al. [14] amongst others, a correct determination of the material rate sensitivity is essential for the design of structures that absorb energy under impact.

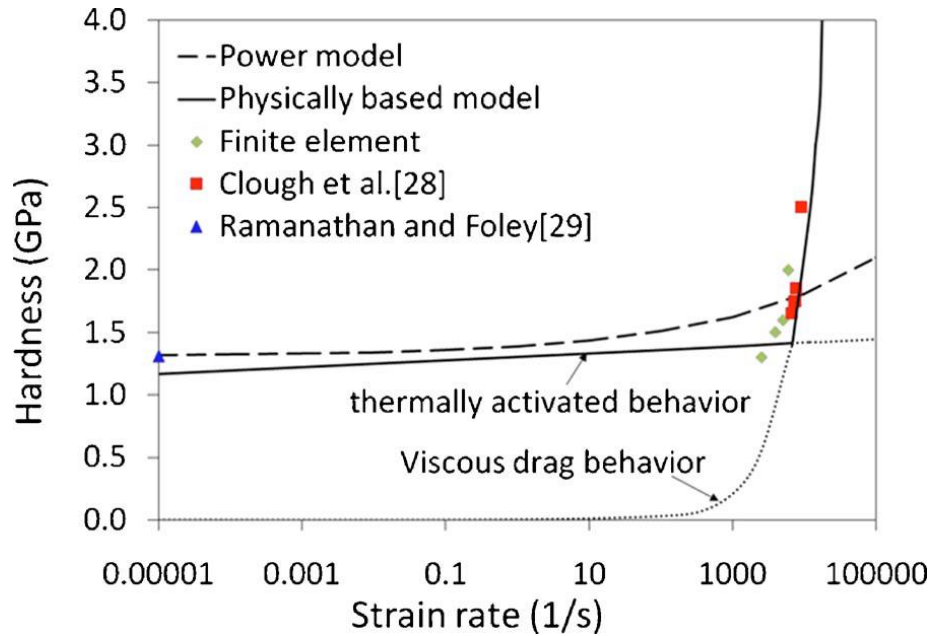


Figure 11: Hardness versus strain rate for 1018 steel [68]

Borodin et al. [71] agree that the strain rate sensitivities under quasi-static and dynamic conditions of loading have different physical nature. In the low strain rate, the

sensitivity arises from inertness of the defect structures evolution. In the dynamic case, the effects of inertness of defective microstructure evolution become dominant and determine the value of the dynamic yield strength of the material, but, in addition, new strain rate sensitivity effects arise that are associated with the micro-localization of the plastic flow near heterogeneities or stress concentrators.

Almasri [72] also identified four different regions for yield stress versus temperature in metals (Figure 12).

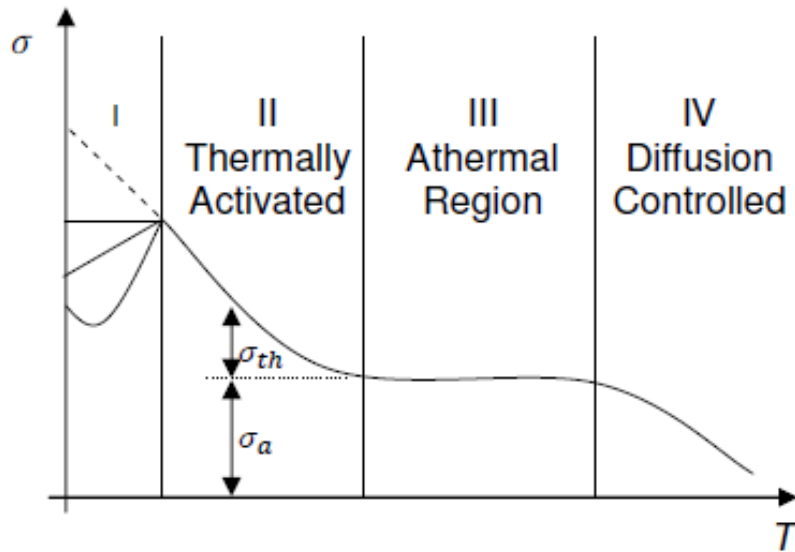


Figure 12: Schematic behavior of yield stress versus temperature of metals [72]

When dealing with high-strain-rate applications at elevated temperature, either inherent in the application (as in jet engine turbine blades containment) or induced by adiabatic heating from deformation, accurate measurements and description of the constitutive behavior is essential. Despite the extensive use of Inconel 718 in engineering

applications, the number of published studies on the dynamic behavior of this material is still limited [73].

Zhang et al. [74] investigated the strain rate hardening at rates ranging from 10^{-3} to 1 s^{-1} and temperature ranging from 960 to 1040 °C of solution treated Inconel 718. They proposed a power law relationship for the flow stress, being a function of the strain, temperature and strain rate. However, these temperatures and strain rates are well below the dynamic range and the typical application temperatures for Inconel 718.

Pereira and Lerch [75] investigated the heat treatment on the ballistic properties of Inconel 718 at room temperatures and found that the annealed and aged states showed a difference in yield stress and in the strain rate sensitivity. DeMange et al. [76] reported results from room temperature high-strain-rate compression tests of Inconel 718 in different heat treatment conditions, confirming a higher strain rate sensitivity in the annealed state.

Kobayashi et al. [77] investigated the plastic deformation behavior of Inconel 718 in shear at strain rates up to 3000 s^{-1} , using a split torsional Hopkinson bar, at room temperature. They also observed the loss of strain hardening with the increasing strain rate, which was attributed by the authors to the thermal softening with a calculated temperature increase at the fracture strain of 200 °C.

Wang et al. [78] characterized aged heat-treated and solution treated Inconel 718 at very high strain rates ($5000\text{--}11000 \text{ s}^{-1}$) and high temperatures (up to 800 °C) and found a strain rate softening effect at high strain rate and found that it was temperature dependent. Sjöberg et al. [79] performed tensile tests on aged Inconel 718 at temperatures

up to 650 °C and strain rates up to 1000 s⁻¹ and found similar results. Both Wang et al. and Sjöberg et al. reported a decrease in the flow stress at higher strain rates during testing at high temperatures. Sjöberg et al. attributed this to a more pronounced effect of adiabatic heating at high temperatures, while Wang et al. attributed it to removal of dispersed phases during high-strain-rate tests.

Lee et al. [80] used a compressive split-Hopkinson pressure bar, and transmission electron microscope (TEM) after testing, to investigate annealed Inconel 718 at temperatures between -150 and 550 °C, with strain rates ranging from 1000 to 5000 s⁻¹. The microstructural observations revealed that changes in the dislocation structure could also play a role. In any case, it is fair to say that the high-strain-rate deformation of Inconel 718, particularly at elevated temperatures, is not fully understood at present (see Figure 13).

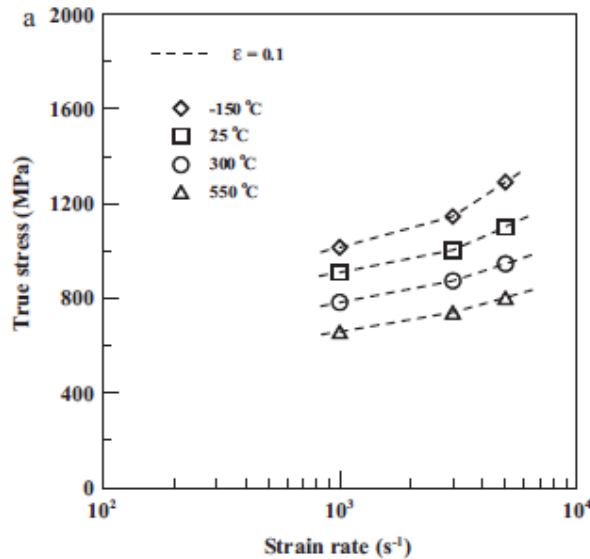


Figure 13: Variation of flow stress with strain rate as function of temperature at true strains of 0.1 [80]

2.2. Differences Between FCC, BCC, and HPC Materials

Many studies have examined the mechanical behavior of a large number of metal alloys but, the specifics of the underlying deformation mechanisms remain far from being understood and in some cases are controversial.

Chen et al. [81] investigated the flow behavior of the 7050-T7451 (FCC) alloy on uniaxial compression tests in a wide range of strain rates (0.0001 s^{-1} , 10000 s^{-1}) and temperatures (20°C , 270°C) and concluded that the work hardening effect decreases with the increase of strain rate. Moreover, dynamic recrystallization with grain refining and phase transition occurred at dynamic conditions according to the microstructure observation, while the dynamic recovery is predominant at most of the quasi-static conditions. The coupled effects of work hardening, and strain rate exist for 7050-T7451 alloy deformation process. Also, the thermal softening rate exhibits a decreasing tendency with the increase of strain rate for different ranges of temperature gradient. The thermal softening rates at the quasi-static conditions are normally larger than those at dynamic conditions. In addition, thermal softening rate exhibits a linear decreasing trend with the increase of strain rate at logarithmic scale.

Polyzois [82] showed that FCC metals are highly strain rate sensitive and exhibit a large plastic region compared to the BCC metals. For these metals, strain hardening, and temperature effects are dependent on the strain rate.

Couque [83] identified the deformation mechanism of the dislocations from quasi-static rate up to 10^3 s^{-1} as thermally activated. This is responsible for a moderate increase

of the strength that is linearly dependent of the strain rate. From 10^{-3} to 10^3 s^{-1} , the resulting increase for metals is about 10–40% for face-centered cubic (FCC) systems, 10–20% for hexagonal closed packed systems and 50–300% for body-centered cubic (BCC) systems. At strain rates ranging from 10^3 to 10^5 s^{-1} the motion of dislocation slows down through a viscous drag phenomenon. This results in a tremendous increase of the flow stress, as shown in Figure 14. Couque also found that the strain-rate threshold characterizing the strengthening of the FCC metals associated with the viscous behavior of the dislocations is within $1.8 \times 10^3 - 4 \times 10^3 \text{ s}^{-1}$, while for BCC metals the transition from the thermally activated behavior of the dislocations to the viscous regime occurs at strain rates ranging from 1×10^3 to $5 \times 10^3 \text{ s}^{-1}$.

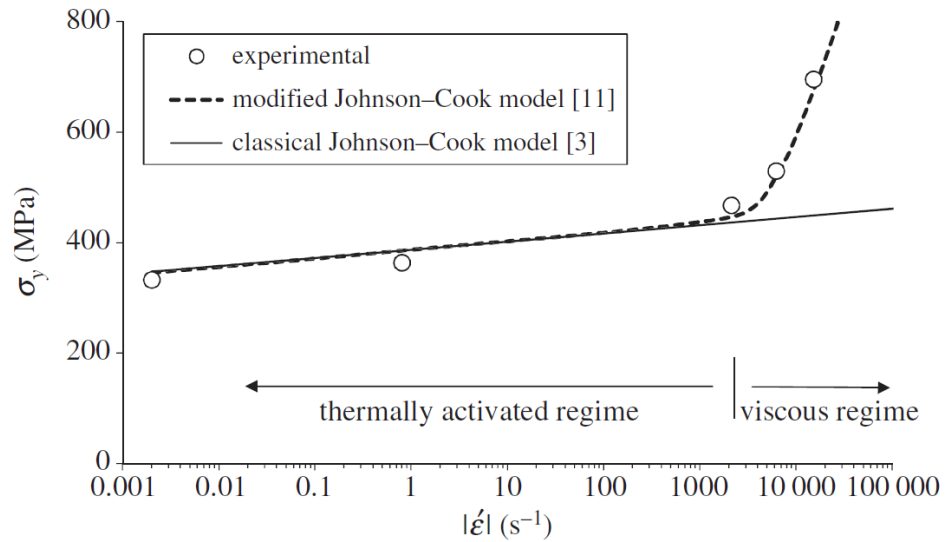


Figure 14: Yield stress versus strain rate for a nickel against two formulations of the Johnson-Cook model [83]

Armstrong and Walley [84] described the high strain rate dependence of the flow stress of metals and alloys, from a dislocation mechanics viewpoint. The test techniques ranged from conventional tension/compression testing through split Hopkinson pressure bar (SHPB) measurements to Charpy pendulum and Taylor solid cylinder impact tests and shock loading or isentropic compression experiment (ICE) results. They found that for BCC metals, the strain rate sensitivity is in the yield stress dependence as compared with the FCC case where the sensitivity is in the strain hardening property. An important consequence is that an opposite ductility influence occurs for the tensile maximum load point strain that decreases with strain rate for the BCC case and increases with strain rate for the FCC case. Different hexagonal close packed HCP metals are shown to follow either the BCC or FCC case.

Almasri [72] also noticed that crystal BCC and FCC structures show distinct differences between them in the mode of hardening, and dependence on the strain rate and temperature. He explained that in BCC metals the thermal yield stress, due to the Peierls barriers, shows strong dependence on the strain rate and temperature. In BCC metals, the plastic strain hardening is independent of them, which represents the athermal stress. In the case of FCC metals, the thermal stress is strongly dependent on the plastic strain due to the domination of the dislocation intersections on the mechanism behavior of the thermal activation analysis. The author attributes the sensitivity of BCC metals to high-temperature and strain rate and their mechanical proprieties to the rate controlling mechanism of the thermal component of the flow stress. He pointed out that while the activation volume has been shown to decrease with plastic strain for FCC metals, it is

seen to be constant for BCC metals. He concludes that an increase in strain rate should only produce a constant increase for the whole stress-strain curve for BCC metals. He also noticed that the activation volume for BCC metals is much smaller than for FCC metals, yielding a much higher temperature and strain-rate sensitivity. Moreover, screw dislocations in BCC metals have non-planar dislocation cores, and so dislocation slip in BCC metals is generally controlled by the high Peierls stress. Thermal activation aids dislocation glide by effectively decreasing the intrinsic lattice friction (lowering the additional energy required to slip), which lowers the flow stress of the material. Thermal activation plays a considerable role in the double kink motion of screw dislocations; a small segment of a screw dislocation advances past an energy barrier forming short lengths of positive and negative edge character which rapidly run out of the crystal, pulling ahead the rest of the screw dislocation in the process.

The yield stress in most BCC metals is strongly temperature-dependent, and a strong rate dependency of the flow stress is also expected. Almasri et al. [72] [85] used a power law instead of an exponential expression to relate dislocation glide velocity for pure iron (BCC) and OFCH copper, showing a very good capability in capturing the strain rate sensitivity (see Figure 15) .

Zerilli and Armstrong [86] suggested a dislocation mechanism concept based on thermal activation analysis to develop a constitutive model for metals with coupled strain rate and temperature dependence. The model was developed for two types of microstructures, BCC and FCC. The differences between the two forms are based on the dislocation characteristics for each specific structure.

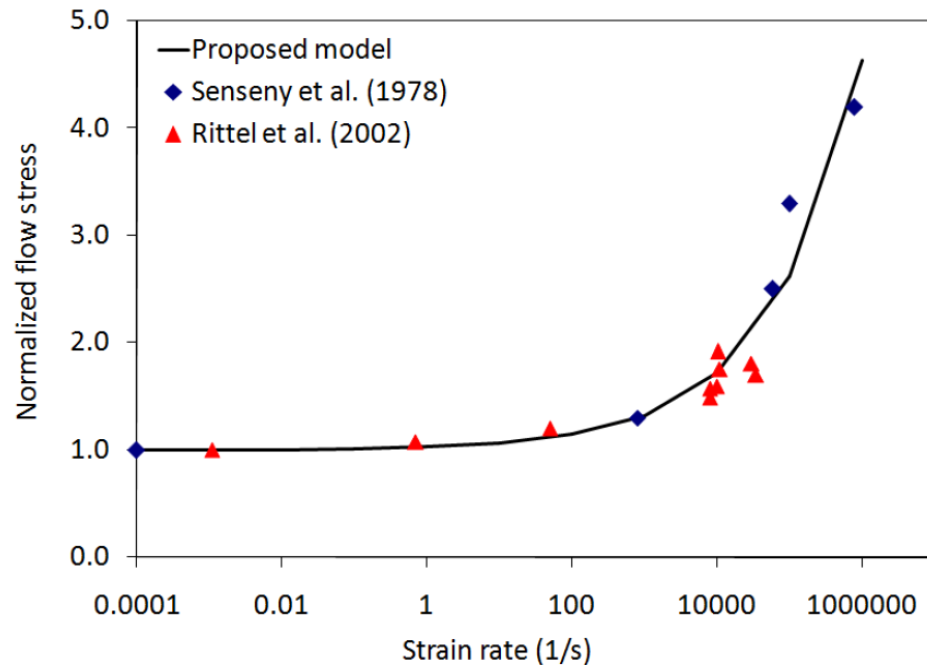


Figure 15: Normalized flow stress versus strain rate of OFHC copper [72]

According to Rusinek et al. in FCC metals, the yield stress depends mainly on strain hardening, while in BCC metals shows stronger dependence on temperature and strain rate (see Figure 16). The cutting of dislocation forests is believed to be the principal mechanism in FCC metals, while in BCC metals the overcoming of Peierls–Nabarro barriers is the principal mechanism. The authors also highlighted that the viscous drag component of flow stress at high strain rate is a more pronounced characteristic of FCC metals (see Figure 17 and Figure 18)

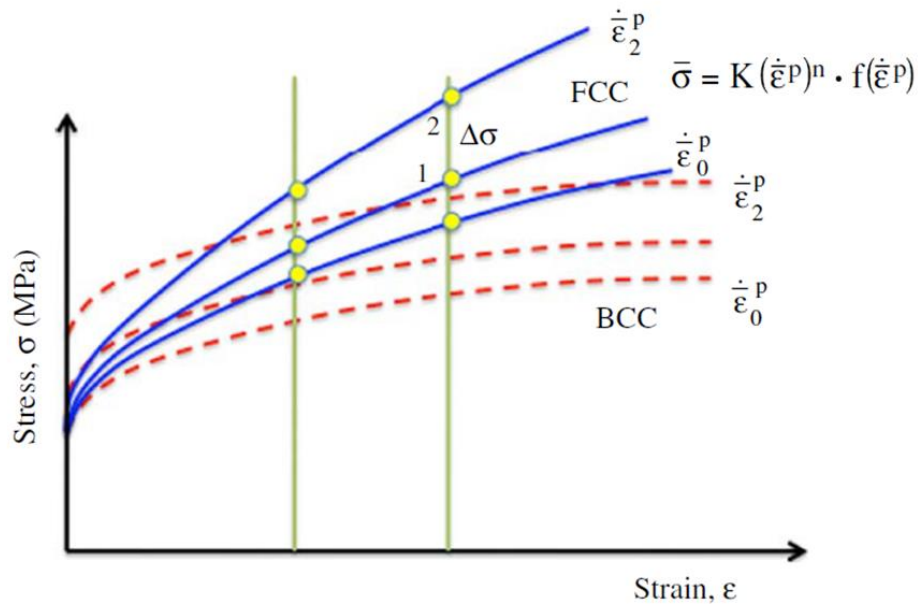


Figure 16: Strain rate sensitivity definition for BCC and FCC metals [36]

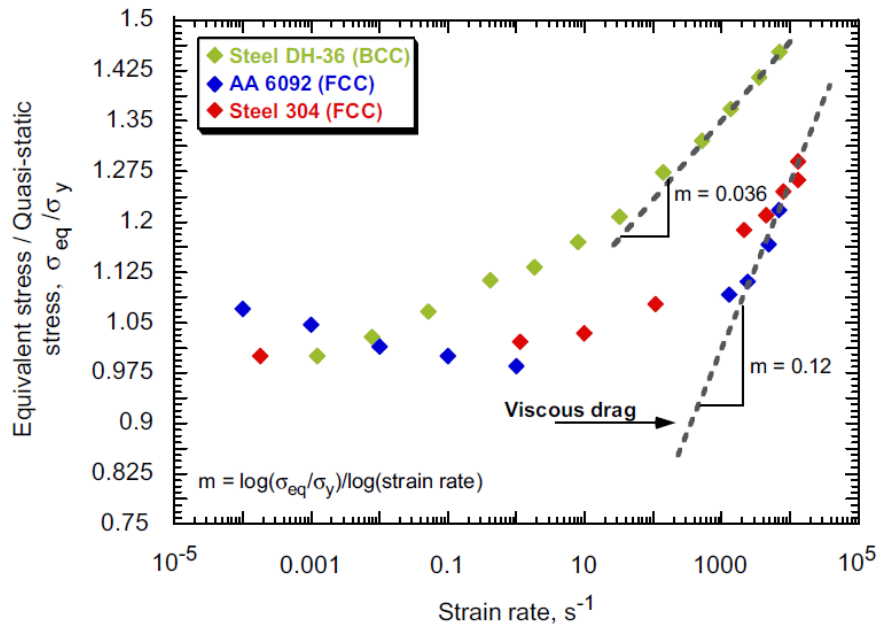


Figure 17: Evolution of the normalized equivalent stress with strain rate for different BCC and FCC metals [36]

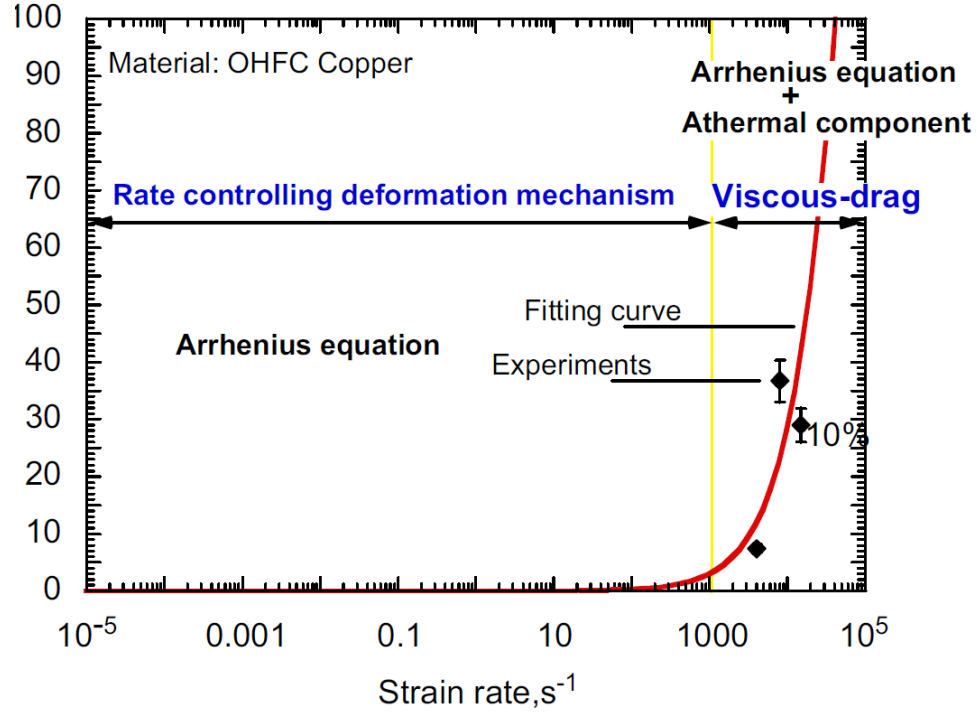


Figure 18: Calibration of the viscous drag stress component for a FCC metal [36]

Ashton [87] highlights that the FCC structure has twelve slip systems. The BCC structure has forty-eight slip systems. Since the slip planes in the BCC structure are not as close-packed as those in the FCC structure, higher shearing stresses are required to cause slip in BCC structures. Also, a screw dislocation in a BCC metal can dissociate on three equivalent slip planes. This dislocation must be constricted before it can glide in any one of the slip planes. This constriction is more difficult to make at lower temperatures or higher strain-rates. Therefore, the yield stress in BCC metals is higher at lower temperatures and higher strain-rates. Also, the yield stress is higher in BCC metals, compared with FCC metals due to the intrinsically higher Peierls-Nabarro stress. In FCC

metals the dislocation can only dissociate on the $\{111\}$ planes. There is no direction in the slip planes along which the dislocation could dissociate on other planes. Therefore, the temperature and strain-rate dependence of the yield stress in FCC metals is small.

Tabei et al. [88] points out that the flow stress behavior of BCC and FCC metals are different, which could be attributed to the different dislocation characteristics for each particular structure. The overcoming of Peierls-Nabarro barriers is the principal mechanism in BCC metals while the cutting of dislocation forests is the principal mechanism in FCC metals. Therefore, the effects of strain rates and temperatures are mainly controlled by the initial yielding in BCC metals and by the strain hardening in FCC metals.

Ardeljian et al. [89] also points out that the deformation behavior is highly anisotropic, both elastically and plastically, for metallic crystals with a hexagonal closed packed (HCP) structure. The latter can be carried by both slip and deformation twinning on multiple systems, differing in crystallography and activation stresses and exhibiting differing dependencies on temperature and strain. As a result, polycrystalline HCP metals and their alloys generally exhibit strong plastic anisotropy and sensitivities to strain rate and temperature.

2.3. Adiabatic Shear Bands

Adiabatic shear bands represent thermo-viscoplastic instabilities and are often observed in ductile metals subjected to high rates of loading, because there is insufficient time to conduct away heat during the event. Such shear bands can be the dominant mode of failure in an impact event and are particularly common in impacts involving ductile

metals subjected to overall compression and also in the perforation and punching of sheets and plates. Adiabatic shear bands are also observed in applications such as high-speed machining, where they limit the speed of the manufacturing process [90].

Gilat and Wu [64] observed that by its nature, plastic deformation generates heat. In low strain rate tests the rate of plastic work is low and there is plenty of time for the heat to dissipate such that the temperature of the specimen remains essentially constant. In the high rate tests the specimen's temperature typically rises. Temperature may also affect the microstructure of the material tested. Moreover, Almasri [72] found that the hydrostatic pressure seems to have noticeable effect in increasing and delaying the instability strain and hence delaying the whole banding process.

Wright and Walter [91] pioneered the use of numerical simulation to follow the evolution of an adiabatic shear band. Feng and Bassim [92] assert that the growth of the ASB is affected by the strain hardening, thermal softening and thermal conduction. Using a rate-dependent equation they were able to simulate an ASB, initiated at local material defects, in ANSYS. They described the evolution of the ASB, based on their modeling, as composed of 3 phases. In the first stage, there is no plastic deformation. In the second stage, the strain hardening, and thermal softening compete with each other. During the third stage, the thermal softening dominates.

Lee and Lin [93] investigated the plastic deformation behavior of titanium alloy (Ti6Al4V) at strain rates ranging from 5×10^2 to $5 \times 10^3 \text{ s}^{-1}$, and temperatures ranging between room temperature and 1100°C . They found that ASB are precursors to fracture, and that the hardness and thickness of the adiabatic shear bands are found to change

directly with the β -transus temperature. The increase in temperature causes a decrease of the microhardness of the shear bands, while the thickness of the shear bands is found to increase with the temperature, i.e. at a strain rate of $2.5 \times 10^3 \text{ s}^{-1}$ and at 500°C , the ASB thickness is $14.7 \mu\text{m}$, while at 1100°C the thickness is $45 \mu\text{m}$. The same authors in another paper [94], studying the high-temperature deformation behavior of Ti6Al4V alloy at constant strain rate of $2.0 \times 10^3 \text{ s}^{-1}$, found that adiabatic shear bands are the sites where the fracture of the material occurs, and that the thickness and microhardness of adiabatic shear bands vary with temperature. It appears by their microstructural observations that the dislocation density decreases linearly with temperature. Moreover, the dislocation cell size increases with temperature, but decreases with dislocation density. The flow stress is related to the dislocation cell size by an inverse linear relationship.

Delorme [95] reports that the mechanism of softening and formation of adiabatic shear bands is still not well understood, but it is generally accepted that the process is related to a phenomenon known as dynamic recrystallization. Dynamic recrystallization refers to a rearrangement of the microstructure in a material undergoing high strain rate and high temperature deformation. This process is characterized by a refinement of grains and decrease in dislocation density and differs from static recrystallization in that the kinetics are much faster and the refined grains are very small. Materials undergoing dynamic recrystallization lose mechanical properties and soften during this process.

Dynamic recrystallization (DRX) was initially observed and proposed as a mechanism for ASB by Meyers and Pak [96] and has since been substantiated by the

studies of De Andrade [97] and Hines and Vecchio [98]. DRX has been studied from a numerical perspective and has been applied to ASB formation by Chichili [99], Medyanik [100] and more recently by Dolinski [101]. The main observation that suggests the occurrence of dynamic recrystallization is that an ASB contains very fine grains with a comparatively low dislocation density. The formation of new grains by a static process has been ruled out by Hines and Vecchio [98] and calculations based on the time required for diffusion under static recrystallization conditions. The mechanism for the initiation of dynamic recrystallization is not yet fully understood. Initially, Meyers and Pak proposed a process of micro-grain rotation and sliding of micro-grain boundaries. Rittel [102] considers the mechanism as an athermal process brought on by buildup of strain energy due to cold work, as opposed to a thermally activated process as in the model of Medyanik. The main argument that Rittel makes for an athermal process is that high temperatures are not a prerequisite for the initiation of ASBs, since the severe temperature rise does not begin to occur until after localization has been initiated. Dynamic recrystallization has been shown to require a critical temperature to initiate by Medyanik, which depends on the applied strain rate. This temperature is shown to be approximately 40% of the melting temperature at strain rates above 100/s.

According to Landau et al. [18] the concurrent occurrence of different mechanisms, including the emergence of dislocations, texture development, grain rotation and refinement, results in the evolution of the microstructure within ASBs. They contest the leading opinion that a competition between strain rate hardening and thermal softening is what determines the onset of the failure. The authors also disagree that

adiabatic shear band propagation is an instability and points out that contrary to the current paradigm, it was recently shown that instead of thermal softening mechanisms, microstructural softening transformations such as dynamic recrystallization (DRX) are responsible for adiabatic shear failure. Those transformations are dictated by the stored energy of cold work, so that energy considerations can be used to macroscopically model the failure mechanism.

Boakye-Yiadom [103] explained that because of the very narrow nature in the microstructure of the ASB (~ 1 to $350\mu\text{m}$) and the rapid rates of deformation, it is virtually impossible to observe their evolution and mechanism of formation during an impact. He explains the evolution in the microstructure of the ASB, and concludes that for BCC Ferritic Pearlitic, hardenable, concurrent occurrence of emergence of dislocations, texture development, breaking of elongated grains, grain rotations and refinements result in the observed structure within ASBs of impacted specimens. It was also asserted that the occurrence of Dynamic Recovery (DR) and Dynamic Recrystallization (DRX) alone would not be sufficient to explain the observed microstructure within the evolved ASBs in impacted 4340 steel specimens because of the presence of refined and nano-grains with high density of dislocation. In this study, it was also observed that the initiation of ASBs in AISI 4340 steel during impact occurs when the microstructure is highly inhomogeneous. Specimens tempered at lower temperatures are more susceptible to the formation of ASBs because of the higher inhomogeneities.

There has been relatively little research on the shear band evolution of Inconel 718. Song et al. [104] studied the effects of different heat treatments on the dynamic

shear response and the adiabatic shear localization characteristic of Inconel 718 alloy and estimated a shear band width of about 10 μ m by the SEM micrograph for aged Inconel tested at a strain rate of $8 \times 10^5 \text{ s}^{-1}$. The results indicate that with aged Inconel 718, which has a higher yield strength and lower strain hardening rate, it is easier to form an ASB under dynamic shear loadings than with solution treated Inconel 718.

Pereira and Lerch [75] showed that during blunt object impacts, exemplified by blade-out containment events in jet engines, annealed Inconel 718 material could absorb a significantly larger amount of energy compared to its precipitation strengthened counterpart. DeMange et al. [76] presented similar results in a combination of high strain rate (10^3 s^{-1}) compression tests and top hat shear tests. This result could indicate that high elongation and better strain hardening capabilities reduced the tendency for adiabatic shear localization and results in more wide-spread deformation. Recently, detailed investigations of the microstructure within shear bands formed in Inconel 718 during machining and controlled dynamic shear-compression deformation were conducted by Johansson et al. [105]. The top-hat tests showed very narrow 4–5 μ m wide shear localized bands, with recrystallized grains down to the order of 20–300 μ m and a very narrow transition zone to adjacent material (Figure 19). Regarding Inconel 718 ASB FEM simulations, most of the publications are focused on the simulation of machining (e.g. Lorentzon et al. [106], Jafarian et al. [107]). Erice et al. [27] studied the ASB generated by a blunt object in impact simulations.

In general, the simulations are able to capture the essential features of shear localization. However, Ozel et al. [108], comparing experimental results of machining of

Inconel 718 with 3D FEM simulations, emphasized the role of the material model, when applied to large strain and high temperature changes cases, as well the importance of using appropriate meshing. In the study by DeMange et al. [76], numerical simulations of Inconel 718 top-hat specimens during dynamic testing were performed.

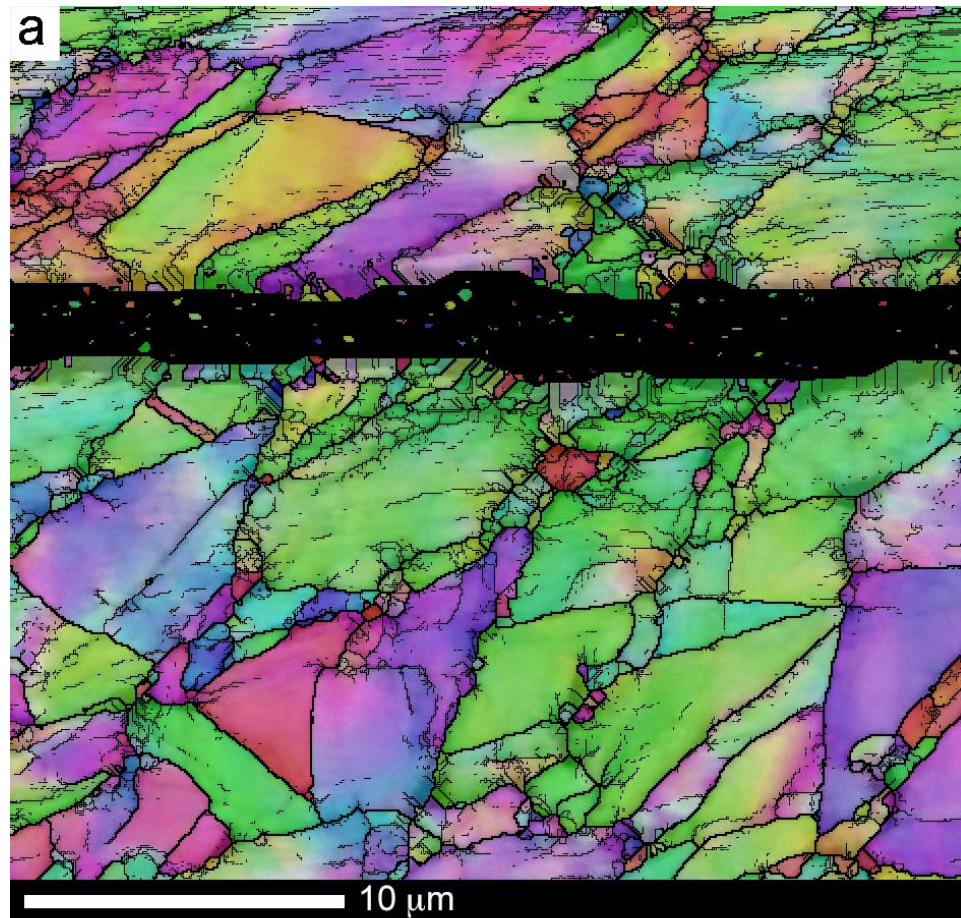


Figure 19: Inconel 718 EBSD map (superimposed on the band contrast) of the region adjacent to the shear[103]

Simulations of the shear band formation resulted in very high strain rates and temperatures, with higher values reached with aged material compared to annealed samples. However, the constitutive model was not calibrated using high-strain-rate tests at elevated temperature. Moreover, the load–displacement curves from the simulations and experiments of the top-hat tests were not compared, therefore the agreement with experiments remains unclear.

Johansson et al. [73] studied the effects of microstructure on the strain localization behavior during dynamic shear deformation of Inconel 718 by experiments and numerical simulations of Split-Hopkinson tests of specimens with top-hat geometry. The results show that strain localization is promoted by small grain size and precipitation hardening, whereas large grains and solution annealing largely suppressed the formation of shear bands. In addition, a smaller fillet radius facilitated the initiation of shear bands. Finite element simulations were able to reproduce the most important features of both global load displacement histories, and presence of shear localization. Simulations of the local deformation during localization showed that temperatures exceeding 750 °C (locally above 1000 °C) and strain rates in the order of $2 \times 10^5 \text{ s}^{-1}$ were reached in the band.

2.4. Taylor-Quinney Coefficient

During the plastic deformation of a solid, the temperature increases in the absence of external heating, due to plastic work. Farren and Taylor [109] and Taylor and Quinney [110] were the first who observed that plastic work is not entirely converted into heat in the deformation of metals. They determined that the efficiency of the thermomechanical conversion, nowadays known as the Taylor–Quinney coefficient (TQC, symbol β) was a

constant assumed to be equal to 0.9. Research by Ravichandran [111] and Rosakis [112] yielded values for the Taylor-Quinney coefficient for α -titanium which were not constant, but were a function of both strain rate and, to a lesser extent, plastic strain. Additionally, [109] and [110] also present variable values of β 's for Al2024, which are a strong function of plastic strain. More recently Rittel [113] shown that the TQC varies greatly within the investigated materials and observed that for Titanium, which exhibits an asymmetric mechanical response in tension and compression, the measured TQC values are mode dependent too.

Zaera et al. [114] in his work addressed the Taylor–Quinney coefficient in a broader sense, when extraneous heat sources other than those related to plastic work dissipation are active. He found that in phase transforming materials there is the possibility of measuring values of β_{diff} or β_{int} greater than unity related to the occurrence of phase transformation through the release of latent heat. He clarified that TQC has to be considered as variable in phase transforming materials, depending on strain, strain rate and stress state. He concluded that a consistent thermo-viscoplastic constitutive model should account for these functional dependencies in order to get a reliable prediction of the temperature increase during the whole range of straining. The study also pointed out that a central issue that has been overlooked in previous studies is the lack of homogeneity of the Taylor–Quinney coefficient along the specimen undergoing dynamic phase transitions that hinders precise and reliable determination of both β_{diff} and β_{int} . This heterogeneity may affect the accuracy of the global

measurements based on spatially averaged stress and strain quantities. Therefore, TQC has to be considered a local variable.

2.5. Mesh Sensitivity Regularization for ASB

Erice et al. [27] performed a numerical and experimental study of ballistic impacts at various temperatures on Inconel 718 superalloy plates using a coupled elasto-plastic damage constitutive model with Lode parameter dependent failure. The numerical study showed that the mesh size is crucial to correctly predict the shear bands detected in the tested plates. Many approaches have been proposed in the literature to overcome the mesh sensitivity of finite element solutions but very few about the specific issues of ASB. Almasri [72] speculates that a nonlocal gradient method associated with a dynamic length scale could be applied to regularize the FEM results and noticed that the kinetic energy and strain energy stored in the body are both related linearly to the shear band length, while viscous dissipation is not.

Teng [115] noticed that one of the simplest ways to remedy mesh size sensitivity is to equip the element size with a physical meaning. This idea can be directly implemented without any modification of commonly used material constitutive models and fracture models. Redanz [116] suggested that the mesh size could be approximately equal to the particle size. Alternatively, the mesh size can be associated with the size of a fracture process zone ahead of a propagating crack, where micro-cracks or micro-voids nucleate, grow, and eventually coalesce with the major crack. The third type of approach is the development of nonlocal constitutive models, in which a characteristic or internal

length scale is implemented. In such a way, the prediction of fracture is not only controlled by stresses and strains but also related to material microstructures.

Several formulations originated from this non-local approach have been proposed, e.g. Tvergaard and Needleman [117]. The characteristic length was considered to represent the average grain size or the average void spacing. However, these approaches are not applicable to the failure analysis of large structures such as aircrafts or car collision, due to the limitation of computational resources. Teng identified high strain gradient and strain softening as two critical factors leading to mesh size sensitivity. He found that crack growth and residual velocities at high impact velocities are not dependent on element size. However, the prediction of ballistic limit and the evolution of adiabatic shear bands is sensitive to the mesh size [115].

It is evident from the literature review that two elements are crucial in correctly predicting the ASB developing process: the correct stress flow at high strain rates and the mesh density. It appears that no successful attempt to regularize mesh size suitable for large analysis to simulate ASB has been reported.

3. MATERIAL MODEL AND CHARACTERIZATION

3.1. Introduction

This chapter describes the theory behind the tabulated J-C material model and the procedures to characterize the Inconel 718 0.5” plate and generate the parameters to populate the input deck of *MAT_224 in LS_DYNA.

3.2. Theoretical Approach

In this section, a general background of the selected material FE model deformation law for the elastic, permanent plastic deformation and failure is provided [28]. A more detailed description of the theory and implementation of the tabulated J-C material can be found in Buyuk [40].

3.2.1. Constitutive Relationship

The tabulated Johnson-Cook [20], [40] model is based on an isotropic elasto-thermo-visco-plastic constitutive relationship which states that stress is dependent on strain, strain rate and temperature:

Equation 1: Constitutive relationship

$$\sigma_{ij} = \sigma_{ij}(\varepsilon_{ij}, \dot{\varepsilon}_{ij}, T)$$

where σ_{ij} is stress, ϵ_{ij} is strain, $\dot{\epsilon}_{ij}$ is the strain rate, and T is the temperature. In the elastic region, the Jaumann rate of the stress tensor, σ^{∇}_{ij} , is obtained as a linear function of elastic strain rates; this is a generalization of hypo-elasticity:

Equation 2: Jaumann rate of the stress tensor

$$\sigma^{\nabla}_{ij} = \lambda (\dot{\epsilon}_{kk} - \dot{\epsilon}^p_{kk}) \delta_{ij} + 2\mu (\dot{\epsilon}_{ij} - \dot{\epsilon}^p_{ij})$$

here $\dot{\epsilon}^p_{kk}$ are the components of the plastic strain rate tensor and λ and μ are Lamé constants. Young's modulus, E , and Poisson's ratio, ν , may be converted by:

Equation 3: Young's modulus

$$E = \frac{\mu(3\lambda + 2\mu)}{\lambda + \mu}$$

Equation 4: Poisson's ratio

$$\nu = \frac{\lambda}{2(\lambda + \mu)}$$

The material response in the plastic region is determined by a von Mises-type yield surface in a six-dimension stress space that can expand and/or contract due to strain hardening, rate effects, and thermal softening:

Equation 5: Von Mises-type yield surface

$$\sigma_{vm}(\sigma_{ij}) \leq \sigma_y(\epsilon^p_{ij}, \dot{\epsilon}^p_{ij}, T) = \sigma_y(\epsilon^p_{eff}, \dot{\epsilon}^p_{eff}, T)$$

where σ_{vm} is the von Mises stress, ε_{eff}^p is the equivalent plastic strain and $\dot{\varepsilon}_{eff}^p$ is the equivalent plastic strain rate. As the material is assumed isotropic, the dependency of the yield surface upon plastic strain and plastic strain rate can be expressed purely as a function of the second invariant of each tensor. Please note that states on the yield surface are plastic, whereas states below the yield surface are elastic. Mathematically, this is expressed as follows:

Equation 6: Dependency of the yield surface upon plastic strain and plastic strain rate

$$\begin{aligned}\sigma_{vm}(\sigma_{ij}) - \sigma_y(\varepsilon_{eff}^p, \dot{\varepsilon}_{eff}^p, T) &\leq 0 \\ \dot{\varepsilon}_{eff}^p &\geq 0 \\ \dot{\varepsilon}_{eff}^p \left(\sigma_{vm}(\sigma_{ij}) - \sigma_y(\varepsilon_{eff}^p, \dot{\varepsilon}_{eff}^p, T) \right) &= 0\end{aligned}$$

The plastic strain rates are determined by associated flow leading to the well-known plastic incompressibility condition typical of metals:

Equation 7: Plastic strain rate

$$\dot{\varepsilon}_{ij}^p = \dot{\varepsilon}_{eff}^p \frac{\partial \sigma_{vm}}{\partial \sigma_{ij}} \rightarrow \sum_{k=1}^3 \dot{\varepsilon}_{kk}^p \equiv 0$$

3.2.2. Accumulated Failure

The failure model determines when element erosion occurs, and currently has four input parameters that calculate the accumulated damage for a given element. The first parameter is a table of curves that defines the plastic failure strain as a function of

triaxiality and Lode parameter. The second parameter is a load curve that scales the plastic failure surface as a function of plastic strain rate. The third parameter is a load curve that scales the plastic failure surface as a function of temperature. The last parameter is a load curve that scales that plastic failure surface as a function of element size and triaxiality. Triaxiality is defined by the equation:

Equation 8: Triaxiality

$$\tau = \frac{p}{\sigma_{vm}}$$

where p is the pressure and σ_{vm} is the von Mises stress. The Lode parameter is defined by the equation:

Equation 9: Lode parameter

$$\theta_L = \frac{27 s_1 s_2 s_3}{2 \sigma_{vm}^3}$$

where s_1 , s_2 , and s_3 are the principal deviatoric stresses and σ_{vm} is the von Mises stress.

Overall, the plastic failure strain is defined by:

Equation 10: Plastic failure strain

$$\varepsilon_{pf} = f(\tau, \theta_L) g(\dot{\varepsilon}_p) h(T) i(l_c)$$

where τ is the triaxiality, θ_L is the Lode parameter, $\dot{\varepsilon}_p$ is the plastic strain rate and l_c is the element size. When more than one of the failure parameters are used, the net plastic

failure strain is the product of the functions defined in the above equation. For reference, the possible range of triaxiality is negative infinity to positive infinity, however the area of interest for this analysis is between triaxialities of negative one to positive four.

The failure criterion is based on an accumulated damage parameter. When this damage parameter is greater than or equal to one in an integration point, the solid element is eroded. The damage parameter is defined by:

Equation 11: Damage parameter

$$D = \int \frac{\dot{\varepsilon}_p}{\varepsilon_{pf}} dt \geq 1 \rightarrow \text{Failure}$$

where $\dot{\varepsilon}_p$ is the plastic strain rate and ε_{pf} is the plastic failure strain. In this model, the modulus is not affected by the damage parameter.

3.3. Incorporation of Inconel-718 Material Test Data into Material Model Input Parameters for Tabulated Johnson-Cook Material [28]

This section describes the procedures for the characterization of Inconel-718 material properties. In the chosen FEM solver LS-DYNA® those material properties are used to populate table tabk1 and table tabkt in the input deck (Figure 20).

```

*KEYWORD
*MAT_TABULATED_JOHNSON_COOK_TITLE
Inco-718
$#      mid      ro      e      pr      cp      tr      beta      num
int
          3      8.19E-6 210.00000 0.290000      435      300 0.800000 1.000
000
$#      tabk1      tabkt      lcf      lcg      lch      lci
          1          2      500      600      700      900

```

Figure 20: *MAT_224 input deck

Many factors contribute to the variations of Inconel-718 measured material properties, including, but not limited to, the manufacturing and post-manufacturing processes, the test specimen orientation in regard to plate grain direction, etc. To minimize some of these discrepancies, the material studied here is Inconel-718 ½-inch plate manufactured by a sole company.

The ½-inch rolled plate metal Inconel-718 material is modeled using the tabulated J-C material (*MAT_224 in LS-DYNA®). This is an isotropic elasto-thermo-visco-plastic constitutive relationship which states that stress is dependent on strain, strain rate and temperature described in paragraph 3.2. The generation of the input parameter for *MAT_224 is described in this section as well as the creation of the failure input tables. Further information on the material characterization can be found in Dolci et al. [28].

3.3.1. Common Elastic-Plastic Modeling Revisited

A review of common plastic material modeling procedures will demonstrate the limitations and error that can be introduced in the process. What follows is a detailed review, including typical assumptions, of the typical elastic-plastic material modeling procedure.

The material modeling begins with a standardized tensile test. A dog-bone specimen under a constant grip speed is pulled in a test machine (see Figure 21).

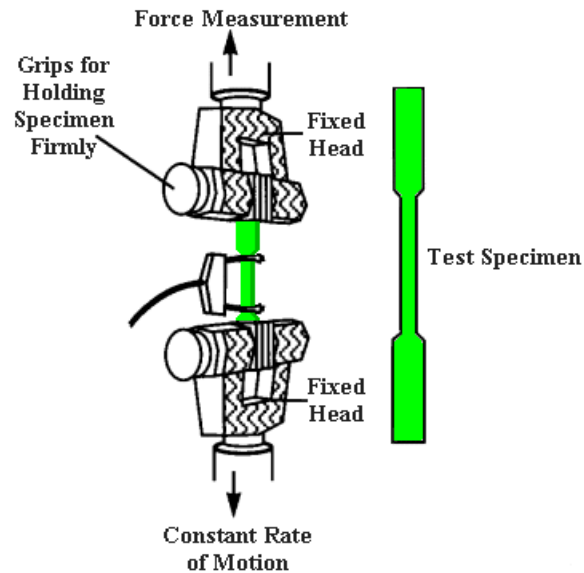


Figure 21: Standard Tensile Test [28]

Two measurements are recorded, the force vs. time relationship, $F(t)$, is measured with the tensile machine, and the displacement vs. time relationship, $D(t)$, is measured by a gauge or an extensometer fixed to the specimen. The force vs. displacement curve is then generated by cross-plotting these two curves.

After acquiring the force vs. displacement curve, simple formulas are used to calculate engineering stress and engineering strain.

Equation 12: Engineering stress

$$\sigma_{eng}(t) = \frac{F(t)}{A_0}$$

Equation 13: Engineering strain

$$\varepsilon_{eng}(t) = \frac{L(t) - L_0}{L_0} = \frac{D(t)}{L_0}$$

where $\sigma_{eng}(t)$ is the engineering stress vs. time relationship, $\varepsilon_{eng}(t)$ is the engineering strain, $F(t)$ is the force in the axial direction, A_0 is the original cross-sectional area, $L(t)$ is the instantaneous gauge length, L_0 is the original gauge length, and D is the displacement.

After knowing σ_{eng} and ε_{eng} , engineering stress may be converted into the true stress using the formula below

Equation 14: True stress

$$\sigma = \sigma_{eng}(1 + \varepsilon_{eng})$$

similarly, true strain may be converted by the following:

Equation 15: True strain

$$\varepsilon = \ln(1 + \varepsilon_{eng})$$

When applying the formulas above, five assumptions have already been made:

- Assumption 1: stress $\sigma_{ij}(t)$ is uniform over the mid cross-section of the specimen at any time.

- Assumption 2: cross-sectional area is constant in the area measured by the extensometer.
- Assumption 3: zero stress exists in the transverse and in the thickness direction.
- Assumption 4: Strain components in the transversal and thickness directions are given as $-k \varepsilon_{11}$, where ε_{11} is longitudinal strain and k is close to 0.5
- Assumption 5: strain is uniform in the area measured by the extensometer.

Any deviation from these assumptions will introduce errors in the derived stress-strain relationship. The final tabulated J-C Inconel-718 material model will use a Young's modulus of 210 GPa [118]. However, this value may not match all the test data exactly. Therefore, when the hardening curves for the various test conditions are developed, a value that matches each specific test is adopted to enable the simulated hardening curve to start at the same point as the test curve. Starting at the same point is required to compare the fit of the hardening curve being developed. When the model is complete, the stress evolution follows the above modulus value up to the proportional limit departure point for the different hardening curves, depending upon stress state, rate and temperature. For modeling the plastic region, the plastic strain is computed as:

Equation 16: Plastic strain

$$\varepsilon_p \stackrel{\text{def}}{=} \varepsilon - \frac{\sigma}{E}$$

After obtaining the plastic strain vs. stress relationship curve, input data are prepared for a piecewise linear plasticity material model (*MAT_024). The stress value of the starting

point of this curve has the same value as the stress at the proportional limit. This is critical to maintain a continuous transition between the elastic and plastic regions.

Under the assumptions that were previously mentioned, the load curve giving longitudinal stress versus longitudinal plastic strain is identical to the relationship between the effective plastic strain, ε_{eff}^p , and yield stress, σ_Y . This relation will be used to determine the deformation behavior after the elastic region.

Effective plastic strain, ε_{eff}^p , is a monotonically increasing scalar value. It is calculated incrementally as a function of $\dot{\varepsilon}_{ij}^p$, the plastic component of the rate of deformation tensor. In tensorial notation, this is expressed as:

Equation 17: Effective plastic strain

$$\varepsilon_{eff}^p = \int_{t=0}^{t1} d\varepsilon_{eff}^p = \int_0^t \sqrt{\frac{2 \dot{\varepsilon}_{ij}^p \cdot \dot{\varepsilon}_{ij}^p}{3}} dt$$

If plastic deformation occurs at constant volume, then:

Equation 18: Plastic strain rate at constant volume

$$\dot{\varepsilon}_{ij}^p = \dot{\varepsilon}_{11}^p \begin{pmatrix} 1 & 0 & 0 \\ 0 & -0.5 & 0 \\ 0 & 0 & -0.5 \end{pmatrix} \rightarrow \dot{\varepsilon}_{eff}^p = \dot{\varepsilon}_{11}^p$$

additionally,

$$\varepsilon_{eff}^p = \int_{t=0}^{t1} d\varepsilon_{eff}^p = \int_0^t \dot{\varepsilon}_{11}^p dt = \varepsilon_{11}^p$$

The yield surface can be determined by Equation 2: Jaumann rate of the stress tensor

Equation 19: Yield surface

$$\sigma_{vm} \leq \sigma_y = f_h(\varepsilon_{eff}^p)$$

where $f_h(\varepsilon_{eff}^p)$ is the tabulated input and $f_h(0)$ is the yield stress that denotes the value of f_h when $\varepsilon_{eff}^p = 0$ (the starting point of the plastic strain vs. stress curve). The effective stress according to von Mises, σ_{vm} , is defined as follows:

Equation 20: Effective von Mises stress

$$\sigma_{vm} = \sqrt{\frac{1}{2} [(\sigma_x - \sigma_y)^2 + (\sigma_y - \sigma_z)^2 + (\sigma_z - \sigma_x)^2 + 6\sigma_{xy}^2 + 6\sigma_{yz}^2 + 6\sigma_{zx}^2]}$$

It can be observed that it is identical to the longitudinal stress under conditions of uniaxial tension:

Equation 21: Stress under uniaxial tension

$$\sigma_{ij} = \sigma_{11} \begin{pmatrix} 1 & 0 & 0 \\ 0 & 0 & 0 \\ 0 & 0 & 0 \end{pmatrix} \rightarrow \sigma_{vm} = \sigma_{11} (\sigma_{11} > 0)$$

3.3.2. Violations of Common Assumptions

The common method for modeling elastic-plastic materials presented in the previous section is invalid after the necking point because at least three out of five assumptions are violated.

- Assumption 1 is still considered valid because the stress $\sigma_{ij}(t)$ varies little over the cross-sectional area at any time.
- Assumption 4 is still valid because the material remains isotropic and plastically incompressible after onset of the plastic instability.
- Assumption 2 is invalid, as the cross-sectional area is much smaller in the localized region after necking and therefore not a constant in the region spanned by an extensometer.
- Assumption 3 is invalid, as transversal stresses will develop after the onset of necking and additional stresses in the thickness direction will develop after the onset of local necking. Consequently, after necking the specimen is no longer in a uniaxial stress condition. Before necking, under uniaxial stress conditions, the only non-zero stress component is the axial stress. After necking, a transverse stress, σ_t , appears because the material will resist shrinking in the transverse direction. As the local necking develops, we see additional stresses in the thickness direction, σ_{tt} :

Equation 22: Stresses in tension post necking

$$\sigma = \begin{pmatrix} \sigma_l & 0 & 0 \\ 0 & \sigma_t & 0 \\ 0 & 0 & \sigma_{tt} \end{pmatrix} \quad \sigma_{vm} \neq \sigma_l$$

An accurate measurement of σ_l can be obtained by applying the instantaneous necking cross-sectional area (measured by digital imaging) in the stress calculation. It is, however, not possible to measure the transverse stress, σ_t , nor the thickness stress, σ_{tt} . Therefore, σ_{vm} is generally unknown after necking.

- Assumption 5 is invalid because the strain is not uniform within the measuring distance of the extensometer. After the onset of necking, the neck will have a higher strain than the rest of the part. An accurate measurement of strain the region of necking can be obtained via a digital image correlation (DIC).

3.3.3. Stress Strain Relationship after Necking

To create an accurate material model and simulate the tensile test in LS-DYNA[®], the method used is as follows:

- Estimate several post-necking plastic stress-strain curves as input by extrapolating the curve before necking.
- Compare the simulation force vs. displacement curve with test results and pick the input curve that gives the closest match. Note that the complete specimen geometry must be precisely modeled by measuring the actual specimen, rather than using the design values on the blueprint. Also note that at this stage in the process, the strain rate effect is not considered in the simulation.
- Input a single stress-strain curve associated with a particular strain rate, thereby making the material model strain rate independent. In other words, at this point in the modeling process, the material model will behave the same no matter the loading speed, as long as inertia effects are sufficiently small. Because of this

strain rate independence, the simulation can be performed with an arbitrary (higher) loading speed instead of the actual loading speed that was used in the test, allowing for a much shorter simulation time. The rate-independent material model will have a dynamic effect if loaded at a very high speed due to the inertia effects.

- The necking point is identified by assuming that necking occurs at maximum load. The necking point is given by the intersection between the true strain versus true stress curve and its own derivative. So, necking occurs where the true stress is equal to the tangent modulus:

Equation 23: Necking conditions

$$\begin{cases} \sigma = \sigma(\varepsilon) \\ \sigma = \frac{d\sigma}{d\varepsilon} \end{cases}$$

The hardening curves are extrapolated after necking using the following formula:

Equation 24: Hardening curves extrapolation formula

$$\sigma = k[\varepsilon_e + \varepsilon_p]^n$$

where k , ε_e , and n are fitting parameters, and the exponent n is expected to vary between 0 and 1 as the hardening curve is expected to be monotonically increasing and to have a monotonically decreasing tangent.

After the necking point is determined, only the part of the strain-stress curve before necking is used for further processing (Figure 22)

At the necking point, this curve should be continuous:

Equation 25: Hardening curves continuity conditions

$$A \equiv \sigma|_{\varepsilon=\varepsilon_0}, B \equiv \varepsilon|_{\varepsilon=\varepsilon_0}$$

and smooth:

Equation 26: Hardening curves smoothing conditions

$$A \equiv \sigma|_{\varepsilon=\varepsilon_0}, C \equiv \left. \frac{d\sigma}{d\varepsilon} \right|_{\varepsilon=\varepsilon_0}$$

where A is the stress at necking, $B \equiv \varepsilon_0$ is the plastic strain at necking, and C is the slope (hardening modulus) at necking. Notice that there are three variables but only two boundary conditions. Therefore, the extrapolation is not uniquely defined, and one of the three parameters can be freely chosen; as it has a bounded domain, it is typical to choose the exponent, n . Given a specific n value, ε_e and k are determined from the following relationships:

Equation 27: Fitting parameters relationships

$$k = A \left(\frac{An}{C} \right)^{-n}$$

$$\varepsilon_e = \frac{An}{C} - B$$

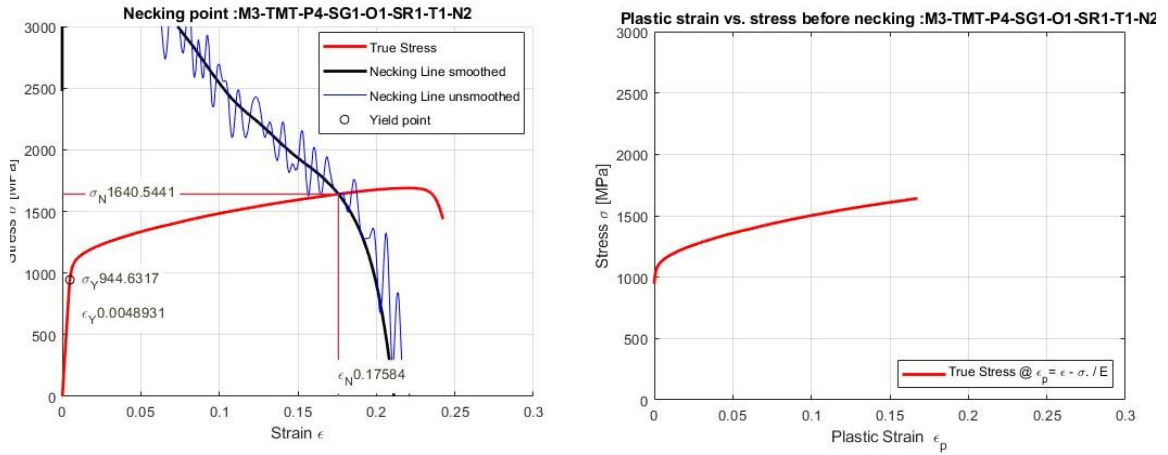


Figure 22: Left: Necking Judgment Line and Stress Strain Curve. Right: Stress Strain Curve after Trimming

- After assuming different n values, a cluster of curves can be generated (Figure 23).
- Several candidate curves were chosen from the generated plastic strain vs. stress curves and these curves were input into the material model to simulate a tensile test.

Figure 24 shows the force displacement curves obtained by a simulation overlaid with the real-life tensile test result. The curve 16 predicts a force displacement curve very close to the test. Therefore, this curve is a good estimation of plastic strain vs. stress relationship.

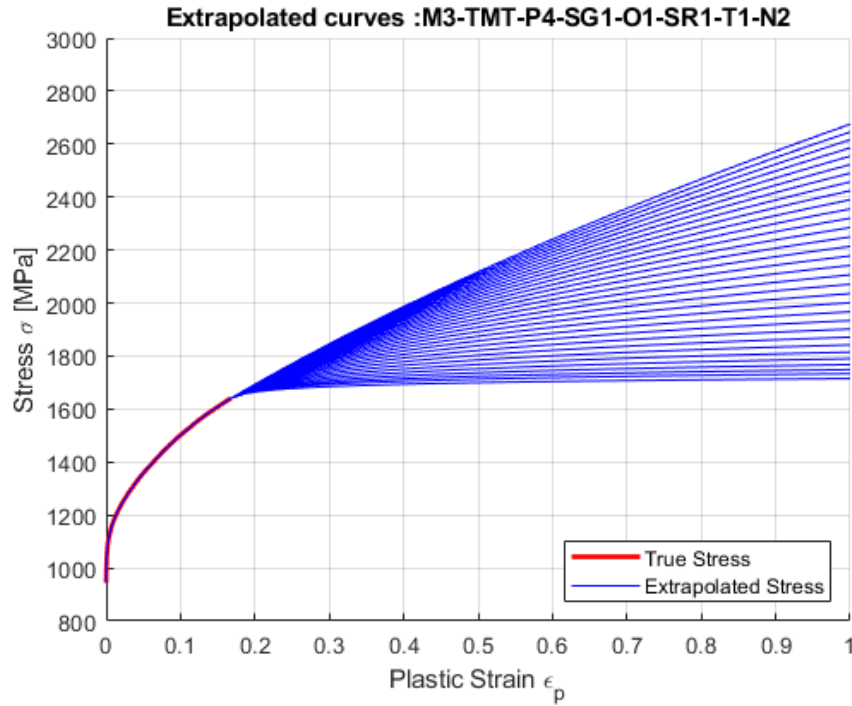


Figure 23: Extrapolated Curves after Necking

- As a supplementary evaluation, the 1st principal plastic strain contour at failure of the simulation is compared with the longitudinal strain digital image correlation data in the physical test. These two contours must be relatively similar to justify the estimated stress-strain relationship curve (Figure 25).

The process described above in this section takes the raw data and smooths it to ensure that the analysis will properly converge and execute. It also avoids using the erroneous assumptions described previously. The input data developed in this process matches the actual test data as closely as possible, while removing high frequency oscillations and negative slope areas that could cause convergence problems.

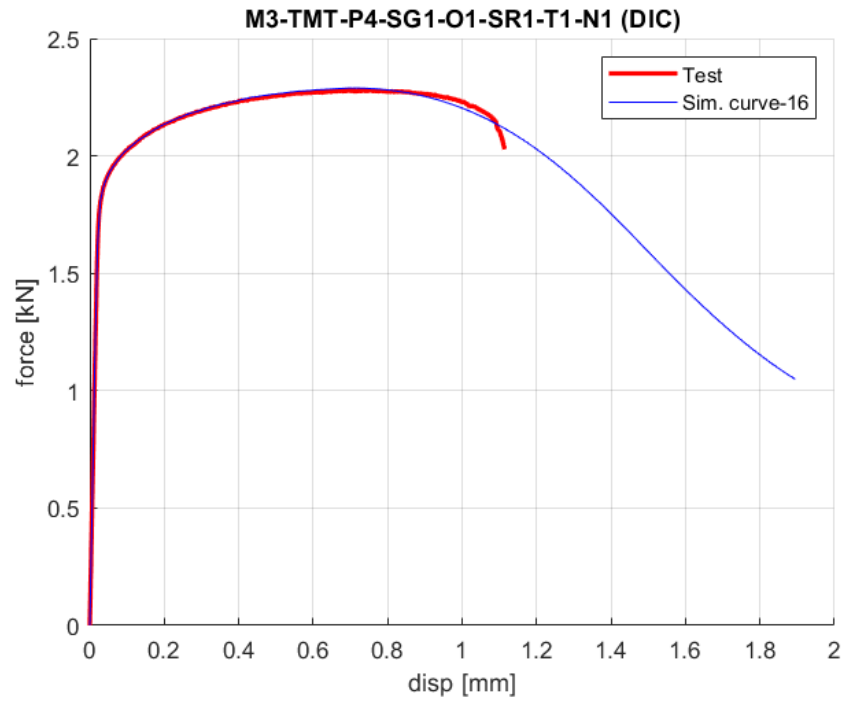


Figure 24: Force Displacement Result of Tensile Test Simulation with Matching Hardening Curve Inputs

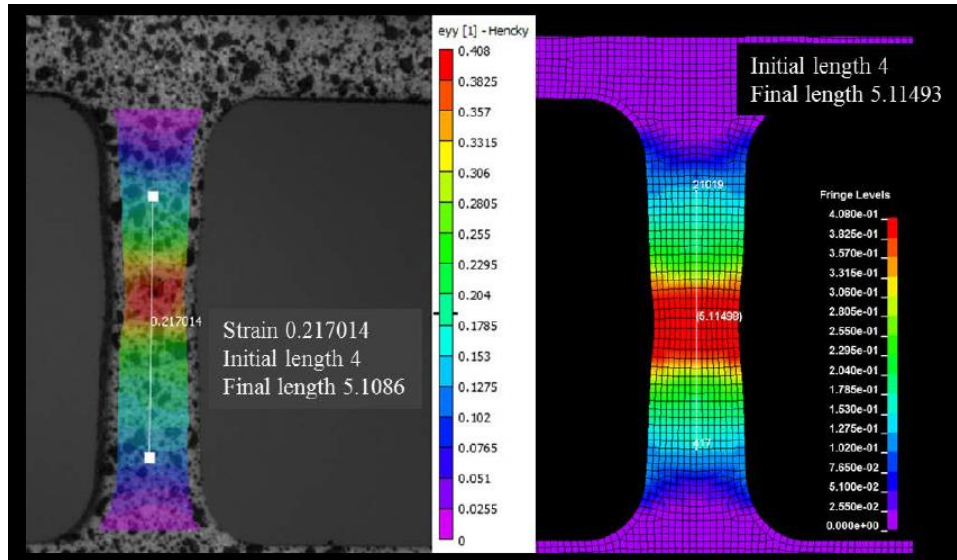


Figure 25: First Principal Plastic Strain Contour at Failure Comparison

3.3.4. Isothermal Effect

The method described above is valid for all quasi-static, isothermal, uniaxial tensile tests, independent of the temperature at which they were performed. The quasi-static testing must be performed at a low enough strain rate such that the process is isothermal, and no thermo-mechanical coupling occurs during the experiment. Then the yield curve obtained by the process described earlier can be assigned to the specific temperature at which the test was conducted, which is necessary, as *MAT_224 requires an isothermal input curve.

3.3.5. Temperature Dependent Tabulated Input

A table of isothermal, temperature-dependent yield curves (tabkt) can be created by individually simulating all high- and low-temperature tensile tests for a given strain rate, without considering any thermal coupling in the simulations following the procedure previously explained. That table can then be used (in conjunction with the table of rate-dependent yield curves) as input for simulations of dynamic experiments in which thermal effects and strain rate effects occur simultaneously and interact with each other. An extra artificial curve at constant stress zero was added at Inconel melting temperature (see Figure 26). Fifteen tests measuring the temperature effect of the material were performed by OSU. Besides the room temperature tests, four additional temperature groups were selected: 200°C, 400°C, 600°C and 800°C.

The temperature effect was studied with input decks for *MAT_224 based on single hardening curves at the test rate of $1\text{E-}3 \text{ s}^{-1}$. All the thermal tests were conducted at this rate.

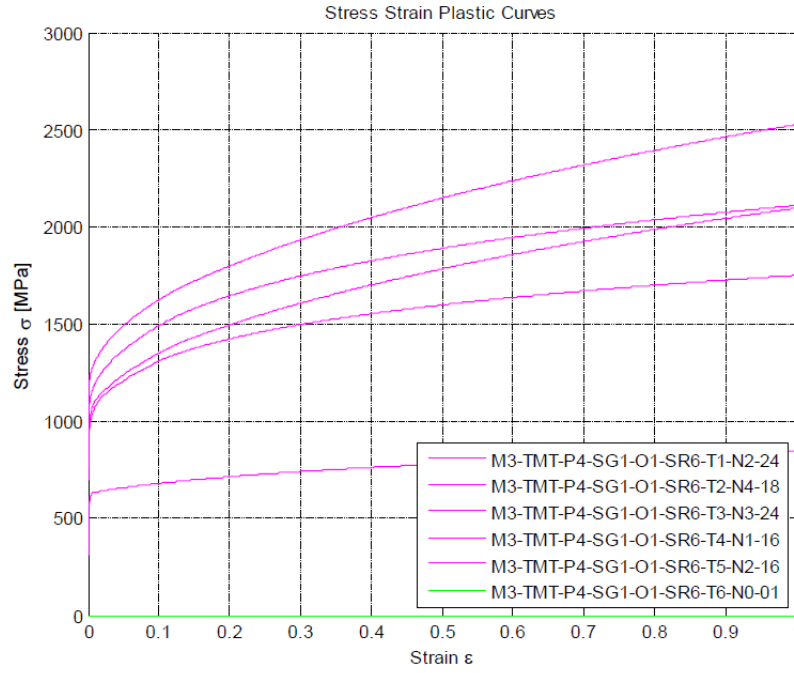


Figure 26: Temperature dependent input curves

3.3.6. Strain Rate Dependent Tabulated Input

Rolled Inconel 718 plate has a strain rate and temperature dependency in the plastic region. Multiple tensile tests were conducted by OSU using different strain rates. A hardening curve was derived for each strain rate ($1e-4$, $1e-2$, 1 , $5e2$ and $2e3 \text{ s}^{-1}$). For the lower strain rates flat dog-bone specimens were pulled at room temperature on the Instron machine. Displacement and force were measured at a fixed time interval. The testing at higher strain rates was performed as described in [119], a method commonly referred to as a split-Hopkinson bar. This method differs from the dog-bone specimen tension testing in that the specimen undergoes impulsive loading, rather than being machine-loaded following a prescribed path, and therefore higher strain rates can be

achieved. Each of the different strain rate tests was processed using the method described previously.

3.3.7. Conversion of Plastic Work into Heat (Taylor-Quinney Effect)

In the higher rate tests within the localized region of necking, there is not sufficient time for conduction to carry away the heat generated by the plastic deformation, and so the process becomes adiabatic. This adiabatic process causes a significant increase in the temperature of the specimen locally and governs the behavior at larger strains. As a result, the simulation of the tension tests is sensitive to the amount of energy generated by the plastic work, which is converted into thermal energy.

The percentage of plastic work that is converted into thermal energy is defined by the Taylor-Quinney coefficient, typically signified as β . A constant β value of 0.8, which best matched the stress-strain test behavior exhibited in the tension tests, was determined through trial-and-error.

With this, a fully coupled thermal solution using *MAT_224 in LS-DYNA® could be performed. This simulates the conduction of thermal energy away from highly strained elements. Without including conduction, temperatures will rise more in the simulations than in tests, leading to non-physical analytical results. This non-physical result will be very small in high rate, short duration simulations, and can be safely ignored. In simulations where both high rate and low-rate loading takes place simultaneously and significant strains are introduced into elements at a lower rate (i.e. longer duration simulation, such as full engine blade loss) as well as at high rates, including conduction may be required for accurate analysis.

Strain Rate Is Not a Constant

Initially, the strain rate is assumed to be either the nominal strain rate of the test, or the grip speed divided by the initial length of the sample covered by the extensometer. However, this assumption is incorrect, and there are two reasons. First, it is easy to show that:

Equation 28: Strain rate is not a constant

$$\frac{d\varepsilon(t)}{dt} = \frac{1}{l(t)} \frac{dl}{dt}$$

consequently, the strain rate is not constant under constant grip loading speed. Although the strain rate is uniform over the sample until necking occurs, it varies with time if the grip speed is constant.

Second, after the onset of necking, all plastic deformation will localize in the necked area, whereas the plastic strain will remain constant outside the neck. Therefore, after necking, the strain rate will increase in the necked area and will no longer be uniform over the sample.

Assuming the deformation at the necking point is still uniform over a smaller distance L_0' , then the engineering strain rate before necking is:

Equation 29: Engineering strain rate before necking

$$\dot{\varepsilon}_{eng_bn} = \frac{\dot{L}(t)}{L_0}$$

whereas the engineering strain rate after necking is:

Equation 30: Engineering strain rate after necking

$$\dot{\epsilon}_{eng_an} = \frac{\dot{L}(t)}{L_0'}$$

and consequently, it is shown that the engineering strain rate will increase considerably in the necked area:

Equation 31: Before and after necking engineering strain rate relationship

$$L_0' \ll L_0$$

$$\dot{\epsilon}_{eng_an} > \dot{\epsilon}_{eng_bn}$$

The same tendency is true for the true strain rate, although somewhat more difficult to show.

Other variations in the testing procedure (e.g., non-constant grip speed, non-fixed boundary conditions, etc.) may also influence the strain rate value and cause the nominal strain rate to deviate from the physical value.

3.3.8. High Strain Rate Sensitivity

As described in the previous section, the strain rate in a test with localization is not a constant. Localization is especially early and extreme in the higher strain rate Inconel-718 tests. The strain rate in the region of localization may reach values significantly above the nominal strain rate for the specimen. As a result, tension test data must be supplemented with synthetic curves generated using rate sensitivity trends from

tension and compression tests. The compression tests reached much higher strain rates than the tension test but, due to friction and boundary conditions, complete stress-strain curves are difficult to derive from compression tests. Therefore, synthetic curves are created using a combination of information from the compression and tension tests. These synthetic curves are combined with the stress-strain curves derived directly from the tension tests. Looking at the stress at a particular strain (specifically, 5% strain) across all tests categorized by differing strain rates demonstrates the strain rate sensitivity (Figure 27).

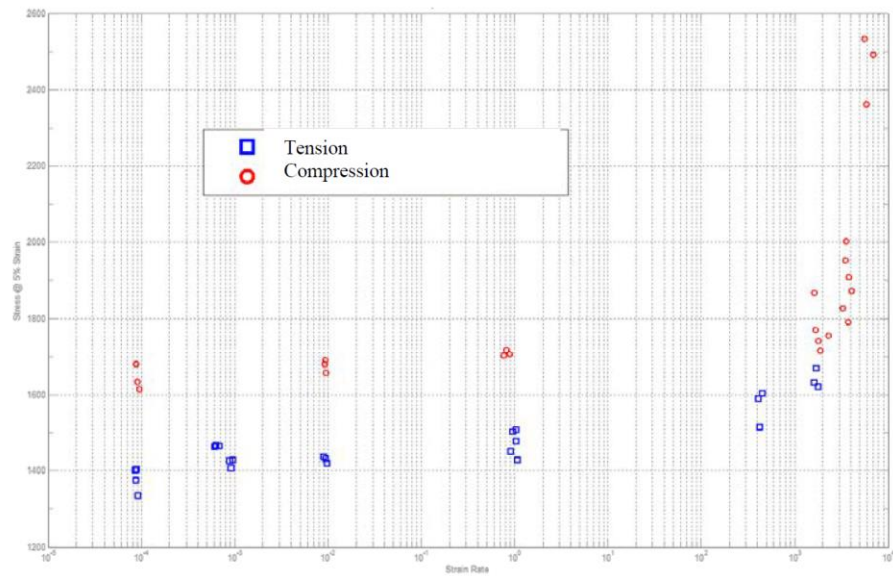


Figure 27: Stress at 5% strain. All tests

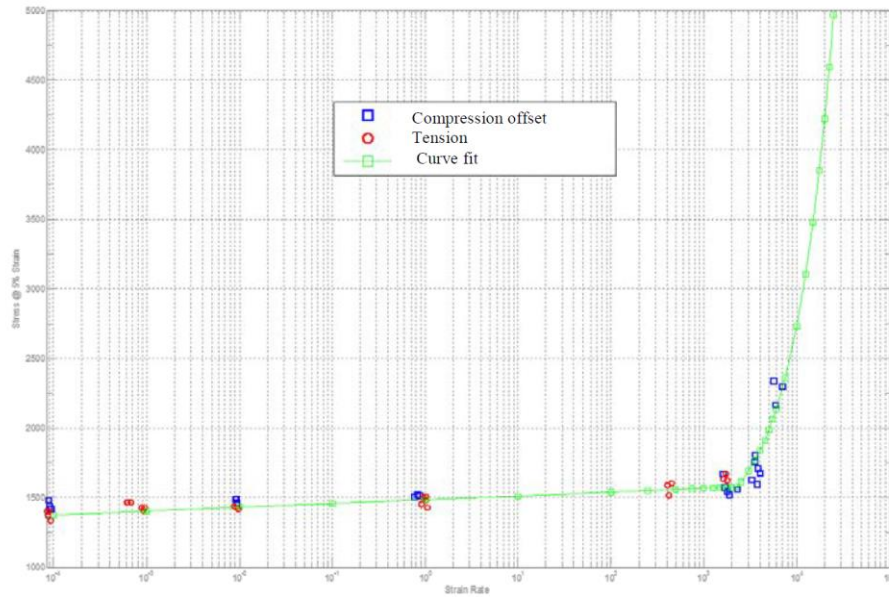


Figure 28: Stress at 5% strain. Global data curve fit

As shown in Figure 27, at any given strain rate, there is a fairly wide spread between the stresses from the compression series and the tension test series. The strain rate abscissa is plotted on a logarithmic scale. The compression tests were translated so that their stresses passed through the tension tests of the ½-inch plate (Figure 28).

In tension tests conducted at the nominal strain rate higher than $\sim 10^3 \text{ s}^{-1}$ the physical processes causing the strain rate sensitive behavior of the material at these intermediate rates is transitioning and is a combination of both the lower and higher rate physics. As a result, the exact stress-strain behavior can neither be obtained by extrapolation, nor by reading it directly from the tests. As mentioned before, the stress-strain curves required by *MAT_224 must be isothermal. The tests at the higher strain rates were not at a constant strain rate and not isothermal; this is another reason why

synthetic stress-strain curves were required. The stress-strain curve generated for the $1\text{E-}4\text{ s}^{-1}$ rate was used as the basis for all of the synthetic higher rate curves. Each curve's stress was translated so that its value at 5% strain was at the desired value. These curves were bundled together as a tabulated input for *MAT_224. Intermediate curves are created internally by LS-DYNA® through linear interpolation between user input curves. Unlike material models which use curve-fitting to fit an analytical formula to the test data and derive values for material constants, this method reads all of the input curves and precisely generates an internal yield surface numerically. The strain rate sensitivity and consequently the iso-rate curves table was established by trial-and-error matching of the tension test data.

3.3.9. Stress Strain Tabulated Input of Multiple Strain Rates and Temperatures

As discussed in the previous section, creating the higher strain rate curves using each high-rate test, one at a time, was not feasible with Inconel-718. The *MAT_224 input curves in the iso-rate table must be at constant temperature and at a constant strain rate. Neither of these conditions was satisfied by the Inconel-718 tests, as explained previously. Also, as explained before, the process employed for creating the higher rate stress-strain curves required combining information from higher rate compression tests with lower, constant strain rate tension tests. Inconel 718 showed a behavior similar to a BCC in relation to hardening curve strain rate dependence (see Figure 16). Therefore, a quasi-static hardening curve was offset to the appropriate yield stress for each strain rate.

An iso-thermal constant strain rate curve needs to be used as a baseline for the synthetic high strain rate hardening curves. The stress-strain curve at the strain rate of $1\text{E-}4\text{ s}^{-1}$ was used as the baseline in the iso-rate table, with an off-set appropriate to match the strain rate sensitivity curve. A trial-and-error process was performed, wherein both the magnitude of the stresses in the transition and higher strain rate regions, and the Taylor-Quinney coefficient, β , were varied simultaneously. Each of the tests was analyzed multiple times, until a satisfactory match to all of the test data was achieved. Many iterations were performed before this satisfactory match was achieved.

The initial and final strain rate sensitivity curve, used to offset the base stress-strain curves, resulting from the trial-and-error process is shown in Figure 29.

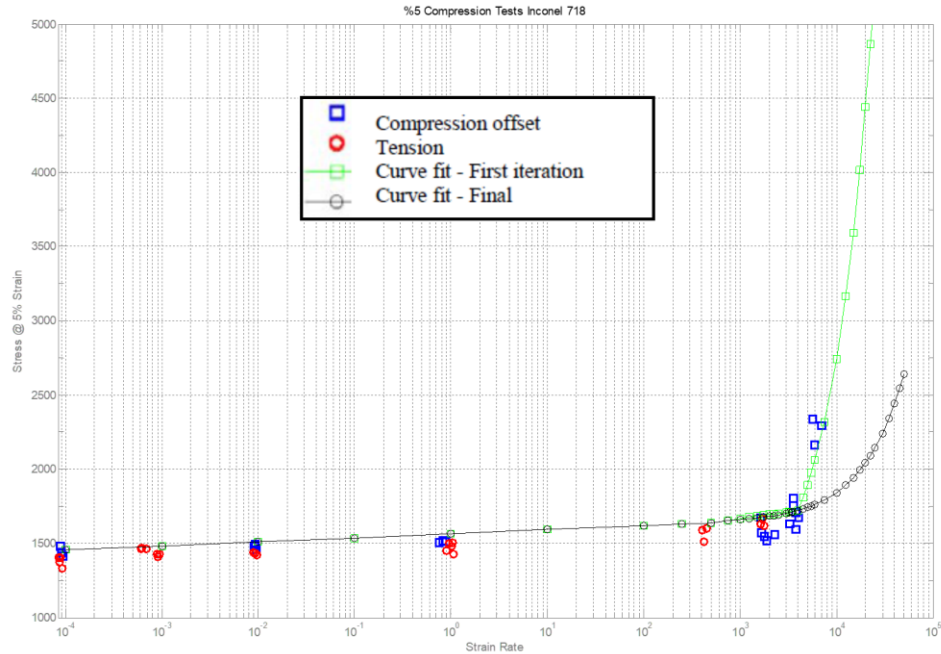


Figure 29: Final strain rate sensitivity at 5% strain

The final strain rate sensitivity curve shown was used to offset the base curve and to create all the iso-rate and iso-thermal input curves. Force vs. displacement, strain rate vs. strain and plastic strain DIC Image vs. principal strain rate from the simulations were also used for comparison between simulations and tests [28].

These simulations were performed by applying the test displacements taken from DIC because neither of the boundary conditions of the split-Hopkinson bar tension tests was fully fixed.

All the higher strain rate tests (nominally 500 s^{-1} and 2000 s^{-1}) were analyzed and comparisons were made to the physical test results. In the region of localization, the strain rate reached approximately 4000 s^{-1} for the nominally 500 s^{-1} test and 8000 s^{-1} for the nominally 2000 s^{-1} test.

Figure 30 and Figure 31 show a comparison of force vs. displacement and strain rate vs. strain for Test: M3-TMT-P4-SG1-O1-SR5-T1-N3 (nominally 2000 s^{-1}) [28]. Only one set of results is shown for space reasons. All the other simulations show a similar match to the tests.

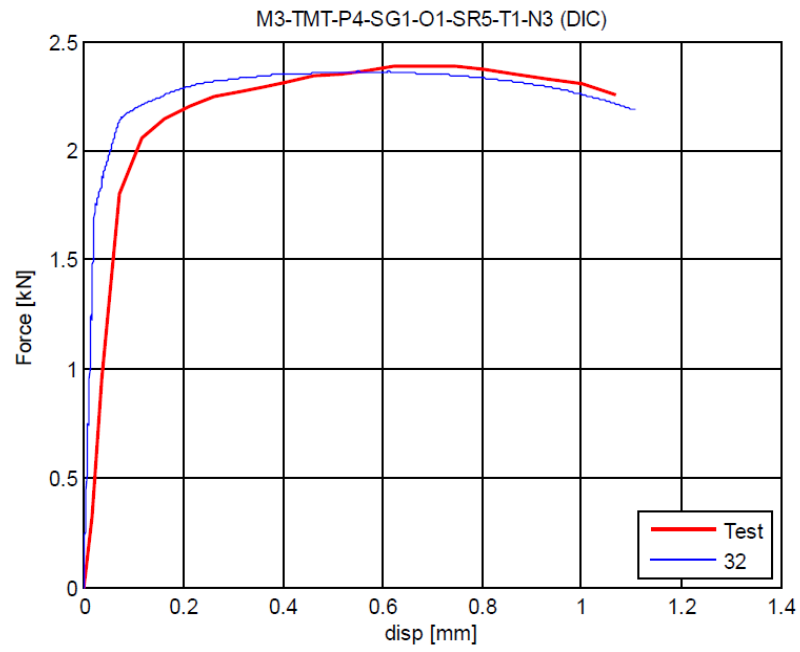


Figure 30: Force vs. displacement

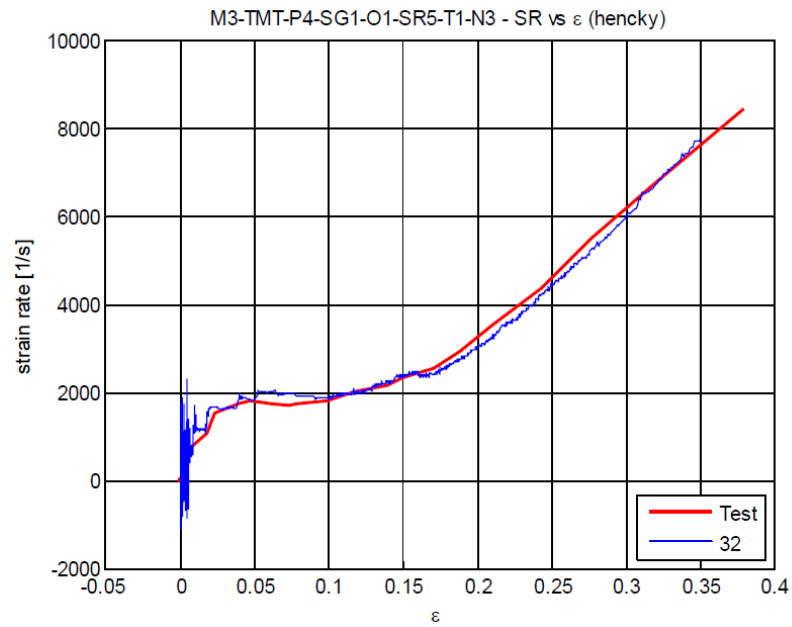


Figure 31: Strain rate vs. strain

3.4. Inconel-718 Updated Very High Strain Rate Model

The material sensitivity at high strain rate developed in paragraph 3.3.9 was used with the failure surface and failure scaling curves developed as reported in paragraph 3.5. While simulating the ballistic impact tests performed by NASA Glenn Research Center, the results obtained were not showing the correct ballistic limit neither a physical failure. The 0.5” Inconel-718 plates, for the impact speeds tested, present a failure mechanism known as adiabatic shear band. The initial simulations performed with the tabulated input characterized in the previous section showed a non-physical mechanism of crushing like failure. An explanation for this discrepancy was sought, and very high strain modeling was investigated.

The procedure used in paragraph 3.3.9 gives accurate results up to the strain rate range covered by the tests ($\approx 8000 \text{ s}^{-1}$). However the ballistic test can reach strain rate above 50000 s^{-1} . Further procedures to characterize Inconel-718 at very high strain rate (10000 and above) need to be implemented. The first method (3.4.1) is to create different extrapolations of the curve fit describe in the previous paragraph above 8000 s^{-1} and evaluate the one that gives the best results in the ballistic impact simulations. The next method (3.4.2) is to use a hybrid analysis to compare the indentations of unpenetrated ballistic tests.

3.4.1. Stress flow sensitivity at very high strain rates

As stated in previously, material proprieties above 10^4 s^{-1} are crucial for accurate modeling but hard to determine by testing. As a result, the alloy properties must be extrapolated outside the test data calibration range. An accurate extrapolation is not

trivial since materials exhibit different strain hardening and softening characteristics at different strains, strain rates, and temperatures. Up to now, the stress flow at very high strain rates has been characterized by matching the data available from the material test (SPHB), typically up to strain rate around $5 \times 10^3 \text{ s}^{-1}$ and then extrapolating stress flow with a heuristic procedure. Too low of a strain rate sensitivity at high rates was identified as a main cause of this crushing-like failure mode.

Three different extrapolations for the material strain rate sensitivity were compared. The first is the original linear extrapolation of Region IV obtained in paragraph 3.3.9, the second one is still a linear extrapolation of Region IV but with a much higher gradient, and the last one is an extrapolation where the strain rate effects above 10^3 s^{-1} are saturated (see Figure 32). All three of the different extrapolations share the same Region I and Region II, which is crucial to match the material characterization tests. All three of the different extrapolations match the material characterization tests.

The current results (Table 2) from the simulations of the Inconel-718 material model (OLD) did not accurately predict the ballistic limit (velocity at which penetration occurs) measured by NASA tests. The strain rates in these analyses went up to 35000 s^{-1} , well into Region IV, while the available mechanical property data went up to 10^3 s^{-1} . The predicted ballistic limit is higher than that of the tests, and so element erosion is deficient. The most likely reason for insufficient element erosion is that the mesh density is not sufficiently high to capture the adiabatic shear bands' extreme local deformation. Consequently, the analysis does not predict the actual rise in temperatures caused by adiabatic heating in the corresponding elements. It appears that in any case, the

simulations presenting the correct failure mechanism (with the initiation of a crack and a plug) are the two with the linear extrapolation in Region IV. The shear band begins to form but does not open fully. It should also be noted that the analysis with the stronger gradient in the extrapolated Region IV predicts higher temperatures, above 600K, somewhat closer to the temperatures where Inconel-718 becomes brittle and in a more localized region [15].

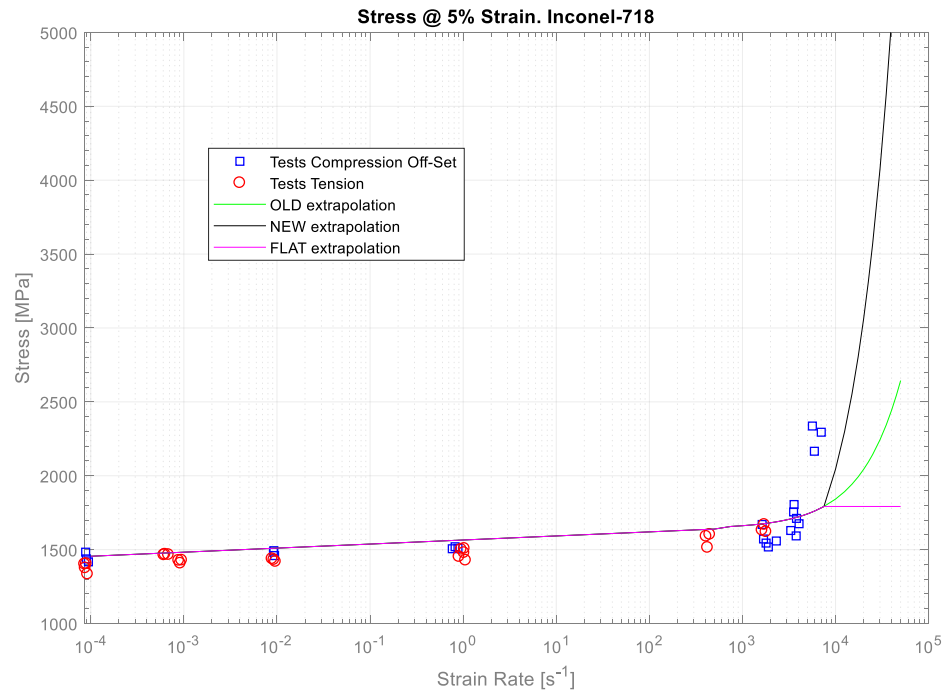
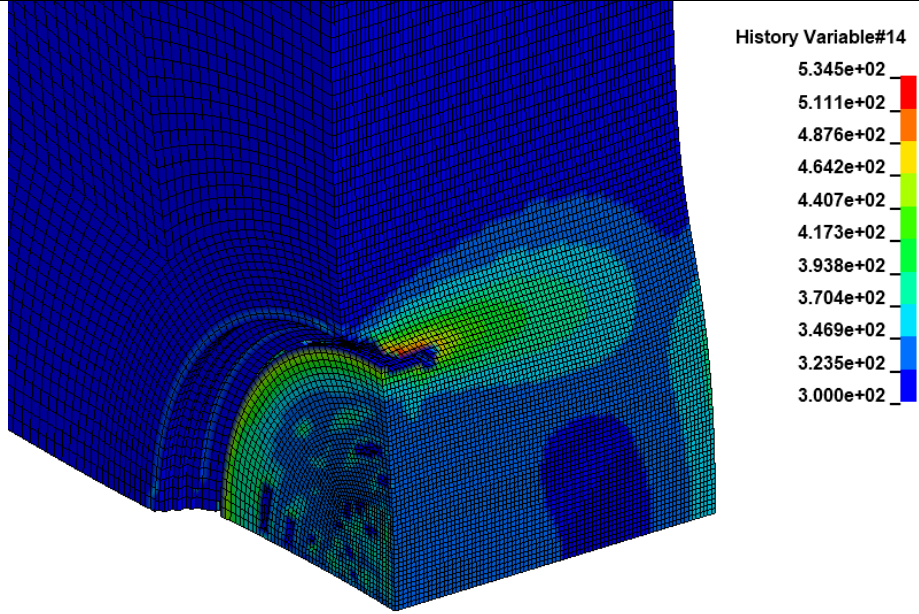
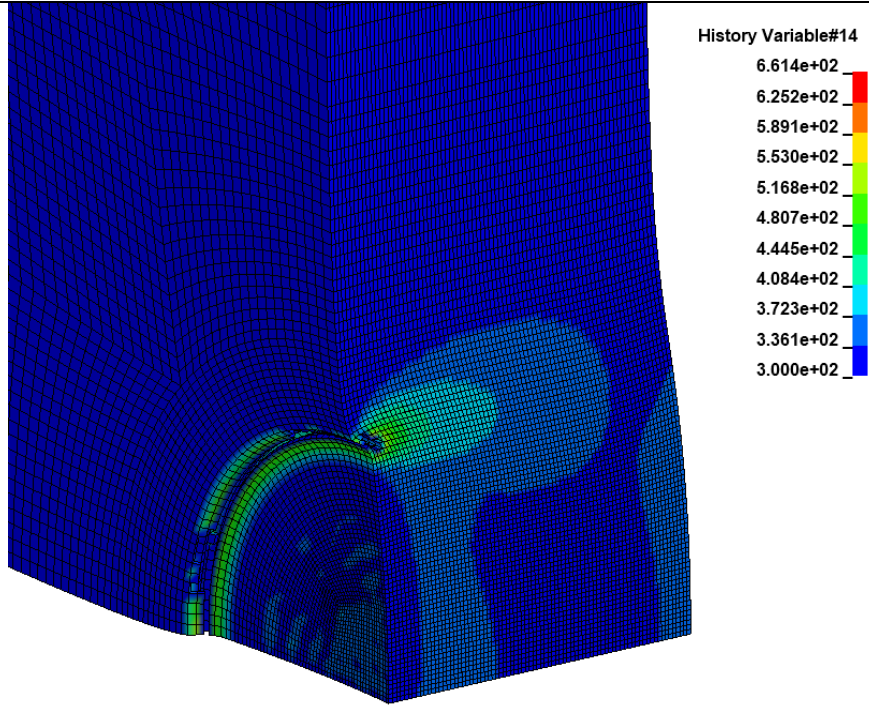
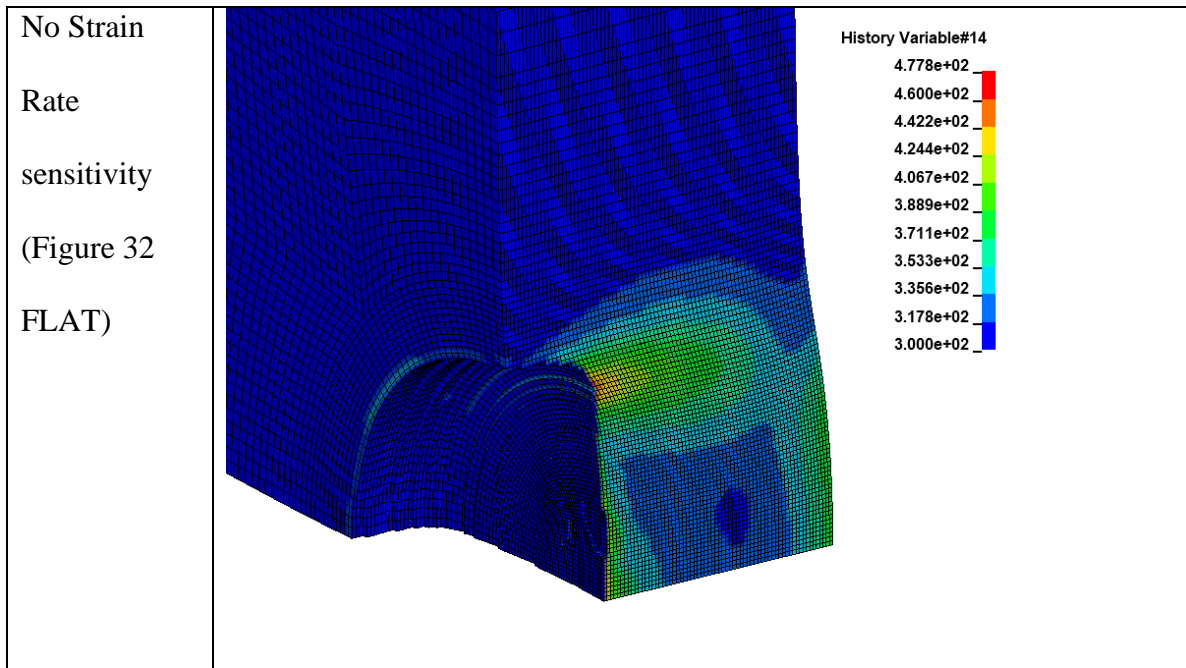


Figure 32: Stress at 5% strain curve fit. Different very high strain rate extrapolations

Table 2: Temperature raise in 0.5" Inconel-718 plate. Impact velocity 203 [m/s], 80 elements trough the thickness, elastic projectile

Simulation of test DB266		Axisymmetric MESH
see (Table 21).		Temperature Contours [K]
Low Strain Rate sensitivity (Figure 32 OLD)	 <p>History Variable#14</p> <ul style="list-style-type: none"> 5.345e+02 5.111e+02 4.876e+02 4.642e+02 4.407e+02 4.173e+02 3.938e+02 3.704e+02 3.469e+02 3.235e+02 3.000e+02 	
High Strain Rate sensitivity (Figure 32 NEW)	 <p>History Variable#14</p> <ul style="list-style-type: none"> 6.614e+02 6.252e+02 5.891e+02 5.530e+02 5.168e+02 4.807e+02 4.445e+02 4.084e+02 3.723e+02 3.361e+02 3.000e+02 	



3.4.2. Indentation Comparison using Hybrid Analysis

The second method to validate the extrapolation of the fitting curve for the flow stress at very high strain rates is the comparison of the indentation of unpenetrated ballistic impact tests. This comparison is a novel approach, which has not been previously used to assess the very high strain rate material behavior. A set of simulations of ballistic impact unpenetrated tests were performed using a hybrid explicit/implicit approach. A blunt projectile impacted a plate of Inconel 718 without fully penetrating it. First, the impacts were modelled with an explicit FEM solver. Then, to obtain the final static equilibrium solution, the resulting stresses and strains were extracted from the explicit simulation. The implicit FEM solver was then used to calculate the static equilibrium displacements. The reason this approach is necessary is that the

computational time needed to reach equilibrium with the explicit solver would be prohibitive. The downside of the approach is that due to memory limitations we were not able to apply the implicit solution to the whole plate but only to the center core (see Figure 33).

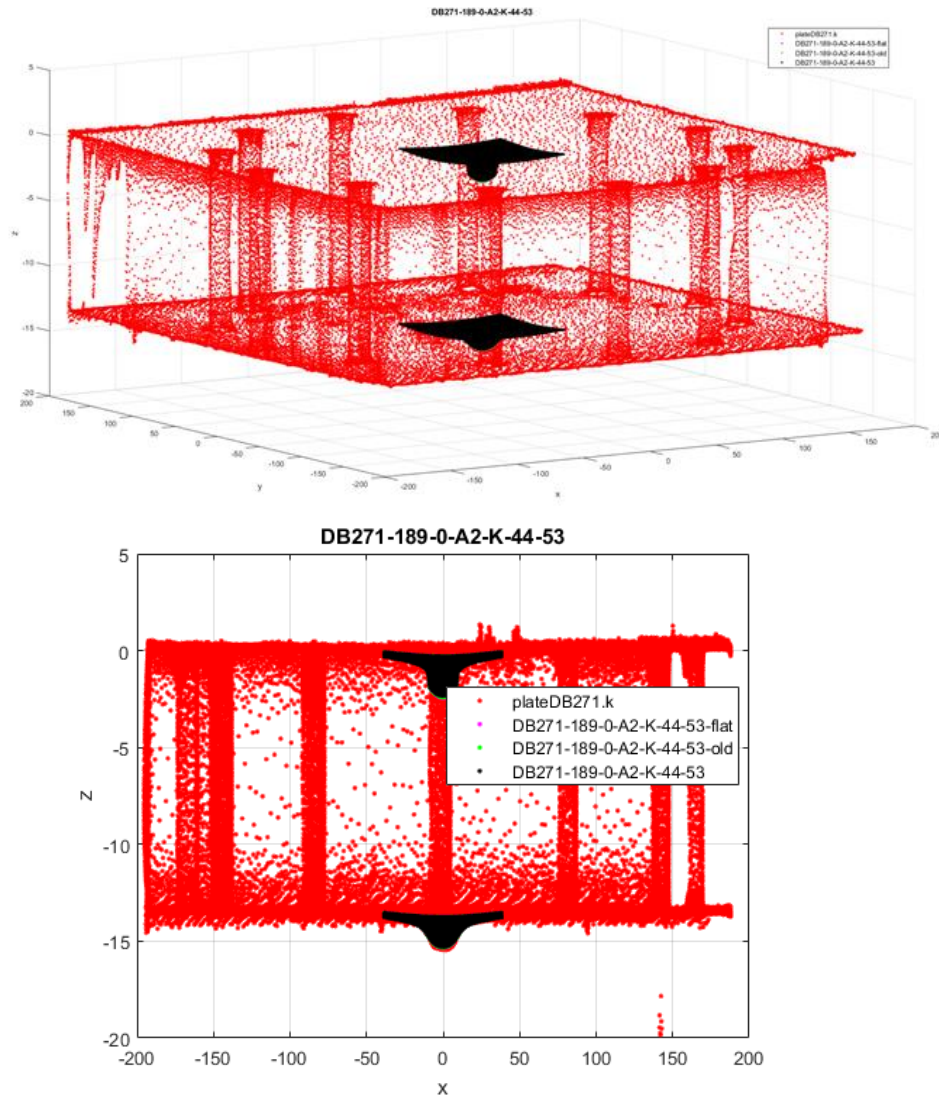


Figure 33: 3D comparison of the scanned plates from the tests and the simulation results

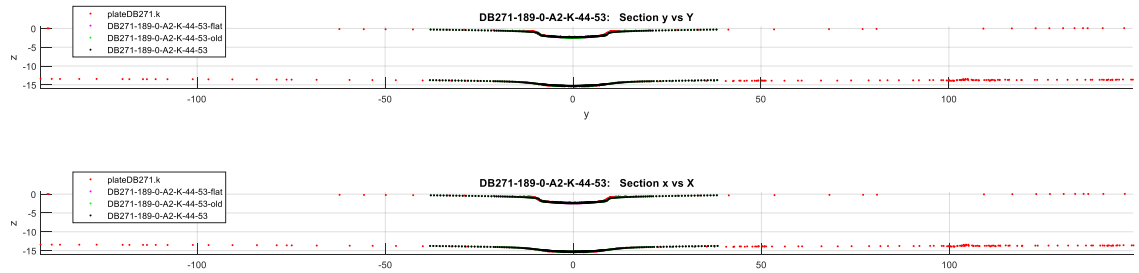


Figure 34: Indentation comparison of unpenetrated test DB271 (see Figure 32) and hybrid simulation results in x and y direction for 3 material very high strain rate models (see Table 21)

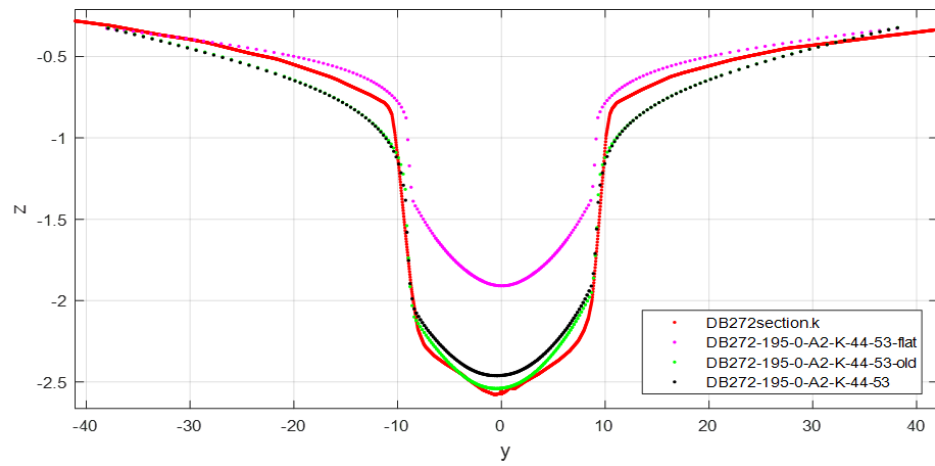


Figure 35: Comparison of the resulting indentation in a section of the top surface of the Inco 0.5" plate for 3 different material high strain rate extrapolations (see Figure 322). Test DB272 (see Table 21)

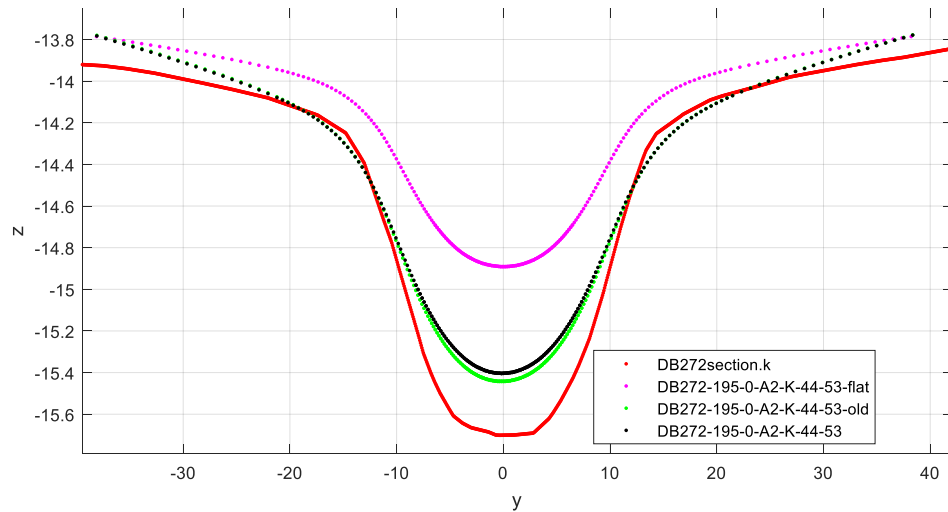


Figure 36: Comparison of the resulting indentation in a section of the bottom surface of the Inco 0.5" plate for 3 different material high strain rate extrapolations (see Figure 32). Test DB272 (see Table 21)

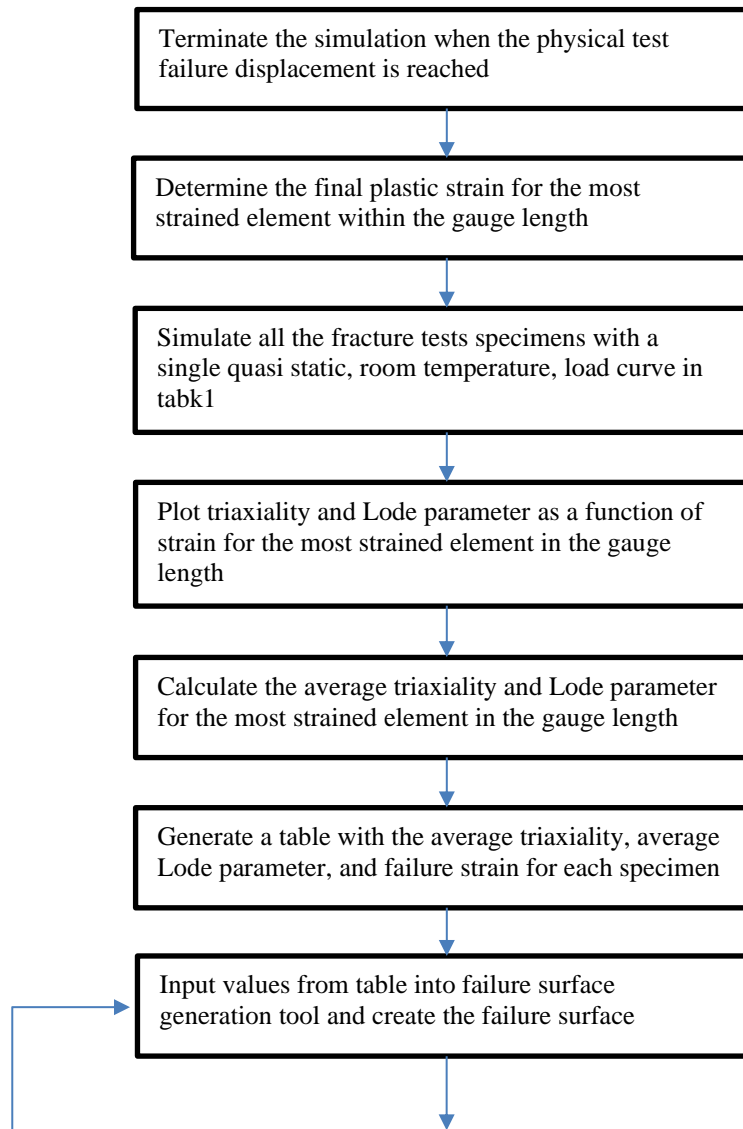
Due to the different scale between the dimension of the plate and the depth of the indentation (see Figure 34) to appreciate the differences in the results between the different material high strain rate extrapolation we need to zoom in the indented region of each top and bottom surfaces (see Figure 35 and Figure 36).

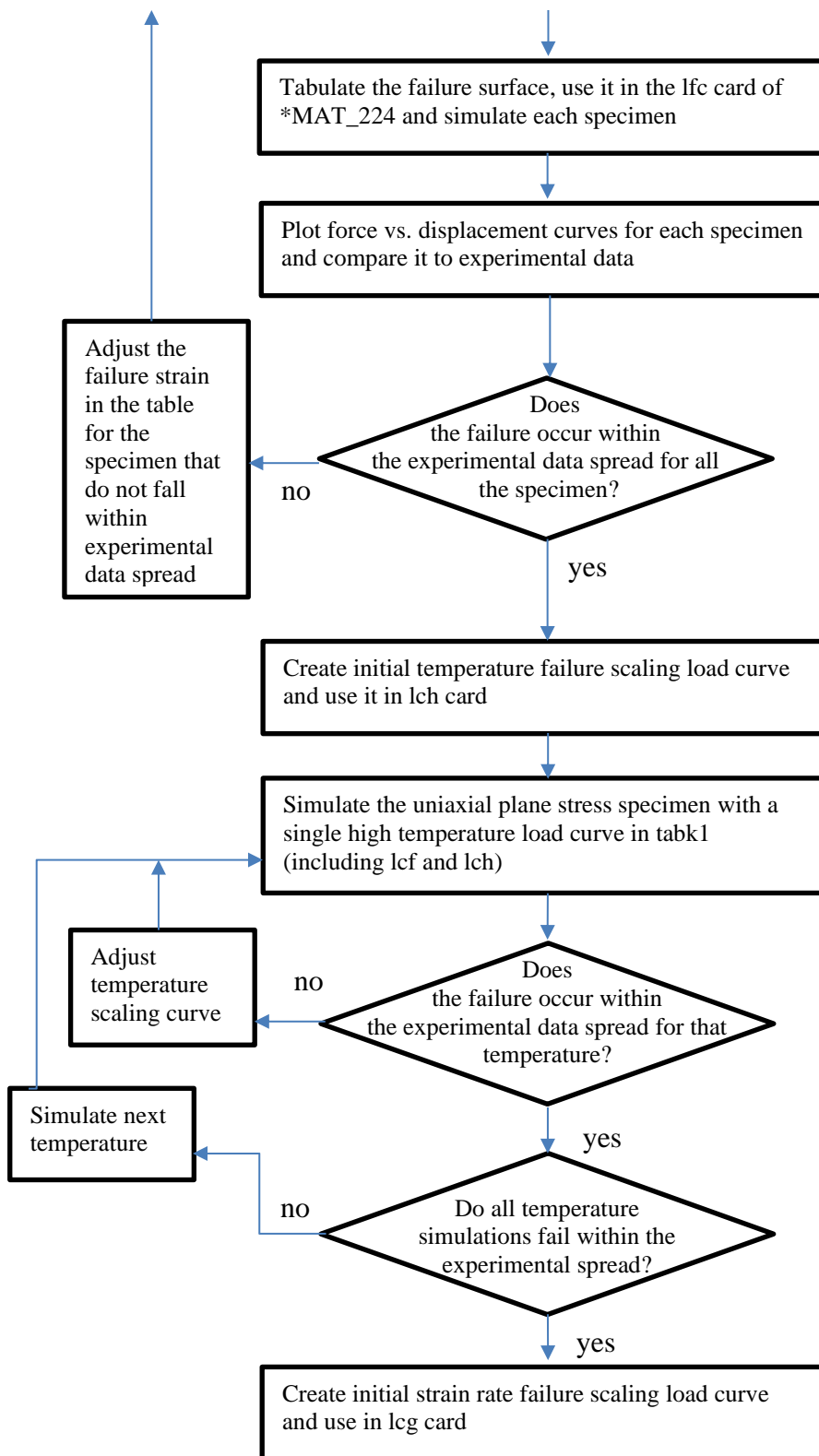
The use of this novel method was successful in determining the general nature of the very high strain rate sensitivity. However, the sensitivity of indentation depth was insufficient to fine tune the high-rate extrapolation. It is possible that alternate test conditions might produce an increase in the sensitivity of indentation depth to the very high strain rate behavior. After analyzing the scans of each unpenetrated test (see Table 21) with the corresponding hybrid simulations the NEW extrapolation (see Figure 32) was considered the most accurate in simulating the unpenetrated tests and the most promising base to develop a modified tabulated J-C material model capable of developing an ASB.

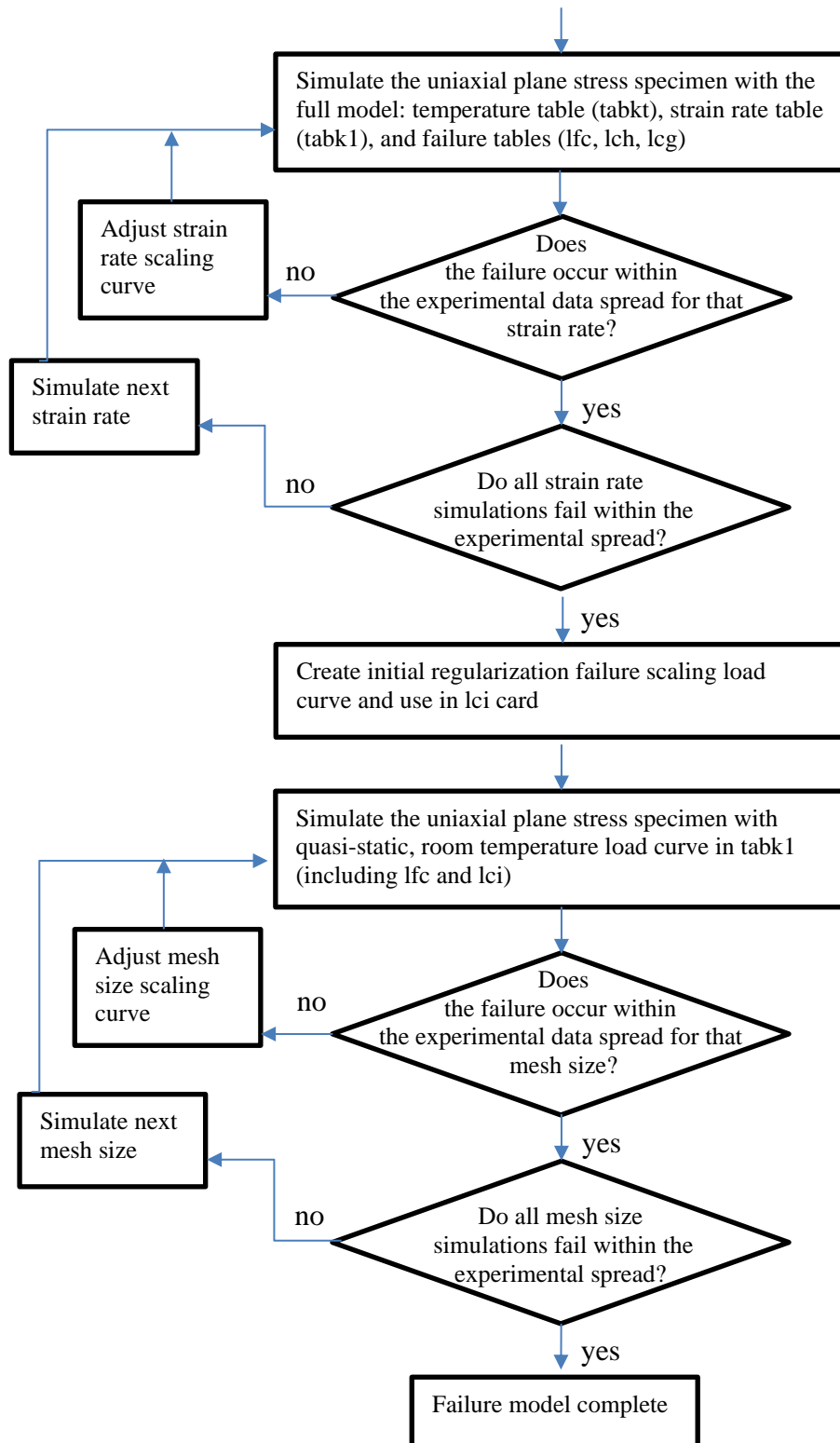
3.5. Characterization of the Failure Surface Locus

*MAT_224 consists of 6 tables to describe strain rate sensitivity and failure characteristics (see Figure 20). The creation of the strain rate sensitivity table (tabk1) and temperature sensitivity table (tabkt) for Inconel-718 material was described in the previous paragraphs (3.3, 3.4). The material model currently has four input parameters that calculate the accumulated damage for a given element. The first parameter is a table of curves that defines the plastic failure strain as a function of triaxiality and Lode parameter (lcf). If the table option is used for this parameter, a failure surface is defined which is appropriate for solid elements. The second parameter is a load curve that defines

the plastic failure strain as a function of plastic strain rate (l_{cg}). The third parameter is a load curve that defines the plastic failure strain as a function of temperature (l_{ch}). The last parameter is a load curve that defines the plastic failure strain as a function of element size and triaxiality (l_{ci}) [15], [39]. Following is a flow chart of the procedure use to develop the failure model [39]. All the specimens have the same mesh element size.







3.5.1. Failure Surface

The first table added to the input deck was the failure surface (lcf). In order to generate an effective failure surface, many different tests using different geometries that produce varying states of stress were completed. These tests vary in both triaxiality and Lode parameter at the point of failure (Figure 37).

The mechanical property tests were performed by Ohio State University, who provided the specimen geometry, force data, displacement data, strain data, and DIC images. In total, 25 different specimens were used to determine the failure surface model.

These 25 specimens are listed below (with abbreviations):

1. SG1: Plane stress specimen (pure tension)
2. SG2: Plane stress specimen (notch radius 14.28mm)
3. SG3: Plane stress specimen (notch radius 4.7625mm)
4. SG4: Plane stress specimen (notch radius 0.396mm)
5. SG5: Axisymmetric specimen (pure tension)
6. SG6: Axisymmetric specimen (notch radius 35.72mm)
7. SG7: Axisymmetric specimen (notch radius 17.46mm)
8. SG8: Axisymmetric specimen (notch radius 9.52mm)
9. SG9: Axisymmetric specimen (notch radius 5.56mm)
10. SG10: Axisymmetric specimen (notch radius 3.175mm)
11. SG11: Plane strain specimen
12. SG12: Plane strain specimen
13. SG13: Plane strain specimen (notch radius 4.7625mm)

14. LR1: Combined (tension/torsion) specimen
15. LR2: Combined (tension/torsion) specimen
16. LR3: Torsion specimen
17. LR4: Combined (compression/torsion) specimen
18. LR5: Combined (compression/torsion) specimen
19. Punch1: Large diameter punch specimen (blunt)
20. Punch2: Large diameter punch specimen (sharp)
21. Punch3: Large diameter punch specimen (hemisphere)
22. Compression: Uniaxial (cylindrical) compression specimen
23. Punch 4: New punch no backing plate
24. Sequential Punch 5: Thin Backing plate
25. Sequential Punch 6: Thick backing plate

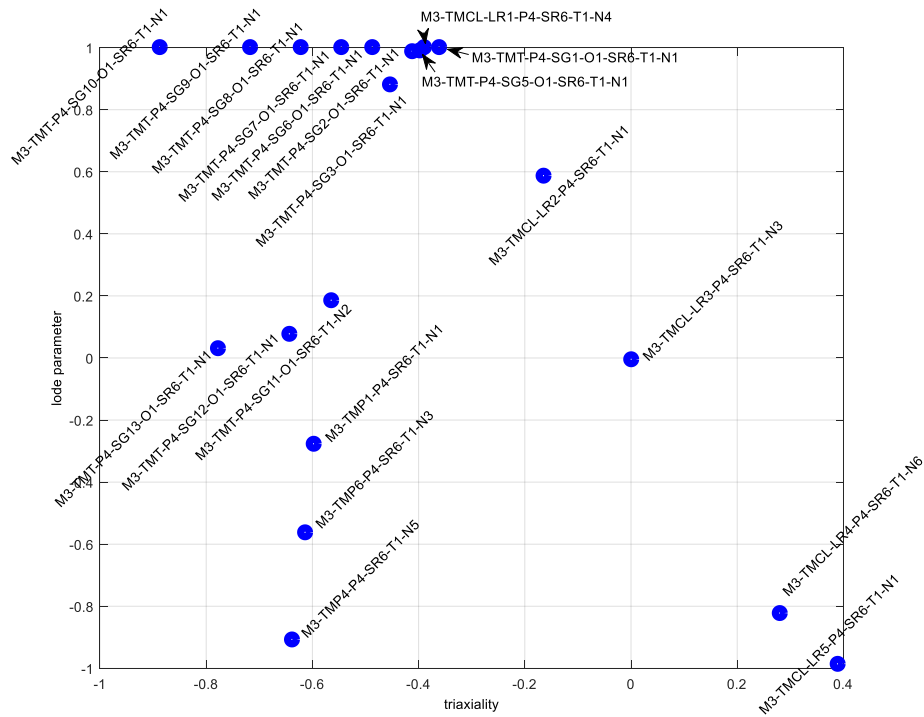


Figure 37: Tests Triaxiality vs Lode Parameter

Note that in the list above, the terms ‘plane stress’ and ‘plane strain’ actually represent families of specimen design, and that only the first of each of these families actually creates plane stress or plane strain. Using the results from these simulations a set of 3D data point were obtained (Table 3). Using these data, a failure surface was constructed, the final failure surface can be seen in Figure 38. A detailed description of all the simulation and results is scheduled to be published.

As expected, some of the failure strains had to be manually updated because some of the specimens did not fail at the correct displacement in the initial set of analyses. To correct this, an adjustment was made to several of the failure strains of the specimens.

Table 3: Data used to construct the failure surface

test	Triaxiality	Lode	Failure Strain
M3-TMT-P4-SG1-O1-SR6-T1-N1	-0.360371775	0.999996903	0.373048
M3-TMT-P4-SG2-O1-SR6-T1-N1	-0.411197974	0.986821413	0.425239
M3-TMT-P4-SG3-O1-SR6-T1-N1	-0.452924851	0.879832338	0.351876
M3-TMT-P4-SG5-O1-SR6-T1-N1	-0.388683291	1.0	0.421788
M3-TMT-P4-SG6-O1-SR6-T1-N1	-0.486287228	1.0	0.431912
M3-TMT-P4-SG7-O1-SR6-T1-N1	-0.544672054	0.999999996	0.430983
M3-TMT-P4-SG8-O1-SR6-T1-N1	-0.620998954	0.999999992	0.40109
M3-TMT-P4-SG9-O1-SR6-T1-N1	-0.71633475	0.999999918	0.242366
M3-TMT-P4-SG10-O1-SR6-T1-N1	-0.886473301	0.999998852	0.172229
M3-TMT-P4-SG11-O1-SR6-T1-N2	-0.563583047	0.184349218	0.246002
M3-TMT-P4-SG12-O1-SR6-T1-N1	-0.64239929	0.076108857	0.280913
M3-TMT-P4-SG13-O1-SR6-T1-N1	-0.776842093	0.029777128	0.4478
M3-TMCL-LR1-P4-SR6-T1-N4	-0.396935213	0.989313044	0.481081
M3-TMCL-LR2-P4-SR6-T1-N1	-0.163694144	0.585690865	0.461228
M3-TMCL-LR3-P4-SR6-T1-N3	0.001339034	-0.005866648	0.46036
M3-TMCL-LR4-P4-SR6-T1-N6	0.225443615	-0.773368816	1.4
M3-TMP1-P4-SR6-T1-N1	-0.596541516	-0.278171678	0.288232
M3-TMP4-P4-SR6-T1-N5	-0.637466208	-0.908720122	0.329874
M3-TMP6-P4-SR6-T1-N3	-0.612773622	-0.563498889	0.378719
unbacked	-0.6038	-0.996	0.505
thick	0.15	-1.0	4.0
thin	0.0	-1.0	1.0

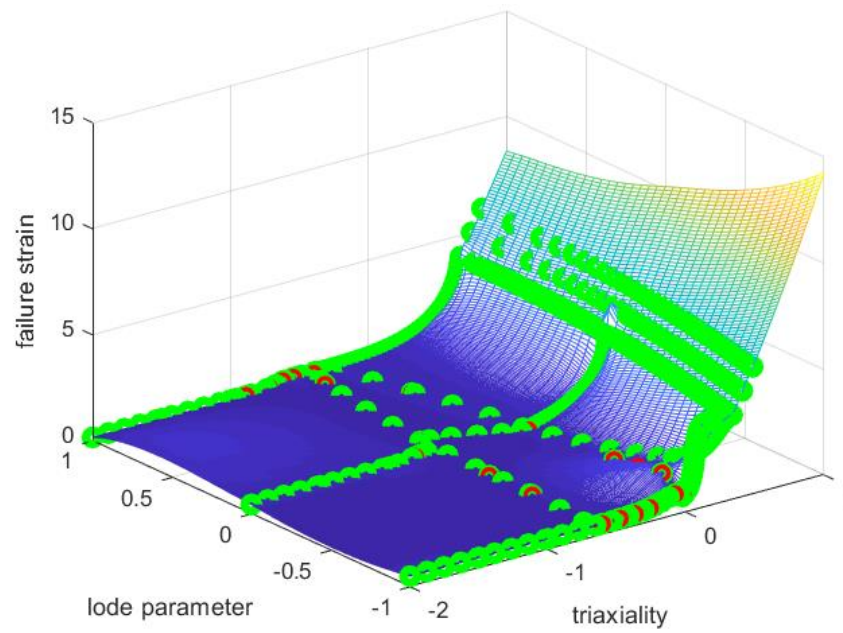


Figure 38: Failure Surface. The red points are the data from Table 3. The green point are used to generate the failure surface and are generated through 3D spline of the data over the plane stress curve, and Lode =1,0 and -1 lines (see Figure 39)

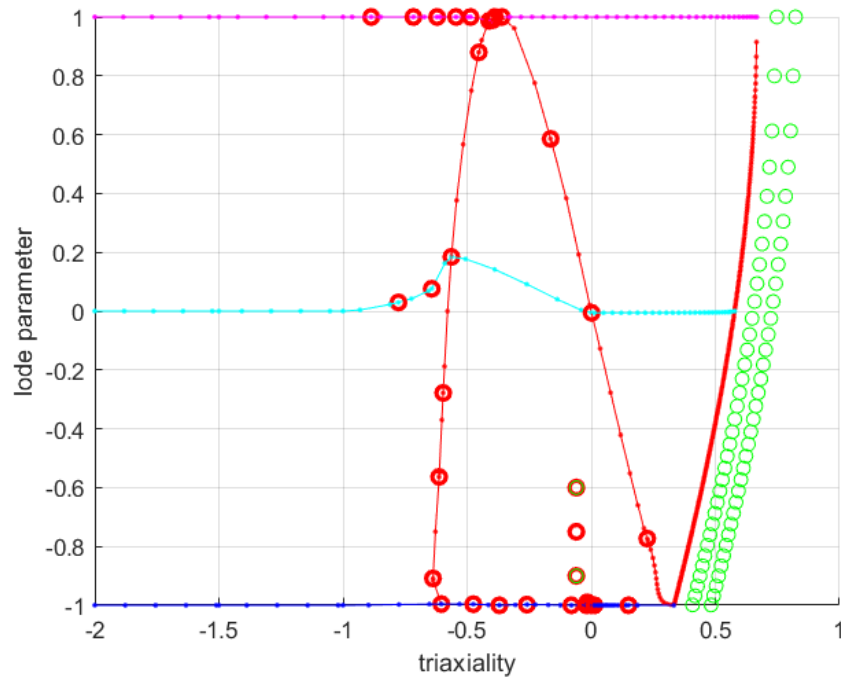


Figure 39: 3D spline interpolation of data points

3.5.2. Temperature Scaling Function

The second component of the implementation of the *MAT_224 failure model is a failure temperature scaling function (lch). This function is scaling factor for the failure surface that is dependent on the temperature of the element. For this study, five different temperatures were tested: 300 K, 473 K, 673 K, 873 K and 1073 K. For each temperature, the pure tension plane stress (SG1 [16]) specimen was used. Inconel becomes brittle at temperatures above 900K. To reflect this peculiarity and still have a monotonic curve the scaling curve was kept constant until the temperature reaches the brittle region (Figure 40).

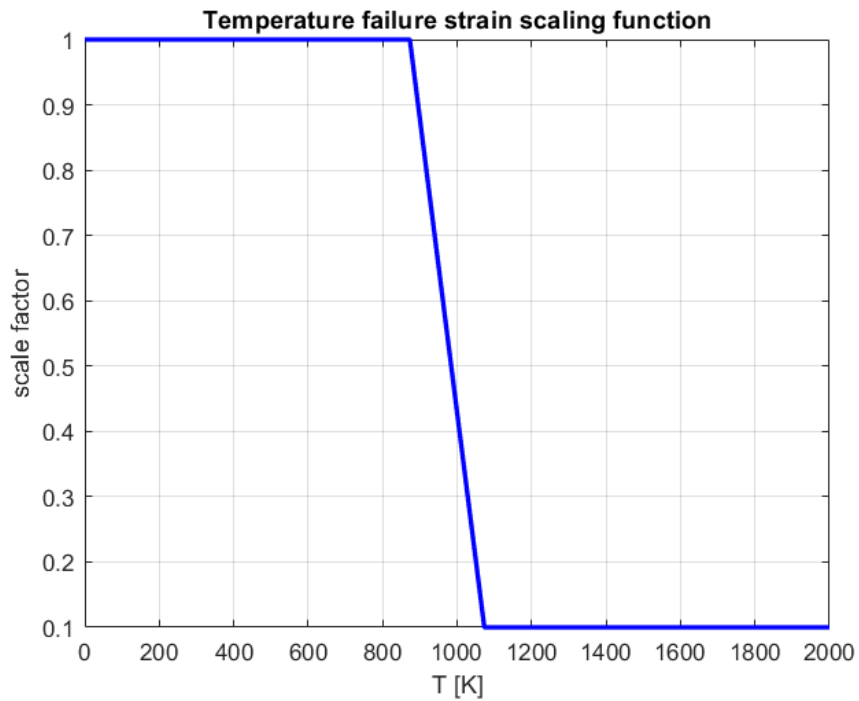


Figure 40: Temperature failure strain scaling function

3.5.3. Strain Rate Scaling Function

Similarly, a failure scaling function was also created for different strain rates. A scaling function allows the material model to scale the failure surface as a function of the elemental strain rate. Each of these strain rate tests were simulated using the same procedure as the original tension plane stress (SG1) test [16], however the full material model (strain rate curves, temperature curves, failure surface, temperature scaling curve) was used. This means that these rate dependent tests are assumed to have rate and heat effects. Inconel failure seems to be independent from strain rate (Figure 41).

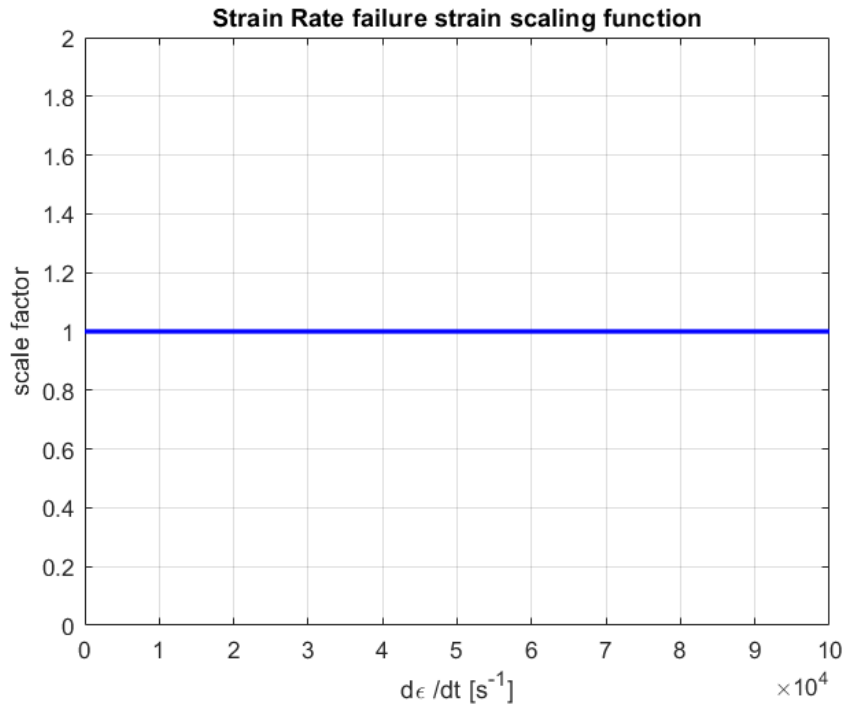


Figure 41: Strain rate failure strain scaling function

3.5.4. Element size regularization curve

The final component of the Inconel-718 failure model is a mesh size regularization scaling function for element erosion (lci). The mesh size regularization scaling function is critical because element erosion simulations do not converge as the mesh size is reduced [120]. This load curve defines the plastic failure strain as a function of the element size. The element size is calculated by the square root of the volume over the maximum area. The regularization curve is developed by simulating the tension specimen with varying mesh sizes. Originally, the mesh size for all the specimens was 0.2 mm. Each specimen was re-meshed with 0.1 mm and 0.4 mm elements (Figure 42).

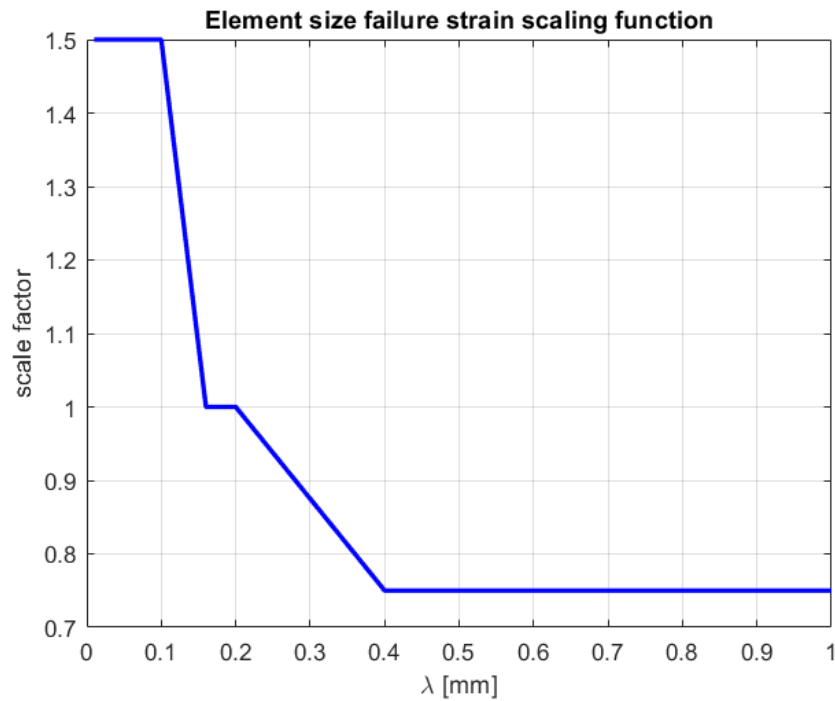


Figure 42: Element size failure strain scaling function

4. ADIABATIC SHEAR BAND 2D SIMULATION

A series of 2D simulations have been performed with in LS-DYNA[®] to verify the capability of the isotropic elasto-thermo-visco-plastic constitutive relationship and stress state depending failure implemented in the tabulated J-C material model to simulate ASBs. The use of specifically designed 2D meshes allows the use of elements of a much smaller size than a full 3D structural representation. The underlying physics and dimensions of the ASB can therefore be investigated in the 2D study. 2D shell element formulation 13, which uses plane strain solid elements to represent a semi-infinite cross-section of a structure were used. The cross-sectional geometry of the simulated structure is depicted in Figure 43 and is the same for each simulation despite having varied overall dimensions, element's dimensions and boundary conditions. The simulation is not of an actual structure, but is idealized in order to readily create ASBs, using a relatively small number of elements. A list of the simulations performed is shown in Table 4.

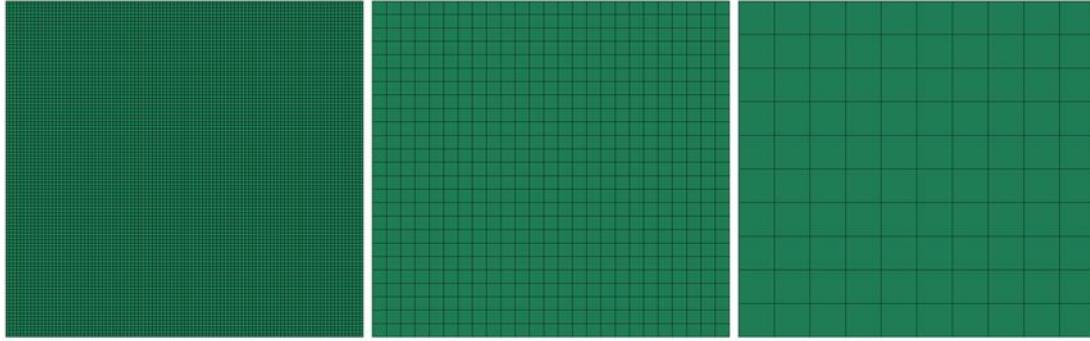


Figure 43: 2D meshes: 10000 elements, 225 elements and 100 elements

Table 4: 2D simulations

Simulation Name	# of Elements	Elements Size [μm]	Boundary Conditions type	Overall Edge Size [μm]
Inco_100x100_BC1_05	10000	0.5	1	50
Inco_100x100_BC1_1	10000	1	1	100
Inco_100x100_BC1_4	10000	4	1	400
Inco_100x100_BC1_20	10000	20	1	2000
Inco_100x100_BC1_200	10000	200	1	20000
Inco_100x100_BC8_05	10000	0.5	2	50
Inco_100x100_BC8_1	10000	1	2	100
Inco_100x100_BC8_4	10000	4	2	400
Inco_100x100_BC8_20	10000	20	2	2000
Inco_100_4_BC1	225	4	1	100
Inco_100_4_BC8	225	4	2	100
Inco_100_10_BC1	100	10	1	100
Inco_100_10_BC8	100	10	2	100

4.1. Boundary Conditions

The simulations were performed with 2 sets of boundary conditions shown in Figure 44. In both sets, the nodes marked with the red were constrained in all directions while a loading curve with velocity in the y direction was applied to the nodes marked in blue. The boundary conditions were varied to determine which set provided a better

match to physical ASB conditions. Note that boundary condition sets 1 and 2 are similar, with boundary condition set 2 having slightly more constrained nodes.

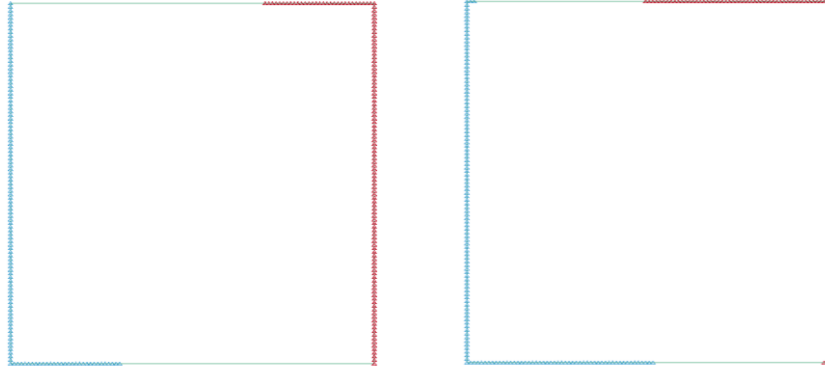


Figure 44: Boundary conditions a) 1 and b) 2

4.2. Results

The simulation results are reported in Table 5 to Table 17. The second image of each table shows the temperature of 5 elements across the shear band located medially on the longitudinal extension of the crack as depicted in Figure 45. It is important to note that the temperature rise is more localized across the shear band in the models with the smaller element size. When the chosen element size is not small enough, the model is not able to simulate the failure with a shear band mode, let alone produce an ASB. For a shear band to be adiabatic, it must show a decisive temperature gradient across the band direction; with the temperature rise only in one element and in a very short time. To be physical, the velocity of propagation of the band must also be extremely high.

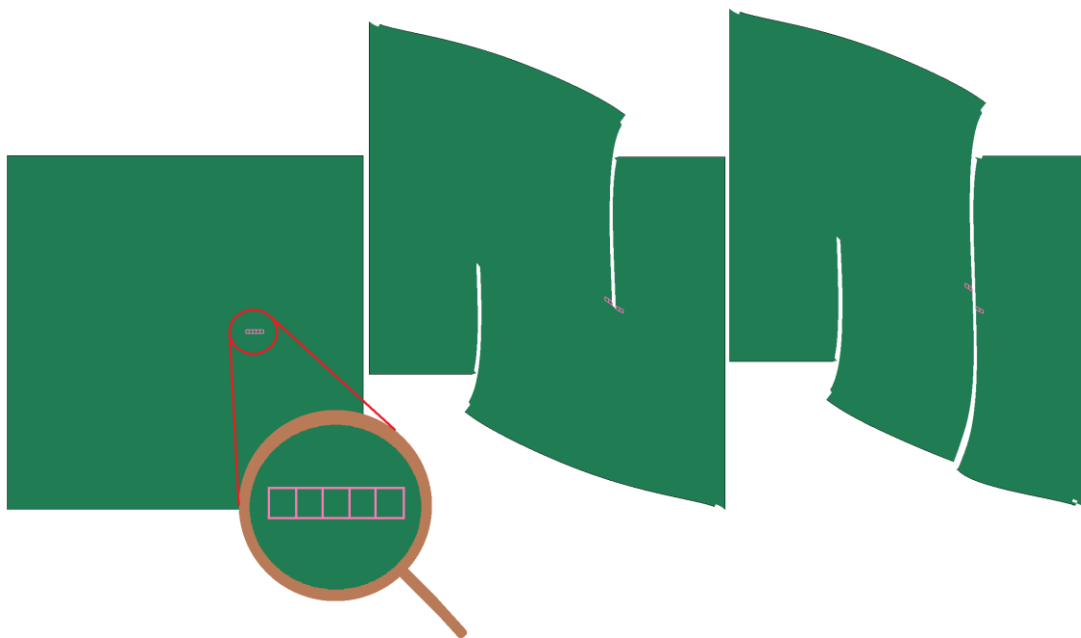


Figure 45: 5 elements across the shear band selection example

Table 5: Inco_100x100_BC1_05 simulation

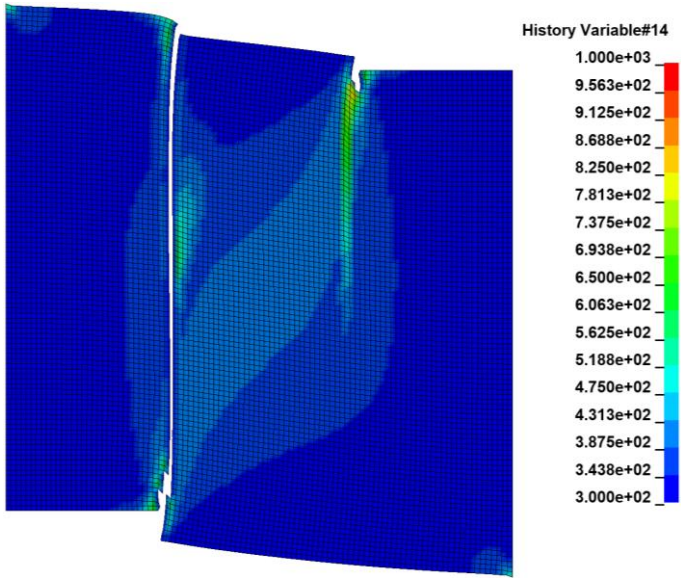
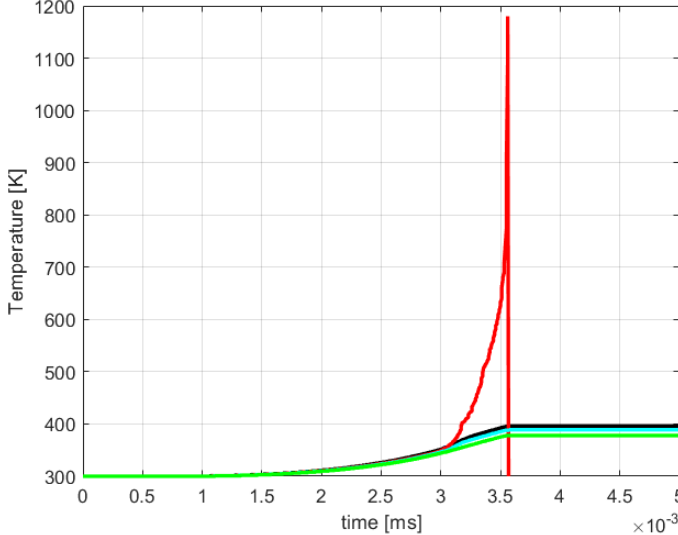
Simulation Name	Inco_100x100_BC1_05	
Temperature Contours	 <p>History Variable#14</p> <ul style="list-style-type: none"> 1.000e+03 9.563e+02 9.125e+02 8.688e+02 8.250e+02 7.813e+02 7.375e+02 6.938e+02 6.500e+02 6.063e+02 5.625e+02 5.188e+02 4.750e+02 4.313e+02 3.875e+02 3.438e+02 3.000e+02 	
Temperature of 5 elements across the crack		
ASB?		Yes
Propagation velocity [m/s]		761

Table 6: Inco_100x100_BC1_1 simulation

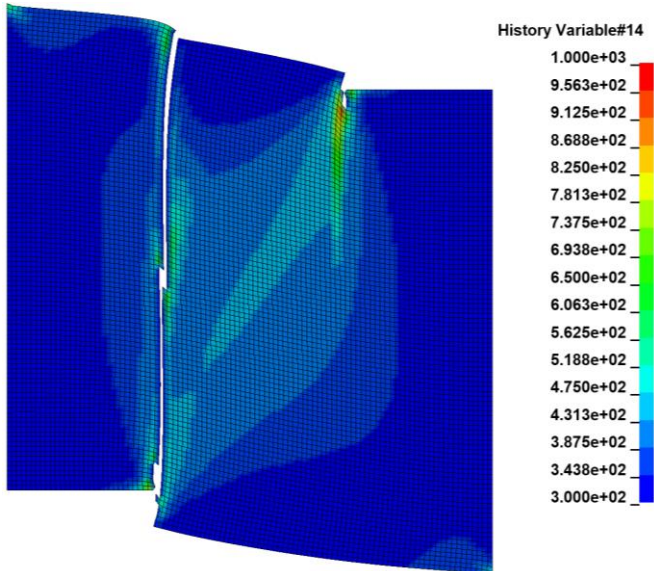
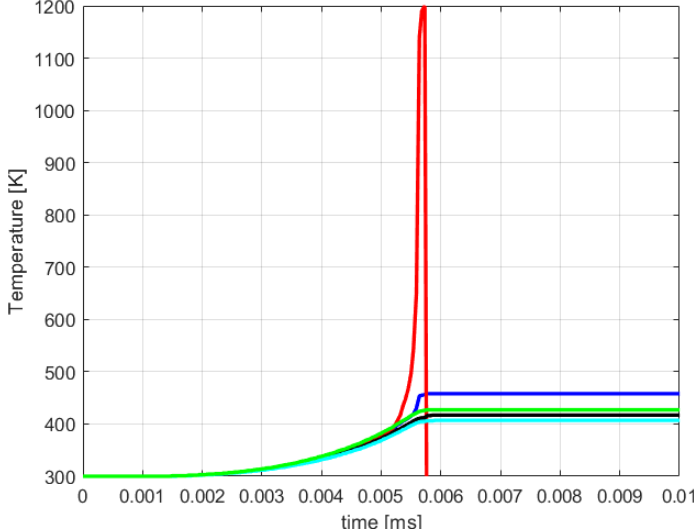
Simulation Name	Inco_100x100_BC1_1
Temperature Contours	 <p>History Variable#14</p> <p>1.000e+03 9.563e+02 9.125e+02 8.688e+02 8.250e+02 7.813e+02 7.375e+02 6.938e+02 6.500e+02 6.063e+02 5.625e+02 5.188e+02 4.750e+02 4.313e+02 3.875e+02 3.438e+02 3.000e+02</p>
Temperature of 5 elements across the crack	 <p>Temperature [K]</p> <p>time [ms]</p>
ASB?	Yes
Propagation velocity [m/s]	315

Table 7: Inco_100x100_BC1_4 simulation

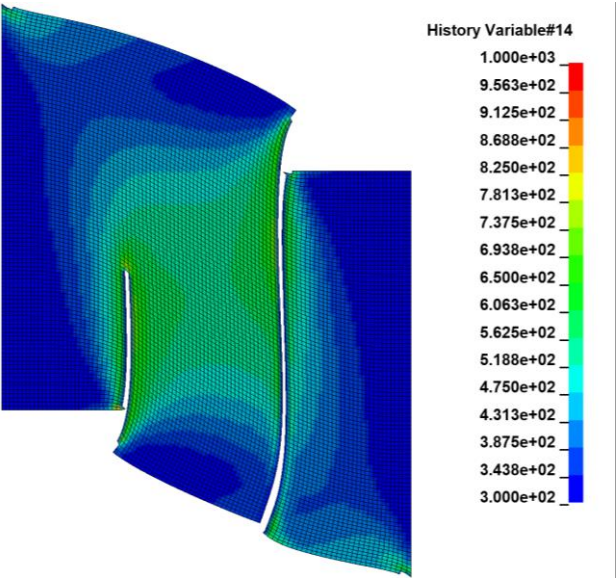
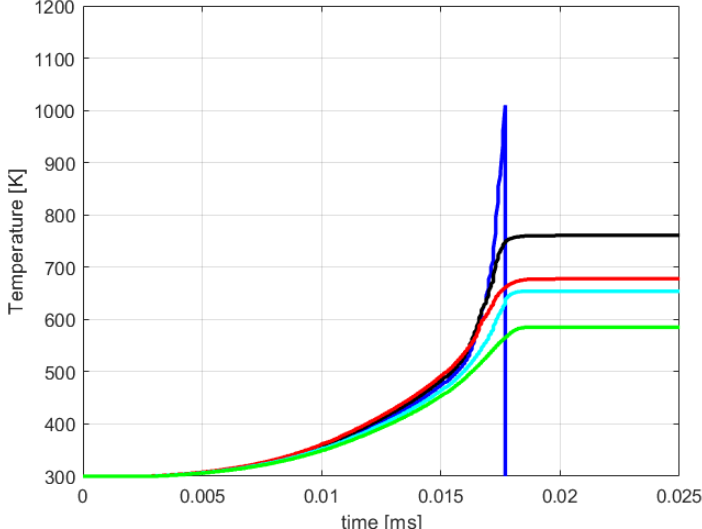
Simulation Name	Inco_100x100_BC1_4
Temperature Contours	 <p>History Variable#14</p> <p>1.000e+03 9.563e+02 9.125e+02 8.688e+02 8.250e+02 7.813e+02 7.375e+02 6.938e+02 6.500e+02 6.063e+02 5.625e+02 5.188e+02 4.750e+02 4.313e+02 3.875e+02 3.438e+02 3.000e+02</p>
Temperature of 5 elements across the crack	 <p>Temperature [K]</p> <p>time [ms]</p>
ASB?	maybe
Propagation velocity [m/s]	98

Table 8: Inco_100x100_BC1_20 simulation

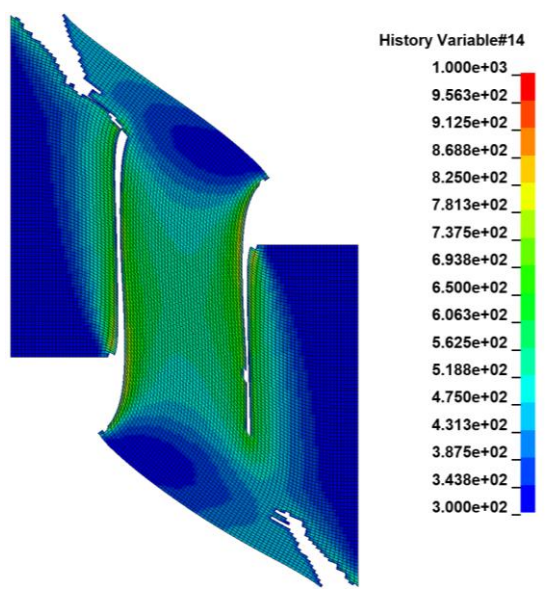
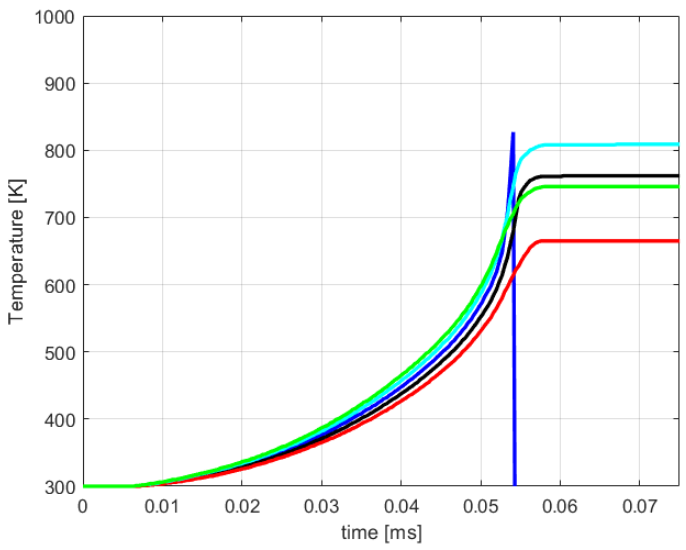
Simulation Name	Inco_100x100_BC1_20	
Temperature Contours		
Temperature of 5 elements across the crack		
ASB?		No
Propagation velocity [m/s]		68

Table 9: Inco_100x100_BC1_200 simulation

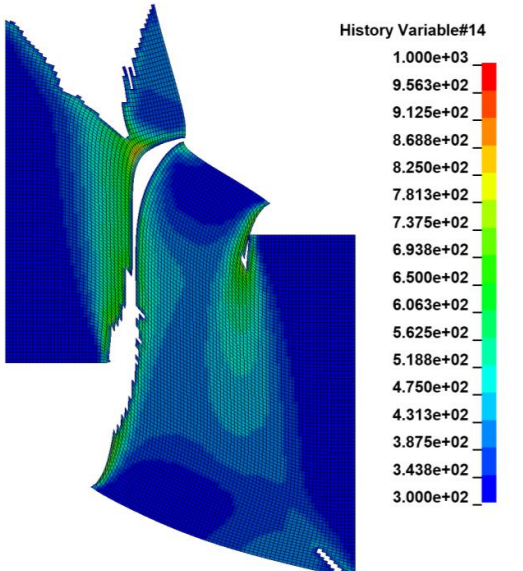
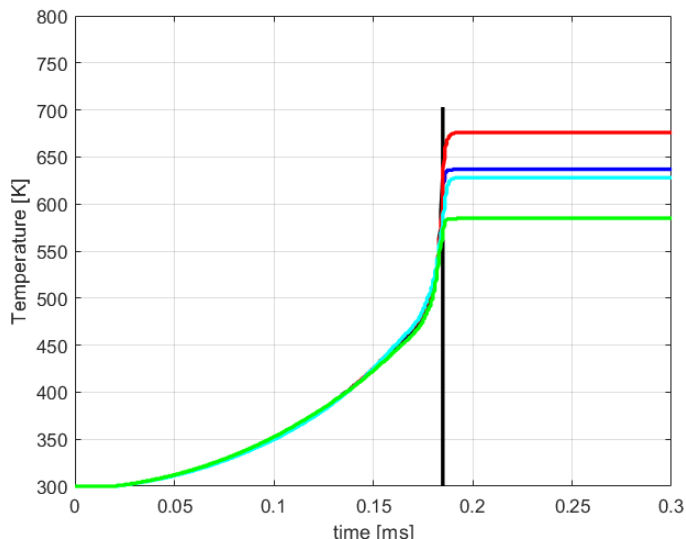
Simulation Name	Inco_100x100_BC1_200	
Temperature Contours		
Temperature of 5 elements across the crack		
ASB?		No
Propagation velocity [m/s]		N/A

Table 10: Inco_100x100_BC8_05 simulation

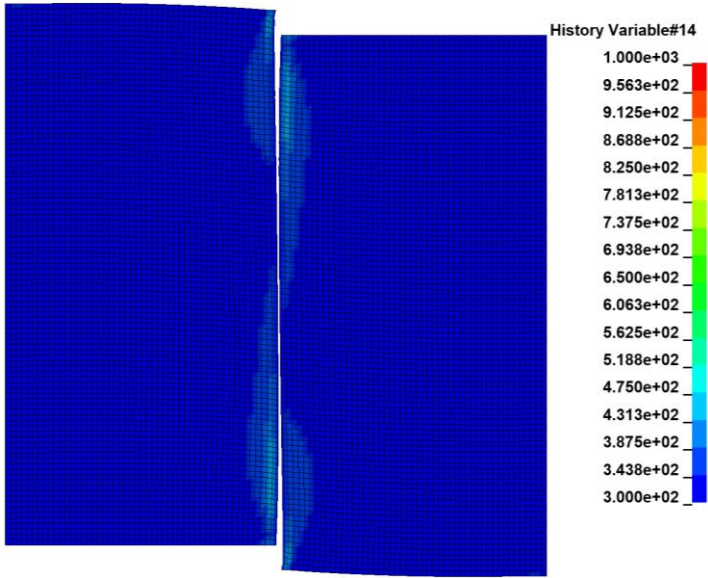
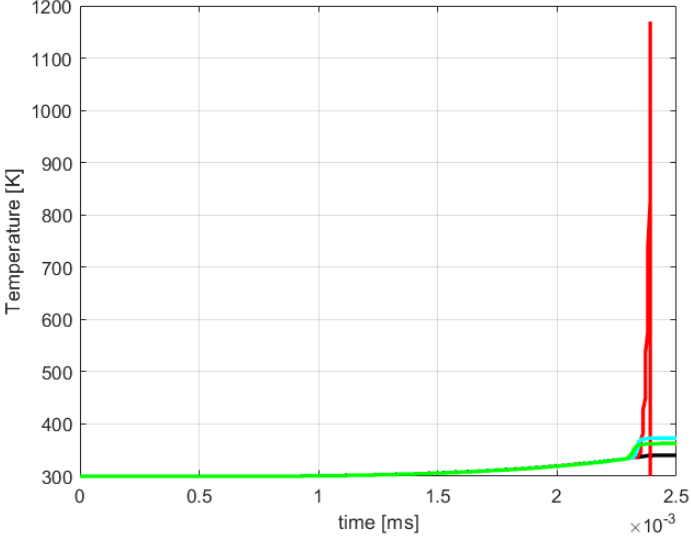
Simulation Name	Inco_100x100_BC8_05
Temperature Contours	 <p>History Variable#14</p> <p>1.000e+03 9.563e+02 9.125e+02 8.688e+02 8.250e+02 7.813e+02 7.375e+02 6.938e+02 6.500e+02 6.063e+02 5.625e+02 5.188e+02 4.750e+02 4.313e+02 3.875e+02 3.438e+02 3.000e+02</p>
Temperature of 5 elements across the crack	 <p>Temperature [K]</p> <p>time [ms] $\times 10^{-3}$</p>
ASB?	Yes
Propagation velocity [m/s]	6596

Table 11: Inco_100x100_BC8_1 simulation

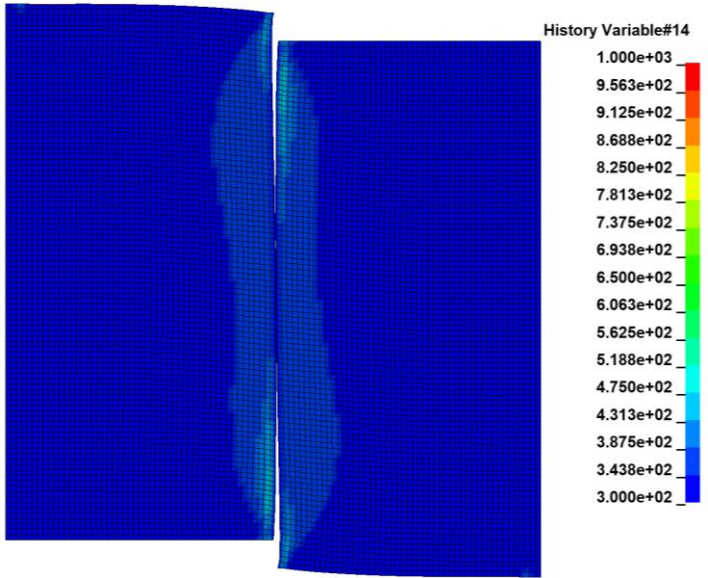
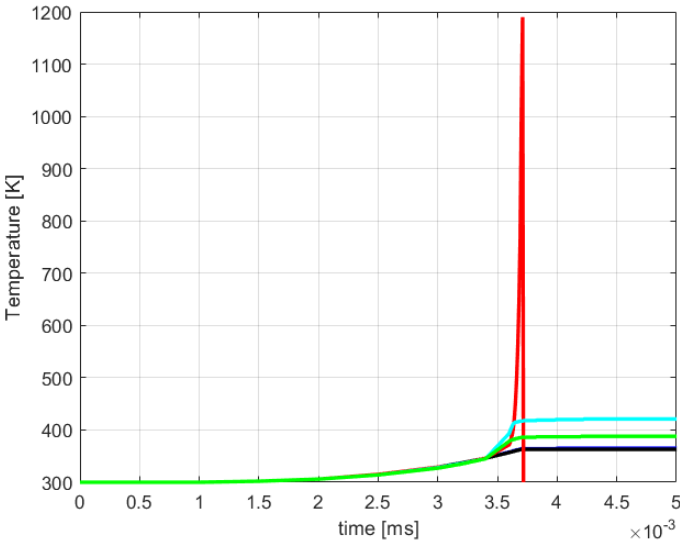
Simulation Name	Inco_100x100_BC8_1
Temperature Contours	 <p>History Variable#14</p> <p>1.000e+03 9.563e+02 9.125e+02 8.688e+02 8.250e+02 7.813e+02 7.375e+02 6.938e+02 6.500e+02 6.063e+02 5.625e+02 5.188e+02 4.750e+02 4.313e+02 3.875e+02 3.438e+02 3.000e+02</p>
Temperature of 5 elements across the crack	 <p>Temperature [K]</p> <p>time [ms] $\times 10^{-3}$</p>
ASB?	Yes
Propagation velocity [m/s]	3300

Table 12: Inco_100x100_BC8_4 simulation

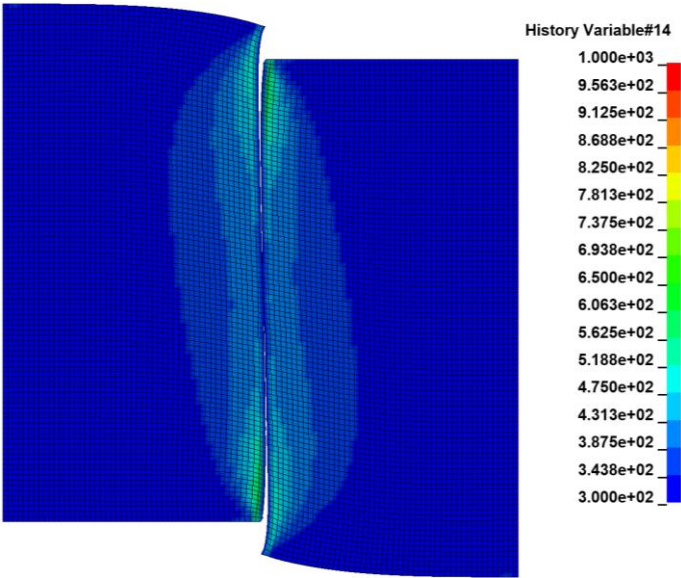
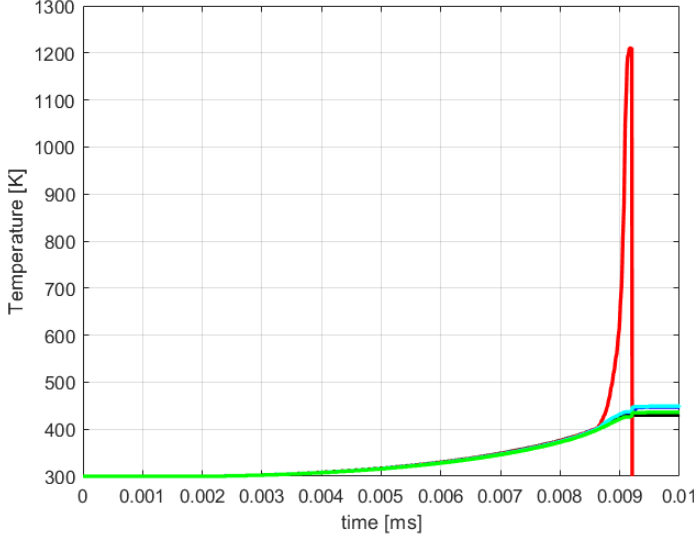
Simulation Name	Inco_100x100_BC8_4
Temperature Contours	 <p>History Variable#14</p> <p>1.000e+03 9.563e+02 9.125e+02 8.688e+02 8.250e+02 7.813e+02 7.375e+02 6.938e+02 6.500e+02 6.063e+02 5.625e+02 5.188e+02 4.750e+02 4.313e+02 3.875e+02 3.438e+02 3.000e+02</p>
Temperature of 5 elements across the crack	 <p>Temperature [K]</p> <p>time [ms]</p>
ASB?	Yes
Propagation velocity [m/s]	1800

Table 13: Inco_100x100_BC8_20 simulation

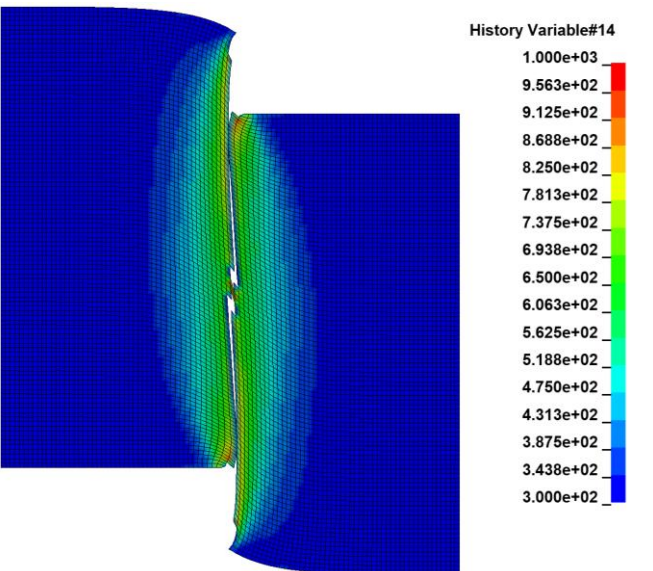
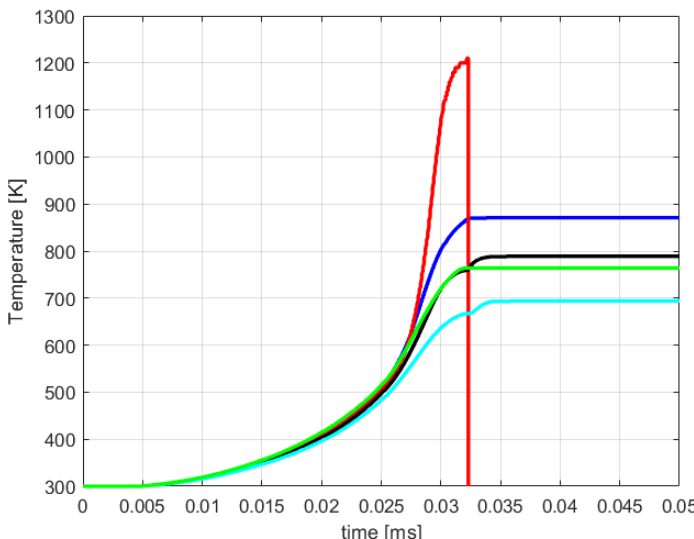
Simulation Name	Inco_100x100_BC8_20	
Temperature Contours		
Temperature of 5 elements across the crack		
ASB?		No
Propagation velocity [m/s]		247

Table 14: Inco_100_4_BC1 simulation

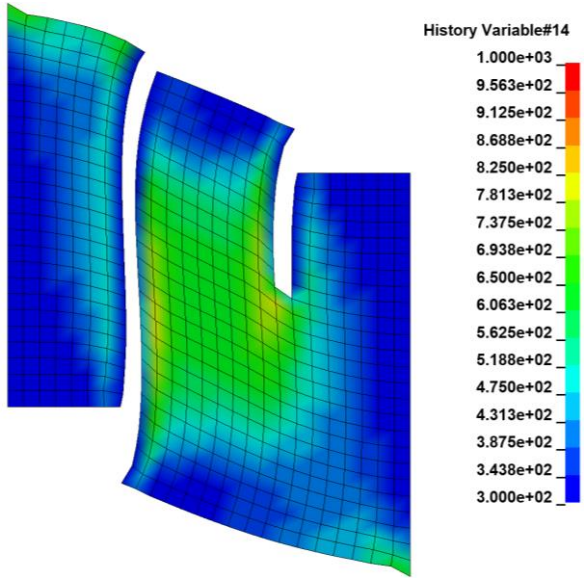
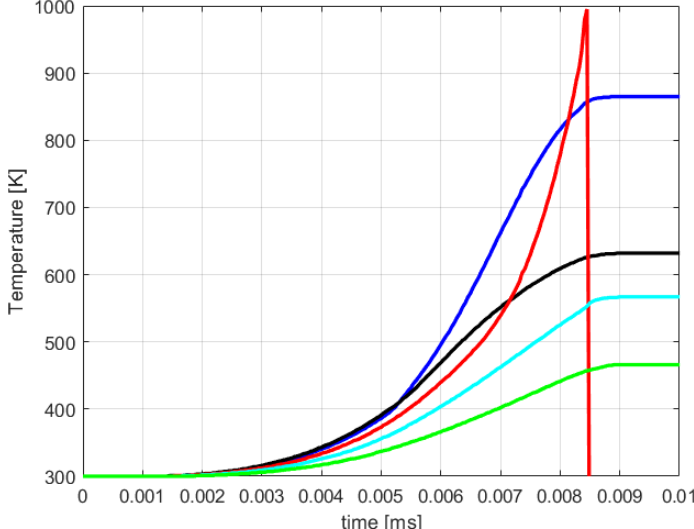
Simulation Name	Inco_100_4_BC1	
Temperature Contours		
Temperature of 5 elements across the crack		
ASB?		No
Propagation velocity [m/s]		115

Table 15: Inco_100_4_BC8 simulation

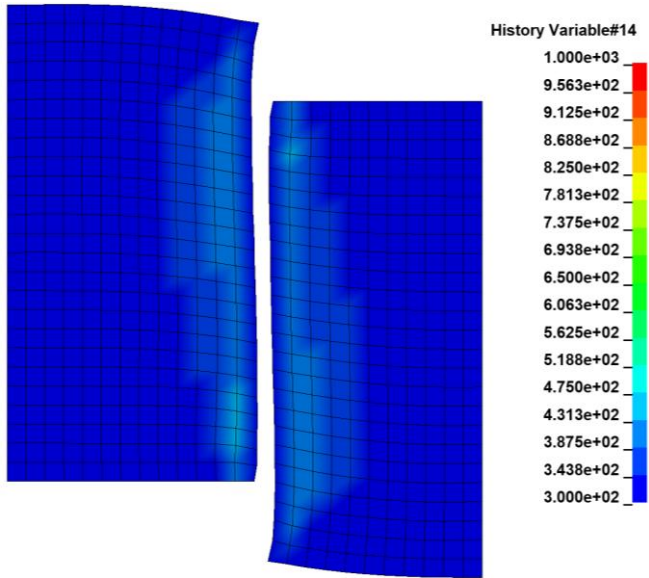
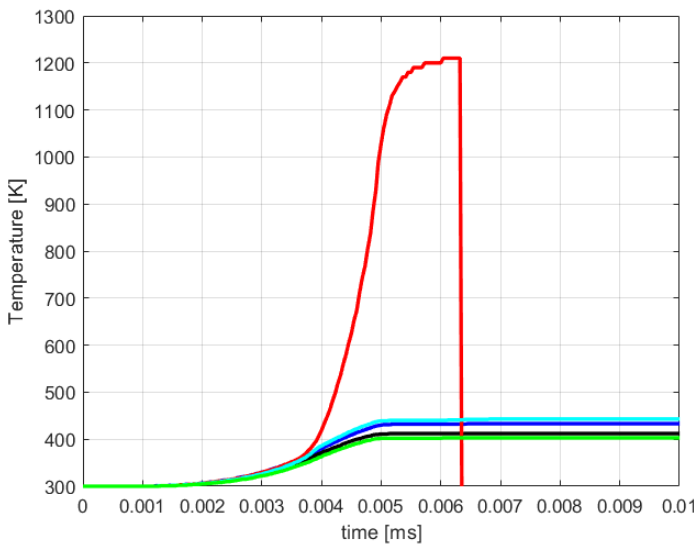
Simulation Name	Inco_100_4_BC8	
Temperature Contours		
Temperature of 5 elements across the crack		
ASB?		Yes
Propagation velocity [m/s]		1101

Table 16: Inco_100_10_BC1 simulation

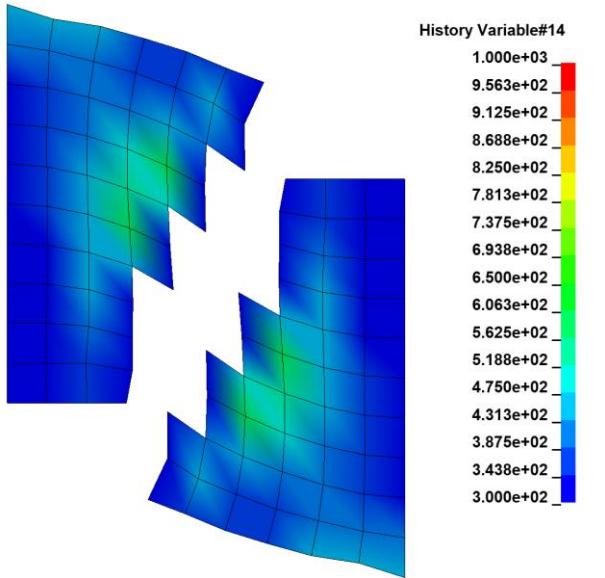
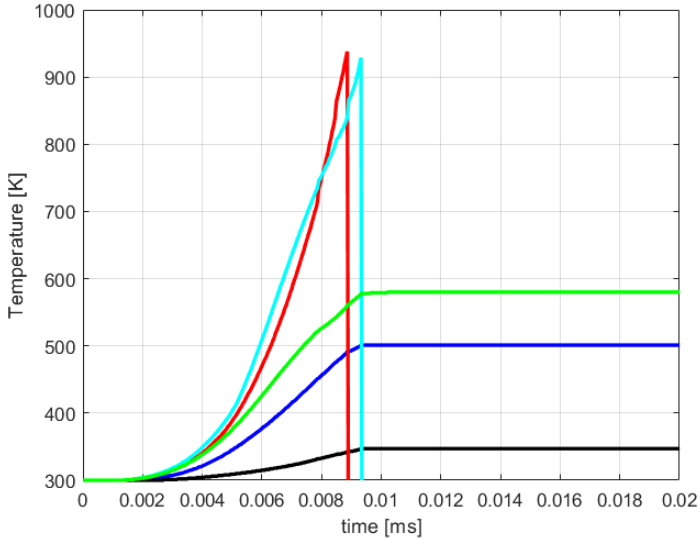
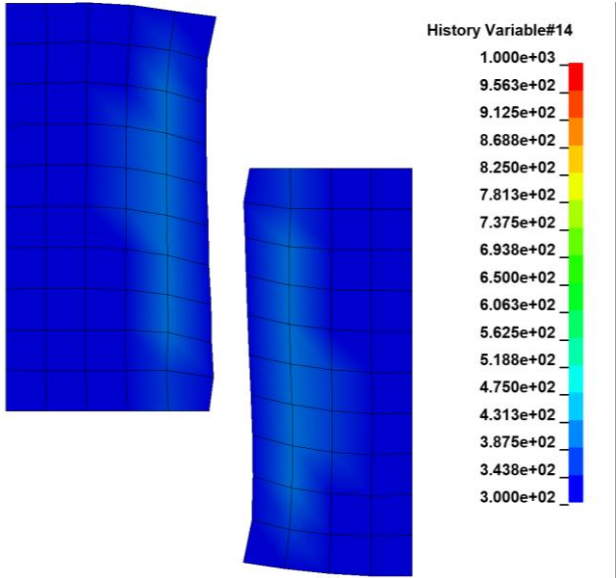
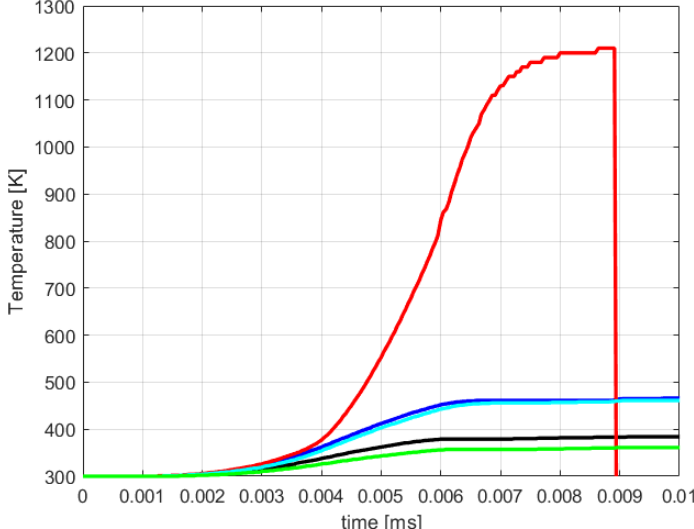
Simulation Name	Inco_100_10_BC1	
Temperature Contours		
Temperature of 5 elements across the crack		
ASB?		No
Propagation velocity [m/s]		N/A

Table 17: Inco_100_10_BC8 simulation

Simulation Name	Inco_100_10_BC8	
Temperature Contours		
Temperature of 5 elements across the crack		
ASB?		Yes
Propagation velocity [m/s]		550

For the first set of boundary conditions mesh sizes smaller than 4 μm , namely 0.5 μm , and 1 μm , can predict a clear ASB with a width of 1 element. The 4 μm mesh size is still able to give a good prediction but the shear band temperature increase is not as localized as in the smaller elements meshes simulations.

For the second set of boundary conditions mesh sizes of 0.5 μm , 1 μm , and 4 μm can predict a clear ASB with a width of 1 element. With boundary condition set 2, the 20 μm mesh size is still able to give a good prediction but the shear band temperature increase is not as localized as in the smaller elements meshes simulations.

Inconel becomes brittle at a temperature of around 973K. This temperature is reached in all the analyses with a mesh size below 4 μm for the first set of boundary condition and for all the analyses with the second set of boundary condition. The curves in some of the graphs are not displaying the actual maximum temperature due to insufficient sampling frequency.

The shear band propagation rate calculated for Inconel is approximately 760 to 6500 m/s (see Table 5 to Table 17) for the smaller element mesh size with a temperature in the shear band reaching over 1200K. The results are consistent with similar tests reported in literature [121]. It appears evident that the failure mechanism in the Inconel model using larger element sizes is not ASB. Therefore, only a sufficiently dense mesh is currently capable of capturing the phenomena.

It is significant that with no changes to the material model, once elements were 4 μm or smaller, adiabatic shear bands appeared in the analysis. The physics of these simulations appear to match the conditions which are described in the literature.

Unfortunately, the mesh size needed to predict adiabatic shear bands is far too small to be of any practical use in actual applications. This confirms the need of a new type of regularization, which can lead to the physical failing mechanism for any mesh size.

4.3. Discussion

As expected from the literature, the ASB can be simulated by the tabulated J-C material model if the element mesh size is small enough. This confirms the hypothesis that element mesh and characterization of the material strain rate sensitivity are crucial to correctly simulate the ASB phenomenon. The width of the ASB in Inconel 718 was shown to be approximately 1 μm . This very small width, and the resulting required mesh size for physically accurate simulations, strongly demonstrates the need of implementing new methods to obtain a correct stress flow characterization, and to develop a mesh size regularization that will adjust the amount of plastic work converted into heat in order to capture the right physical behavior of the ASB.

5. IMPLEMENTATION

This chapter focuses on the implementation of the improvement on the Tabulated J-C material model that is described in Buyuk [40]. The described methodology can be implemented into most of the currently available Finite Element codes.

The implementation into the commercial Finite Element solver LS-DYNA® is described in this chapter. LS-DYNA® is written in the FORTRAN programming language; as such, FORTRAN was chosen for the developed modified material subroutine. First, the theory at the base of the upgrade of the material model is discussed and then the algorithm is explained in the form of a high-level flowchart.

5.1. Taylor-Quinney Coefficient

The tabulated J-C material model utilizes an isotropic von Mises plasticity algorithm with isotropic hardening, strain rate hardening and temperature softening where adiabatic heating due to plastic work is also considered. The model is formulated as a multiplicative decomposition of flow stress as:

Equation 32: Constitutive relationship

$$\sigma_y = k1(\varepsilon_p, \dot{\varepsilon}_p)kt(\varepsilon_p, T)$$

where ε_p is the plastic strain, $\dot{\varepsilon}_p$ is the equivalent plastic strain rate and T is the temperature. The model resembles J-C in terms of the decomposition but utilizes

tabulated inputs of strain rate dependent isothermal hardening curves at room temperature $k1(\varepsilon_p, \dot{\varepsilon}_p)$ and temperature dependent quasi-static hardening curves $kt(\varepsilon_p, T)$. The TQC is used in the constitutive relation of the material model to calculate the increment in temperature and represents the portion of plastic work converted into adiabatic heating:

Equation 33: Temperature increment

$$dT = \frac{\beta}{C_p \rho} \sigma_y d\varepsilon_p$$

where dT is the temperature increment, β is the differential form of the TQC, C_p is the specific heat at constant pressure, ρ is the density, σ_y is the flow stress and ε_p is the plastic strain [40]. The flow chart of the solving scheme is described in detail in the next paragraph however it can be summarized into solving this nonlinear equation system for every element:

Equation 34: Nonlinear equation system for tabulated J-C material model

$$\left\{ \begin{array}{l} w_p^{n+1} = w_p^n + \left[\frac{\sigma_y^{n+1} + \sigma_y^n}{2} \right] \Delta \varepsilon_p \\ T^{n+1} = T^n + \left[\frac{w_p^{n+1} - w_p^n}{\rho C_p} \right] \beta \\ \varepsilon_p^{n+1} = \varepsilon_p^n + \Delta \varepsilon_p \\ \sigma_y^{n+1} = f(\varepsilon_p^{n+1}, T^{n+1}, \dot{\varepsilon}_p^{n+1/2}) \\ \sigma_y^{n+1} = \sigma_{VM}^{n+1} \\ \sigma_{VM}^{n+1} = \sigma_{VM}^e - 3G\Delta \varepsilon_p \end{array} \right.$$

where n is the time step, w_p is the plastic work, σ_y is the yield stress, ε_p is the plastic strain, $\dot{\varepsilon}_p$ is the plastic strain rate, T is the temperature, C_p is the specific heat capacity, ρ is the density, σ_{VM} is the von Mises stress, σ_{VM}^e is the elastic trial stress, G is the shear modulus and β is the effective differential TQC value compensating the fact that we are not modelling diffusion. It is important to mention that β is defined as differential formulation (β_{diff}) which differs from the integral calculation of β known as β_{int} . This difference, often causing misunderstanding, was highlighted by Rittel [113], [122]. Here this is described by the following equations:

Equation 35: TQC integral formulation

$$\beta_{int} = \frac{\int \dot{Q} dt}{\int \dot{w}_p dt}$$

Equation 36: TQC differential formulation used in tabulated J-C material model

$$\beta_{diff} = \frac{\dot{Q}}{\dot{w}_p}$$

where \dot{Q} is the rate of the heat generated during the plastic deformation and \dot{w}_p is the plastic power. Naturally, β_{int} and β_{diff} will be the same if they are constants. In any case, β_{int} is a value equal or lower to 1, but this limitation does not apply to β_{diff} [108].

However, as highlighted in the literature review, the TQC can be used in a broader sense by considering sources of heating other than the plastic work, for instance the latent heat due to phase changes as suggested by Zaera [114]. The material model was

improved from a model where the TQC is considered as the effective portion of plastic work converted into heat,

Equation 37: Definition of TQC in J-C material model

$$\beta = \beta_{diff}(\Delta T, w_p)$$

into a model where the TQC is the effective combination of the portion of plastic work converted into heat, the latent heat released in the ASB, the state of stress, the strain rate and a factor which accounts for the element size. This model is represented by the following equation:

Equation 38: Definition of modified TQC in modified J-C material model

$$\beta^* = f(\beta_{diff}(\Delta T, w_p), \Delta T_{SB}(Q_L, w_p^{SB}), \frac{W_{SB}}{\lambda}, \tau, \theta, \dot{\epsilon}_p)$$

where ΔT_{SB} is the difference in temperature in the ASB relative to the temperature of the material outside the ASB, Q_L is the latent heat released in the ASB due to the changes of phase, w_p^{SB} is the plastic work in the shear band, W_{SB} is the width of the ASB and λ is the element size, τ is the triaxiality and θ is the Lode parameter. The new coefficient has been made a function of the state of stress and the plastic strain rate, as also suggested by Rittel [113]. Moreover ΔT_{SB} is considered a function of the latent heat released during the change of phase in the ASB due to DRX as suggested by Zaera [114]. This modification accounts for the demonstration that TQC is not constant, is dependent on loading mode, and that heat is released due to phase changes.

For the implementation of the newly defined TQC into the existing material model we proceeded to include a new tabulated β^* into the material model. The new tabulated β^* was implemented specifically to simulate ASB, with element sizes that can be reasonably used in real applications. The modified tabulated material J-C allows to define a tabulated TQC as:

Equation 39: Tabulated modified TQC as a function of tabulated parameters

$$\beta^* = f(\gamma_{max}, \lambda, \dot{\epsilon}_p)$$

where the maximum shear strain γ_{max} is the max difference between two principal strains:

Equation 40: Maximum shear strain

$$\gamma_{max} = \max(|\epsilon_1 - \epsilon_2|, |\epsilon_2 - \epsilon_3|, |\epsilon_3 - \epsilon_1|)$$

These variables were chosen because they are optimal for defining the element subject to ASB conditions, γ_{max} together with $\dot{\epsilon}_p$, allows the identification of the shear band conditions and λ allows the regularization of the element size. When γ_{max} and $\dot{\epsilon}_p$ identify conditions that lead to ASB, the maximum value of $\beta^*(\beta_{max}^*)$ is invoked, and this results in an appropriate ΔT_{SB} .

The system becomes:

Equation 41: Nonlinear equation system for the modified tabulated J-C material model

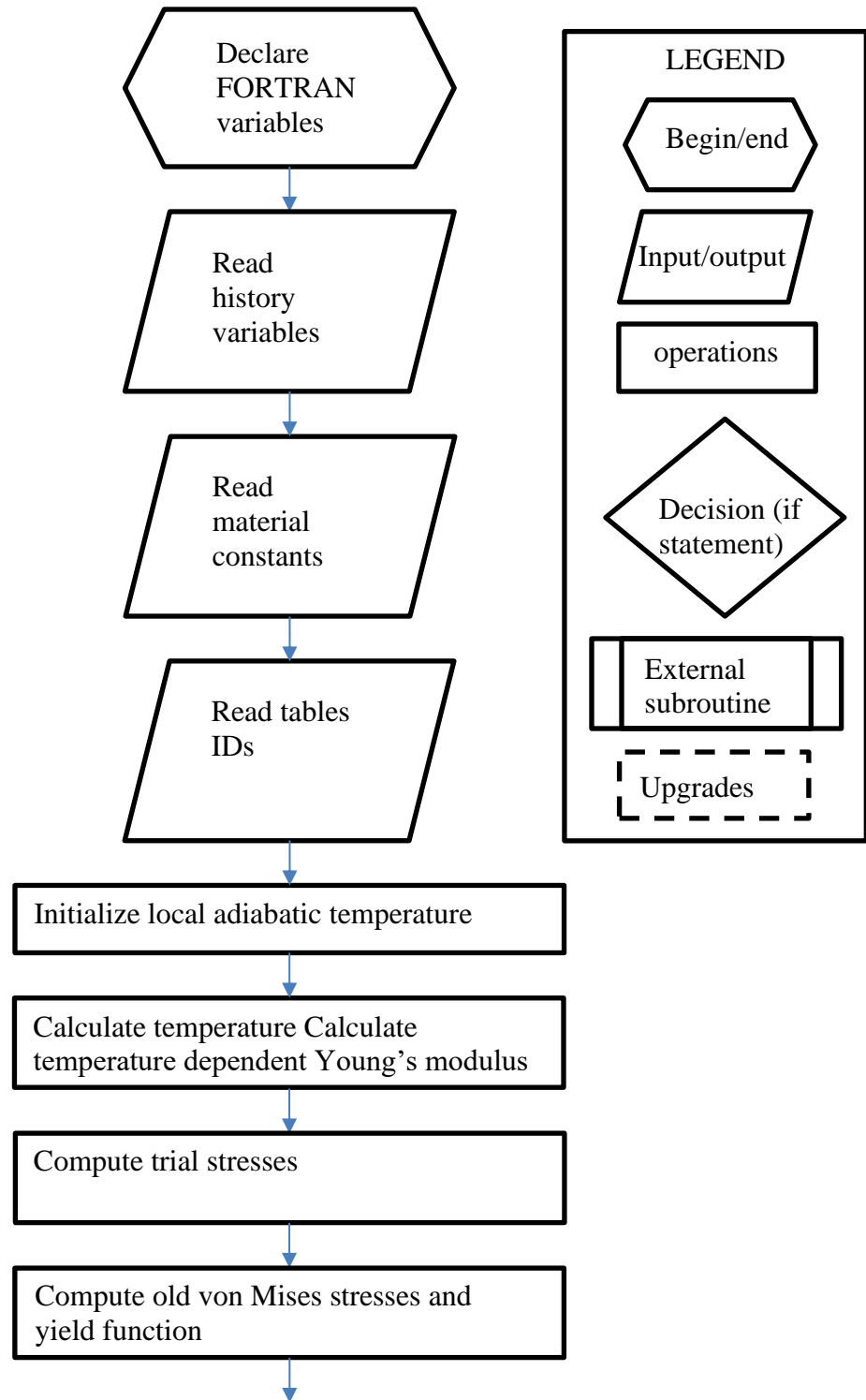
$$\left\{ \begin{array}{l} w_p^{n+1} = w_p^n + \left[\frac{\sigma_y^{n+1} + \sigma_y^n}{2} \right] \Delta \varepsilon_p \\ T^{n+1} = T^n + \left[\frac{w_p^{n+1} - w_p^n}{\rho C_p} \right] \beta^* \\ \varepsilon_p^{n+1} = \varepsilon_p^n + \Delta \varepsilon_p \\ \sigma_y^{n+1} = f(\varepsilon_p^{n+1}, T^{n+1}, \dot{\varepsilon}_p^{n+1/2}) \\ \beta^* = f(\gamma_{max}^{n+1}, \lambda, \dot{\varepsilon}_p^{n+1}) \\ \sigma_y^{n+1} = \sigma_{VM}^{n+1} \\ \sigma_{VM}^{n+1} = \sigma_{VM}^e - 3G\Delta \varepsilon_p \end{array} \right.$$

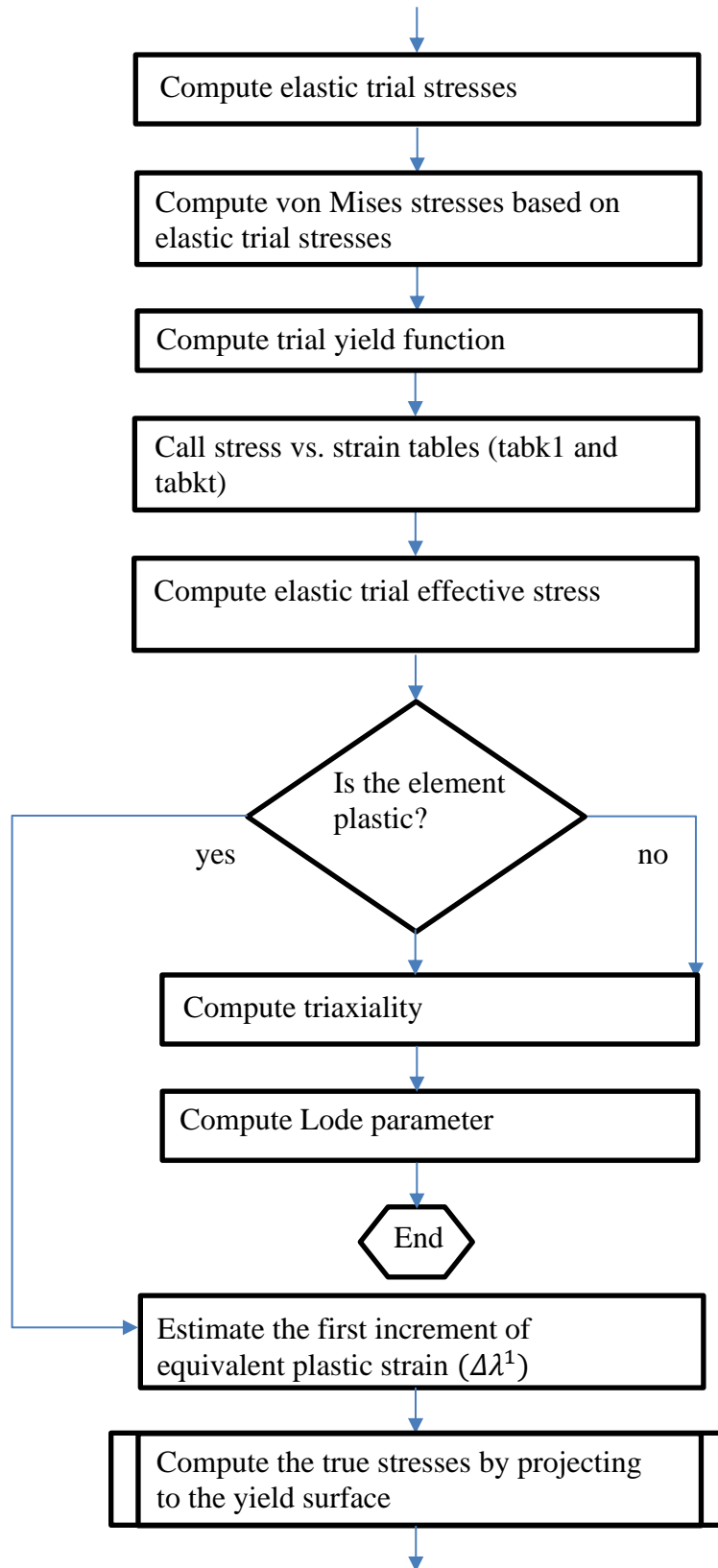
This system has been included into the material implementation as a tabulated input allowing for a precise calibration of the condition that triggers the ASB. An example of a tabulated beta input deck can be seen in APPENDIX C.

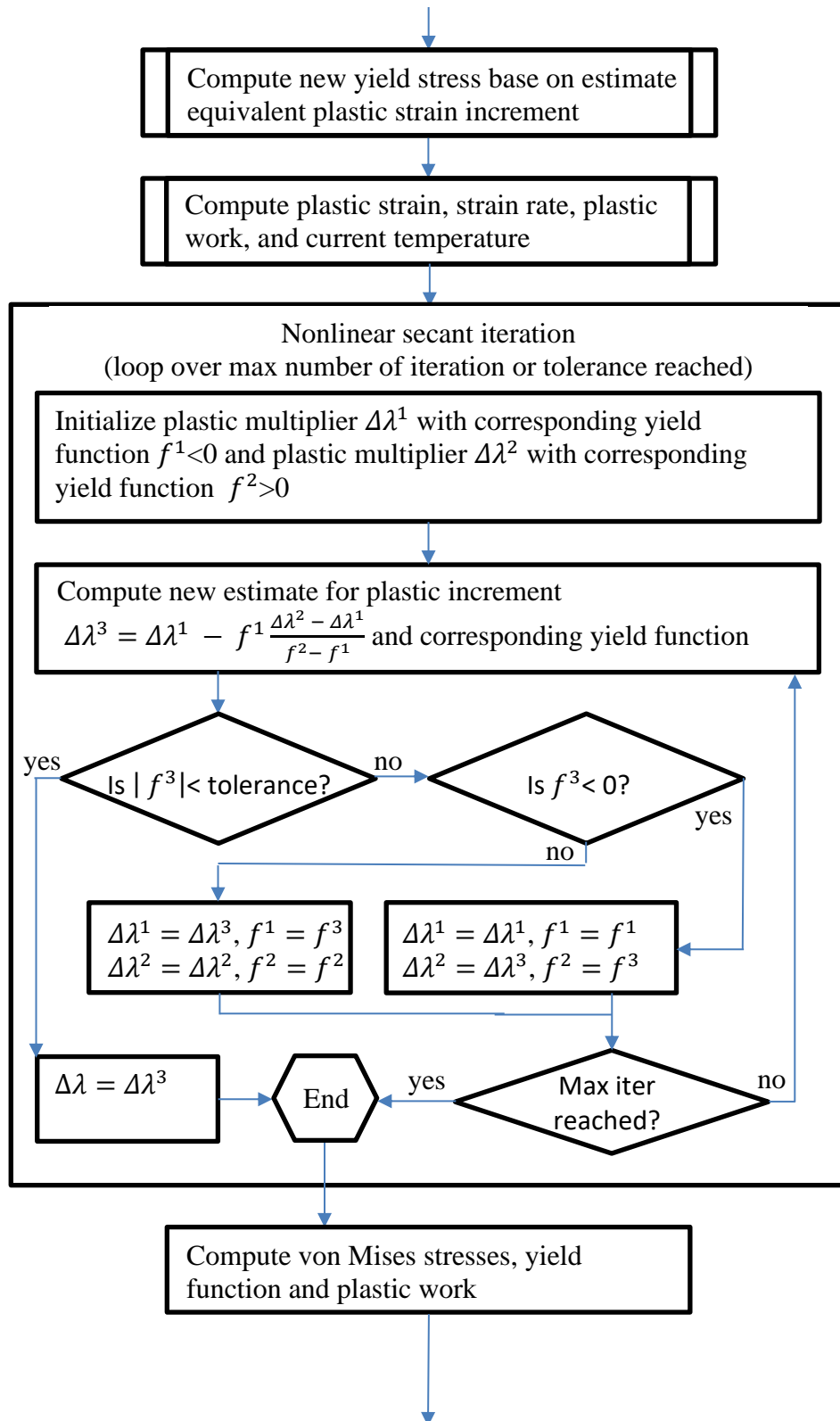
5.2. Algorithm

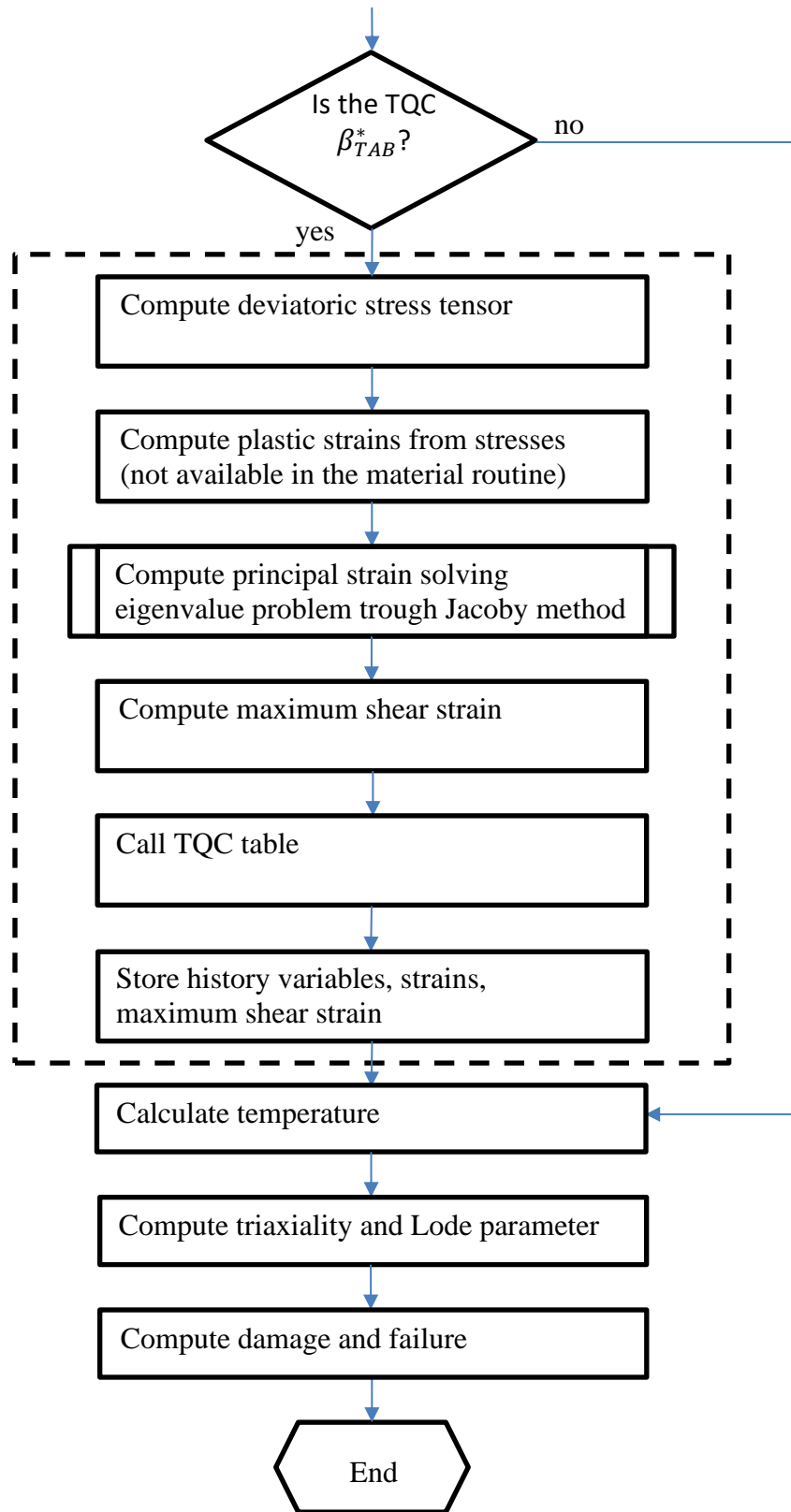
This section describes the algorithm used in the implementation of the original available material model developed by Buyuk [40] and the modifications developed in this work to account for instabilities and thermal effects associated with ASBs. The following paragraph provides a full overview of the material subroutine portion of the finite element code in the form of a flow chart. As indicated in the legend, the modifications to the algorithm are shown within a dashed-line box. The tabulated failure criterion subroutine remained unchanged from the original tabulated J-C material developed by Buyuk [40].

5.2.1. Flow chart









5.3. Single Element Verification

To assure the proper behavior of the material model after the introduction of the tabulated TQC a series of one element simulations were performed to test the correct response of the modified material model. To verify the implementation of the modifications, one element simulations were performed using a test TQC input deck (β_{test}^*) created using the code available in Appendix A. The parameters of the TQC used for the one element verifications can be found in Table 18. The specific mesh-size dependent values of γ_{max} , $\dot{\epsilon}_p$, and β_{max}^* were determined using the procedure explained in paragraph 6.2.2.

Table 18: TQC β_{test}^* : parameters for the transition from normal to ASB condition and maximum value of TQC inside the ASB for each element size.

Mesh [mm]	γ_{max}	$\dot{\epsilon}_p [s^{-1}]$	β_{max}^*
0.2	0.25	8000	10
0.4	0.23	8000	12.5
0.8	0.18	8000	13
1.6	0.15	8000	23

Both tension and shear simulations were performed for redundancy, using a constant imposed velocity. See Figure 46 for the boundary conditions.

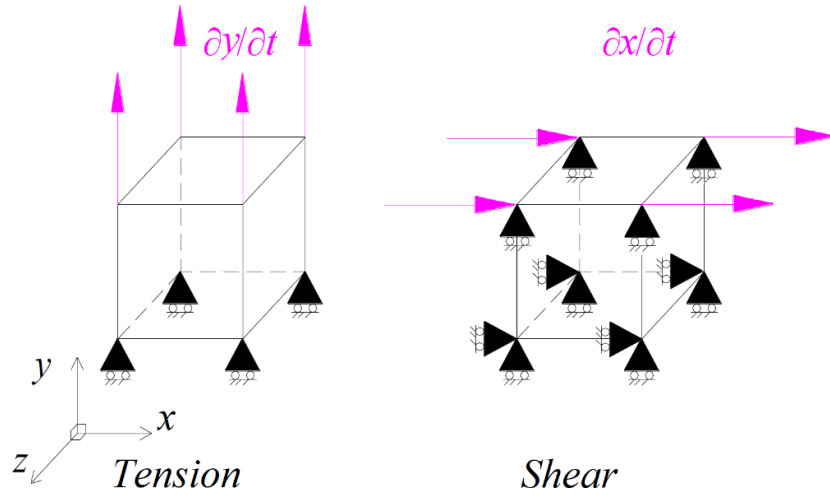


Figure 46: Boundary conditions of the one element simulations

It was verified that the transition of the TQC values, between the non-ASB conditions and the ASB condition, occurred at the required levels of maximum shear strain and strain rate. Moreover, to assure the correct implementation of the element size regularization, the simulations were performed on all different size elements. The verification results can be found in Figure 47 to Figure 54. All the transitions happened around the expected values; however, it must be noted that the graphs report the overall values for the element, not for the single, indicative integration point. In these simulations, fully integrated solid elements with 8 integration point were used. Moreover, not all the time steps are plotted, which justifies some slight differences of the transition values in relation to the inputs.

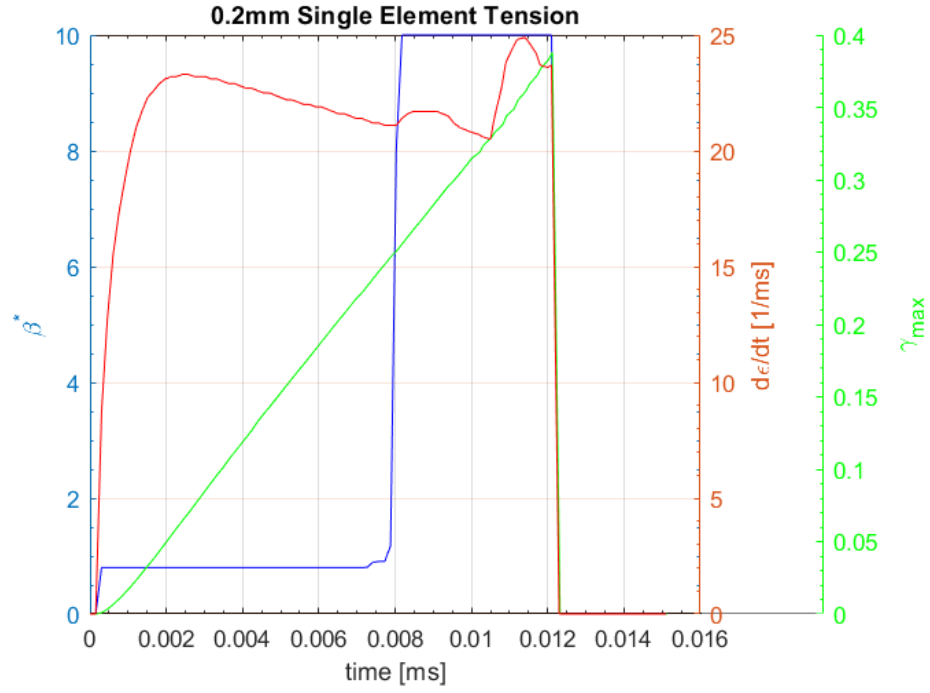


Figure 47: Single element 0.2 mm, Tension. Transition to $\beta_{max}^* = 10$ expected at $\gamma_{max} > 0.25$ and $\dot{\epsilon}_p > 8000$

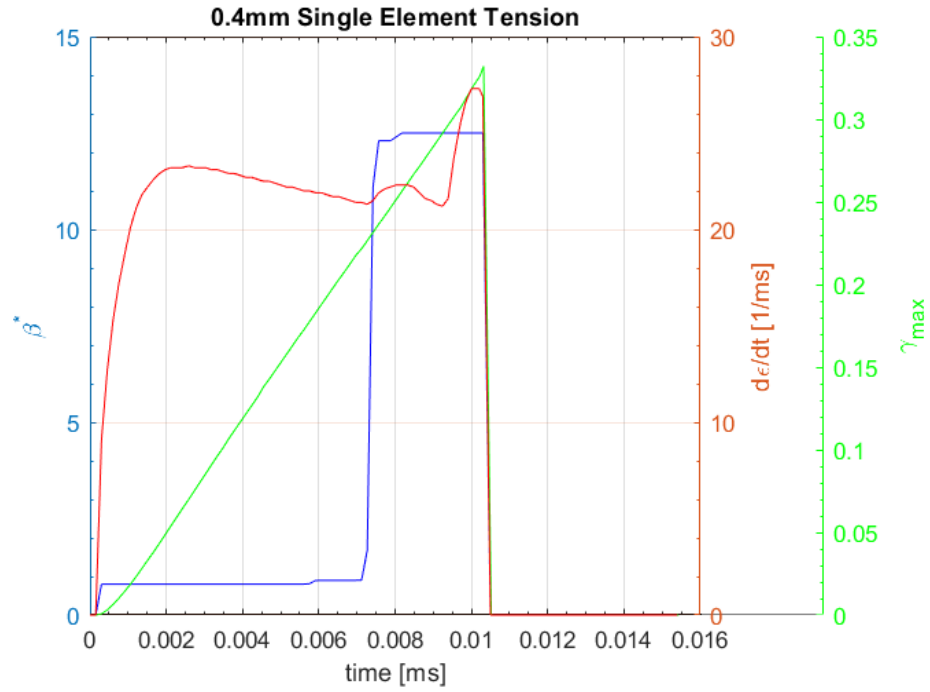


Figure 48: Single element 0.4 mm, Tension. Transition to $\beta_{max}^* = 12.5$ expected at $\gamma_{max} > 0.23$ and $\dot{\epsilon}_p > 8000$

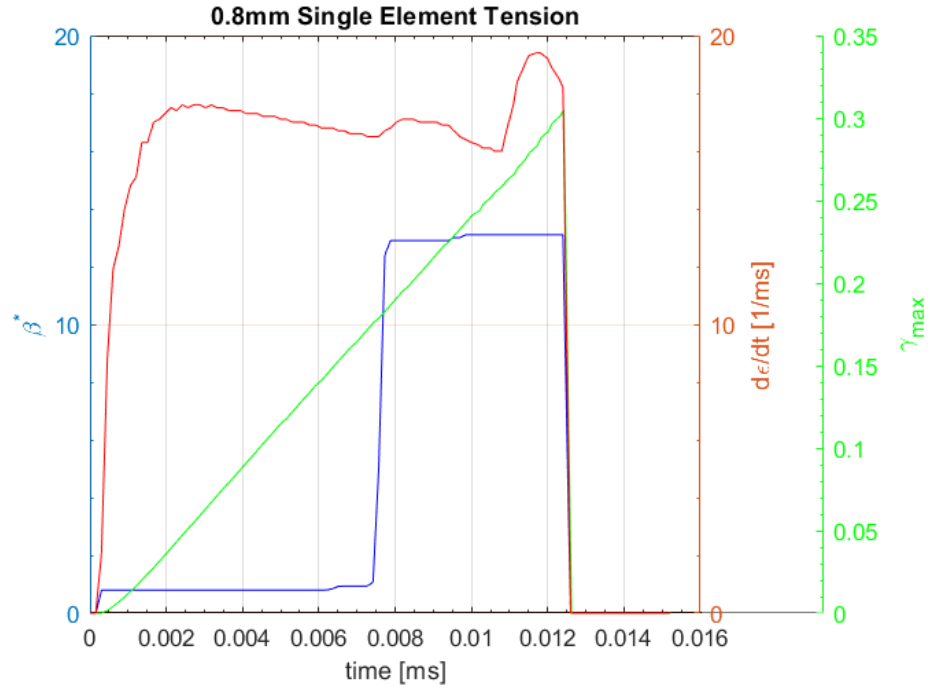


Figure 49: Single element 0.8 mm, Tension. Transition to $\beta_{max}^* = 13$ expected at $\gamma_{max} > 0.18$ and $\dot{\epsilon}_p > 8000 \text{ s}^{-1}$

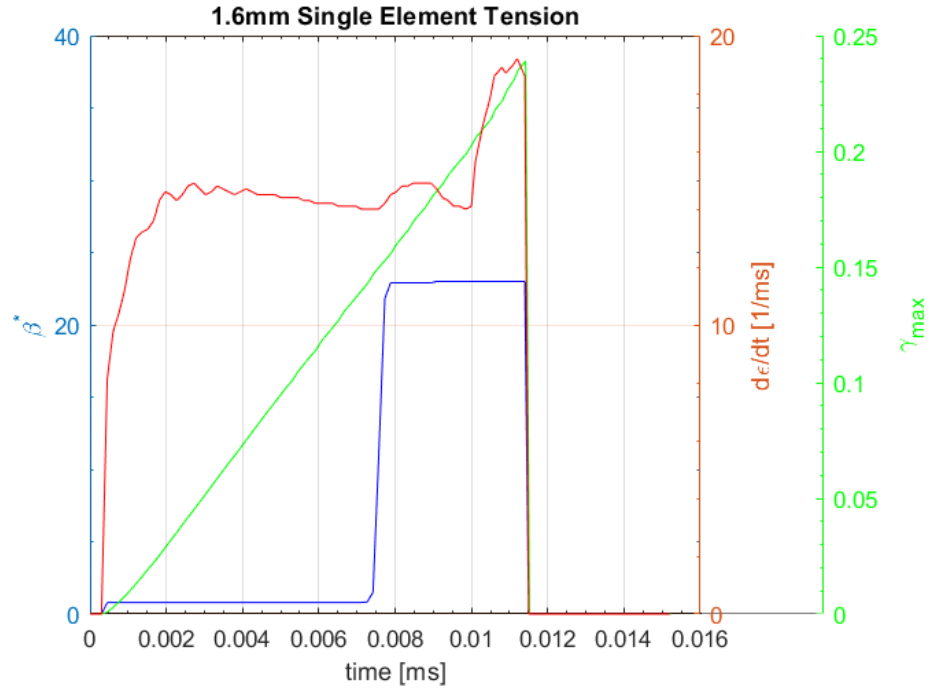


Figure 50: Single element 1.6 mm, Tension. Transition to $\beta_{max}^* = 23$ expected at $\gamma_{max} > 0.15$ and $\dot{\epsilon}_p > 8000 \text{ s}^{-1}$

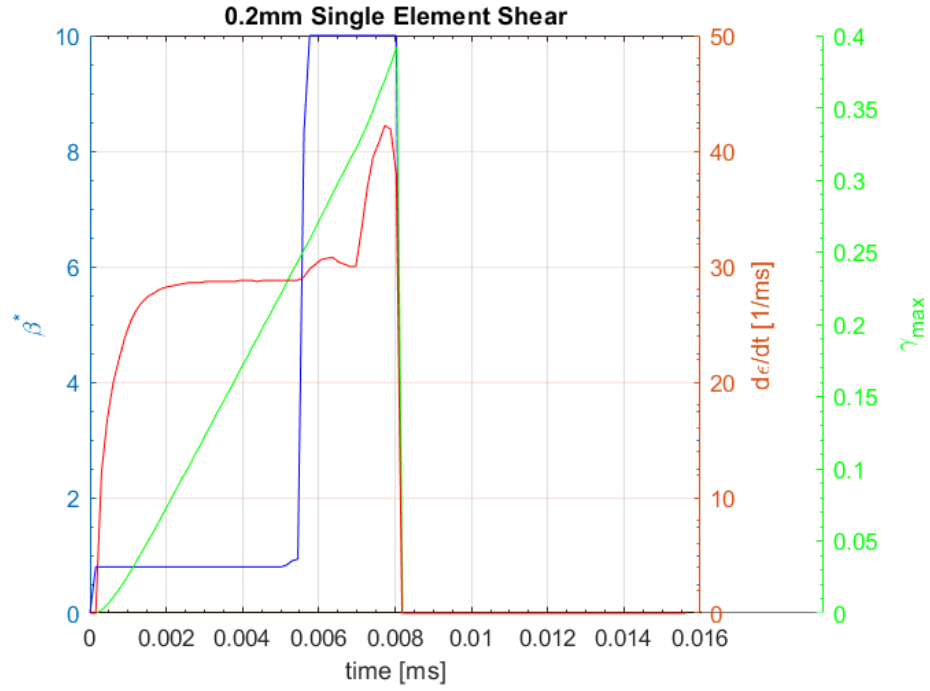


Figure 51: Single element 0.2 mm, Shear. Transition to $\beta_{max}^* = 10$ expected at $\gamma_{max} > 0.25$ and $\dot{\epsilon}_p > 8000 \text{ s}^{-1}$

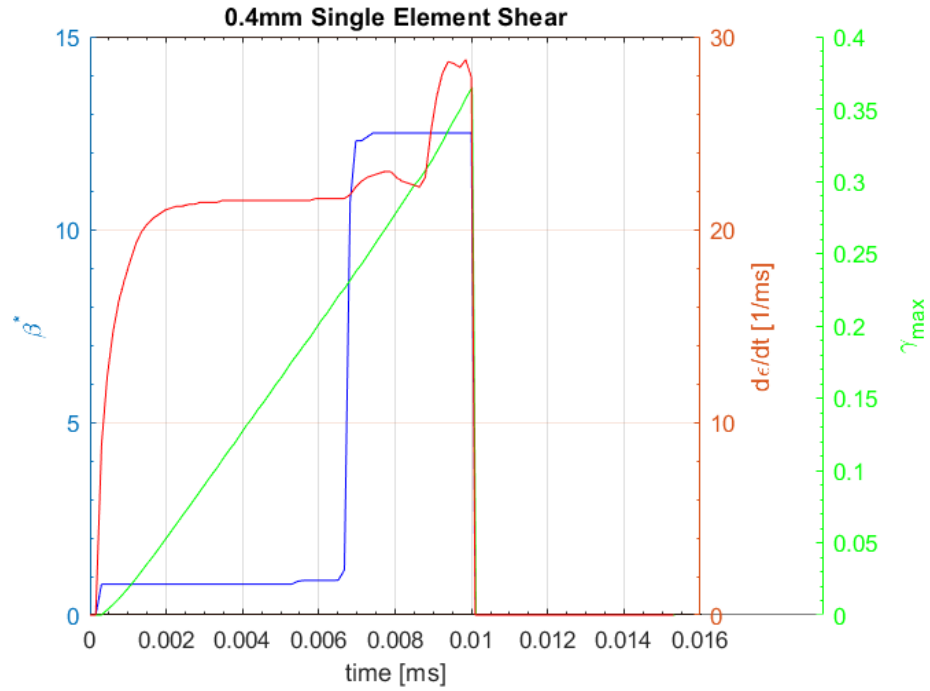


Figure 52: Single element 0.4 mm, Shear. Transition to $\beta_{max}^* = 12.5$ expected at $\gamma_{max} > 0.23$ and $\dot{\epsilon}_p > 8000 \text{ s}^{-1}$

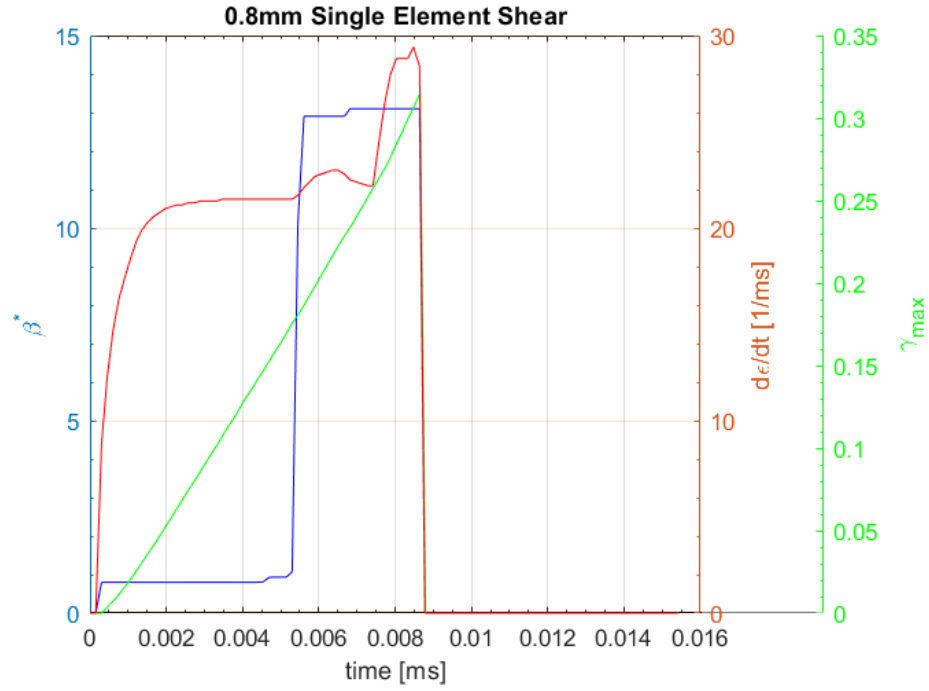


Figure 53: Single element 0.8 mm, Shear. Transition to $\beta_{max}^* = 13$ expected at $\gamma_{max} > 0.18$ and $\dot{\epsilon}_p > 8000 \text{ s}^{-1}$

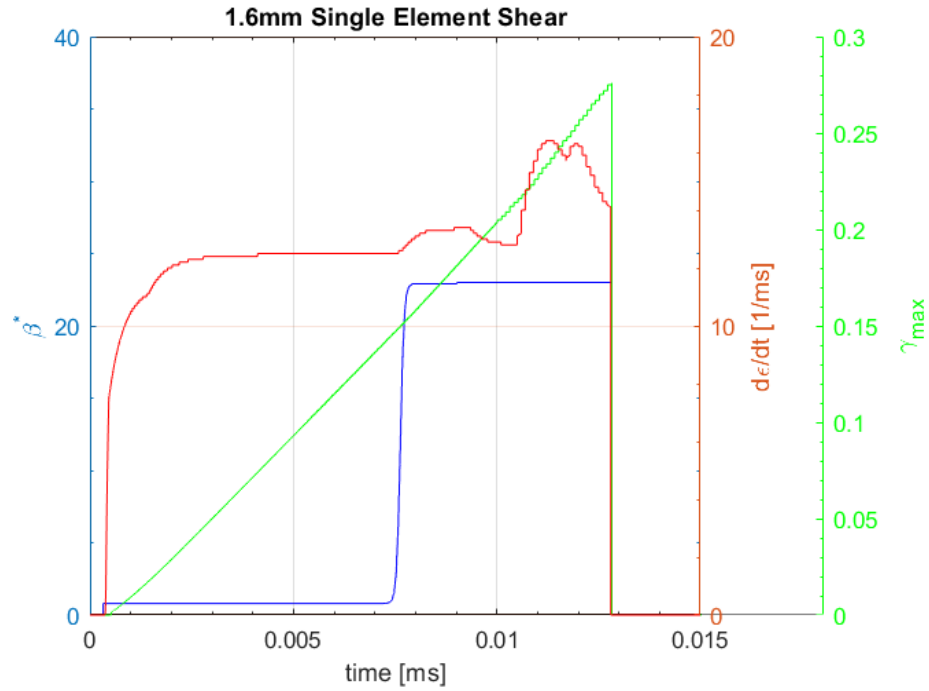
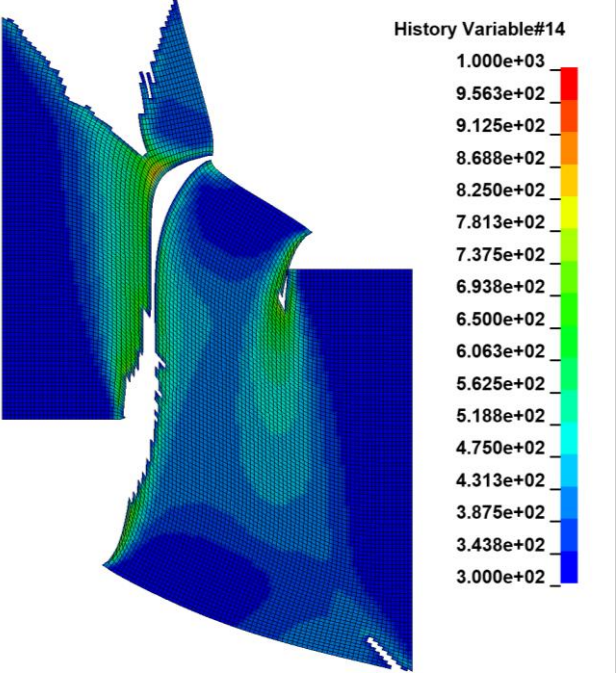
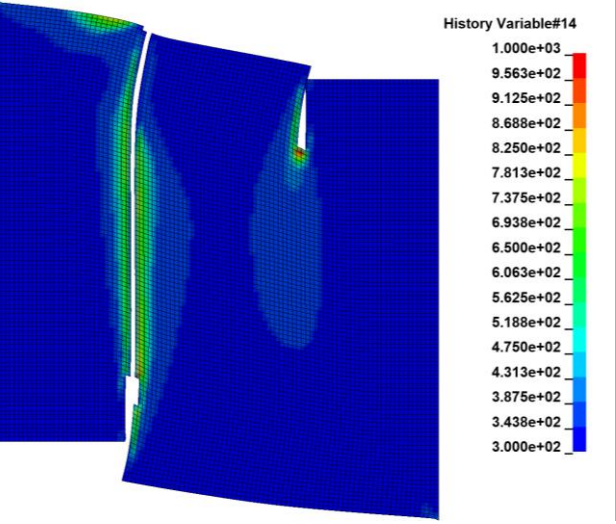


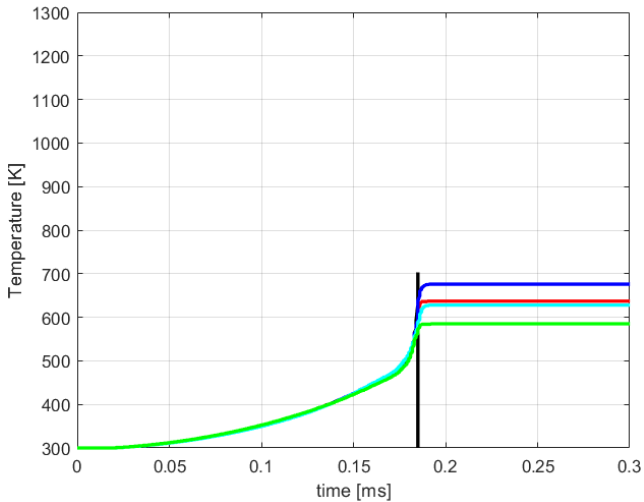
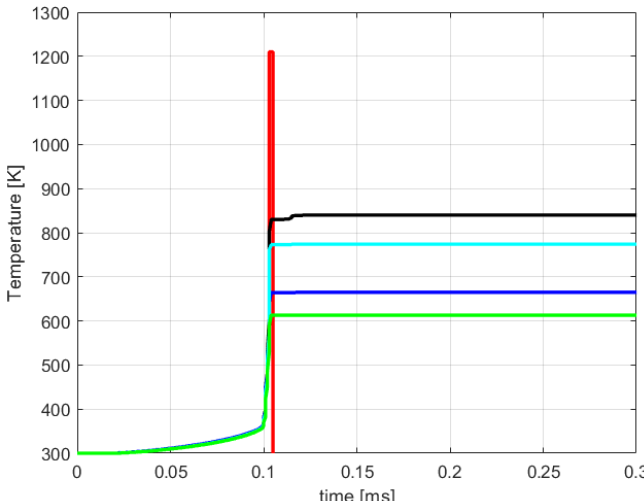
Figure 54: Single element 1.6 mm, Shear. Transition to $\beta_{max}^* = 23$ expected at $\gamma_{max} > 0.15$ and $\dot{\epsilon}_p > 8000 \text{ s}^{-1}$

5.4. 2D Simulation Verification

The simulation Inco_100x100_BC1_200 from the 2D ASB analysis presented in Chapter 4 was updated with the modified J-C material Model. A tabulated TQC ($\beta_{test,2D}^*$ see Appendix D) was defined to test the capability of the novel material model to enucleate an ASB on a controlled simulation using a mesh composed of elements of a size where it was previously not achievable. The simulation with the upgraded material model was then performed and compared with the previous version. The comparison is reported in Table 19. The results show that (with a minimal amount of time spent to tune up the TQC table), the modified J-C material model is able to replicate results that are similar to the ones achieved with the $1\mu\text{m}$ element size mesh, both in terms of temperatures across the shear band and propagation speed, using a mesh with elements 200 times larger. An example of the transition to β_{max}^* for an element in the ASB, to verify the correct behavior of the modified tabulated J-C material model and the relative tabulated TQC, is shown in Figure 55. It can be noted that the transition happened at the correct strain rate and maximum shear strain. The values visualized are the averaged overall values for the element and not for the individual integration points, hence this is the reason why the plotted TQC did not reach β_{max}^* .

Table 19: Comparison of simulation Inco_100x100_BC1_200: original vs. modified material model

TEMPERATURE CONTOURS	
Original material (β)	 <p>History Variable#14</p> <p>1.000e+03 9.563e+02 9.125e+02 8.688e+02 8.250e+02 7.813e+02 7.375e+02 6.938e+02 6.500e+02 6.063e+02 5.625e+02 5.188e+02 4.750e+02 4.313e+02 3.875e+02 3.438e+02 3.000e+02</p>
Modified material ($\beta_{test,2D}^*$)	 <p>History Variable#14</p> <p>1.000e+03 9.563e+02 9.125e+02 8.688e+02 8.250e+02 7.813e+02 7.375e+02 6.938e+02 6.500e+02 6.063e+02 5.625e+02 5.188e+02 4.750e+02 4.313e+02 3.875e+02 3.438e+02 3.000e+02</p>

TEMPERATURE OF 5 ELEMENTS ACROSS THE CRACK		
Original material (β)		
Modified material ($\beta_{test,2D}^*$)		
ASB?		
<ul style="list-style-type: none">Original material (β)Modified material ($\beta_{test,2D}^*$)	<div>No</div> <div>Yes</div>	
PROPAGATION VELOCITY [m/s]		
<ul style="list-style-type: none">Original material (β)Modified material ($\beta_{test,2D}^*$)	<div>N/A</div> <div>404</div>	

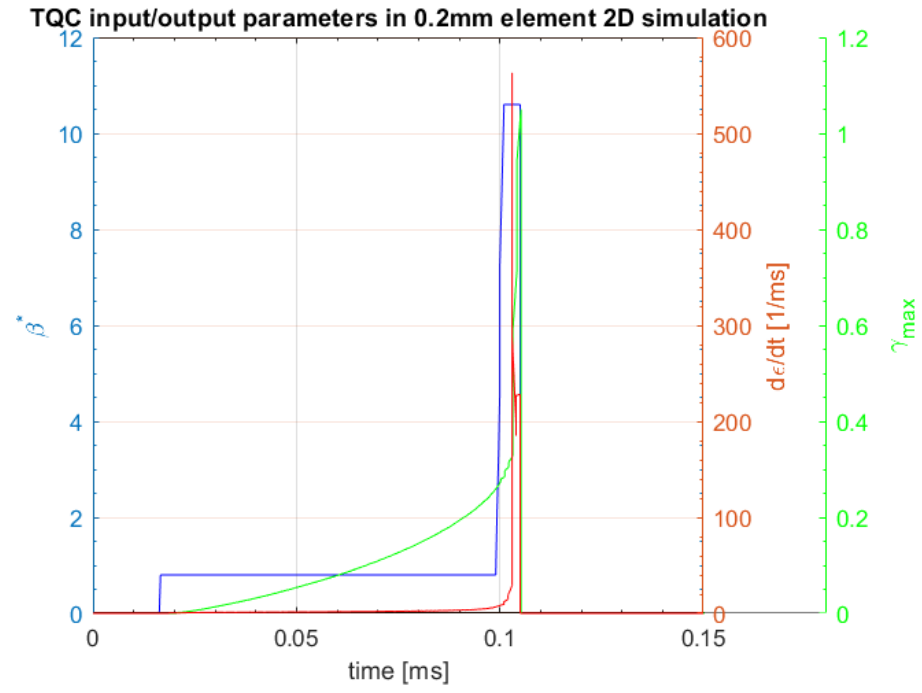


Figure 55: 0.2mm mesh 2D simulation. Element in the shear band transition to $\beta_{max}^* = 15$ expected at $\gamma_{max} > 0.25$ and $\dot{\epsilon}_p > 8000 \text{ s}^{-1}$

6. VALIDATION/BALLISTIC LIMIT SIMULATIONS

High strain rate behavior and instabilities of metal alloys and super-alloys were investigated in the previous chapters. A modified version of the tabulated Johnson-Cook material model was developed to address the challenges of the ASB nucleation during impact phenomenon that are described in detail in the previous chapters. The original material model and characterized material input was validated by a series of material tests at different loading regimes and boundary conditions.

In this chapter the predictive applications of the modified material model are assessed by simulating ballistic impact tests performed at NASA Glenn Research Center by Pereira et al. [123] presented in paragraph 6.1 and listed in Table 21. The tabulated TQC input for the modified J-C material model was characterized through an iterative process and validated against the ballistic test. The final results of this iterative procedure to obtain the tabulated TQC parameters are presented in this chapter together with the steps needed to obtain the tabulated TQC input deck. The simulations were performed with both versions of material models. The overall goal is to compare the accuracy, robustness, performance, and predictive capabilities of the modified tabulated J-C material model against the original tabulated J-C material model currently available.

6.1. Ballistic Impact Tests

A set of tests performed by Pereira et al. [123] at NASA Glenn Research center were used to compare the accuracy, robustness, and performance of the new modified tabulated J-C material model and data set against the original tabulated J-C material model. The focus of the comparison is to verify that the modified material can simulate the appearance of ASB; therefore among all the tests performed by Pereira et al. [123] this research focused on the 12.7mm (0.5 inch) plates tests, which were the set that showed an ASB failure mechanism.

6.1.1. Target Geometry

The target geometries were tested at 12.7mm thickness in the form of a square plate with 381mm edge length. Using a heavy steel fixture, the targets were rigidly constrained between two plates with a 254mm diameter circular opening, connected with bolts, as illustrated in Figure 56.

6.1.2. Cylindrical Projectile

The projectiles used were made of A2 tool steel and had a cylindrical geometry. The geometry and dimension of the projectile can be seen in Table 20 and Figure 57 [40], [123] .

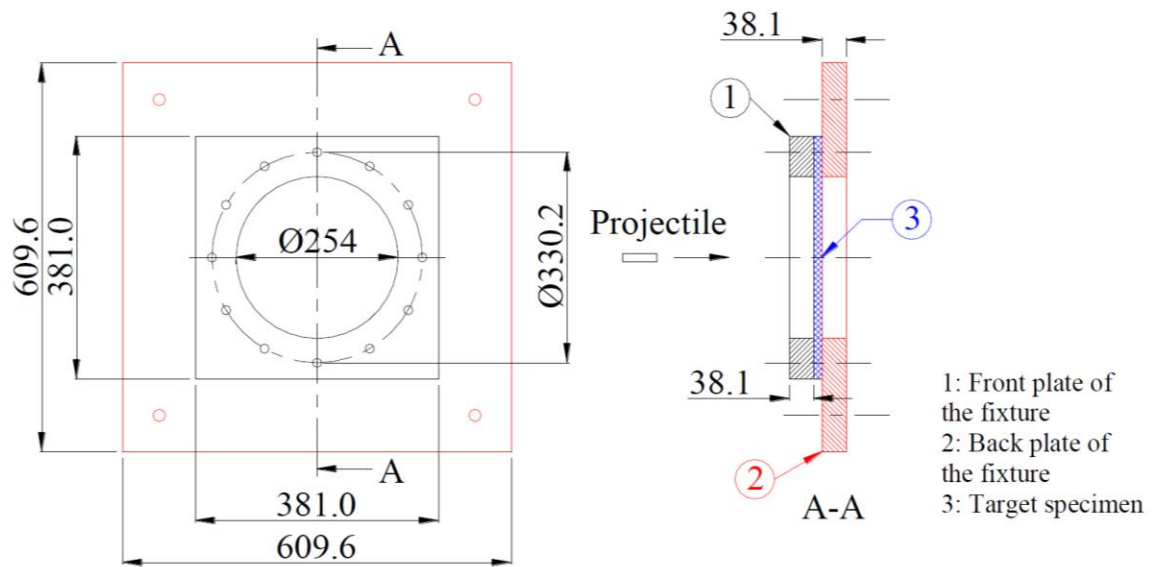


Figure 56: Specimen and fixture geometry [40]

Table 20: Projectile dimensions

Panel Thickness [mm]	Projectile material	Projectile Length [mm]	Projectile Diameter [mm]	Average mass [g]
12.7	A2 tool Steel	57	19.05	126.4

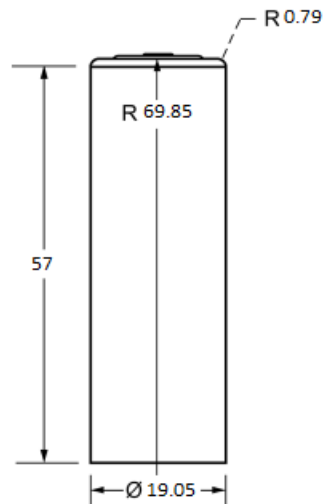


Figure 57: Projectile geometry (dimensions in mm) [40]

6.1.3. Ballistic Impact Tests Apparatus

A helium propelled gas gun with a vacuum chamber was utilized as the accelerator for the projectiles carried by a polycarbonate sabot within a 50.8mm diameter barrel. The gun barrel had a length of 3.65m and a bore of 50.8mm. The pressure vessel had a total volume of $1.116 \times 10^7 \text{ mm}^3$. The gun barrel protruded into the vacuum chamber, which held the fixture for the specimens. The sabot was stopped at the end of the gun barrel by a stopper plate [123].



Figure 58: Large vacuum gas gun. Shown with 76.2mm (3 inch) diameter gun barrel [123]. (Image with 50.8 mm diameter barrel is not available.)

6.1.4. Test Results

The results of the ballistic impact tests are summarized in Table 21. Only 2 of the tests showed a full penetration and the trend was not consistent, further adding difficulties in identifying a precise ballistic limit. However, this is likely due to slightly different impact angles and to the natural expected variability of experimental tests.

The logistic regression of the tests data identified that the impact velocity at which the probability of penetration is 50% is 195m/s (Figure 60). Examples of a contained test and a fully penetrated test illustrated in Figure 61 and Figure 62, respectively. Of note is the perfectly sharp edge created by the plug as can be seen in Figure 62.

Table 21: Panel Impact Test Results [123]

Test	Impact velocity [m/s]	Exit velocity [m/s]	Penetrate	Comments
DB266	203.8	52.5	yes	Plug exit velocity 65.8m/s
DB267	161.0	0.0	no	Created a dent but no visible crack
DB268	190.8	54.6	yes	Plug exit velocity 67m/s
DB269	180.4	0.0	no	No visible crack
DB270	183.8	0.0	no	No visible crack
DB271	189.1	0.0	no	No visible crack
DB272	195.7	0.0	no	No visible crack

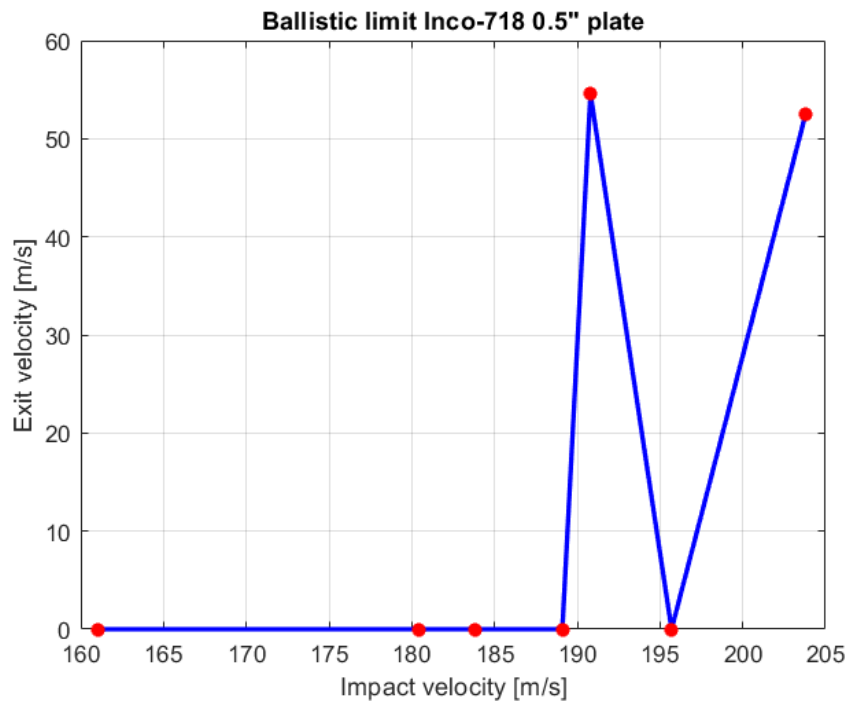


Figure 59: Ballistic limit Inconel-718 12.7mm (0.5inch) plate tests

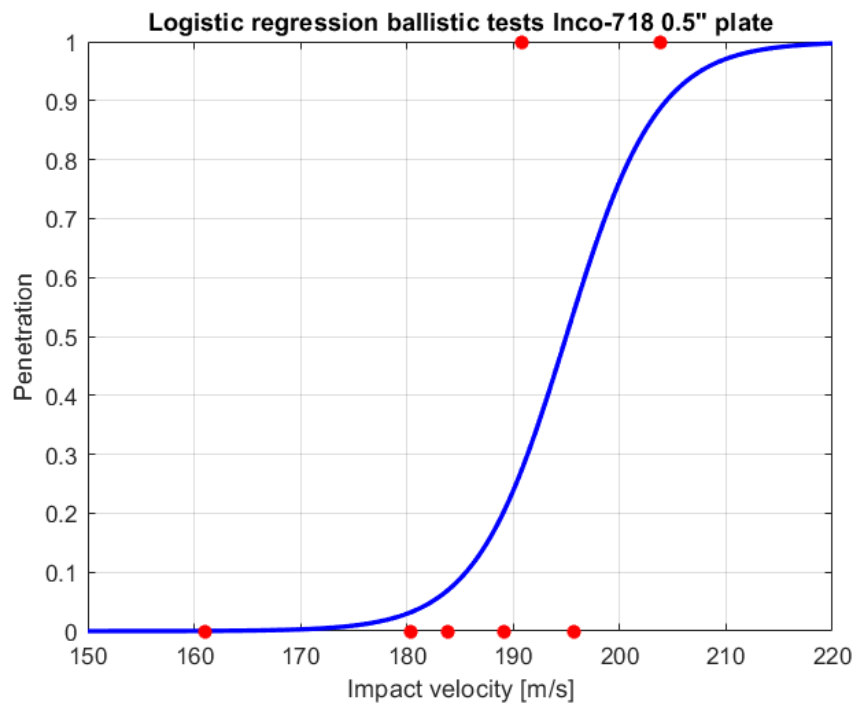


Figure 60: Penetration results for 12.7mm (0.5inch) panels. Velocity at which probability of penetration is 50% was 195m/s [123]

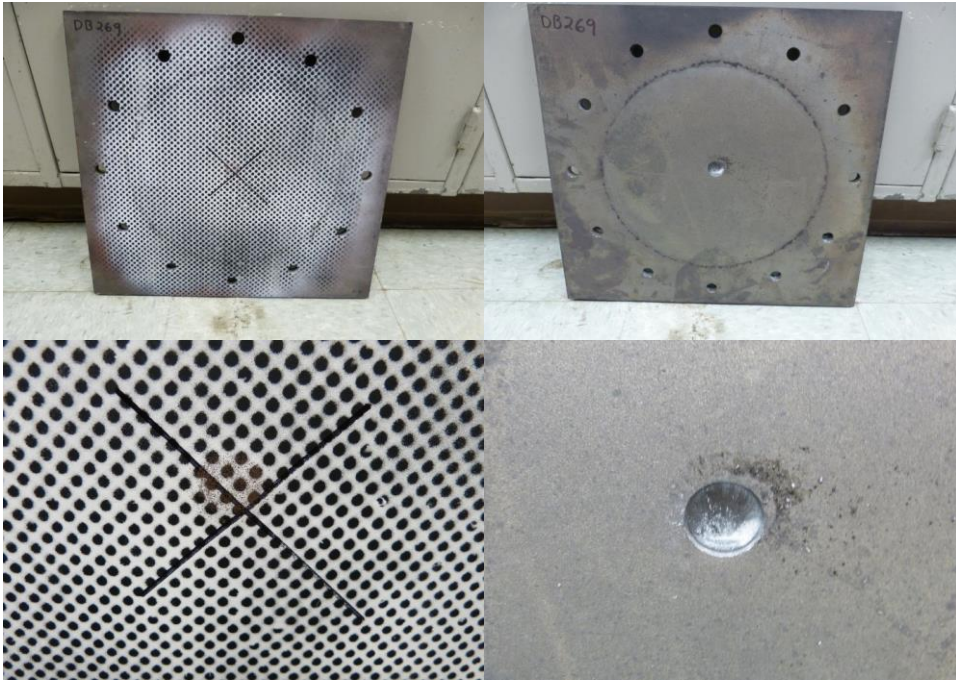


Figure 61: Fully contained test (DB269 - 180.4 m/s) plate post-test. Clock wise: rear view, front view, front view close-up, rear view close up



Figure 62: Fully penetrated tests (DB266 – 203.8 m/s) plate post-test. Clock wise: front view, rear view, rear view close up, front view close-up

6.2. Ballistic Impacts Simulations

In order to demonstrate the improved predictive capability and performance of the modified J-C tabulated material, the ballistic tests were simulated using both the original and the enhanced J-C material models. The results of the simulations were compared to the tests results.

6.2.1. Numerical models of the ballistic impact with cylindrical projectiles

Both the tabulated J-C material model and the modified tabulated J-C material model were used to simulate the aforementioned ballistic impact tests performed by NASA. The materials have the same parameter characterization with the exception of the Taylor-Quinney coefficient which is a tabulated function in the modified version and a constant parameter set to 0.8 in the original material model. Both the material models were simulated using the same FEM mesh that can be seen in Table 22. Each simulation was initialized by applying the corresponding impact velocity and projectile angles at the impact measured with high-speed cameras during the tests.

Table 22: Ballistic impact simulations 0.2 mm elements mesh characteristics

Number of elements	2582604	
Element size [mm]	0.2	
Plate material model	*MAT_TABULATED_JOHNSON_COOK *MAT_TABULATED_JOHNSON_COOK_MODIFIED	
Projectile material model	*MAT_ELASTIC	

6.2.2. Tabulated Beta Characterization

The set of parameters used to create the tabulated beta input is presented in Table 23. The MatLab code developed to generate the tabulated table input deck can be found in Appendix A. The tables were developed using a mesh of 0.2mm solid elements.

Table 23: Taylor-Quinney Tabulated input parameter set

MESH [mm]	Tabulated input	γ_{max} @ transition	$\dot{\epsilon}_p$ @ transition [1/s]	β_{min}^*	β_{max}^*
0.2	$\beta_{TAB,02}^*$	0.26	8000	0.8	10

and a new TQC was defined as a function of strain rate and max shear strain without element size regularization. The MatLab code developed allows for a choice of the values of β_{min}^* (“outside ASB conditions”) and β_{max}^* (“inside the ASB”), and what values of strain rate and maximum shear strain trigger the transition between the two conditions. In the final tabulated TQC the curves from the “outside of ASB” conditions to the “inside ASB” conditions were defined with a hyperbolic tangent function in both strain rate and max shear strain dominions and were discretized with 901 points in each dimension (Figure 63). This was done to capture the structural instability pertaining to the ASB without causing numerical instabilities. The code then selects only the point in the transition to isolate a compact enough data set to create the input file to be used by LS-DYNA[®]. The parameters were calibrated through an iterative process to find the optimal match with the tests.

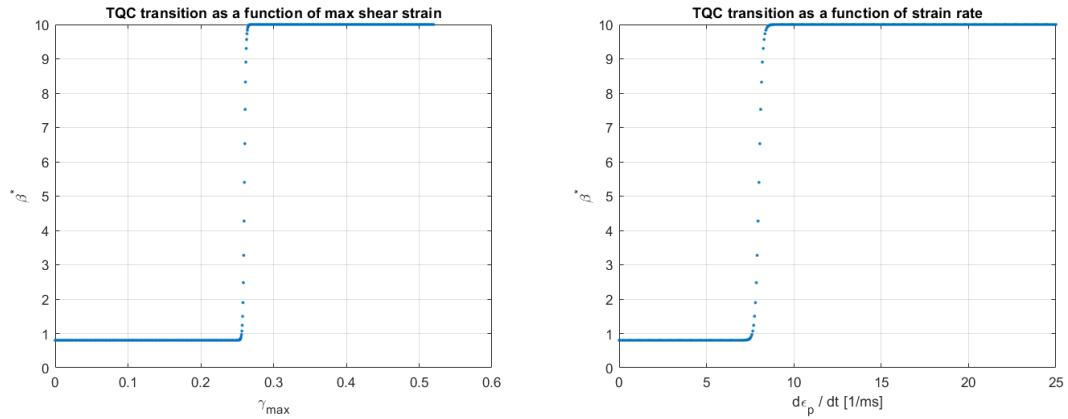


Figure 63: TQC discretization curves TQC as function of maximum shear strain and strain rate

6.2.3. Results

The results of the ballistic impact tests are summarized in terms of exit velocities in Table 24. Figure 64 shows the ballistic limit diagram for the original and modified materials. The exit velocity reported is the filtered velocity of the central node of the bottom of the projectile in the normal direction of the plate (see Figure 65). A sequence of the simulation of test DB266 with the enhanced code is depicted in Figure 66.

Table 24: Ballistic simulations exit velocity results

Test simulation	DB266		DB267		DB268	
Impact/exit velocity [m/s]	203.8/52.5		161.0/0		190.8/54.6	
Mesh [mm]	TQC		TQC		TQC	
	β	$\beta^*_{TAB,0.2}$	β	$\beta^*_{TAB,0.2}$	β	$\beta^*_{TAB,0.2}$
0.2	0	47.8	0	0	0	(0) Full plug

Test simulation	DB269		DB270		DB271		DB272	
Impact/exit velocity [m/s]	180.4/0		183.8/0		189.1/0		195.7/0	
Mesh [mm]	TQC		TQC		TQC		TQC	
	β	$\beta^*_{TAB,0.2}$	β	$\beta^*_{TAB,0.2}$	β	$\beta^*_{TAB,0.2}$	β	$\beta^*_{TAB,0.2}$
0.2	0	0	0	0	0	0	0	15.8

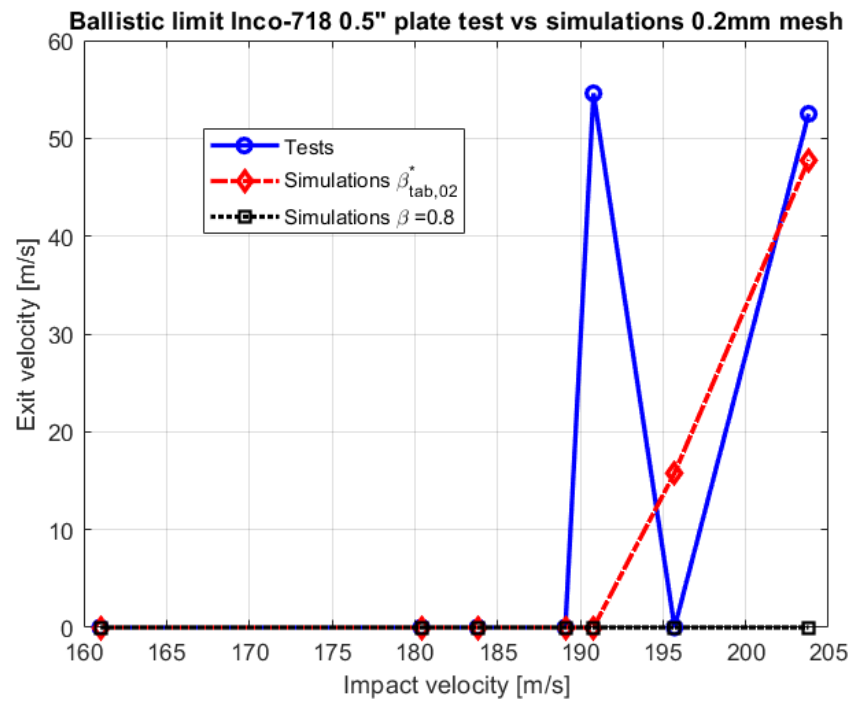


Figure 64: Ballistic limit Inconel 718 12.7mm (0.5inch) plate tests vs. simulations

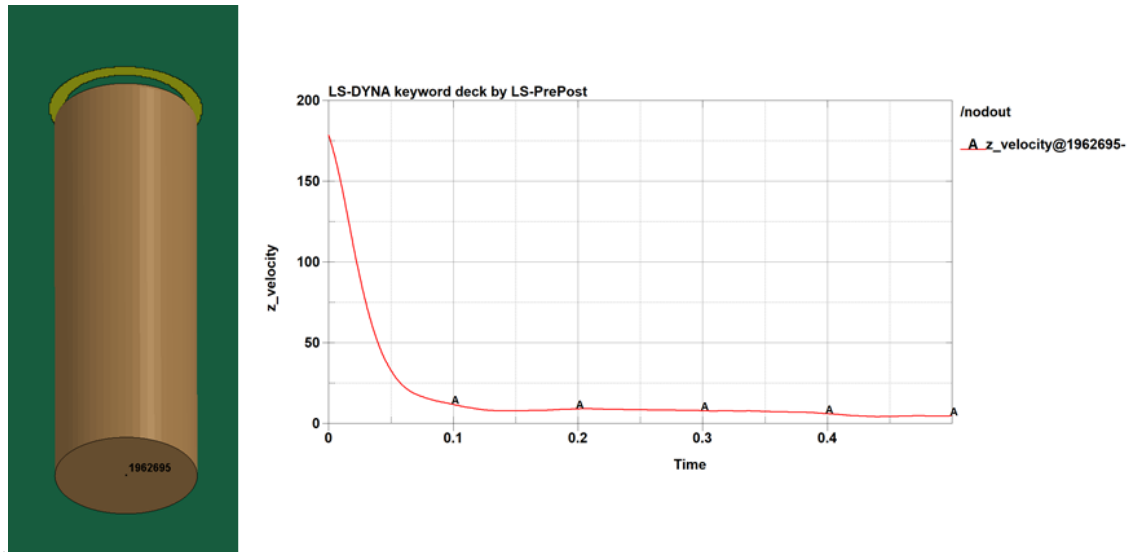


Figure 65: Projectile bottom node z-velocity SAE 6000Hz filter

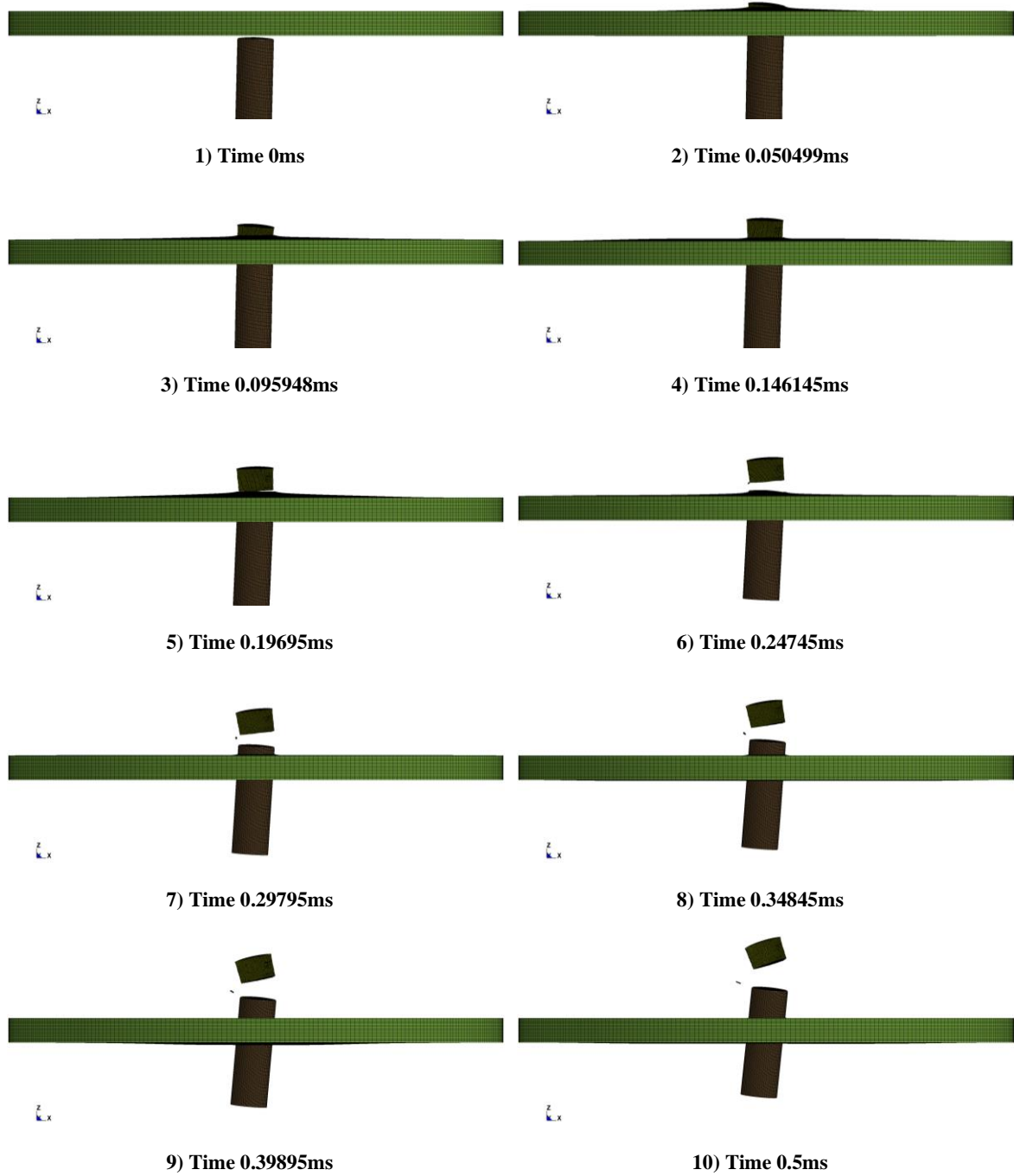


Figure 66: DB266 – 203.8m/s ballistic impact simulation

A sequence of the development of the temperature in the ASB of test DB266 simulation using the enhanced material model can be seen in section A-A (Figure 68) of the “bull’s eye” part (Figure 67) of the plate in Figure 70, while Figure 69 shows the temperature of a row of elements across the shear band in section A-A (Figure 68).

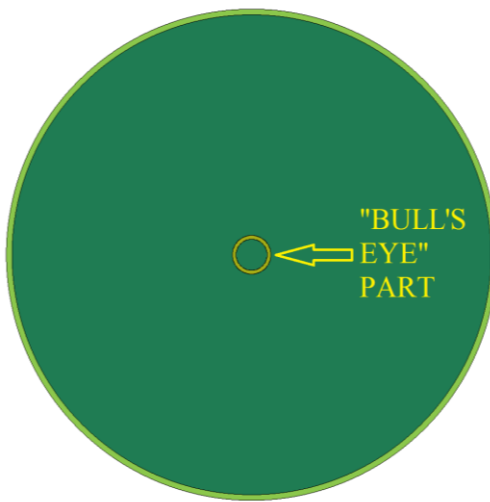


Figure 67: “Bull's eye” part

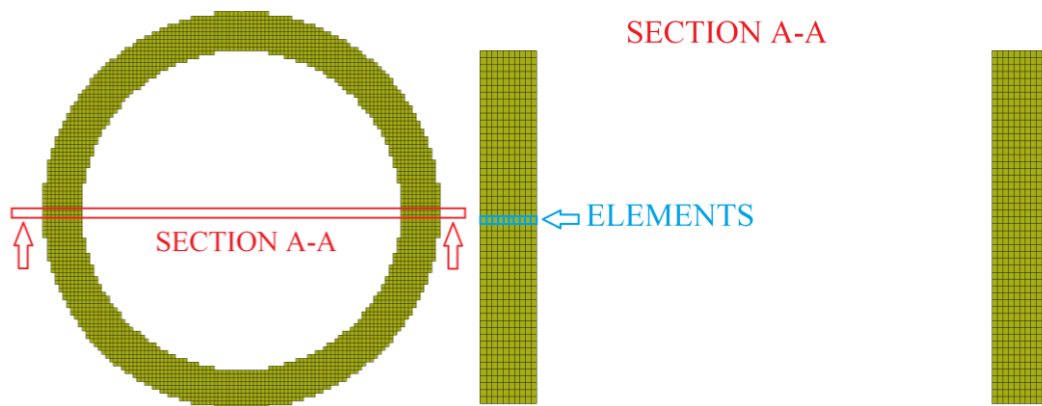


Figure 68: “Bull's eye” part section (A-A) and elements selected in the section

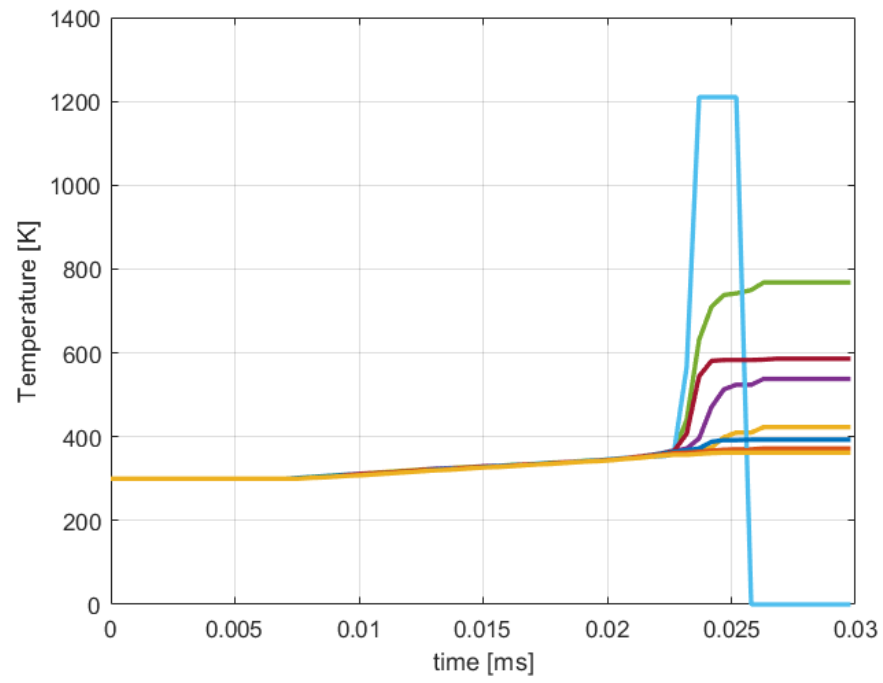
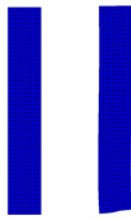


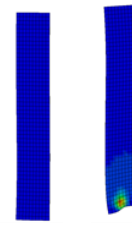
Figure 69: DB266 – 203.8m/s $\beta_{TAB,0.2}^*$ temperature of the elements across the ASB (see Figure 68)



1) Time 0ms



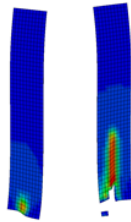
2) Time 0.0095946ms



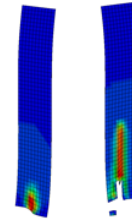
3) Time 0.014644ms



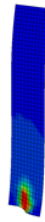
4) Time 0.019895ms



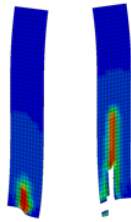
5) Time 0.02121ms



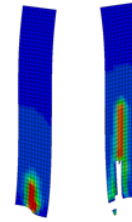
6) Time 0.021714ms



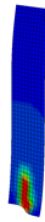
7) Time 0.02222ms



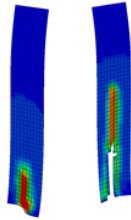
8) Time 0.022725ms



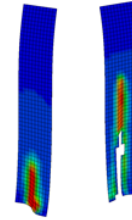
9) Time 0.02323ms



10) Time 0.023734ms



11) Time 0.024239ms



12) Time 0.024744ms

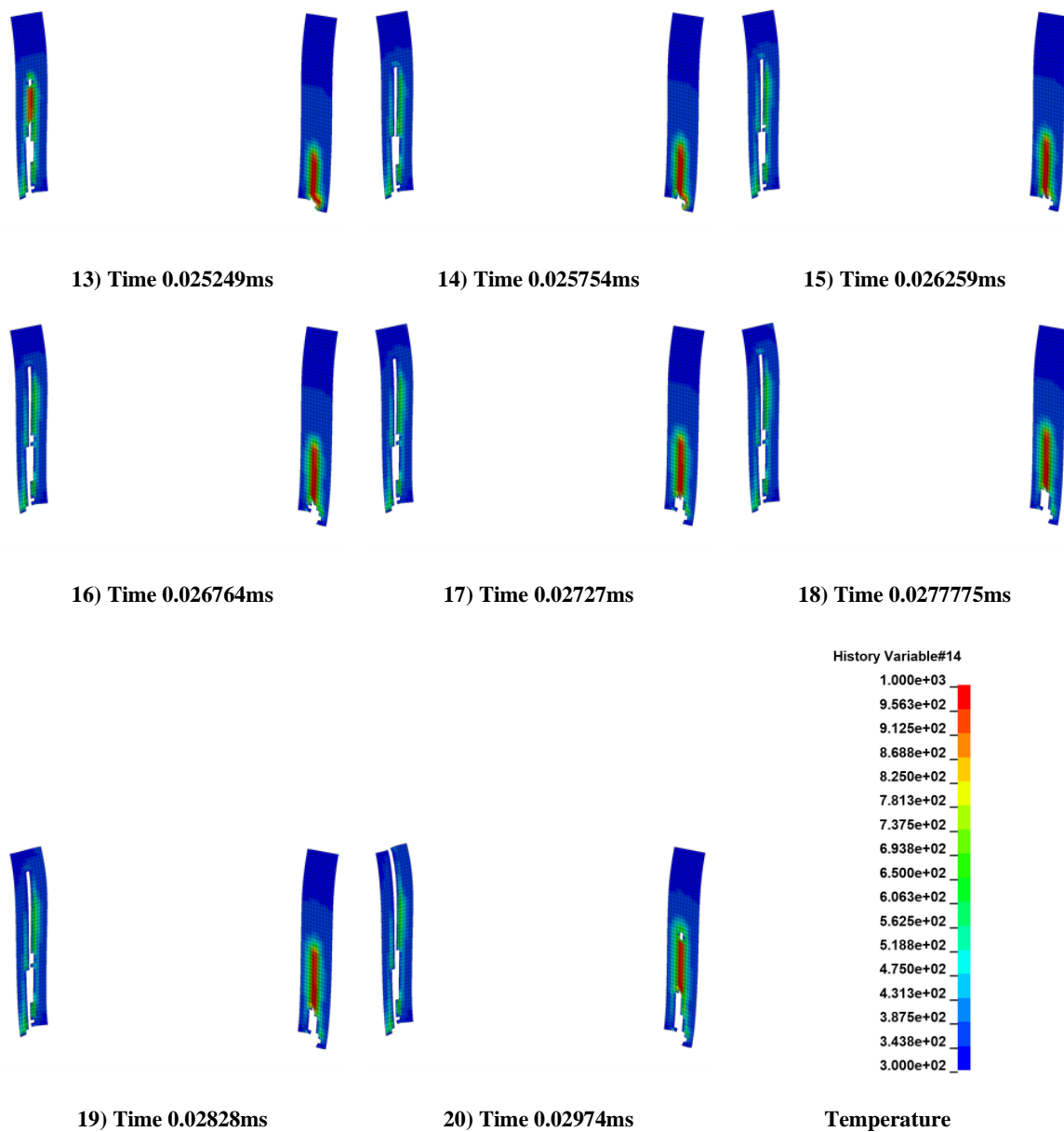


Figure 70: DB266 – 203.8m/s ballistic impact simulation. ASB development on the “bull's eye” part, section A-A (see Figure 68). Temperature contours.

To obtain an efficient visualization of the plate sections intersected by the ASB the plates were cut from the center of the plate in the top view, along the positive x and y directions. This allows the visualization of the element subject to shear band condition through the thickness (z-direction) along the x and y directions (Figure 71).

Table 25 reports the sequence of the temperature contours of DB266 test simulations for both the original material model (right), and the enhanced material model (left).

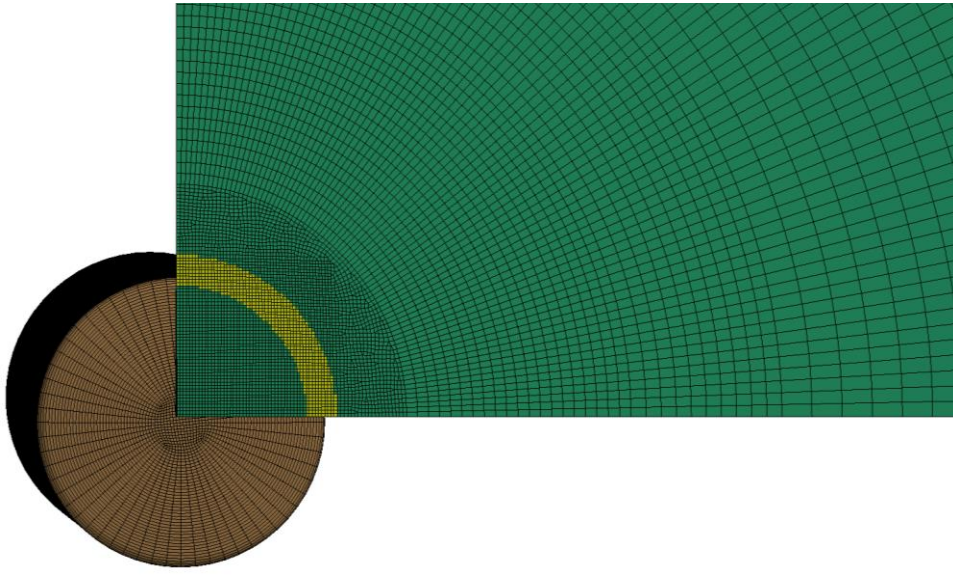
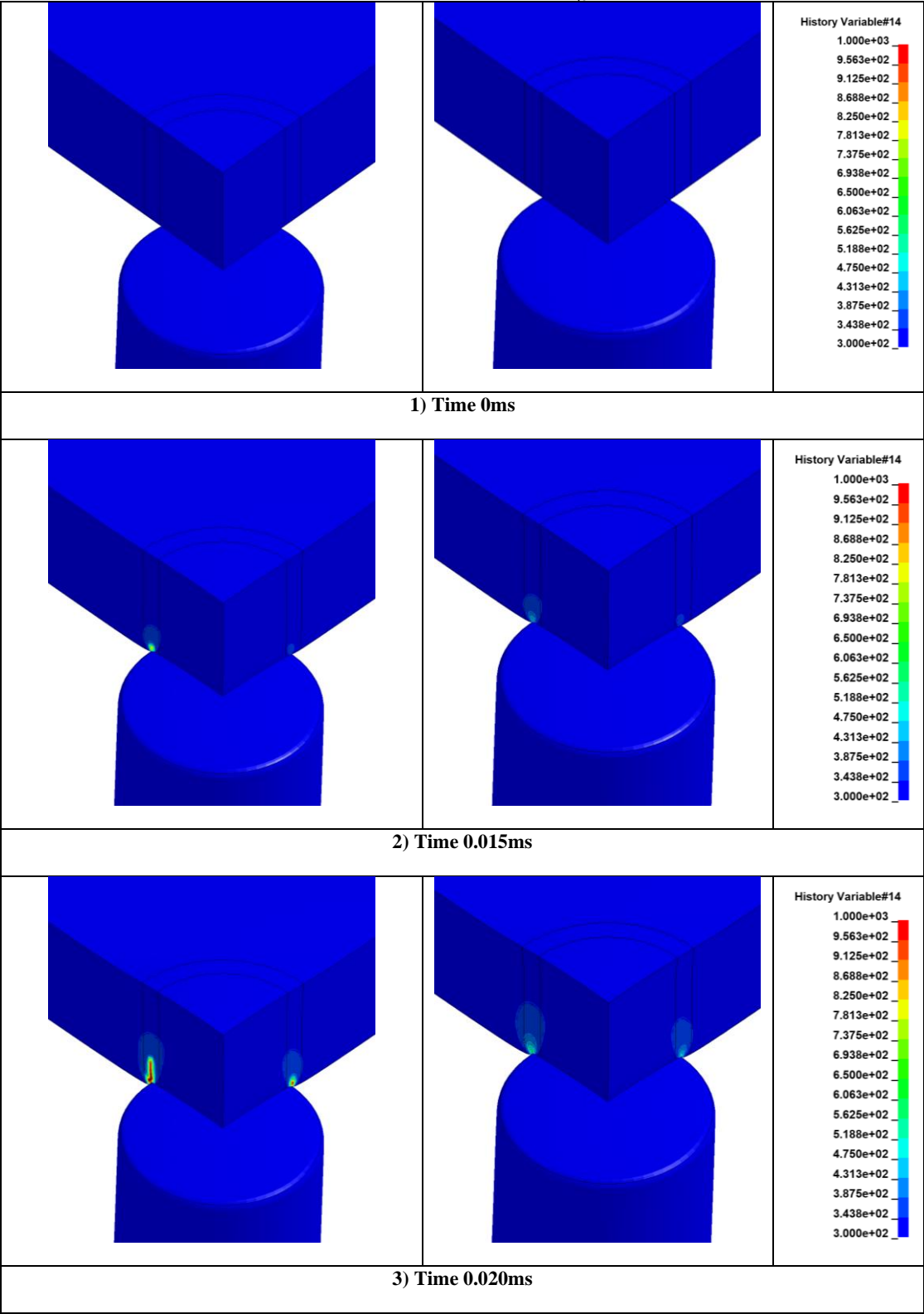
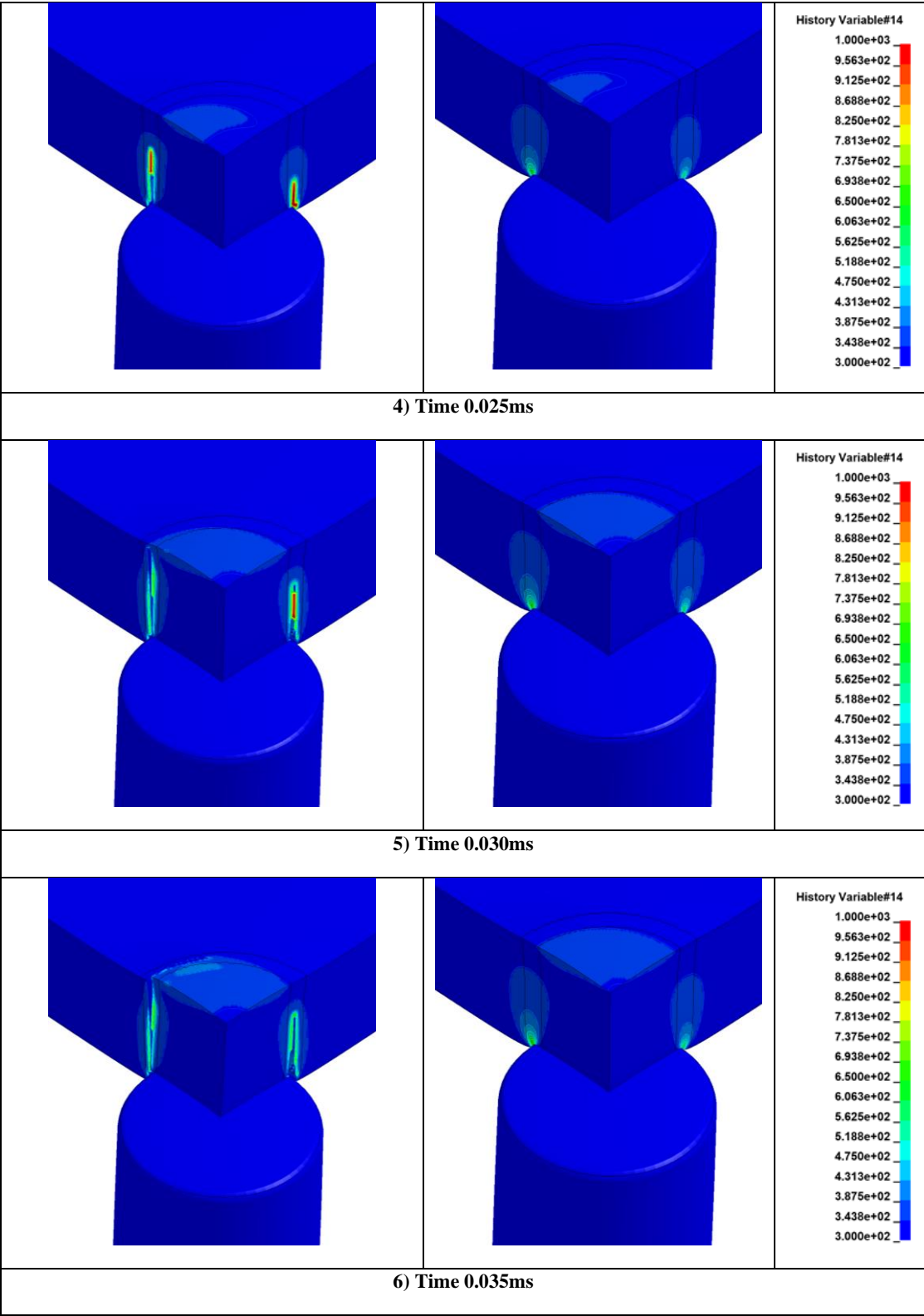
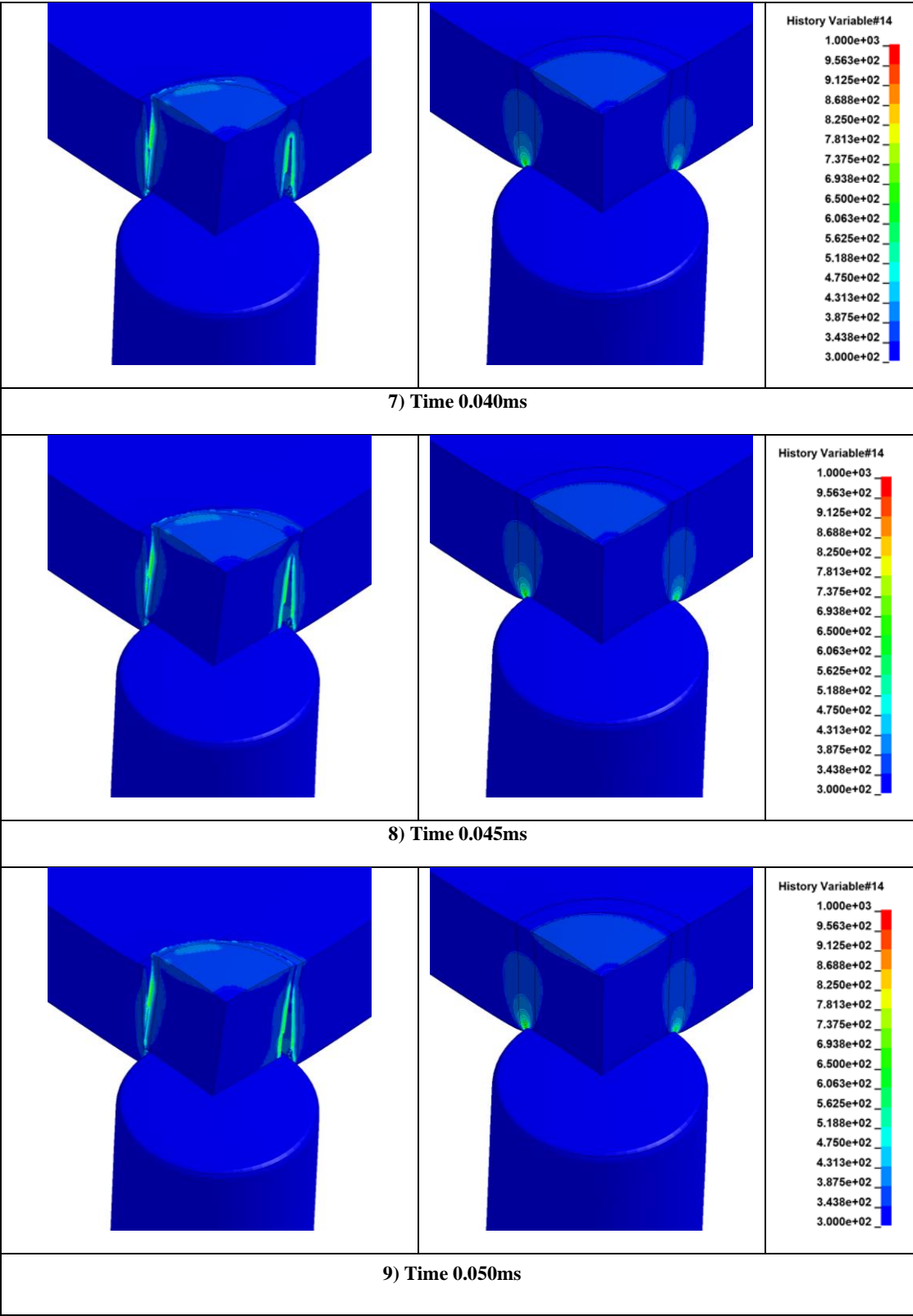


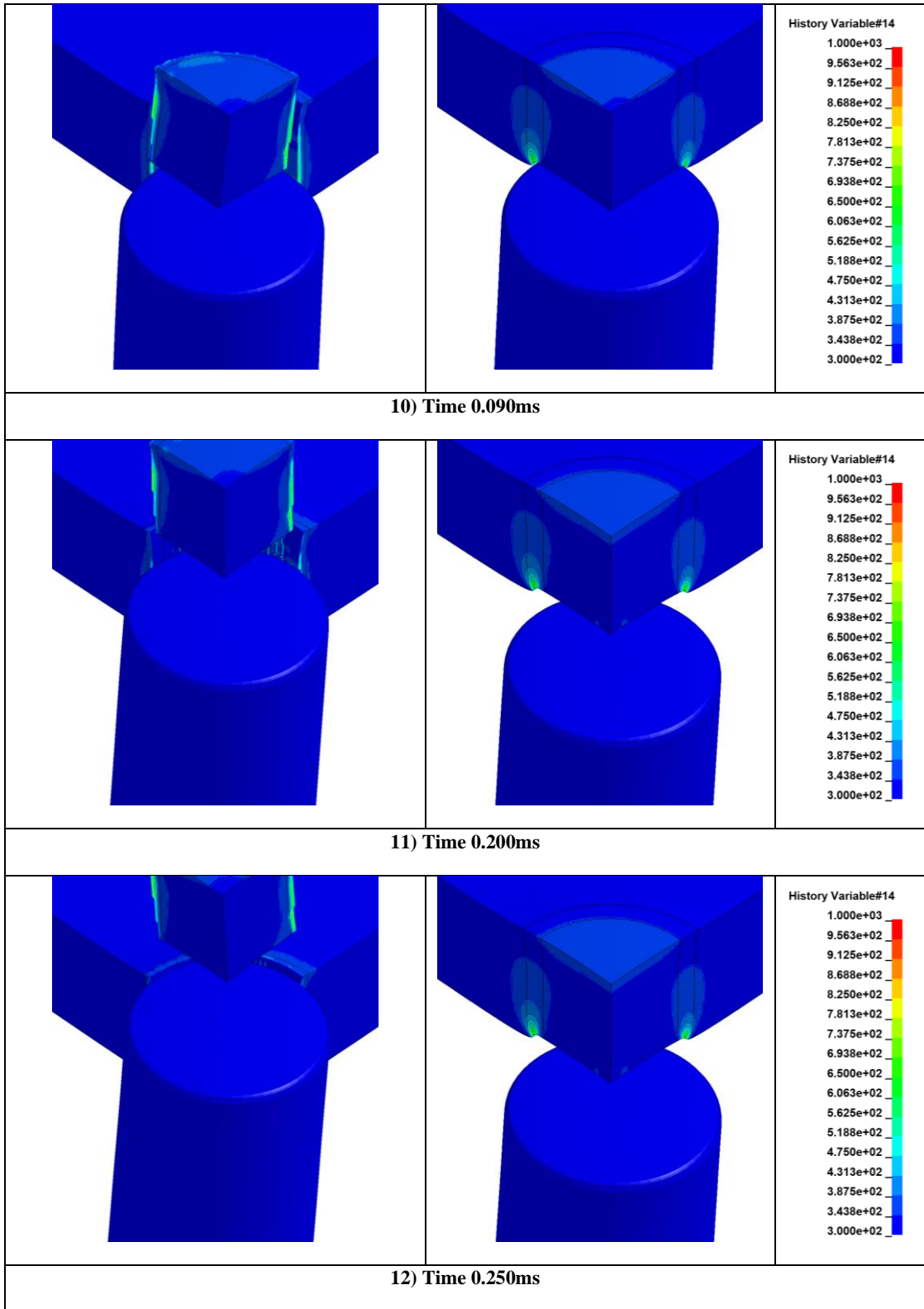
Figure 71: Plates cut for results visualization purpose

Table 25: DB266 Simulation Results. Temperature line contours $\beta_{TAB,0.2}^*$ (left) vs. $\beta=0.8$ (right)









6.3. Discussion

The modified tabulated J-C material model shows a much better prediction of the impact physics, and therefore of the ballistic limit, compared to the original tabulated J-C material model simulations. For the higher impact velocities, the temperature inside the ASB reached values above 1200K, 227K beyond the temperature that in static condition causes the change of phase from γ " to δ that makes Inconel brittle. The average speed of propagation of the crack through the total thickness was about 1200m/s, with an actual ASB propagation speed of about 4000m/s, which is consistent with the literature and with the 2D simulations. Moreover, the width of the ASB was of only 1 element. It has been demonstrated in previous studies [15] that this result is not achievable by simply tweaking the parameters of the original materials (for example modifying the high strain rates proprieties, the failure surface, or the stress strain curves as a function of the temperature). The original tabulated material is not capable of reproducing the physics of ASBs unless the mesh size is so small that it becomes inapplicable to virtually any real-life application. The modified tabulated J-C material model on the other end shows very good adherence to the tests.

7. REGULARIZATION FOR ELEMENT SIZE

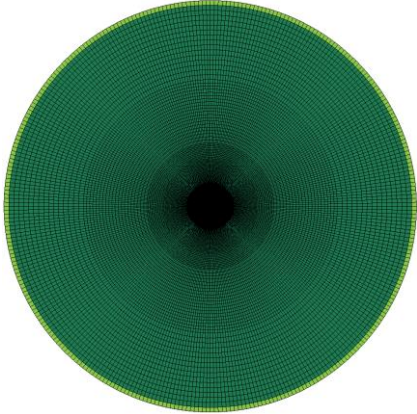
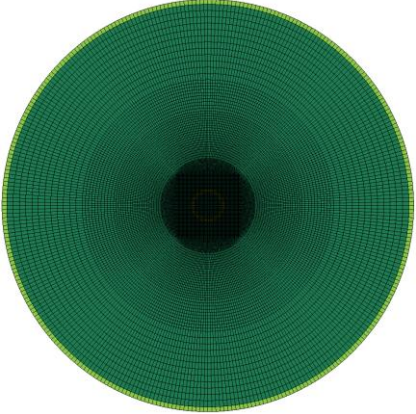



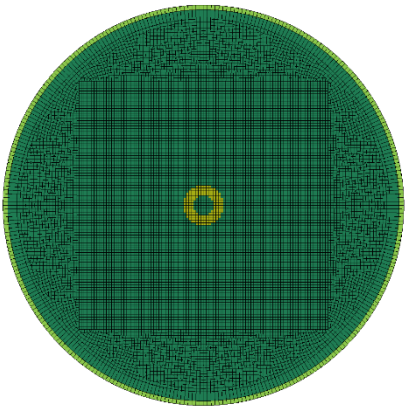


To assure the predictive capabilities of the modified J-C material model in high velocity impacts, concerning ASB enucleation, it is necessary to account for different mesh sizes while defining the correct tabulated TQC. For this purpose, a set of meshes of different sizes were used to develop independent tabulated TQC input decks to account for $\frac{W_{SB}}{\lambda}$ dependency. Three of the ballistic tests presented in the previous chapter were simulated with the different size meshes, introduced in paragraph 7.1, to develop a regularized TQC, using a procedure explained in paragraph 7.2. For each mesh size model, the procedure was performed to determine the specific mesh size dependent values of γ_{max} , $\dot{\epsilon}_p$, and β_{max}^* . The TQC parameters from the different mesh size simulations were then used to create a tabulated TQC set of tables that fully regularize for element size. The fully regularized tabulated TQC (β_{TAB}^*) simulations of the tests, with impact velocity above the first penetration, were then compared to the tabulated TQC developed for the 0.2mm mesh in chapter 6 ($\beta_{TAB,0.2}^*$) to demonstrate the effectivity of element size TQC regularization.

7.1. Numerical models of the ballistic impact with cylindrical projectiles

A set of meshes with element sizes ranging from 0.2 to 1.6 mm were created to develop a tabulated TQC fully regularized for element size. Further details on the mesh

properties can be found in Table 26. The projectile was modeled with the same mesh in all cases, using an elastic material model (*MAT_ELASTIC).

Table 26: Meshes for various element sizes

Element size [mm]	0.2	0.4
Number of elements	2582604	1482644
Top view		
Side view		
Element size [mm]	0.8	1.6
Number of elements	1022652	855972
Top view		
Side view		

7.2. Procedure

Each mesh was used to develop an independent set of TQC tables calibrated to match the ballistic tests presented in paragraph 6.1, with a procedure analogous to that which was explained in paragraph 6.2.2. The single TQC input decks were calibrated through an iterative procedure for each mesh, and the final parameters selected during the calibrations are shown in Table 27. The trend lines of the evolution of transitioning γ_{max} and β_{max}^* inside the ASB with element size are reported in Figure 72. Note that γ_{max} decreases with larger element size, which is comparable to element erosion criteria regularization. Also note that β_{max}^* increases with larger element size.

Table 28 shows the results of the TQCs calibration for each mesh in terms of exit velocity. The parameters selected were used to create a separate set of tables for the TQC for each mesh ($\beta_{TAB,0.2}^*$, $\beta_{TAB,0.4}^*$, $\beta_{TAB,0.8}^*$ and $\beta_{TAB,1.6}^*$) using the code in Appendix A. The separate sets of tables for the TQC for each mesh were finally merged to generate a fully regularized tabulated TQC input deck (β_{TAB}^*) using the code in Appendix B.

Table 27: Maximum shear strain and plastic strain rate where the transition from normal to ASB condition initiate and maximum value of TQC inside the ASB for each mesh.

Mesh [mm]	γ_{max}	$\dot{\epsilon}_p$ [1/s]	β_{max}^*
0.2	0.26	8000	10
0.4	0.23	8000	12.5
0.8	0.18	8000	13
1.6	0.15	8000	23

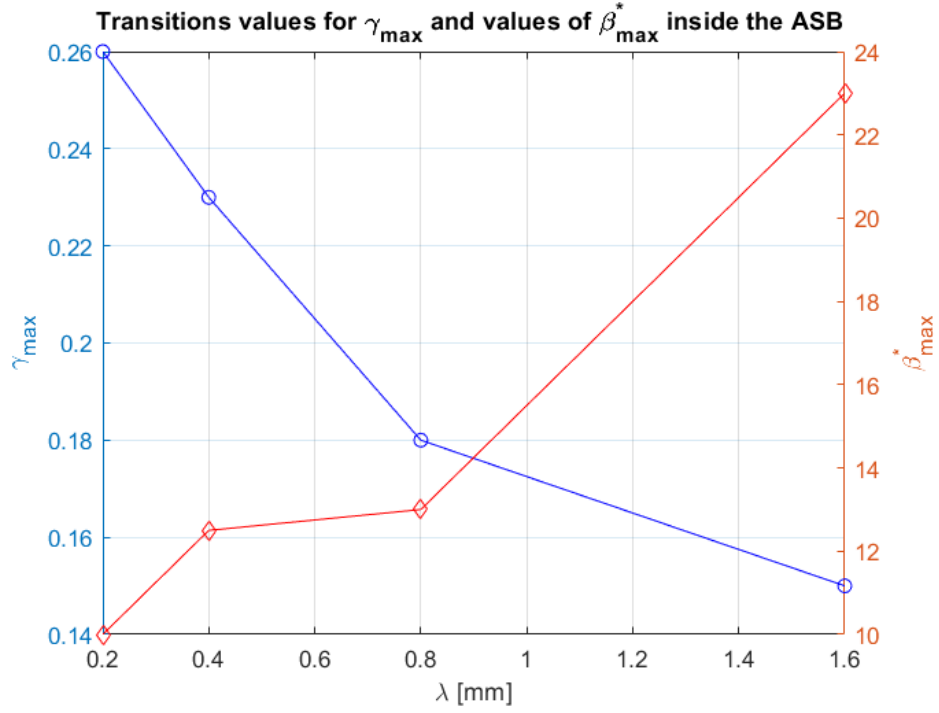


Figure 72: Evolution of transition maximum shear strain and maximum TQC inside the ASB with element size

Table 28: Element size regularization procedure: exit velocity simulated for 3 tests for each mesh using a specifically characterized TQC for each element size.

Test		DB266	DB268	DB272
Impact velocity [m/s]		203	191	189
Exit velocity [m/s]		52	54	0
Mesh [mm]	TQC name	Simulation exit velocity [m/s]		
0.2	$\beta_{TAB,0.2}^*$	47.8	Full plug	0
0.4	$\beta_{TAB,0.4}^*$	47.8	Full plug	0
0.8	$\beta_{TAB,0.8}^*$	52.0	Full plug	0
1.6	$\beta_{TAB,1.6}^*$	51.5	partial plug	0

7.3. Results

After characterizing a tabulated TQC for each element size the simulations for each mesh were then repeated with the full and final TQC input deck regularized for element size (β_{TAB}^*). The results were then compared with the original tabulated TQC input deck ($\beta_{TAB,0.2}^*$) developed in paragraph 6.2 for the 0.2 mm element size mesh to demonstrate the effectivity of element size regularization. Table 29 shows the comparison between the simulations of 3 tests using different meshes for the regularized (β_{TAB}^*) and original ($\beta_{TAB,0.2}^*$) TQC in terms of impact and exit velocity. Table 30 and Figure 73 shows the crack and ASB propagation velocity in the same tests' simulations. Crack propagation velocity is calculated as the plate thickness divided by the time it takes for a row of elements across the thickness of the plate to become completely eroded. The ASB velocity is calculated similarly but only considering a portion of the thickness where the erosion occurs at very high shear deformation and at temperatures in excess of 1000K. Because the rendering of the outputs is not generated for every timestep this calculation has to be considered an estimate, particularly for the DB266 test simulations where the time of ASB propagation was so short that the output data intervals were relatively coarse. Figure 74 shows two curve fittings of β_{max}^* as a function of element size (λ). It can be noted that β_{max}^* initially increases sharply as the ratio between element size (λ) and ASB width (w_{SB}) increases from one to two hundred; from here to the region where the element size (λ) is three order of magnitude larger than the ASB width (w_{SB}) the increase in β_{max}^* is less steep. The extremely high β_{max}^* values are justified because of

the extreme difference between w_{SB} and λ . Table 31 to Table 33 show the last temperature contour of each mesh size for tests DB272, DB268, and DB266 respectively. From Table 34 to Table 37 the comparison of the ballistic impacts' sequences of the test DB266 simulations, for the 0.2mm, 0.4mm, 0.8mm, and 1.6mm element size meshes, are reported. Figure 75 shows a comparison of the ballistic limit across all meshes between the fully regularized and original TQC. Finally, Figure 76 shows global energies for the simulations of all meshes of test DB266, while Figure 77 to Figure 80 show the energies by part of test DB266 for each mesh size simulation. These results will be discussed in the next section.

Table 29: Comparison of the exit velocities between the simulations of the modified J-C material model equipped with the TQC developed for the 0.2mm mesh ($\beta_{TAB,0.2}^*$), equipped with the TQC regularized per mesh element size (β_{TAB}^*) and tests

Test simulation	DB268		DB272		DB266	
Impact/exit velocity [m/s]	190.8/54.6		195.7/0		203.8/52.5	
Mesh [mm]	$\beta_{TAB,0.2}^*$	β_{TAB}^*	$\beta_{TAB,0.2}^*$	β_{TAB}^*	$\beta_{TAB,0.2}^*$	β_{TAB}^*
0.2	(0) Full plug	(0) Full plug	15.8	15.2	47.8	44.8
0.4	0	(0) Full plug	0	16.2	(0) Partial plug	46.2
0.8	0	(0) Full plug	0	21.4	0	50.9
1.6	0	(0) Partial plug	0	15.6	0	51.5

Table 30: Modified J-C material model simulations with the TQC regularized per mesh element size (β_{TAB}^*), estimated crack propagation velocity

Test simulation (β_{TAB}^*)	DB268		DB272	DB266	
Impact/ exit velocity [m/s]	190.8/54.6		195.7/0	203.8/52.5	
Mesh [mm]	Crack [m/s]	ASB [m/s]	Crack [m/s] ²	Crack [m/s]	ASB [m/s]
0.2	426	2717	508	1143	3299
0.4	419	1128	502	967	2095
0.8	474		786	1479	
1.6	230		360	1143	

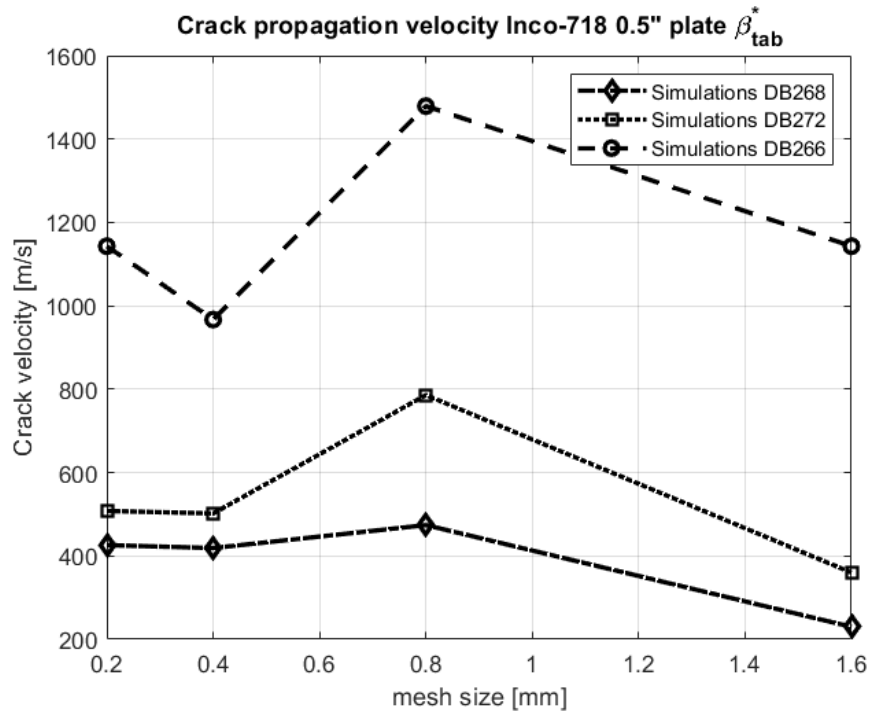


Figure 73: Crack propagation velocity

²ASB velocity was not estimated because of the insufficient frequency of the results output

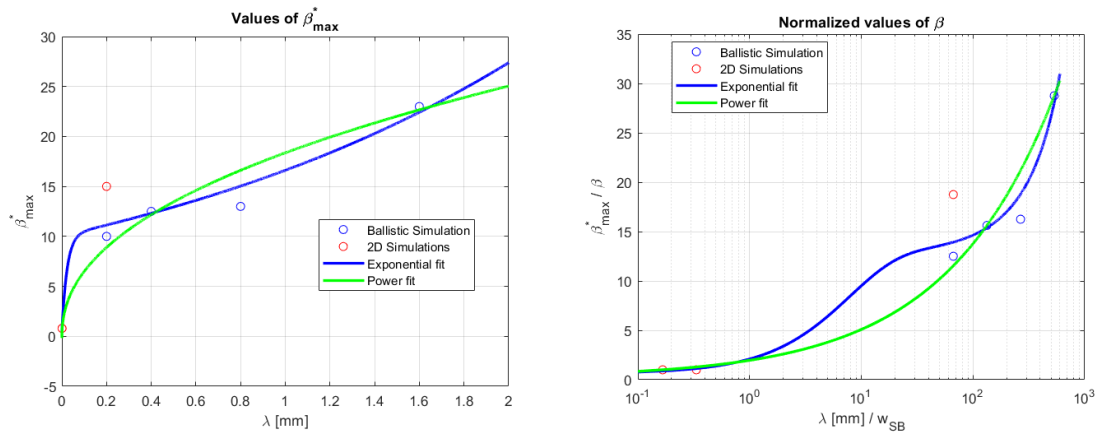


Figure 74: β_{\max}^* data curve fitting of 2D simulations and ballistic limit simulations with various element size

Table 31: DB272 temperature comparison at 0.5ms for all meshes

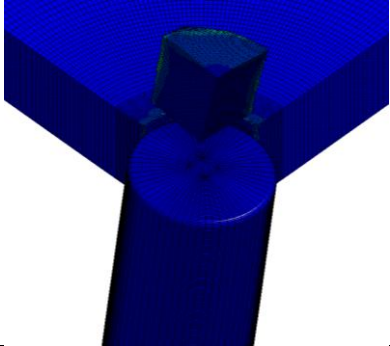
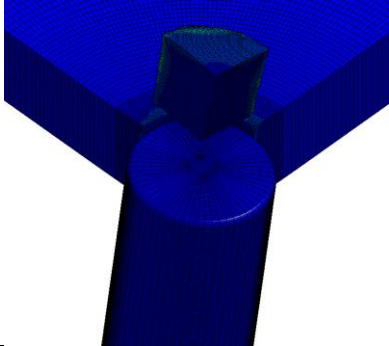
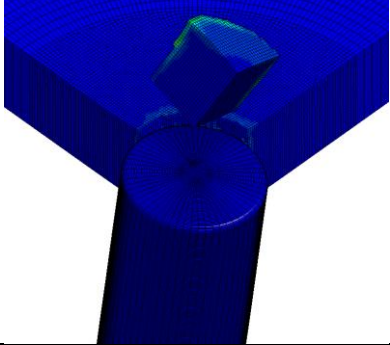
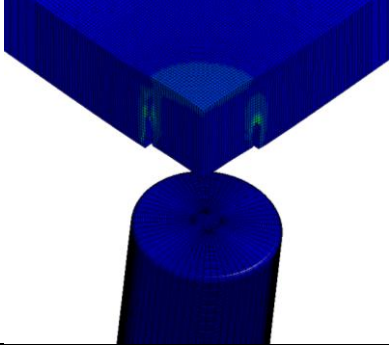
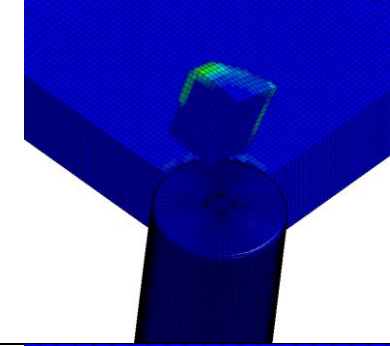
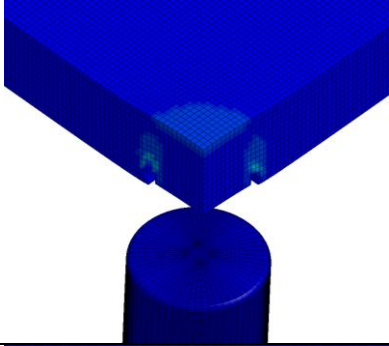
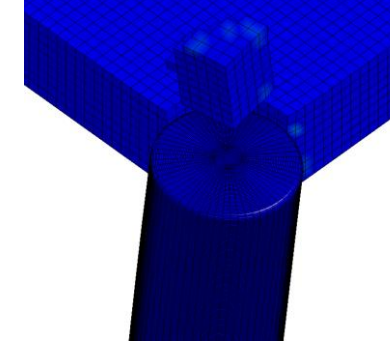
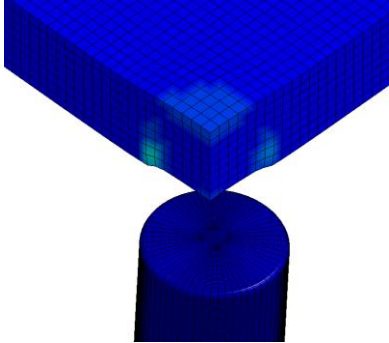
Mesh	β_{TAB}^*	$\beta_{TAB,0.2}^*$	History Variable#14 1.000e+03 9.563e+02 9.125e+02 8.688e+02 8.250e+02 7.813e+02 7.375e+02 6.938e+02 6.500e+02 6.063e+02 5.625e+02 5.188e+02 4.750e+02 4.313e+02 3.875e+02 3.438e+02 3.000e+02
0.2			
0.4			
0.8			
1.6			

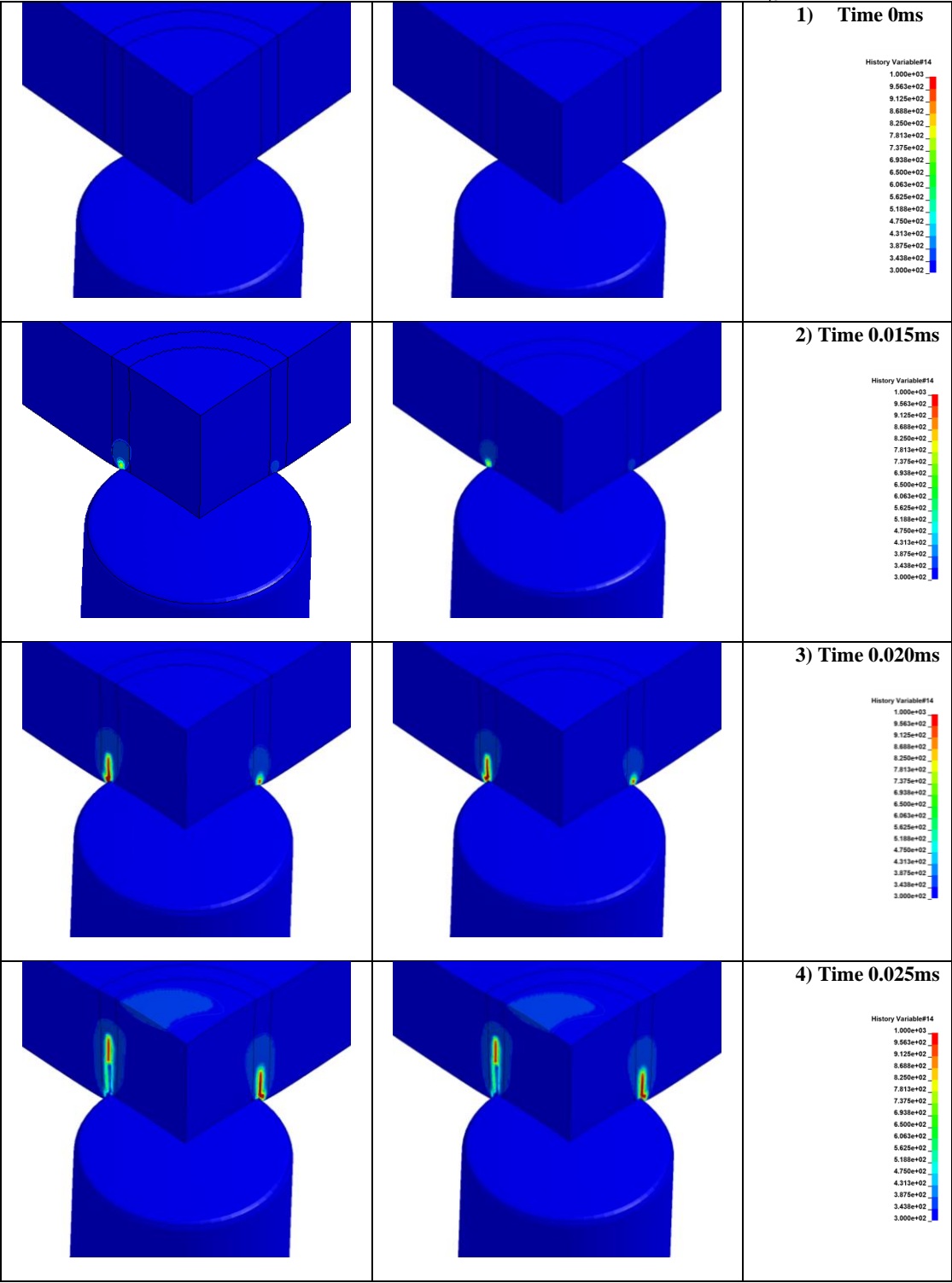
Table 32: DB268 temperature comparison at 0.5ms for all meshes

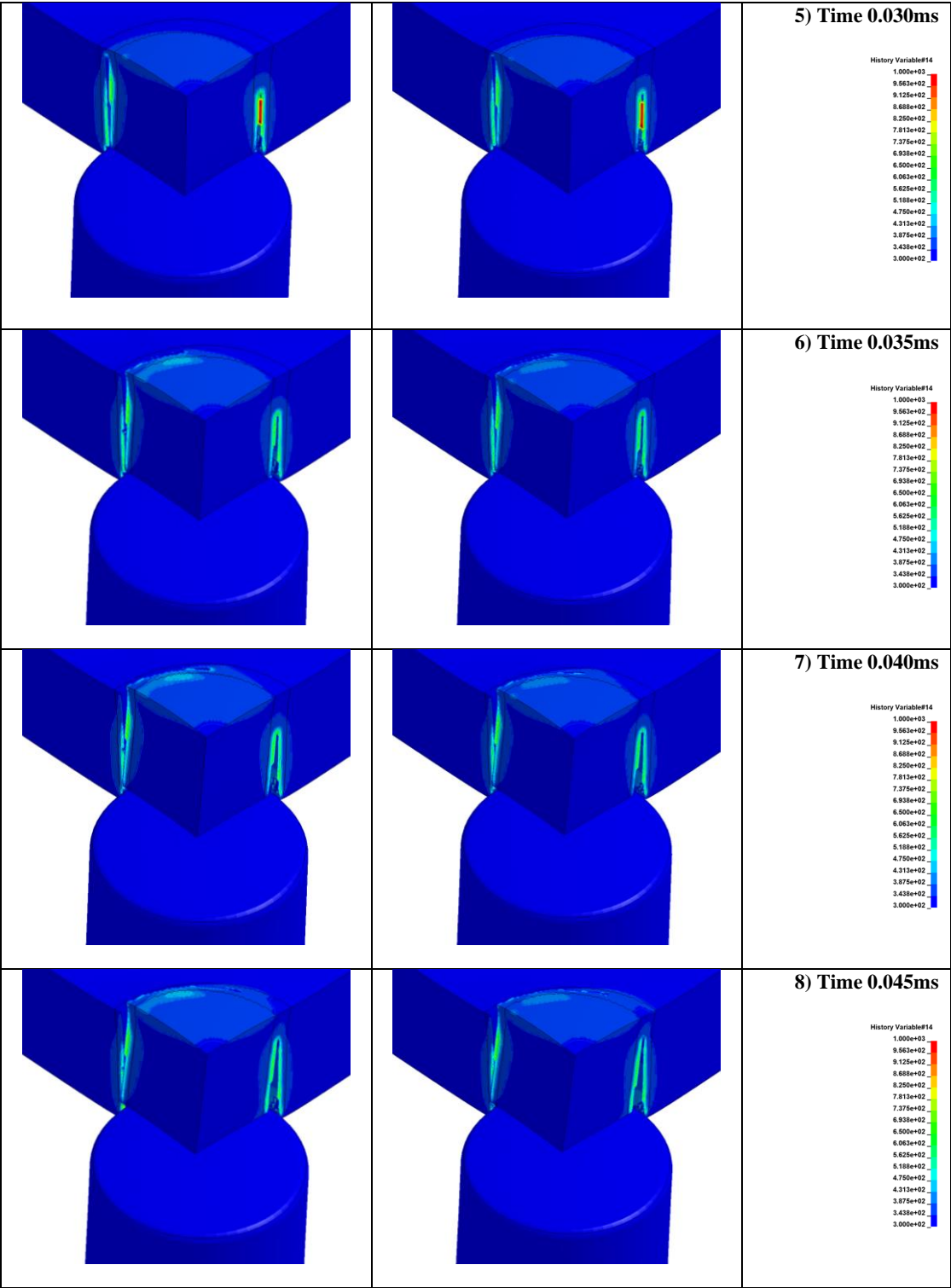
Mesh	β_{TAB}^*	$\beta_{TAB,0.2}^*$	History Variable#14 1.000e+03 9.563e+02 9.125e+02 8.688e+02 8.250e+02 7.813e+02 7.375e+02 6.938e+02 6.500e+02 6.063e+02 5.625e+02 5.188e+02 4.750e+02 4.313e+02 3.875e+02 3.438e+02 3.000e+02
0.2			
0.4			
0.8			
1.6			

Table 33: DB266 temperature comparison at 0.5ms for all meshes

Mesh	β_{TAB}^*	$\beta_{TAB,0.2}^*$	<p>History Variable#14</p> <p>1.000e+03 9.563e+02 9.125e+02 8.688e+02 8.250e+02 7.813e+02 7.375e+02 6.938e+02 6.500e+02 6.063e+02 5.625e+02 5.188e+02 4.750e+02 4.313e+02 3.875e+02 3.438e+02 3.000e+02</p>
0.2			
0.4			
0.8			
1.6			

Table 34: DB266 temperature comparison sequence for 0.2mm mesh. β_{TAB}^* (left) vs. $\beta_{TAB,0.2}^*$ (right)





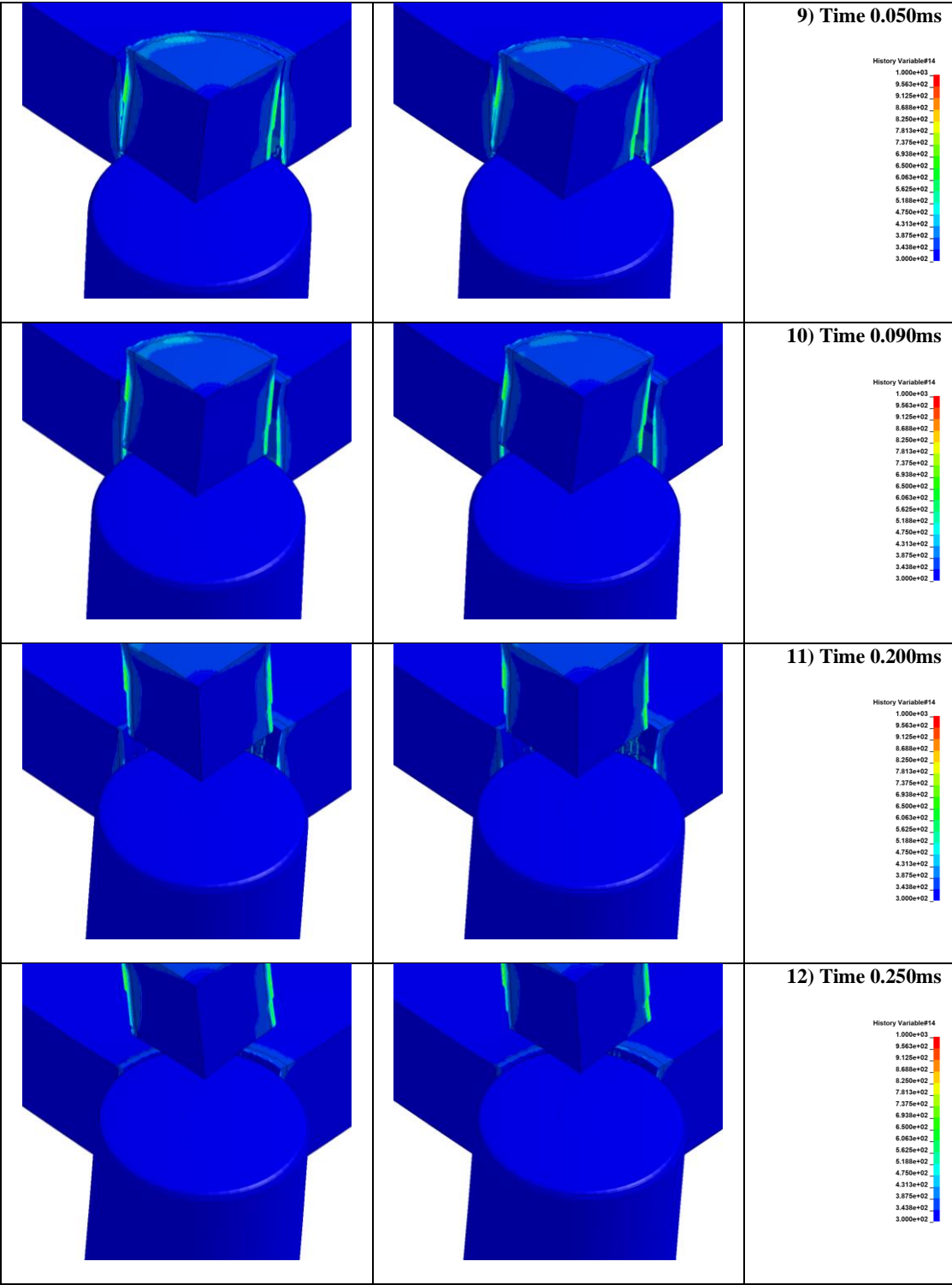
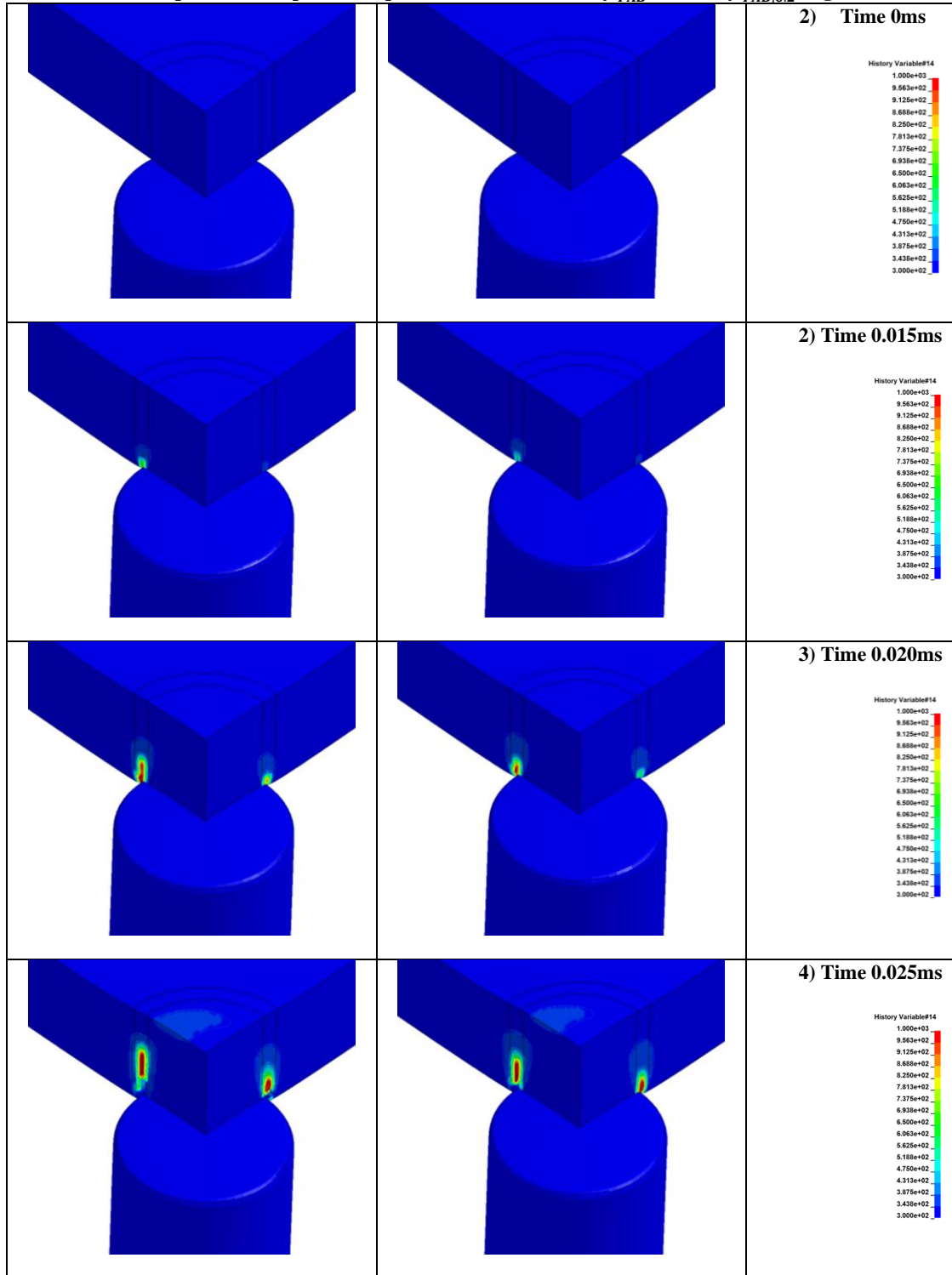
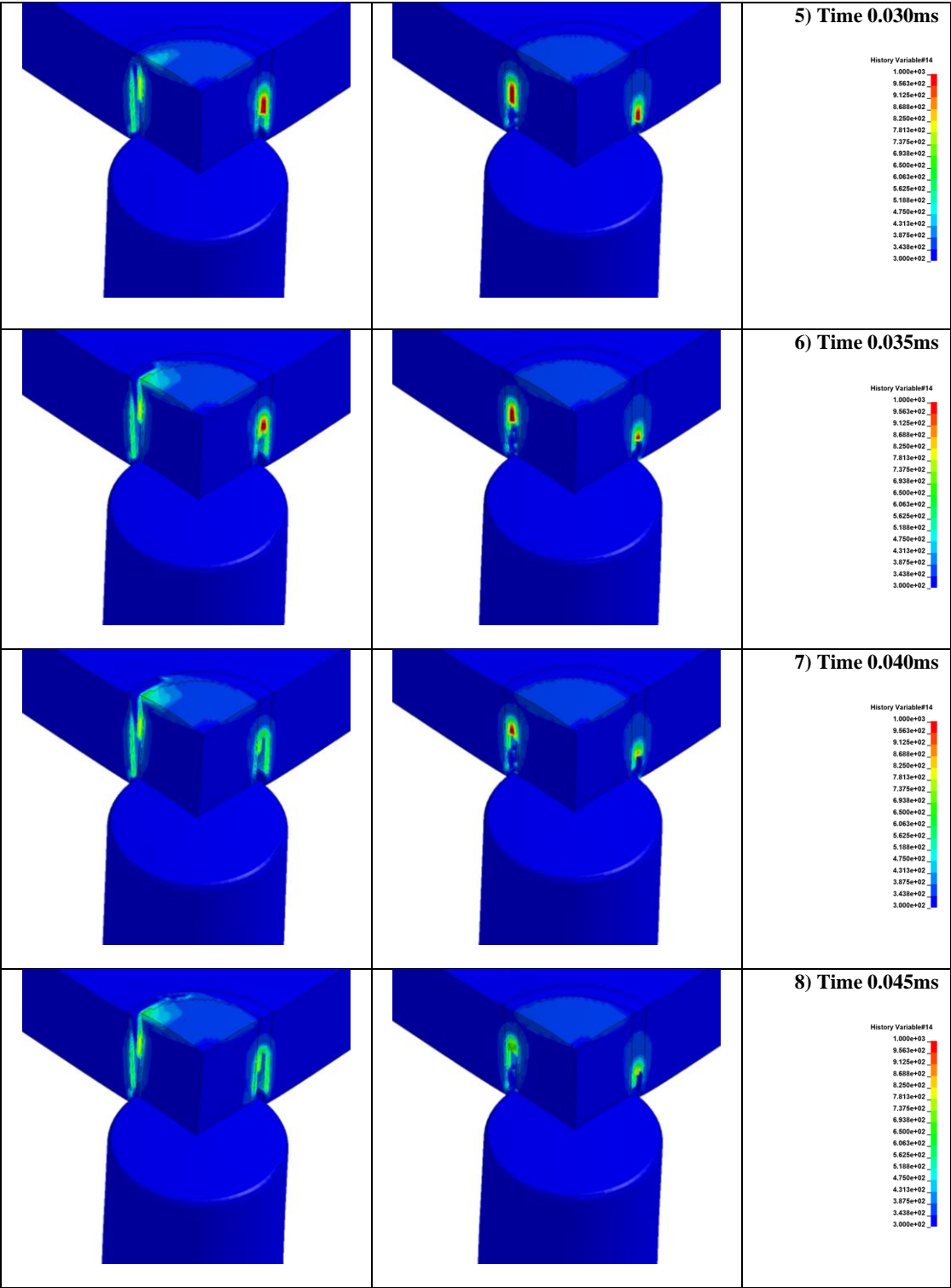


Table 35: DB266 temperature comparison sequence for 0.4mm mesh. β_{TAB}^* (left) vs. $\beta_{TAB,0.2}^*$ (right)





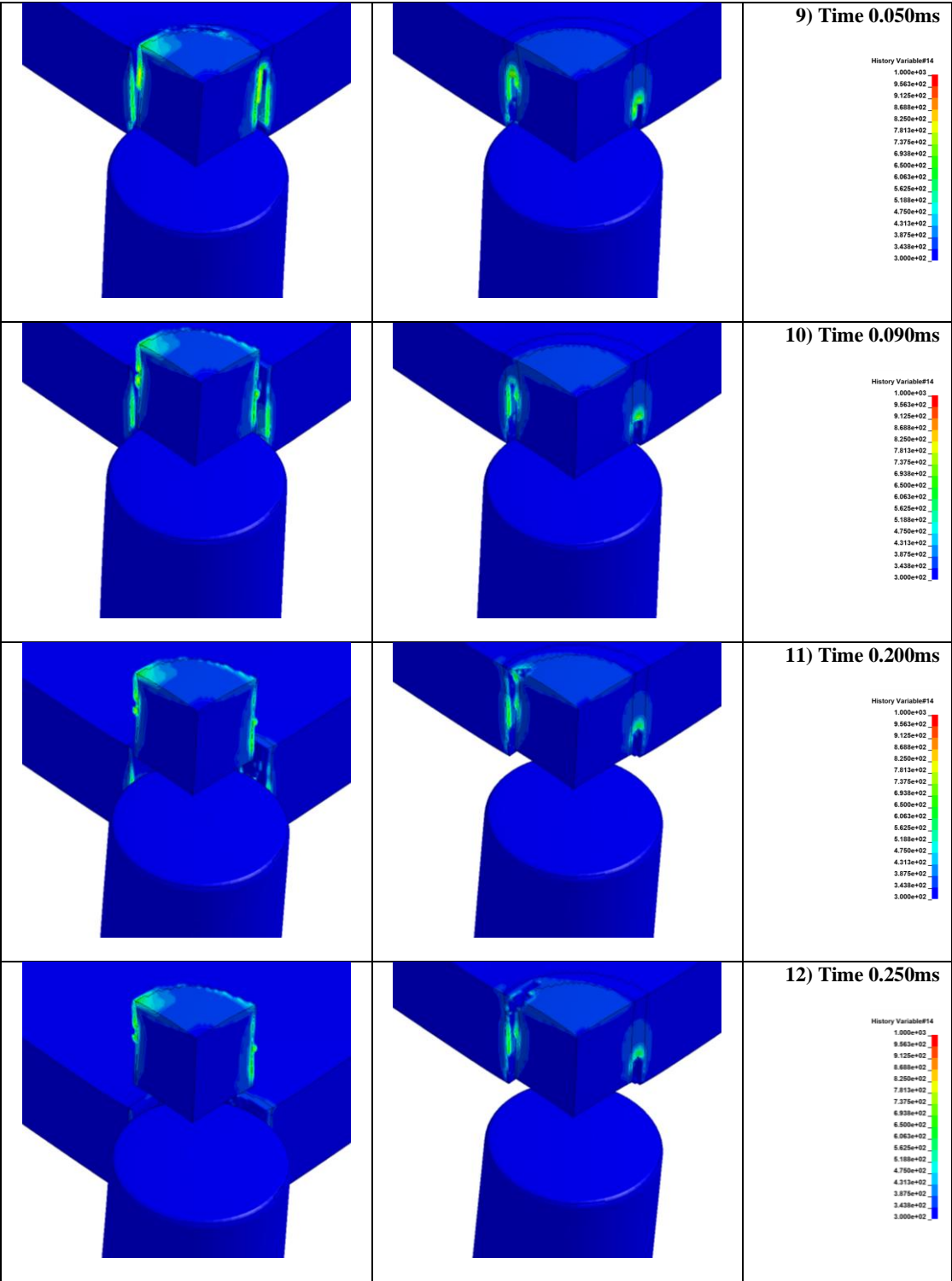
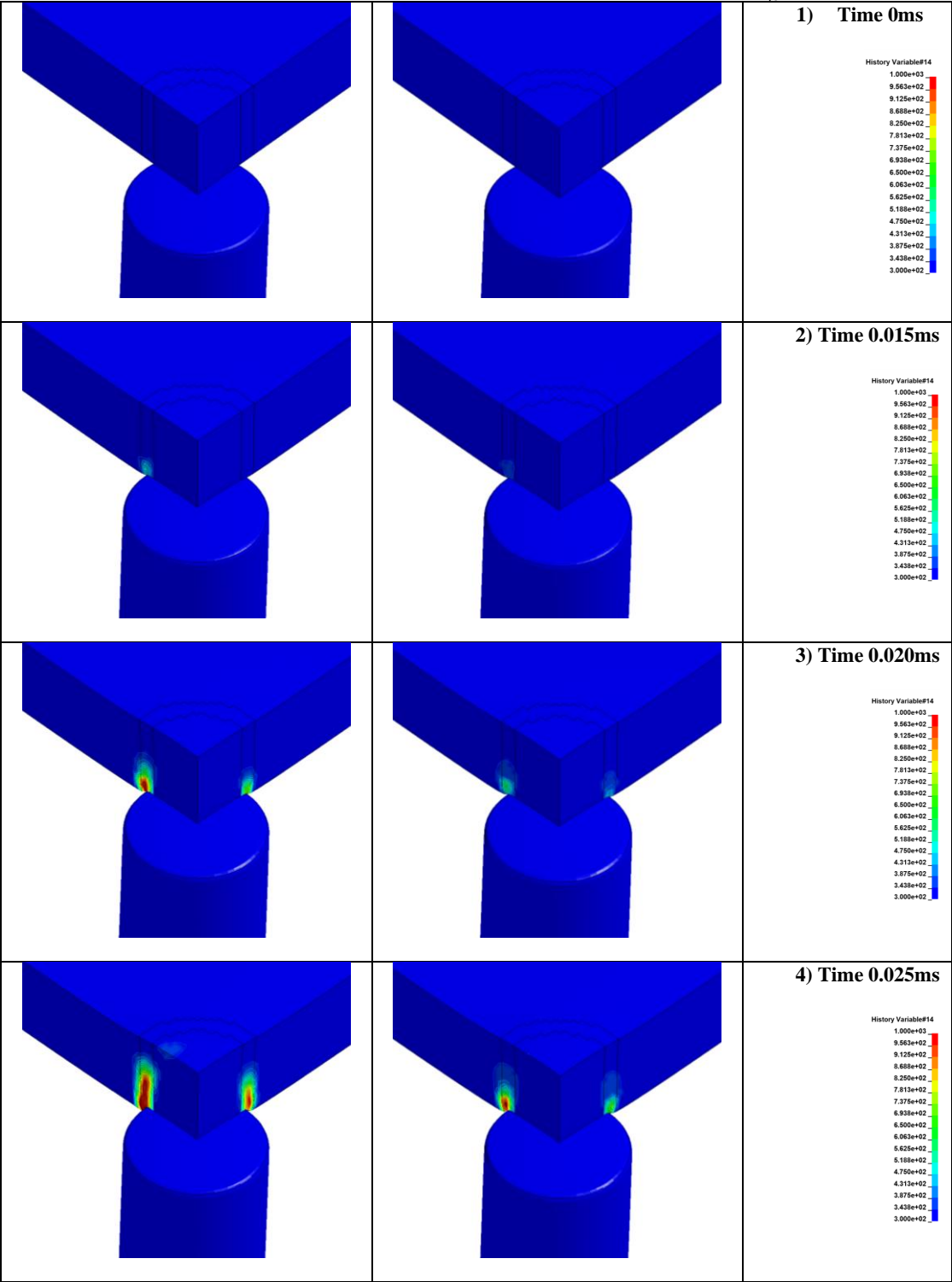
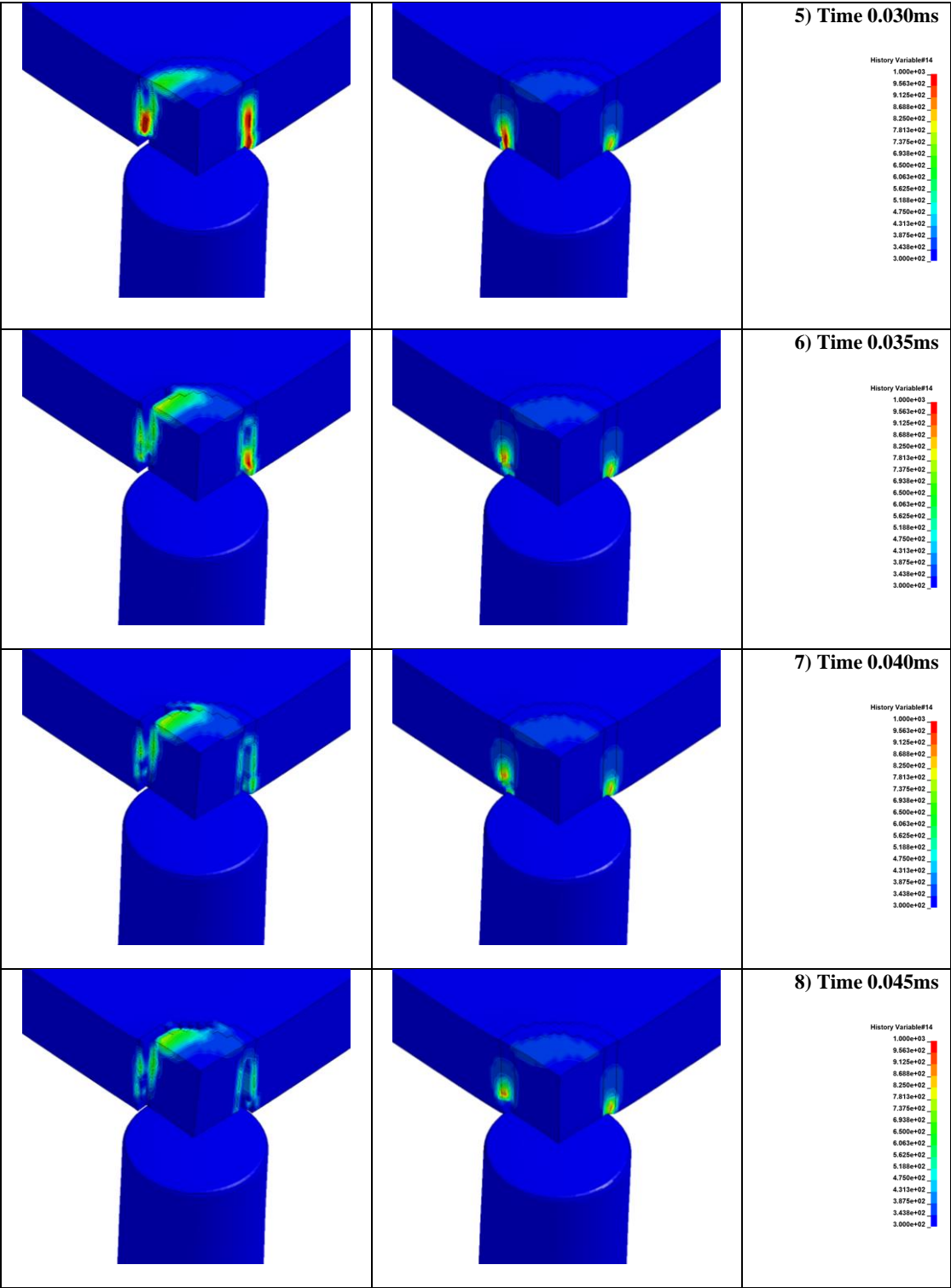


Table 36: DB266 temperature comparison sequence for 0.8mm mesh. β_{TAB}^* (left) vs. $\beta_{TAB,0.2}^*$ (right)





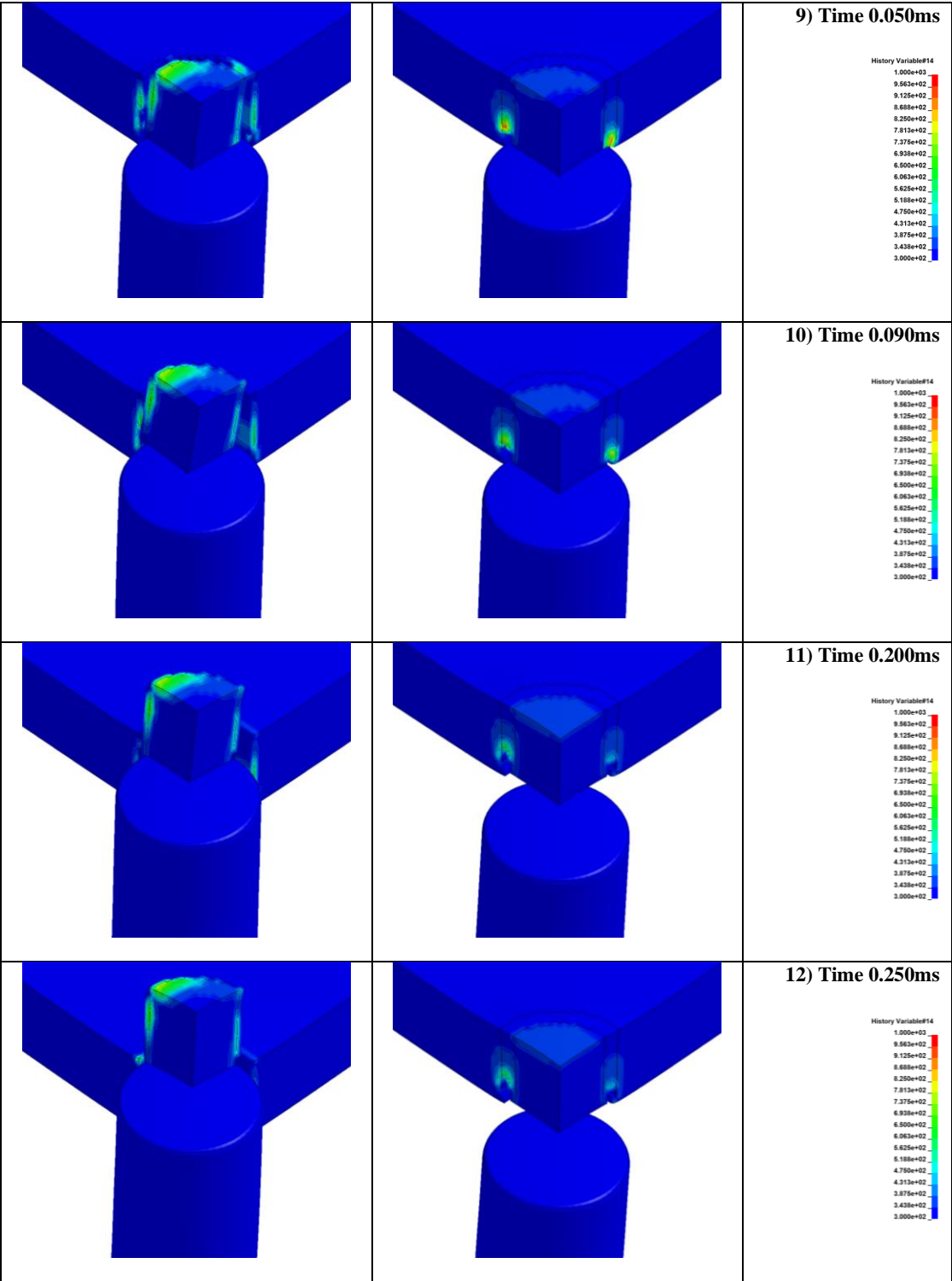
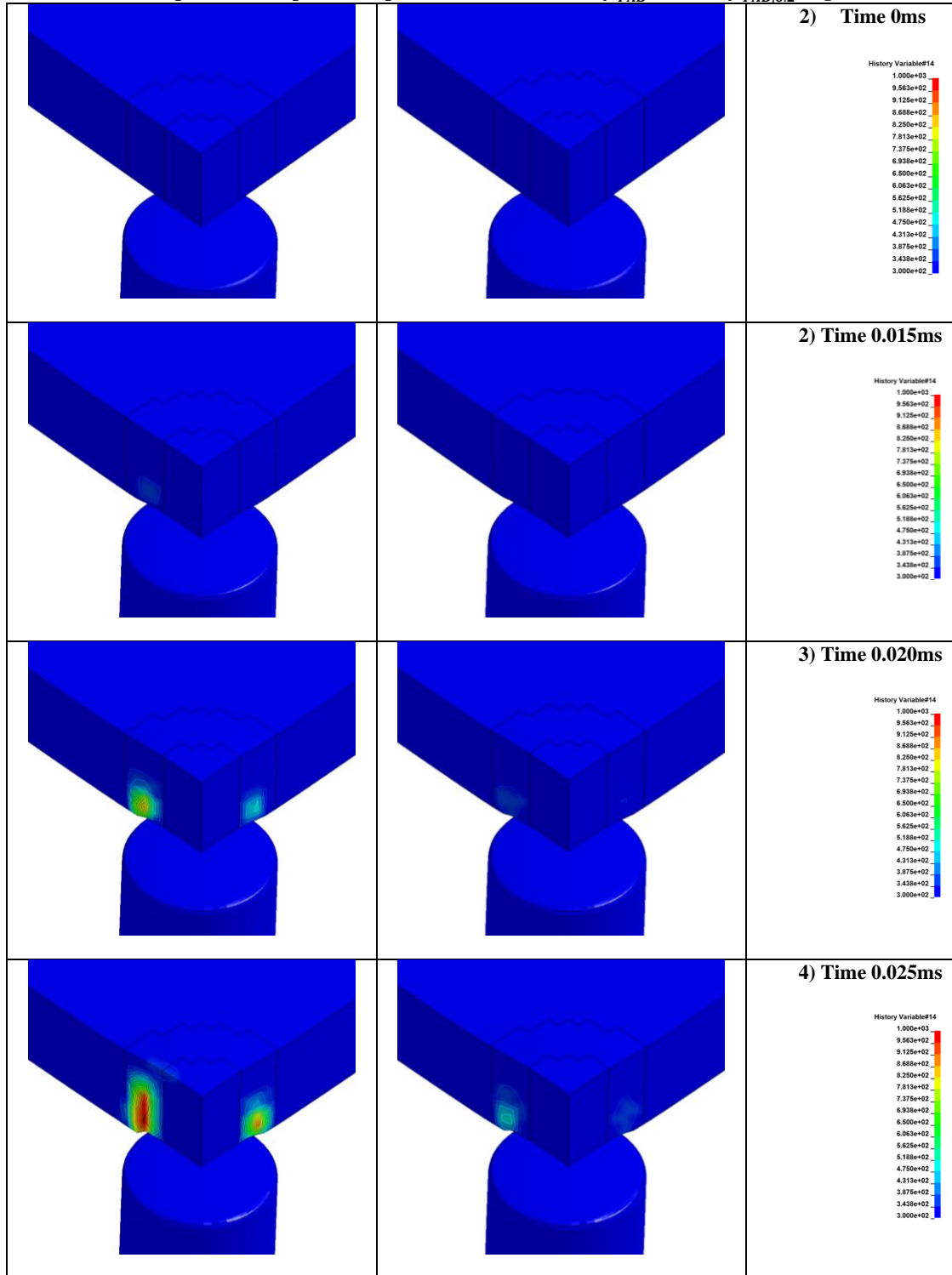
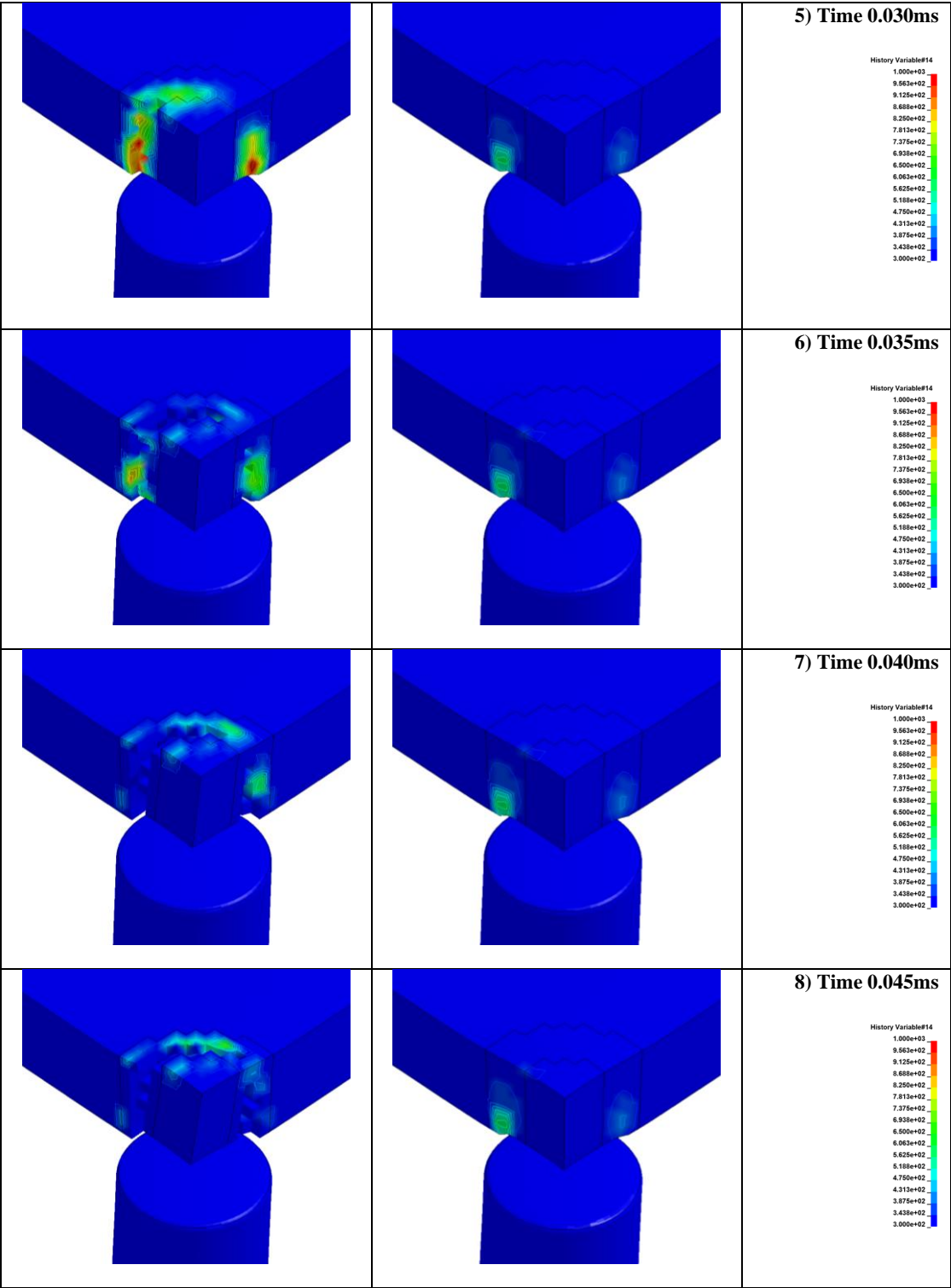
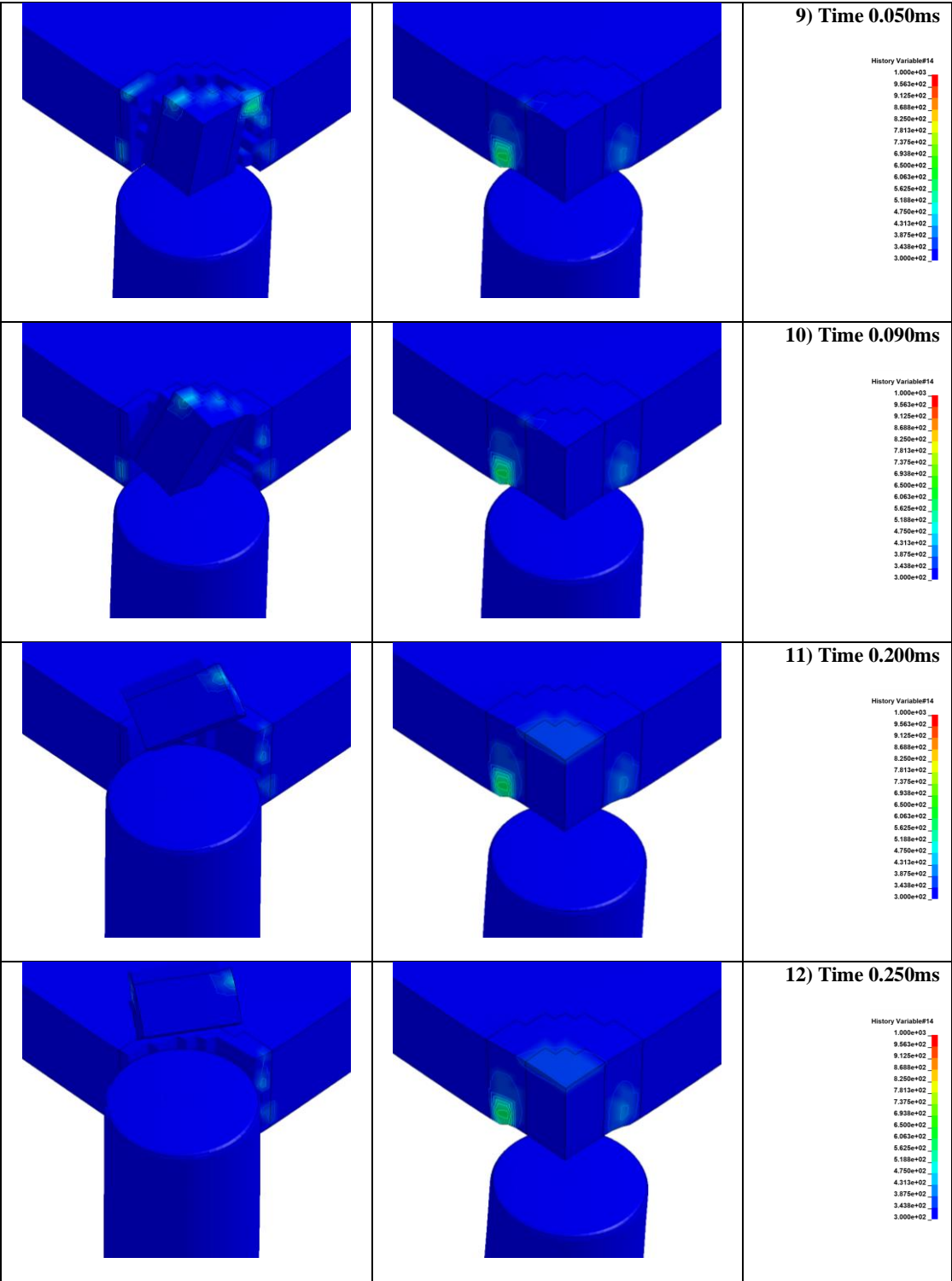


Table 37: DB266 temperature comparison sequence for 1.6mm mesh. β_{TAB}^* (left) vs. $\beta_{TAB,0.2}^*$ (right)







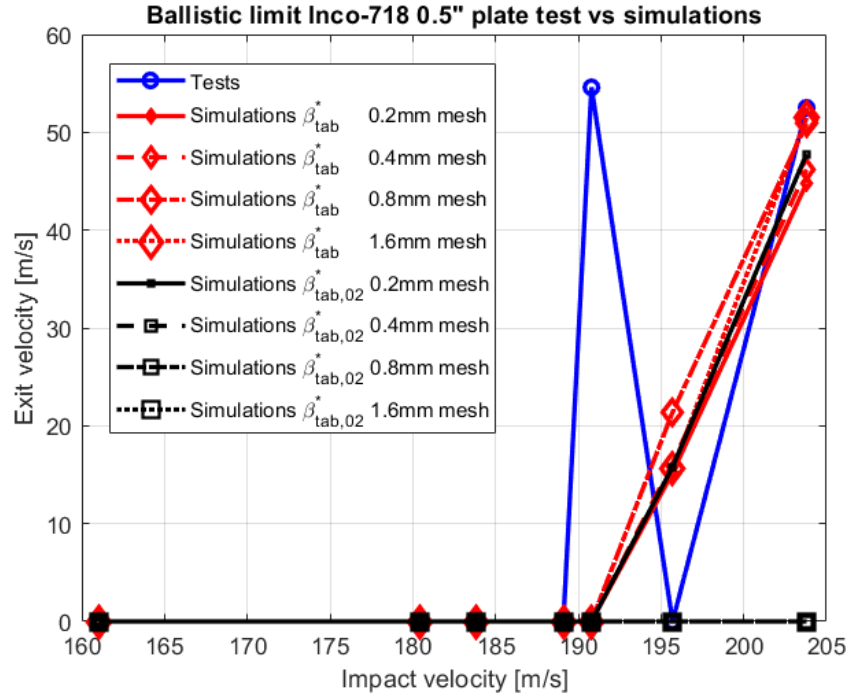


Figure 75: Ballistic limit simulations, β_{TAB}^* vs. $\beta_{TAB,0.2}^*$

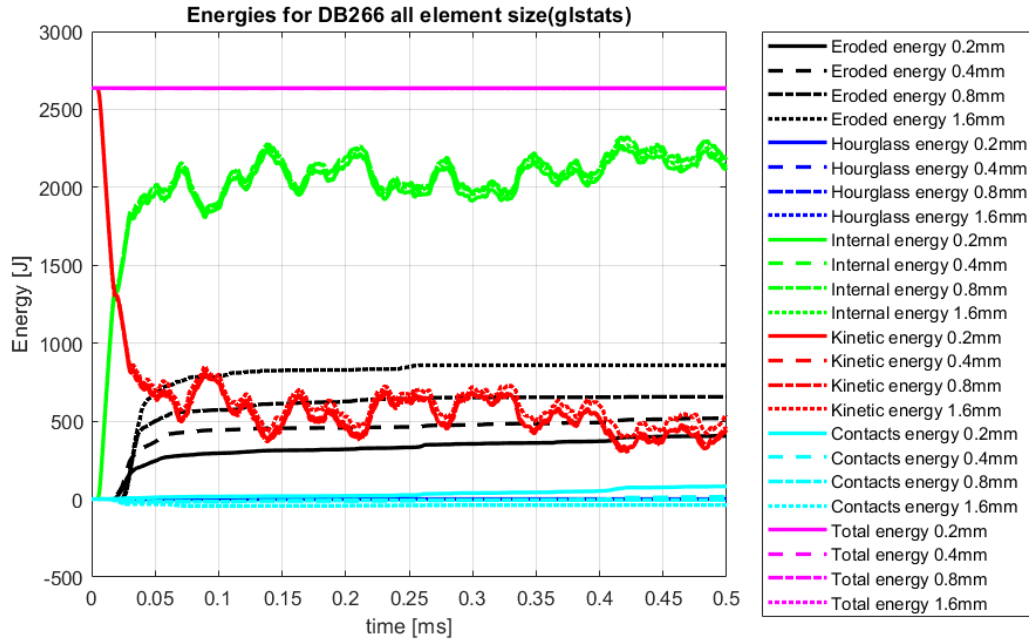


Figure 76: Energies for the simulations of test DB266

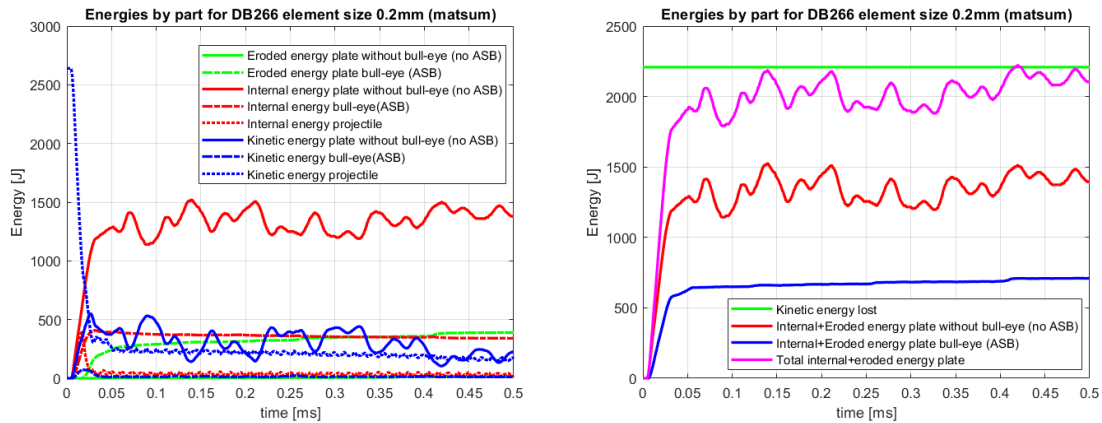


Figure 77: Energy by part for 0.2mm element size mesh of test DB266

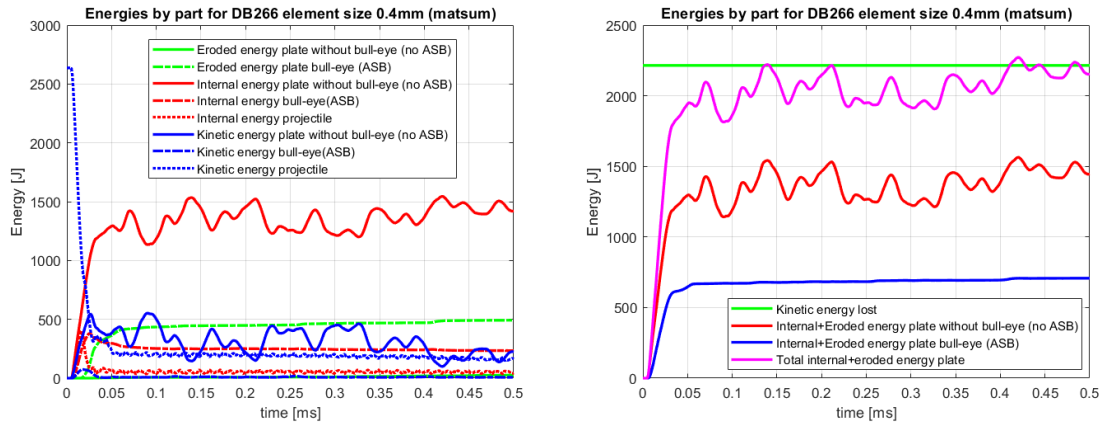


Figure 78: Energy by part for 0.4mm element size mesh of test DB266

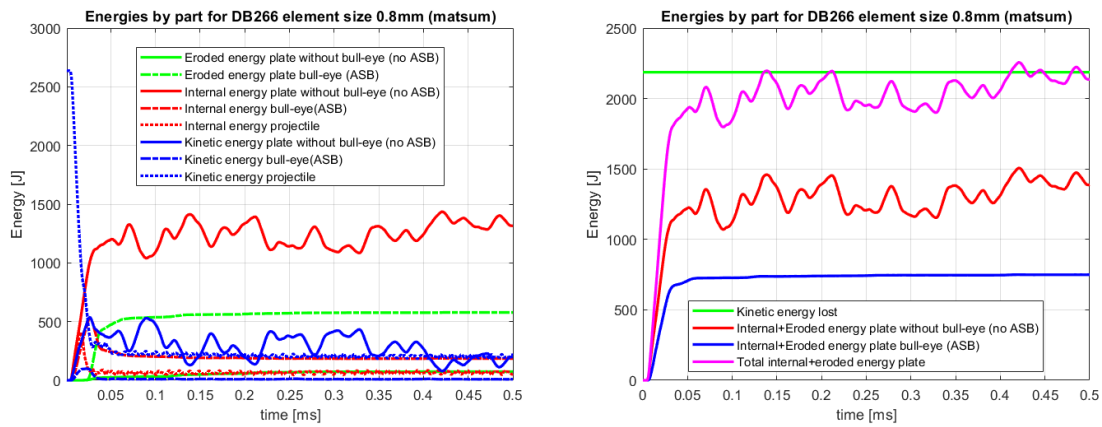


Figure 79: Energy by part for 0.8mm element size mesh of test DB266

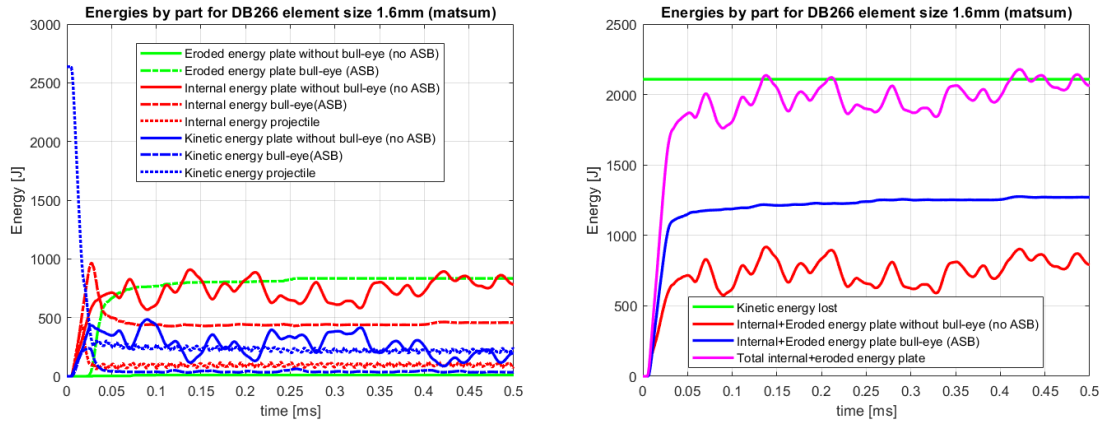


Figure 80: Energy by part for 1.6mm element size mesh of test DB266

7.4. Discussion

The simulations performed with various mesh sizes demonstrated that even with a tabulated TQC function in place, the modified tabulated J-C material model cannot capture the enucleation of the ASB without the implementation of a regularization function that modifies the TQC accounting for element size. It is evident that it becomes harder and harder to develop an ASB with the progressively increasing element size without a regularization of the tabulated TQC accounting for the element size. Furthermore, when a regularization function for the Taylor-Quinney coefficient is included in the material model the modified tabulated J-C material is performing consistently among a wide range of mesh element sizes and maintains its predictive capability across all meshes. The crack propagation speed across various meshes is fairly consistent for all the tests simulated and the temperature reached in the ASB is above 1200K in all the simulations that developed a plug.

From an energy perspective, it is crucial to note that not all the kinetic energy of the projectile goes in the adiabatic shear band. In the simulations that generated a free plug (DB266), the part of the plate not subjected to the ASB deformation absorbed most of the energy. This differs from the common assumption, made by Rosenberg and Dekel [124] amongst others, that the total energy in the ASB is equal to the sum of the kinetic energy lost by the projectile during the impact minus the kinetic energy of the plug (or in other words equal to the total deformation energy of the plate). As can be seen in Figure 77 to Figure 80 in the test DB266 simulations, it appears that about 2/3 of the energy is absorbed by the part of the plate that is not subject to ASB. The simulations performed do not rely on any simplifying assumption and they appear to be reliable; having constant total energy, no hourglass energy, reasonable contact energy (Figure 76) and being a good match to the tests. It can also be noted how the eroded energy increases with the mesh size, which is expected considering that larger elements have been eroded.

8. CONCLUSIONS

This research has produced an improved computational material model for simulating dynamic solid mechanics problems. This model is helpful to the engineering community because of the lack of material models in finite element codes (such as LS-DYNA[®]) with the capability of simulating ASB enucleation using a mesh with element size relevant to practical applications. As of recent, to simulate an ASB in a metal alloy in finite element codes, engineers were forced to use incredibly small elements, and therefore the models could not represent a real structure. In contrast, this material model has been developed for use in dynamic impact or crash simulations of actual structures, while including the generation of material and thermal instabilities. The objective of this research was to design a material subroutine within an existing finite element code that can allow for the simulation of ASB in metal alloys with an industrial size mesh. This means that the material exhibits different behavior under the same deformation depending on the strain rate and the maximum shear stress, and this dependency is regularized for the element size.

The formulation of this model is based on the Johnson-Cook and Tabulated Johnson-Cook material models that incorporate both strain rate and temperature dependency. Additionally, the material conserves the peculiarities of the original tabulated J-C. This means that the flow stress can be provided directly from test data as a

function of the plastic strain. This is different than most existing material models that have limited flexibility of defining the flow stress. For a given strain rate, an input yield curve is provided. Thermal softening is also incorporated into this material model. In this model, the strain rate effects, thermal effects, stress flow, and finally TQC are tabulated allowing for a precise definition of all the physical characteristics of the material. This method allows the user to have more control over the material response and therefore more accurate results will be generated.

First, the original material was characterized using an extensive methodology with a focus on high strain rate and temperature characteristics. Failure surface properties were also characterized using an extensive set of tests.

2D simulations were performed to prove that ASB simulations were achievable using the J-C material model if the element size is small enough to capture the strain localization typical of the ASB phenomenon. A modified J-C material model was then developed using a new tabulated TQC as a function of strain rate, maximum shear strain, and element size to simulate the sudden and extreme change in temperature that happens in ASBs.

The theory behind the new material model was implemented using FORTRAN programming language and used in conjunction with the LS-DYNA[®] finite element code. This research provides a full overview of the original and modified material routine in the form of a flow chart.

Single element simulations were used to verify the material model.

2D simulations were used to verify that the modified material is capable of predicting ASB using a mesh size where the original material model would not produce an ASB. This verification step shows that the material model can reproduce structural instabilities even if the mesh size is too large to capture the localization causing it.

The modified material model was then tested with a large finite element model to prove its enhanced predictive capabilities. A finite element model was created to simulate a high velocity impact between a cylindrical projectile and a 0.5-inch Inconel plate. Strain rate and temperature effects of the plate's material were determined, and a full implementation of the material model was generated.

The impact was simulated and compared to the original J-C material model with the same input parameters with the exception of the enhanced TQC. The results show that the new material model is able to accurately replicate the physics of the ASB and therefore of the impact, where the original tabulated J-C failed.

Lastly, a regularization for TQC based on mesh size was developed. Results show that even with the tabulated TQC, only with a regularization for the element size can the larger meshes replicate the physics of the impact.

It is recommended that more research be completed on superalloys ASBs. For example, while this model catches the temperature raise in the ASB allowing the material to achieve extreme strain localizations, it does not account directly for the microstructural changes in the ASB that cause the temperature raise. Furthermore, the same improvements developed in this work and applied to the tabulated J-C material model

could be applied to the anisotropic tabulated J-C material model (*_MAT_264) to define the material behavior and failure more accurately as a function of material direction.

APPENDIX

Appendix A.

The MatLab script shown as Code A.1, allows to compute the required tabulated Taylor-Quinney coefficient input for the modified material model for a given mesh size. The complete tabulated input will be saved as a *.k file that can be included in the LS-DYNA[®] input deck.

Code A.1: MatLab script to compute the tabulated Taylor-Quinney coefficient

and generate related input deck.

```

%%%%%%%%%%%%%%%%%%%%%%%%%%%%%%%%%%%%%%%%%%%%%%%%%%%%%%%%%%%%%%%%%%%%%%%%
%   Center for Collision Safety and Analysis (CCSA)   %
%   George Mason University (GMU)                   %
%   Federal Aviation Administration (FAA)             %
%   Inco718      Material Modeling                   %
%   Stefano Dolci                                     %
%   Table_XD *.k file Generation                     %
%%%%%%%%%%%%%%%%%%%%%%%%%%%%%%%%%%%%%%%%%%%%%%%%%%%%%%%%%%%%%%%%%%%%%%%%
clear all; clc; close all; format long
%% Initialize
[fname,answer,B]=datainput(); % data input
[~,c]=size(answer);A=cell(c,2);d=68000;
%sfa=1.0;
%offa=0.00125;
%% Calculate curves
for i=1:c
    %calculating hyperbolic tangents
    [A]=calc_hyptag(i,answer,B,A);
end
% creating all the curves
ii=1;
for i=1:c
    j=1;
        xy{i,1}(j)=A{i,1}(1);xy{i,2}(j)=A{i,2}(1);
        j=j+1;
        for ii=2: length(A{i,1})-1
            if A{i,2}(ii)==A{i,2}(ii-1) && A{i,2}(ii)~=A{i,2}(ii+1) && A{i
,2}(ii)== A{i,2}(1) %if isequal than previous and initial and different than
next and
                xy{i,1}(j)=A{i,1}(ii);xy{i,2}(j)=A{i,2}(ii);
                j=j+1;
            elseif A{i,2}(ii)~= A{i,2}(ii-1) % if different than
previous
                xy{i,1}(j)=A{i,1}(ii);xy{i,2}(j)=A{i,2}(ii);
                j=j+1;
            end
        end
        xy{i,1}(j)=A{i,1}(end);xy{i,2}(j)=A{i,2}(end);
        nn(i)=j;N=prod(nn(1:end-1));
    end
%% Create Keyword File
[C]=nuovo_file(fname);
Keyword = fopen(C,'w+t');j=1;k=1;l=1;newlength=1;f=1;
    for i=c:-1:1
fprintf(Keyword,'%s\n','$$$$$$$$$$$$$$$$$$$$$$$$$$$$$$$$$$$$$$$$$$$$
$$$$');
        for jj=1:newlength
            f=f+1;
            if i~=1% if is a table
                stringa=strcat('*DEFINE_TABLE_',num2str(i),'D');
                fprintf(Keyword,'%s\n',stringa);
                stringa=char(strcat('$',{' '},answer{2,i}));
                fprintf(Keyword,'%s\n',stringa);
            end
        end
    end

```

```

        stringa='$#      tbid      sfa      offa';
        fprintf(Keyword,'%s\n',stringa);
    else% if is a curve
        stringa='*DEFINE_CURVE';
        fprintf(Keyword,'%s\n',stringa);
        stringa=char(strcat('$ ',{' '},answer{2,i}));
        fprintf(Keyword,'%s\n',stringa);
        stringa='$#      cid';
        fprintf(Keyword,'%s\n',stringa);
    end
    if i==c
%        fprintf(Keyword,'%10.0f%10.0f%10.6f\n',6701,sfa,offa);
        fprintf(Keyword,'%10.0f\n',6701);

    else
        fprintf(Keyword,'%10.0f\n',d+j);
        j=j+1;
    end
    if i~=1% if is a table
        stringa='$          value          lcid';
    else% if is a curve
        stringa='$          absc          ord';
    end
    fprintf(Keyword,'%s\n',stringa);
    for ii=1:length(xy{i,1})
        dk=d+k;
        beta(k,1:2)=[dk,xy{i,2,1}(ii)];
        if i==c
            fprintf(Keyword,'%20.10f%20.0f\n',xy{i,1}(ii),dk);
        else
            bb(ii,1)=xy{i,1}(ii);
            if beta(j-1,2) ==B(1)
                beta(k,2)=B(1);
                bb(ii,2)=beta(k,2);
            elseif beta(j-1,2) ~=B(1)
                if i~=1 % if is not a curve
                    per=(beta(j-1,2)-B(1))/(xy{i,2}(length(xy{i,
1}))) -B(1));

                    beta(k,2)=( (beta(k,2)-B(1)) *per+B(1);
                    bb(ii,2)=beta(k,2);
                else
                    beta(k,2)=beta(j-1,2);
                    bb(ii,2)=beta(k,2);
                end
            end
            if i~=1
                fprintf(Keyword,'%20.10f%20.0f\n',xy{i,1}(ii),dk);
            else
                fprintf(Keyword,'%20.10f%20.5f\n',xy{i,1}(ii),beta(
k,2));
            end
        end
        k=k+1;
    end
end
newlength=prod(nn(1:1));
last_ID=dk-newlength;
l=l+1;
end

```

```

fprintf(Keyword,'%s\n','*END');
fclose(Keyword);d,'%s\n',stringa);
function [fname,answer,B]=datainput()
prompt = {'name'};
dlg_title = 'Table NAME';
num_lines = 1;
name='BetaTable';
def = {name};
answ= inputdlg(prompt,dlg_title,num_lines,def);
fname=strcat(answ{1},'.k');

prompt = {'Beta min','Beta Max'};
dlg_title = 'Beta';
num_lines = 1;
bmin='0.8';
bmax='10';
def = {bmin,bmax};
ansr= inputdlg(prompt,dlg_title,num_lines,def);
B=[str2double(ansr{1});str2double(ansr{2})];

C1=menu('Table dimension','curve','2','3');
for i =1:C1
    prompt = {'dimension','title','transition@','range min','range max'};
    dlg_title = 'Table';
    num_lines = 1;
    switch i
        case 1
            des='Plastic strain';
            tra='0.45';
            min='0';
            max='0.9';
        case 2
            des='SR';
            tra='8';
            min='0';
            max='25';
        case 3
            des='Max shear strain';
            tra='0.25';
            min='0';
            max='0.5';
            min=' ';
            max=' ';
    end
    if max==' '
        warning('Parameters not assigned')
    end
    def = {num2str(i),des,tra,min,max};
    answer(1:5,i)= inputdlg(prompt,dlg_title,num_lines,def);
end

function [A]=calc_hyptag(n,answer,B,A)
x1=str2double(answer(4,n));%min
x2=str2double(answer(5,n));%max
x3=str2double(answer(3,n));%trans

% calculate hyperbolic tangent based based on range and gradient

```

```

a=(B(2)-B(1))/2;
b=B(2)-a;
h=howmanydec(x3); %order of magnitude
c=10^h; %steepness
d=1/(9*c); %points density
x=x1:d:x2;
steepness=5*c;
th=round(b+a*tanh(steepness*(x-x3)),4);

A{n,1}=x;
A{n,2}=th;
figure()
plot(x,th, '.')
title(strcat('\beta vs.',answer(2,n)));
xlabel(answer(2,n))
ylabel('\beta')
grid on

function [C]=nuovo_file(fname)
[B, indirizzo] = uinputfile(fname, '.k file name');
C=fullfile(indirizzo,B);

```

Appendix B.

The MatLab script shown as Code A.2, allows to compute the required tabulated Taylor-Quinney coefficient input for the modified material model regularized for a range of mesh sizes. The complete tabulated input will be saved as a *.k file that can be included in the LS-DYNA.

Code A.2: MatLab script to compute the tabulated Taylor-Quinney coefficient

and generate the related input deck with mesh size regularization.

```

%%%%%%%%%%%%%%%%%%%%%%%%%%%%%%%%%%%%%%%%%%%%%%%%%%%%%%%%%%%%%%%%%%%%%%%%
%   Center for Collision Safety and Analysis (CCSA)   %
%   George Mason University (GMU)                   %
%   Federal Aviation Administration (FAA)             %
%   Inco718      Material Modeling                   %
%   Stefano Dolci                                     %
%   Table_3D regularized *.k file Generation          %
%%%%%%%%%%%%%%%%%%%%%%%%%%%%%%%%%%%%%%%%%%%%%%%%%%%%%%%%%%%%%%%%%%%%%%%%
clear all; clc; close all;
%% Initialize
mesh=[0.2,0.4,0.8,1.6];
[fname,answer]=datainput2(mesh);% data input
[r,c,p]=size(answer);A=cell(c-1,2,p);d=68000;

%% Calculate curves
% regularization curves
for i=1:p
    B(i,1:2)=[str2double(answer{4,1,i});str2double(answer{5,1,i})];
    for j=1:2
        %calculating hyperbolic tangents
        A=calc_hyptag2(i,j,answer,B(i,1:2),A);
    end
end
% creating all the curves

%% next is done to reduce the size of the output file selecting only the signi
ficant point for each mesh size/ variable
for i=1:p
    for j=1:c-1
        jj=1;ii=1;
        xy{j,1,i}(jj)=A{j,1,i}(ii);xy{j,2,i}(jj)=A{j,2,i}(ii);
        jj=jj+1;
        for ii=2:length(A{j,1,i})-1
            if A{j,2,i}(ii)==A{j,2,i}(ii-1) && A{j,2,i}(ii)~=A{j,2,i}(ii+1) &
& A{j,2,i}(ii)== A{j,2,i}(1) %if isequal than previous and initial and differ
ent than next and
                xy{j,1,i}(jj)=A{j,1,i}(ii);xy{j,2,i}(jj)=A{j,2,i}(ii);
                jj=jj+1;
            elseif A{j,2,i}(ii)~= A{j,2,i}(ii-1)% if different than previous
                xy{j,1,i}(jj)=A{j,1,i}(ii);xy{j,2,i}(jj)=A{j,2,i}(ii);
                jj=jj+1;
            end
        end
        xy{j,1,i}(jj)=A{j,1,i}(end);xy{j,2,i}(jj)=A{j,2,i}(end);
    end
end
end

```



```

%% find the x to be used based on the regularization
% I put together the reduced set for all the mesh sizes in each variable for
consistency
% first I identify which are the points
X={};jj=1;
    for i=1:p
        for j=1:c-1
            for ii=1:length(xy{j,1,i})
                X{j}(jj)=xy{j,1,i}(ii);
                jj=jj+1;
            end
        end
    end
for j=1:c-1
    for ii=1:length(X{j})
        X{j}(ii)=round(X{j}(ii),4);
    end
    X{j}=sort(X{j});
    X{j}=unique(X{j});
end
%%%%%%%%%%%%%%%%%%%%%%%%%%%%%%%%%%%%%%%%%%%%%%%%%%%%%%%%%%%%%%%%%%%%%%%%
% then I recreate each set using the points from all the others
clear xy
    for i=1:p
        for j=1:c-1
            clear x xx
            x=X(j);
            jj=1;ii=1;
            for ii=1:length(A{j,1,i})
                if ismember(A{j,1,i}(ii),X{j})%if x point is a member of the
array of significant points I keep it
                    xy{j,1,i}(jj)=A{j,1,i}(ii);xy{j,2,i}(jj)=A{j,2,i}(ii);
                    jj=jj+1;
                end
            end
            if A{j,1,i}(end)~=X{j}(end) % if the current array max(x) is less
than max(x) i fill up the rest
                [Lid,Loc]=ismember(A{j,1,i}(end),X{j});
                for ii=Loc+1:length(X{j})
                    xy{j,1,i}(jj)=X{j}(ii);xy{j,2,i}(jj)=A{j,2,i}(end);
                    jj=jj+1;
                end
            end
        end
    end
end
nn=[length(xy{2,1,1}),length(xy{1,1,1}),p];

```



```

per=(beta(j-1,w+1)-B(w,1))/(xy{kk,2,w}(length(xy{kk,1,w}))-B(w,1));
beta(k,w+1)=(beta(k,w+1)-B(w,1))*per+B(w,1);
    end
end
end
if i~=1% if is not a curve
    fprintf(Keyword,'%20.5f%20.0f\n',xy{kk,1,1}(ii),dk);
    k=k+1;
else
    fprintf(Keyword,'%20.5f%20.5f\n',0,beta(j-1,2));
    k=k+1;
    for w=1:p
        dk=d+k;
        fprintf(Keyword,'%20.5f%20.5f\n',str2double(answer{3,1,w}),beta(j-1,w+1));
        k=k+1;
    end
    fprintf(Keyword,'%20.5f%20.5f\n',2,beta(j-1,5));
    k=k+1;
end
end
end
newlength=prod(nn(1:l));
last_ID=dk-newlength;
l=l+1;
end
fprintf(Keyword,'%s\n','*END');
fclose(Keyword);

function [fname,answer]=datainput2(mesh)
prompt = {'name'};options.Resize='on';
dlg_title = 'Table NAME';
num_lines = [1 50];
name='BetaTable';
def = {name};
answ= inputdlg(prompt,dlg_title,num_lines,def);
fname=strcat(answ{1},'.k');

for ii=1:length(mesh)
for i =1:3

switch i
case 1
    prompt = {'dimension','title','mesh size','Beta min','Beta max'};options.Resize='on';
    dlg_title = 'Table';
    num_lines = [1 50];
    des='Mesh';
    tra=num2str(mesh(ii));
    min='0.8';

```

```

        switch ii
            case 1
                max='10';
            case 2
                max='12.5';
            case 3
                max='13';
            case 4
                max='23';
        end
    case 2
        prompt = {'dimension','title','transition@','range min','range max'}
        ;options.Resize='on';
        dlg_title = num2str(mesh(ii));
        num_lines = [1 50];
        des='SR';
        tra='8';
        min='0';
        max='25';
    case 3
        prompt = {'dimension','title','transition@','range min','range max'}
        ;options.Resize='on';
        dlg_title = num2str(mesh(ii));
        num_lines = [1 50];
        des='Max shear strain';
        switch ii
            case 1
                tra='0.25';
                min='0';
                max='0.5';
            case 2
                tra='0.23';
                min='0';
                max='0.46';
            case 3
                tra='0.18';
                min='0';
                max='0.36';
            case 4
                tra='0.15';
                min='0';
                max='0.3';
        end
    end

    def = {num2str(i),des,tra,min,max};
    answer(1:5,i,ii)= inputdlg(prompt,dlg_title,num_lines,def);
end
end

```

```

function [A]=calc_hyptag2(n,j,answer,B,A)
x1=str2double(answer(4,j+1,n));%min
x2=str2double(answer(5,j+1,n));%max
x3=str2double(answer(3,j+1,n));%trans

% calculate hyperbolic tangent based on range and gradient
a=(B(2)-B(1))/2;
b=B(2)-a;
h=howmanydec(x3); % order of magnitude
c=10^h;%steepness
d=1/(9*c); % points density

x=x1:d:x2;
steepness=5*c;%5*c;
th=round(b+a*tanh(steepness*(x-x3)),4);

A{j,1,n}=round(x,4);
A{j,2,n}=th;
figure()
plot(x,th,'.')
title(strcat('\beta vs.',answer(2,j+1,n),{' '},'Mesh',answer(3,1,n)))
;
xlabel(answer(2,j+1,n))
ylabel('\beta')
grid on

```

Appendix C.

Tabulated Taylor-Quinney coefficient example input for the modified material model.

This is a simplified tabulated TQC intended only for the purpose of providing an example of the input tables structure.


```

*DEFINE_CURVE
$ element size
$#      cid      sfa      offa
      6301
$          absc          ord
          0.001          8e-01
          0.200          8e-01
          0.400          8e-01

*DEFINE_CURVE
$ element size
$#      cid      sfa      offa
      6302
$          absc          ord
          0.001          8e-01
          0.200          8e-01
          0.400          8e-01

*DEFINE_CURVE
$ element size
$#      cid      sfa      offa
      6303
$          absc          ord
          0.001          9e-01
          0.200          9e-01
          0.400          9e-01

*DEFINE_CURVE
$ element size
$#      cid      sfa      offa
      6304
$          absc          ord
          0.001          9e-01
          0.200          9e-01
          0.400          9e-01

*DEFINE_CURVE
$ element size
$#      cid      sfa      offa
      6305
$          absc          ord
          0.001          8e-01
          0.200          8e-01
          0.400          8e-01

*DEFINE_CURVE
$ element size
$#      cid      sfa      offa
      6306
$          absc          ord
          0.001          9e-01
          0.200          9e-01
          0.400          9e-01

*DEFINE_CURVE
$ element size
$#      cid      sfa      offa
      6307
$          absc          ord
          0.001          9e-01
          0.200          9.000
          0.400          9.000

```

```

*DEFINE_CURVE
$ element size
$#      cid      sfa      offa
      6308
$          absc          ord
          0.001          9e-01
          0.200          10
          0.400          10

*DEFINE_CURVE
$ element size
$#      cid      sfa      offa
      6309
$          absc          ord
          0.001          8e-01
          0.200          8e-01
          0.400          8e-01

*DEFINE_CURVE
$ element size
$#      cid      sfa      offa
      6310
$          absc          ord
          0.001          9e-01
          0.200          9e-01
          0.400          9e-01

*DEFINE_CURVE
$ element size
$#      cid      sfa      offa
      6311
$          absc          ord
          0.001          2
          0.200          10
          0.400          10

*DEFINE_CURVE
$ element size
$#      cid      sfa      offa
      6312
$          absc          ord
          0.001          3
          0.200          12
          0.400          15

*END

```

Appendix D.

Tabulated Taylor-Quinney coefficient input for the modified material model. This is a test tabulated TQC intended only for the purpose of developing an ASB in the 2D simulation presented in paragraph 5.4.

202

203

```

*DEFINE_CURVE
$ Element Length
$#      cid      sfa      offa
      6304
$      cabsc      cord
      1.000e-04      8e-01
      1.500e-03      9e-01
      4.000e-03      5
      2.000e-02      10.
      2.000e-01      15
      3.000      15
*END

```

REFERENCES

- [1] “Four Recent Uncontained Engine Failure Events Prompt NTSB to Issue Urgent Safety Recommendations to FAA.” https://www.nts.gov/news/press-releases/Pages/Four_Recent_Uncontained_Engine_Failure_Events_Prompt_NTSB_to_Issue_Urgent_Safety_Recommendations_to_FAA.aspx (accessed Oct. 19, 2018).
- [2] C.E. Franeknberger, III, “Large Engine Uncontained Debris Analysis.” Federal Airways Administration, May 1999.
- [3] “2nd TECHNICAL REPORT on Propulsion System and Auxiliary Power Unit (APU) Related Aircraft Safety Hazards.” Jan. 31, 2005.
- [4] “American Airlines Flight 383 (2016),” *Wikipedia*. Sep. 27, 2018. Accessed: Oct. 19, 2018. [Online]. Available: [https://en.wikipedia.org/w/index.php?title=American_Airlines_Flight_383_\(2016\)&oldid=861485315](https://en.wikipedia.org/w/index.php?title=American_Airlines_Flight_383_(2016)&oldid=861485315)
- [5] “Air France Flight 66,” *Wikipedia*. Sep. 28, 2018. Accessed: Oct. 19, 2018. [Online]. Available: https://en.wikipedia.org/w/index.php?title=Air_France_Flight_66&oldid=861532281
- [6] “Southwest Airlines Flight 1380,” *Wikipedia*. Oct. 05, 2018. Accessed: Oct. 19, 2018. [Online]. Available: https://en.wikipedia.org/w/index.php?title=Southwest_Airlines_Flight_1380&oldid=862624267
- [7] “United Airlines Flight 328,” *Wikipedia*. Feb. 22, 2021. Accessed: Feb. 22, 2021. [Online]. Available: https://en.wikipedia.org/w/index.php?title=United_Airlines_Flight_328&oldid=1008343193
- [8] Reuters, “Passenger sues Southwest Airlines over fatal engine explosion,” *New York Post*, Apr. 28, 2018. <https://nypost.com/2018/04/27/passenger-sues-southwest-airlines-over-fatal-engine-explosion/> (accessed Oct. 19, 2018).
- [9] European Aviation Safety Agency, “Certification Specifications for Engines CS-E.” European Aviation Safety Agency, Dec. 23, 2010.
- [10] Federal Aviation Administration., “Federal aviation regulation part 33, Section 33.94. 1984.” <https://www.gpo.gov/fdsys/pkg/CFR-2008-title14-vol1/pdf/CFR-2008-title14-vol1-sec33-94.pdf>
- [11] Federal Aviation Administration, “Federal aviation regulation part 25.”
- [12] K. S. Carney, C. Lawrence, and D. Carney, “Aircraft engine blade-out dynamics,” Livermore CA, USA, p. 11.
- [13] T. J. Vasco, “Fan blade bird-strike analysis and design,” 2000.

- [14] K. S. Carney, J. M. Pereira, D. M. Revilock, and P. Matheny, "Jet engine fan blade containment using an alternate geometry," *Int. J. Impact Eng.*, vol. 36, no. 5, pp. 720–728, May 2009, doi: 10.1016/j.ijimpeng.2008.10.002.
- [15] S. Dolci, K. S. Carney, L. Wang, P. Du Bois, and C.-D. Kan, "The effect of Inconel-718 high strain rate sensitivity on ballistic impact response using *MAT_224," 2018, p. 16.
- [16] "Adiabatic shear band," *Wikipedia*. Nov. 11, 2014. Accessed: Oct. 25, 2018. [Online]. Available: https://en.wikipedia.org/w/index.php?title=Adiabatic_shear_band&oldid=633356643
- [17] J. Peirs *et al.*, "Microstructure of adiabatic shear bands in Ti6Al4V," *Mater. Charact.*, vol. 75, pp. 79–92, Jan. 2013, doi: 10.1016/j.matchar.2012.10.009.
- [18] P. Landau, S. Osovski, A. Venkert, V. Gärtnerová, and D. Rittel, "The genesis of adiabatic shear bands," *Sci. Rep.*, vol. 6, no. 1, Dec. 2016, doi: 10.1038/srep37226.
- [19] Q. H. Zhang, B. L. Li, X. Chen, J. M. Yin, Z. R. Nie, and T. Y. Zuo, "Characteristic microstructure and microstructure evolution in Al–Cu–Mn alloy under projectile impact," *Mater. Sci. Eng. A*, vol. 531, pp. 12–17, Jan. 2012, doi: 10.1016/j.msea.2011.09.109.
- [20] G. R. Johnson and W. H. Cook, "Fracture characteristics of three metals subjected to various strains, strain rates, temperatures and pressures," *Eng. Fract. Mech.*, vol. 21, no. 1, pp. 31–48, Jan. 1985, doi: 10.1016/0013-7944(85)90052-9.
- [21] Center for Collision Safety and Analysis, "Material Model Development and Its Application Using Finite Element Methods in Engine Failure Analysis." unpublished, Oct. 20, 2018.
- [22] LIVERMORE SOFTWARE TECHNOLOGY CORPORATION (LSTC), "LS-DYNA®KEYWORD USER'S MANUAL VOLUME II, Material Models." http://ftp.lstc.com/anonymous/outgoing/jday/manuals/DRAFT_Vol_II.pdf (accessed Nov. 01, 2018).
- [23] D. Wedberg, "Modelling of high strain rate plasticity and metal cutting," *DIVA*, 2013, Accessed: Sep. 19, 2018. [Online]. Available: <http://urn.kb.se/resolve?urn=urn:nbn:se:ltu:diva-25989>
- [24] A. Majorell, S. Srivatsa, and R. C. Picu, "Mechanical behavior of Ti–6Al–4V at high and moderate temperatures—Part I: Experimental results," *Mater. Sci. Eng. A*, vol. 326, no. 2, pp. 297–305, Mar. 2002, doi: 10.1016/S0921-5093(01)01507-6.
- [25] T. Leguey, R. Schäublin, P. Marmy, and M. Victoria, "Microstructure of Ti5Al2.5Sn and Ti6Al4V deformed in tensile and fatigue tests," *J. Nucl. Mater.*, vol. 305, no. 1, pp. 52–59, Sep. 2002, doi: 10.1016/S0022-3115(02)00888-7.
- [26] F. C. Campbell, *Manufacturing Technology for Aerospace Structural Materials*. Elsevier, 2011.
- [27] B. Erice and F. Gálvez, "A coupled elastoplastic-damage constitutive model with Lode angle dependent failure criterion," *Int. J. Solids Struct.*, vol. 51, no. 1, pp. 93–110, Jan. 2014, doi: 10.1016/j.ijsolstr.2013.09.015.
- [28] S. Dolci, K. S. Carney, L. Wang, P. Du Bois, and C.-D. Kan, "Incorporation of Inconel-718 material test data into material model input parameters for

- *MAT_224,” presented at the 14th International LS-DYNA Users Conference, Jun. 2016.
- [29] Y. Desvallées, M. Bouzidi, F. Bois, and N. Beaude, “Delta phase in Inconel 718: mechanical properties and forging process requirements,” *Superalloys*, vol. 718, no. 625, pp. 281–291, 1994.
 - [30] S. Kalluri, K. B. S. Rao, G. R. Halford, and M. A. McGaw, “Deformation and Damage Mechanisms in Inconel 718 Superalloy,” in *Superalloys 718, 625, 706 and Various Derivatives (1994)*, 1994, pp. 593–606. doi: 10.7449/1994/Superalloys_1994_593_606.
 - [31] J. F. Radavich, “The Physical Metallurgy of Cast and Wrought Alloy 718,” in *Superalloys 718 Metallurgy and Applications (1989)*, 2004, pp. 229–240. doi: 10.7449/1989/Superalloys_1989_229_240.
 - [32] J. Belan, “High Frequency Fatigue Test of IN 718 Alloy – Microstructure and Fractography Evaluation,” *Metal. 2015*, vol. 54, no. 1, pp. 59–62, 2015.
 - [33] M. Jambor, O. Bokůvka, F. Nový, L. Trško, and J. Belan, “Phase transformations in nickel base superalloy INCONEL 718 during cyclic loading at high temperature,” *Prod. Eng. Arch.*, vol. 15, pp. 15–18, Jun. 2017, doi: 10.30657/pea.2017.15.04.
 - [34] R. G. Carlson and J. F. Radavich, “Microstructural Characterization of Cast 718,” in *Superalloys 718 Metallurgy and Applications (1989)*, 1989, pp. 79–95. doi: 10.7449/1989/Superalloys_1989_79_95.
 - [35] M. J. Donachie and S. J. Donachie, *Superalloys: A Technical Guide, 2nd Edition*. ASM International, 2002.
 - [36] A. Rusinek, J. A. Rodríguez-Martínez, and A. Arias, “A thermo-viscoplastic constitutive model for FCC metals with application to OFHC copper,” *Int. J. Mech. Sci.*, vol. 52, no. 2, pp. 120–135, Feb. 2010, doi: 10.1016/j.ijmecsci.2009.07.001.
 - [37] MatWeb, “Special Metals INCONEL® Alloy 718.” <http://www.matweb.com/search/DataSheet.aspx?MatGUID=94950a2d209040a09b89952d45086134&ckck=1> (accessed Nov. 08, 2018).
 - [38] MatWeb, “Titanium Ti-6Al-4V (Grade 5), Annealed.” <http://www.matweb.com/search/datasheet.aspx?MatGUID=a0655d261898456b958e5f825ae85390> (accessed Nov. 08, 2018).
 - [39] S. Haight, L. Wang, P. Du Bois, K. S. Carney, and C.-D. Kan, “Development of a Titanium Alloy Ti-6Al-4V Material Model Used in LS-DYNA.” May 26, 2015.
 - [40] M. Buyuk, “Development of A Tabulated Thermo-Viscoplastic Material Model with Regularized Failure for Dynamic Ductile Failure Prediction of Structures under Impact Loading,” p. 666.
 - [41] T. Nicholas, “Dynamic Tensile Testing of Structural Materials Using a Split Hopkinson Bar Apparatus;,” Defense Technical Information Center, Fort Belvoir, VA, Oct. 1980. doi: 10.21236/ADA092832.
 - [42] A. Salam, “A Literature Survey of the Combined Effects of Strain Rate and Elevated Temperature on the Mechanical Properties of Metals,” p. 131.
 - [43] J. D. Campbell and W. G. Ferguson, “The temperature and strain-rate dependence of the shear strength of mild steel,” *Philos. Mag. J. Theor. Exp. Appl. Phys.*, vol. 21, no. 169, pp. 63–82, Jan. 1970, doi: 10.1080/14786437008238397.

- [44] A. R. Dowling and J. Harding, "Tensile properties of mild steel under high strain rates," 1967.
- [45] J. D. Campbell and R. H. Cooper, "Physical basis of yield and fracture," *Inst Phys Phys Soc Co*, no. 1, p. 77, 1966.
- [46] A. R. Dowling, "The dynamic punching of metals," *J. Inst. Met.*, vol. 98, pp. 215–224, 1970.
- [47] D. Lesuer, "Experimental Investigations of Material Models for Ti-6AL4V and 2024-T3," p. 36.
- [48] G. L. Wulf, "High strain rate compression of titanium and some titanium alloys," *Int. J. Mech. Sci.*, vol. 21, no. 12, pp. 713–718, Jan. 1979, doi: 10.1016/0020-7403(79)90051-1.
- [49] Lw. Meyer, "Strength and ductility of a titanium-alloy TiAl 6 V 4 in tensile and compressive loading under low, medium, and high rates of strain," *Titan. Sci. Technol.*, pp. 1851–1858, 1985.
- [50] D. A. Gorham, "The effect of specimen dimensions on high strain rate compression measurements of copper," *J. Phys. Appl. Phys.*, vol. 24, no. 8, pp. 1489–1492, Aug. 1991, doi: 10.1088/0022-3727/24/8/041.
- [51] N. N. Dioh, A. Ivankovic, P. S. Leever, and J. G. Williams, "Stress wave propagation effects in split Hopkinson pressure bar tests," *Proc R Soc Lond A*, vol. 449, no. 1936, pp. 187–204, May 1995, doi: 10.1098/rspa.1995.0039.
- [52] J. E. Field, S. M. Walley, W. G. Proud, H. T. Goldrein, and C. R. Siviour, "Review of experimental techniques for high rate deformation and shock studies," *Int. J. Impact Eng.*, vol. 30, no. 7, pp. 725–775, Aug. 2004, doi: 10.1016/j.ijimpeng.2004.03.005.
- [53] D. Jia, "A Rigorous Assessment of the Benefits of Miniaturization in the Kolsky Bar System," *Exp. Mech.*, vol. 44, no. 5, pp. 445–454, Oct. 2004, doi: 10.1177/0014485104047608.
- [54] L. D. Oosterkamp, A. Ivankovic, and G. Venizelos, "High strain rate properties of selected aluminium alloys," *Mater. Sci. Eng. A*, vol. 278, no. 1–2, pp. 225–235, Feb. 2000, doi: 10.1016/S0921-5093(99)00570-5.
- [55] D. A. Gorham, "Specimen inertia in high strain-rate compression," *J. Phys. Appl. Phys.*, vol. 22, no. 12, pp. 1888–1893, Dec. 1989, doi: 10.1088/0022-3727/22/12/014.
- [56] Y. Shui-sheng, L. Yu-bin, and C. Yong, "The strain-rate effect of engineering materials and its unified model," *Lat. Am. J. Solids Struct.*, vol. 10, no. 4, pp. 833–844, Jul. 2013, doi: 10.1590/S1679-78252013000400010.
- [57] D. J. Steinberg and C. M. Lund, "A constitutive model for strain rates from 10–4 to 106 s⁻¹," p. 7.
- [58] J. A. RODRIGUEZ-MARTINEZ, M. RODRIGUEZ-MILLAN, A. RUSINEK, and A. ARIAS, "A dislocation-based constitutive description for modeling the behavior of FCC metals within wide ranges of strain rate and temperature," *Dislocation-Based Const. Descr. Model. Behav. FCC Met. Wide Ranges Strain Rate Temp.*, vol. 43, no. 12, pp. 901–912, 2011.

- [59] J. R. Klepaczko, "Remarks on impact shearing," *J. Mech. Phys. Solids*, vol. 46, no. 10, pp. 2139–2153, Oct. 1998, doi: 10.1016/S0022-5096(98)00025-8.
- [60] D. Rittel, G. Ravichandran, and S. Lee, "Large strain constitutive behavior of OFHC copper over a wide range of strain rates using the shear compression specimen," *Mech. Mater.*, vol. 34, no. 10, pp. 627–642, Oct. 2002, doi: 10.1016/S0167-6636(02)00164-3.
- [61] M. Vural, G. Ravichandran, and D. Rittel, "Large strain mechanical behavior of 1018 cold-rolled steel over a wide range of strain rates," *Metall. Mater. Trans. A*, vol. 34, no. 12, pp. 2873–2885, Dec. 2003, doi: 10.1007/s11661-003-0188-8.
- [62] B. A. Remington, P. Allen, E. M. Bringa, J. Hawreliak, and et al, "Material dynamics under extreme conditions of pressure and strain rate," *Mater. Sci. Technol. MST Lond.*, vol. 22, no. 4, pp. 474–488, Apr. 2006.
- [63] T. Z. Blazynski, *Materials at High Strain Rates*. Springer Science & Business Media, 1987.
- [64] A. Gilat and X. Wu, "Plastic deformation of 1020 steel over a wide range of strain rates and temperatures," *Int. J. Plast.*, vol. 13, no. 6, pp. 611–632, Jan. 1997, doi: 10.1016/S0749-6419(97)00028-4.
- [65] A. A. Gruzdkov, E. V. Sitnikova, N. F. Morozov, and Y. V. Petrov, "Thermal Effect in Dynamic Yielding and Fracture of Metals and Alloys," *Math. Mech. Solids*, vol. 14, no. 1–2, pp. 72–87, Jan. 2009, doi: 10.1177/1081286508092603.
- [66] R. W. Armstrong, W. Arnold, and F. J. Zerilli, "Dislocation Mechanics of Shock-Induced Plasticity," *Metall. Mater. Trans. A*, vol. 38, no. 11, pp. 2605–2610, Oct. 2007, doi: 10.1007/s11661-007-9142-5.
- [67] S. Nemat-Nasser, J.-Y. Choi, W.-G. Guo, and J. B. Isaacs, "Very high strain-rate response of a NiTi shape-memory alloy," *Mech. Mater.*, vol. 37, no. 2–3, pp. 287–298, Feb. 2005, doi: 10.1016/j.mechmat.2004.03.007.
- [68] A. H. Almasri and G. Z. Voyiadjis, "Effect of Strain Rate on the Dynamic Hardness in Metals," *J. Eng. Mater. Technol.*, vol. 129, no. 4, pp. 505–512, Apr. 2007, doi: 10.1115/1.2744430.
- [69] W. Moćko, J. A. Rodríguez-Martínez, Z. L. Kowalewski, and A. Rusinek, "Compressive Viscoplastic Response of 6082-T6 and 7075-T6 Aluminium Alloys Under Wide Range of Strain Rate at Room Temperature: Experiments and Modelling," *Strain*, vol. 48, no. 6, pp. 498–509, Dec. 2012, doi: 10.1111/j.1475-1305.2012.00847.x.
- [70] G. Vadillo, J. A. Rodríguez-Martínez, and J. Fernández-Sáez, "On the interplay between strain rate and strain rate sensitivity on flow localization in the dynamic expansion of ductile rings," *Int. J. Solids Struct.*, vol. 49, no. 3, pp. 481–491, Feb. 2012, doi: 10.1016/j.ijsolstr.2011.10.020.
- [71] E. N. Borodin, A. A. Gruzdkov, A. E. Mayer, and N. S. Selyutina, "Physical nature of strain rate sensitivity of metals and alloys at high strain rates," *J. Phys. Conf. Ser.*, vol. 991, p. 012012, Apr. 2018, doi: 10.1088/1742-6596/991/1/012012.
- [72] A. Almasri, "Dynamic Shear Bands in Metals under High Strain Rates," *LSU Dr. Diss.*, Jan. 2008, [Online]. Available: https://digitalcommons.lsu.edu/gradschool_dissertations/197

- [73] J. Johansson, C. Persson, G. Testa, A. Ruggiero, N. Bonora, and Colliander, "Effect of microstructure on dynamic shear localisation in Alloy 718 | Elsevier Enhanced Reader." <https://reader.elsevier.com/reader/sd/pii/S0167663616303854?token=D8B498690542F345A47DE82D6FF2D1CCDFC2E5B0D5F9C46D21B834EA370F2559A7E31825F732AE9AAA4EBC48A944D4C4> (accessed Mar. 15, 2019).
- [74] J. M. Zhang, Z. Y. Gao, J. Y. Zhuang, Z. Y. Zhong, and P. Janschek, "Strain-rate hardening behavior of superalloy IN718," *J. Mater. Process. Technol.*, vol. 70, no. 1, pp. 252–257, Oct. 1997, doi: 10.1016/S0924-0136(97)00073-3.
- [75] J. M. Pereira and B. A. Lerch, "Effects of heat treatment on the ballistic impact properties of Inconel 718 for jet engine fan containment applications," *Int. J. Impact Eng.*, vol. 25, no. 8, pp. 715–733, Sep. 2001, doi: 10.1016/S0734-743X(01)00018-5.
- [76] J. J. DeMange, V. Prakash, and J. M. Pereira, "Effects of material microstructure on blunt projectile penetration of a nickel-based super alloy," *Int. J. Impact Eng.*, vol. 36, no. 8, pp. 1027–1043, Aug. 2009, doi: 10.1016/j.ijimpeng.2009.01.007.
- [77] T. Kobayashi, J. W. Simons, C. S. Brown, and D. A. Shockey, "Plastic flow behavior of Inconel 718 under dynamic shear loads," *Int. J. Impact Eng.*, vol. 35, no. 5, pp. 389–396, May 2008, doi: 10.1016/j.ijimpeng.2007.03.005.
- [78] X. Wang, C. Huang, B. Zou, H. Liu, H. Zhu, and J. Wang, "Dynamic behavior and a modified Johnson–Cook constitutive model of Inconel 718 at high strain rate and elevated temperature," *Mater. Sci. Eng. A*, vol. 580, pp. 385–390, Sep. 2013, doi: 10.1016/j.msea.2013.05.062.
- [79] T. Sjöberg, K. G. Sundin, and M. Oldenburg, "CALIBRATION AND VALIDATION OF PLASTIC HIGH STRAIN RATE MODELS FOR ALLOY 718," p. 11.
- [80] W.-S. Lee, C.-F. Lin, T.-H. Chen, and H.-W. Chen, "Dynamic mechanical behaviour and dislocation substructure evolution of Inconel 718 over wide temperature range," *Mater. Sci. Eng. A*, vol. 528, no. 19, pp. 6279–6286, Jul. 2011, doi: 10.1016/j.msea.2011.04.079.
- [81] G. Chen, C. Ren, Z. Ke, J. Li, and X. Yang, "Modeling of flow behavior for 7050-T7451 aluminum alloy considering microstructural evolution over a wide range of strain rates," *Mech. Mater.*, vol. 95, pp. 146–157, Apr. 2016, doi: 10.1016/j.mechmat.2016.01.006.
- [82] I. Polyzois, "Finite Element Modeling of the Behavior of Armor Materials Under High Strain Rates and Large Strains," p. 119.
- [83] H. Couque, "The use of the direct impact Hopkinson pressure bar technique to describe thermally activated and viscous regimes of metallic materials," *Phil Trans R Soc A*, vol. 372, no. 2023, p. 20130218, Aug. 2014, doi: 10.1098/rsta.2013.0218.
- [84] R. W. Armstrong and S. M. Walley, "High strain rate properties of metals and alloys," *Int. Mater. Rev.*, vol. 53, no. 3, pp. 105–128, Jun. 2008, doi: 10.1179/174328008X277795.
- [85] Almasri Amin and Voyiadjis George Z., "Physically Based Constitutive Model for Body Centered Cubic Metals with Applications to Iron," *J. Eng. Mech.*, vol. 134, no. 7, pp. 521–529, Jul. 2008, doi: 10.1061/(ASCE)0733-9399(2008)134:7(521).

- [86] F. J. Zerilli and R. W. Armstrong, "Dislocation-mechanics-based constitutive relations for material dynamics calculations," *J. Appl. Phys.*, vol. 61, no. 5, pp. 1816–1825, Mar. 1987, doi: 10.1063/1.338024.
- [87] M. Ashton, "Behaviour of metals as a function of strain rate and temperature," Thesis, © Mark Ashton, 1999. Accessed: Sep. 19, 2018. [Online]. Available: <https://dspace.lboro.ac.uk/dspace-jspui/handle/2134/10449>
- [88] A. Tabei, F. H. Abed, G. Z. Voyiadjis, and H. Garmestani, "Constitutive modeling of Ti-6Al-4V at a wide range of temperatures and strain rates," *Eur. J. Mech. - ASolids*, vol. 63, pp. 128–135, May 2017, doi: 10.1016/j.euromechsol.2017.01.005.
- [89] M. Ardeljan, I. J. Beyerlein, B. A. McWilliams, and M. Knezevic, "Strain rate and temperature sensitive multi-level crystal plasticity model for large plastic deformation behavior: Application to AZ31 magnesium alloy," *Int. J. Plast.*, vol. 83, pp. 90–109, Aug. 2016, doi: 10.1016/j.ijplas.2016.04.005.
- [90] K. T. Ramesh, "High Strain Rate Part D 33. High Strain Rate and Impact Experiments," p. 31.
- [91] T. W. Wright and J. W. Walter, "On Stress Collapse in Adiabatic Shear Bands.," p. 46.
- [92] H. Feng and M. N. Bassim, "Finite element modeling of the formation of adiabatic shear bands in AISI 4340 steel," *Mater. Sci. Eng. A*, vol. 266, no. 1, pp. 255–260, Jun. 1999, doi: 10.1016/S0921-5093(99)00026-X.
- [93] W.-S. Lee and C.-F. Lin, "Plastic deformation and fracture behaviour of Ti–6Al–4V alloy loaded with high strain rate under various temperatures," *Mater. Sci. Eng. A*, vol. 241, no. 1, pp. 48–59, Jan. 1998, doi: 10.1016/S0921-5093(97)00471-1.
- [94] W.-S. Lee and C.-F. Lin, "High-temperature deformation behaviour of Ti6Al4V alloy evaluated by high strain-rate compression tests," *J. Mater. Process. Technol.*, vol. 75, no. 1, pp. 127–136, Mar. 1998, doi: 10.1016/S0924-0136(97)00302-6.
- [95] J. Delorme, "Extension of a finite element model to 2D for the prediction of adiabatic shear bands," Sep. 2012, Accessed: Sep. 19, 2018. [Online]. Available: <https://mspace.lib.umanitoba.ca/xmlui/handle/1993/8916>
- [96] M. Meyers and H.-R. Pak, "Observation_of_an_adiabatic_shear_band_i20160422-29854-16ih0oh.pdf." https://s3.amazonaws.com/academia.edu.documents/44996847/Observation_of_an_adiabatic_shear_band_i20160422-29854-16ih0oh.pdf?AWSAccessKeyId=AKIAIWOWYYGZ2Y53UL3A&Expires=1551393628&Signature=qeojPmbzd4AkEOWyf5giii05XXc%3D&response-content-disposition=inline%3B%20filename%3DObservation_of_an_adiabatic_shear_band_i.pdf (accessed Feb. 28, 2019).
- [97] U. De Andrade, M. Meyers, A. Chokshi, and K. Vecchio, "Dynamic recrystallization and grain size effects in shock hardened copper," *J. Phys. IV Colloq.*, vol. 04, no. C8, pp. C8-361-C8-366, 1994, doi: 10.1051/jp4:1994855.
- [98] J. A. Hines and K. S. Vecchio, "Recrystallization kinetics within adiabatic shear bands," *Acta Mater.*, vol. 45, no. 2, pp. 635–649, Feb. 1997, doi: 10.1016/S1359-6454(96)00193-0.

- [99] D. R. Chichili, K. T. Ramesh, and K. J. Hemker, “Adiabatic shear localization in α -titanium: experiments, modeling and microstructural evolution,” *J. Mech. Phys. Solids*, vol. 52, no. 8, pp. 1889–1909, Aug. 2004, doi: 10.1016/j.jmps.2004.02.013.
- [100] S. Medyanik, W. Liu, and S. Li, “On criteria for dynamic adiabatic shear band propagation,” *J. Mech. Phys. Solids*, vol. 55, no. 7, pp. 1439–1461, Jul. 2007, doi: 10.1016/j.jmps.2006.12.006.
- [101] M. Dolinski, D. Rittel, and A. Dorogoy, “Modeling adiabatic shear failure from energy considerations,” *J. Mech. Phys. Solids*, vol. 58, no. 11, pp. 1759–1775, Nov. 2010, doi: 10.1016/j.jmps.2010.08.007.
- [102] D. Rittel, “A different viewpoint on adiabatic shear localization,” *J. Phys. Appl. Phys.*, vol. 42, no. 21, p. 214009, Nov. 2009, doi: 10.1088/0022-3727/42/21/214009.
- [103] S. Boakye-Yiadom, “Microstructural evolution of adiabatic shear bands in steel by impact,” 2014, Accessed: Sep. 19, 2018. [Online]. Available: <https://mspace.lib.umanitoba.ca/xmlui/handle/1993/24095>
- [104] W. Song, M. Hu, H. Zhang, and Y. Jin, “Effects of different heat treatments on the dynamic shear response and shear localization in Inconel 718 alloy | Elsevier Enhanced Reader.” <https://reader.elsevier.com/reader/sd/pii/S0921509318305070?token=1B20F65DB474A87503BCCD9A9674329D8BEB3E2BC05C19315F068F2B8875BB3094A3DE56F402F5B15832A6E248B72C7C> (accessed Mar. 15, 2019).
- [105] J. Johansson, C. Persson, H. Lai, and M. Hörnqvist Colliander, “Microstructural examination of shear localisation during high strain rate deformation of Alloy 718,” *Mater. Sci. Eng. A*, vol. 662, pp. 363–372, Apr. 2016, doi: 10.1016/j.msea.2016.03.080.
- [106] J. Lorentzon, N. Järvstråt, and B. L. Josefson, “Modelling chip formation of alloy 718,” *J. Mater. Process. Technol.*, vol. 209, no. 10, pp. 4645–4653, Jun. 2009, doi: 10.1016/j.jmatprotec.2008.11.029.
- [107] F. Jafarian, M. Imaz Ciaran, D. Umbrello, P. J. Arrazola, L. Filice, and H. Amirabadi, “Finite element simulation of machining Inconel 718 alloy including microstructure changes,” *Int. J. Mech. Sci.*, vol. 88, pp. 110–121, Nov. 2014, doi: 10.1016/j.ijmecsci.2014.08.007.
- [108] T. Ozel, I. Llanos, J. Soriano, and P.-J. Arrazola, “3d Finite Element Modelling of Chip Formation Process for Machining Inconel 718: Comparison of Fe Software Predictions,” *Mach. Sci. Technol.*, vol. 15, no. 1, pp. 21–46, Apr. 2011, doi: 10.1080/10910344.2011.557950.
- [109] “The heat developed during plastic extension of metals,” p. 30.
- [110] I. Taylor, “The plastic distortion of metals,” p. 44.
- [111] G. Ravichandran, “On the Conversion of Plastic Work into Heat During High-Strain-Rate Deformation,” in *AIP Conference Proceedings*, Atlanta, Georgia (USA), 2002, vol. 620, pp. 557–562. doi: 10.1063/1.1483600.
- [112] P. Rosakis, A. J. Rosakis, G. Ravichandran, and J. Hodowany, “A thermodynamic internal variable model for the partition of plastic work into heat and stored energy

- in metals,” *J. Mech. Phys. Solids*, vol. 48, no. 3, pp. 581–607, Mar. 2000, doi: 10.1016/S0022-5096(99)00048-4.
- [113] D. Rittel, L. H. Zhang, and S. Osovski, “The dependence of the Taylor–Quinney coefficient on the dynamic loading mode,” *J. Mech. Phys. Solids*, vol. 107, pp. 96–114, Oct. 2017, doi: 10.1016/j.jmps.2017.06.016.
- [114] R. Zaera, J. A. Rodríguez-Martínez, and D. Rittel, “On the Taylor–Quinney coefficient in dynamically phase transforming materials. Application to 304 stainless steel,” *Int. J. Plast.*, vol. 40, pp. 185–201, Jan. 2013, doi: 10.1016/j.ijplas.2012.08.003.
- [115] X. Teng, “High Velocity Impact Fracture,” p. 330.
- [116] P. Redanz, N. A. Fleck, and R. M. McMECKING, “Failure of a Porous Solid from a Deep Notch,” p. 17.
- [117] V. Tvergaard and A. Needleman, “Effects of nonlocal damage in porous plastic solids,” *Int. J. Solids Struct.*, vol. 32, no. 8–9, pp. 1063–1077, Apr. 1995, doi: 10.1016/0020-7683(94)00185-Y.
- [118] “Inconel 718 Tech Data.”
<http://www.hightempmetals.com/techdata/hitempInconel718data.php> (accessed Mar. 23, 2021).
- [119] A. Ressa, T. Liutkus, J. D. Seidt, and A. Gilat, “Time Dependent Response of Inconel 718,” in *Challenges in Mechanics of Time Dependent Materials, Volume 2*, Cham, 2016, pp. 101–104. doi: 10.1007/978-3-319-22443-5_12.
- [120] AWG, “LS-DYNA Aerospace Working Group Modeling Guidelines Document.” 30 2019.
- [121] M. Zhou, A. J. Rosakis, and G. Ravichandran, “Dynamically propagating shear bands in impact-loaded prenotched plates—I. Experimental investigations of temperature signatures and propagation speed,” *J. Mech. Phys. Solids*, vol. 44, no. 6, pp. 981–1006, Jun. 1996, doi: 10.1016/0022-5096(96)00003-8.
- [122] D. Rittel, “On the conversion of plastic work to heat during high strain rate deformation of glassy polymers,” *Mech. Mater.*, vol. 31, no. 2, pp. 131–139, Feb. 1999, doi: 10.1016/S0167-6636(98)00063-5.
- [123] J. M. Pereira, D. M. Revilock, and C. R. Ruggeri, “Impact Testing of Inconel 718 for Material Impact Model Development,” p. 164, 2020.
- [124] Z. Rosenberg and E. Dekel, *Terminal Ballistics*. Cham: Springer International Publishing, 2020. doi: 10.1007/978-3-030-46612-1.

BIOGRAPHY

Stefano Dolci graduated from Liceo Classico Celana, Italy in 2000 (high school). He received his Laurea in Aerospace engineering from Politecnico di Milano, Italy in 2007 (B.Sc. equivalent). He received his Laurea Specialistica in Aeronautical engineering in 2012 (M.Sc. equivalent) after spending two years working at The George Washington University. Since 2013 he has been working as a research associate for the Center for Collision Safety and Analysis (CCSA) at George Mason University.